New nitrogen-containing materials for hydrogen storage and their characterization by high-pressure microbalance

Vestbø, Andreas Peter

Publication date:
2009

Document Version
Publisher's PDF, also known as Version of record

NEW NITROGEN-CONTAINING MATERIALS FOR HYDROGEN STORAGE AND THEIR CHARACTERIZATION BY HIGH PRESSURE MICROBALANCE

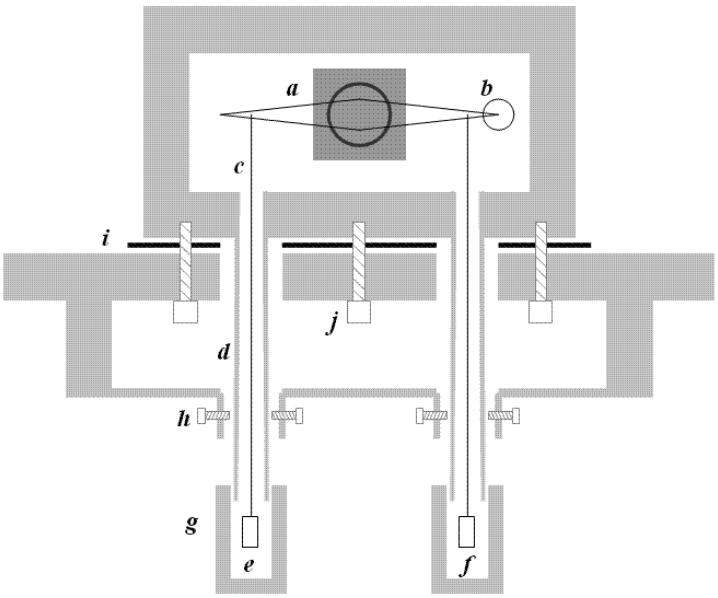

Ph.D. Thesis

Andreas Peter Vestbø

December 2008

Department of Chemistry
Technical University of Denmark

NEW NITROGEN-CONTAINING MATERIALS FOR HYDROGEN STORAGE AND THEIR CHARACTERIZATION BY HIGH PRESSURE MICROBALANCE

Ph.D. Thesis

Supervisors: *Associate Professor Jens Oluf Jensen*
Professor Niels J. Bjerrum

Andreas Peter Vestbø
December 2008

Department of Chemistry
Technical University of Denmark

PREFACE

This thesis was written as part of the requirements for obtaining a Ph.D. degree at the Technical University of Denmark. The main part of the work was done at the Department of Chemistry and in the Energy and Materials Science group in the time period November 2005 to July 2008. During the summer of 2007 I had the pleasure of having a stay of research in the group of Professor Ping Chen at the Department of Physics at the National University of Singapore. This was a very fruitful time with much inspiration and obtained experience in the specialized field of hydrogen storage in complex hydrides. I am especially indebted to Dr. Zhitao Xiong of her group who provided me with the opportunity to study together with such experienced people in the field.

During this study, I involuntarily learned the inherit difficulty of experimental research with complex hydrides. Work with these substances had to necessarily be kept away from atmospheric air at all times, because of their volatility. This means that virtually every experimental procedure had to be done in glovebox environments. Even in a fully equipped laboratory for inorganic chemistry with many workplaces with gloveboxes like in the Energy and Materials Science group, many additions for equipment had to be made, and this is undoubtedly generally the circumstance for labs everywhere that desire to embark in this field.

The thesis therefore includes some weight on experimental methods, especially the development of a high pressure microbalance for measuring pressure-composition isotherms on hydrogen storage materials. This piece of equipment is a counter-part to the Sieverts' apparatus which calculates hydrogen uptake indirectly by measuring the pressure change in a closed system. Together with the volumetric Sieverts' type, it serves as a heart in any laboratory for work on hydrogen storage materials.

Despite the large volume of research done worldwide and seemingly modest returns in terms of workable materials for practical use, I personally feel that the field still contains much promise for solutions for practical hydrogen storage and that we soon or later will see it used in mass scale. The field can barely said to have left the stage of infancy in terms of development, and new and surprising results are often seen, which leads to surges of new or renewed interest and efforts. Other opinions are of course present. In the opinion of one researcher (whose name will left unsaid) in a prominent group, he would like to abandon research among complex hydrides and start working on magnesium hydride! Of course, magnesium hydride is a classic among metal hydrides and work has been attempted for decades to realize this old dream to make it suitable for practical applications.

The experimental work in relation to the thesis contained many attempts that were not successful and are not contained or only shortly referred to in this text—however they led to the end results which are presented here.

Many thanks go to Dr. Jens Oluf Jensen for his constant willingness to put work aside amid a hectic work schedule and guide me in my efforts. His enthusiasm for hydrogen storage was contagious and

led me to do decide to do this study. Also thanks to Professor Niels J. Bjerrum for his good guidance throughout the study. Much collaboration was made with the Hydrogen Storage Group headed by Dr. Allan Schrøder Pedersen and Dr. Tejs Vegge at Risø-DTU and thanks go to them for good discussions and help with experimental work.

Andreas Peter Vestbø

DTU, Lyngby, November 19th 2008

ABSTRACT

Hydrogen storage for practical applications is under intense scrutiny worldwide since hopes are prevalent of being able to use hydrogen as energy vector in a continually difficult time in terms of having access to clean and affordable energy in the world. Hydrogen can be stored in compressed or liquid form, technologies that are well developed and usable, but not energy efficient. Certain metals and alloys are able to contain hydrogen within practical pressure and temperature ranges very efficient volume-wise, but they are too heavy for use in cars. Recently, attention has turned to the so-called *complex hydrides*, which contain hydrogen bound covalently often in very light materials involving elements such as lithium, sodium, nitrogen and aluminum. While these materials typically have high decomposition temperatures, the combination with other compounds helps to destabilize the material resulting in lowered effective dehydrogenation temperatures.

From the discovery in 1996 by Borislav Bogdanović and his group that catalyzed sodium alanate, $NaAlH_4$, can release hydrogen reversibly below 200 °C relatively fast, hydrogen storage in nitrogen-containing compounds beginning with lithium nitride, Li_3N, was considered a next major step in the succession of research in complex hydrides. Many complex hydrides involving nitrogen are presently under examination. This thesis reviews some of the results so far and embarks on a study of hydrogen storage in some of the compounds.

Following a brief introduction in Chapter 1, Chapter 2 of the text deals with general principles and an overview for hydrogen storage in solid materials.

Chapter 3-5 deals with the development of an in-house high pressure microbalance in a glovebox built from scratch for the use of characterizing new hydrogen storage materials including giving an example of characterization on a well-known hydrogen storage material, $CaNi_5$.

Chapter 6 contains results on a new system based on Li, Al and N for hydrogen storage. It was shown that Li_3AlN_2 can be synthesized from Li_3N and Al under nitrogen pressure. Furthermore, the compound was proven to be able to store hydrogen reversibly.

Chapter 7 describes first time results for a new hydrogen system based on Li, Si, and N. It discusses the synthesis of Li_5SiN_3 and Li_2SiN_2. Li_5SiN_3 was treated in-depth and was seen to be able to store hydrogen reversibly at fairly moderate conditions. Furthermore, the effect of doping a system of lithium amide and silicon, $LiNH_2$+Si, with $TiCl_3$ was examined, showing vastly improved desorption conditions with increased doping loads.

Chapter 8 is about the newly publicized “hydrogen” pill, which in this work was attempted to be turned into a real hydrogen pill as opposed to an ammonia pill. The findings point to the possibility of combining the material in the ammonia pill with other compounds, which make it possible to store hydrogen reversibly.

RESUMÉ

Brintlagring til praktiske anvendelser er genstand for grundig forskning verden over, idet håbet er stort med hensyn til at kunne bruge brint som energivektor i en stadig sværere tid i forhold til at have adgang til grøn og økonomisk energi i verden. Brint kan lagres i komprimeret form eller på væskeform—teknologier der er veludviklede og brugbare, dog ikke energieffektive. Visse metaller og legeringer er i stand til at opbevare brint inden for praktiske tryk- og temperaturgrænser særligt effektivt volumetrisk set, men de for tunge til at kunne anvendes i biler. På det sidste er man begyndt at fokusere på de såkaldte *komplekse hydrider*, hvilke indeholder brint bundet kovalent i ofte meget lette materialer der indeholder grundstoffer såsom lithium, natrium, nitrogen og aluminium. Selv om disse materialer typisk har høje dekomponeringstemperaturer, kan en kombination med andre stoffer forårsage, at materialet bliver destabiliseret, hvilket resulterer i lavere effektive de-hydrogeneringstemperaturer.

Siden opdagelsen i 1996 af Borislav Bogdanović og hans gruppe, at katalyseret natrium alanat, $NaAlH_4$, kan afgive brint reversibelt under 200 °C relativt hurtigt, blev brintlagring i stoffer indeholdende nitrogen begyndende med lithiumnitrid, Li_3N, afset for at være et stort næste skridt i rækkefølgen af forskning inden for komplekse hydrider. Mange komplekse hydrider med nitrogen er i øjeblikket genstand for stor opmærksomhed. Denne afhandling gennemgår nogle af resultaterne til dato og begiver sig ind på et studium af brintlagring i nogle af stofferne.

Efter en kort indledning i Kapitel 1, handler Kapitel 2 om generelle principper og et overblik over brintlagring i faste stoffer.

Kapitel 3-5 handler om udvikling af en højtryksmikrovægt i en handskeboks, der blev bygget fra bunden af, til brug af at karakterisere nye brintlagringsmaterialer, inklusive et eksempel på karakterisering af et velkendt brintlagringsmateriale, $CaNi_5$.

Kapitel 6 indeholder resultater for et nyt system baseret på Li, Al og N til brintlagring. Det blev vist, at Li_3AlN_2 kan syntetiseres fra Li_3N og Al under nitrogentryk. Materialet blev vist at kunne large brint reversibelt.

Kapitel 7 beskriver resultater, publiceret for første gang, for et nyt system baseret på Li, Si og N. Synteser af Li_5SiN_3 og Li_2SiN_2 belyses. Li_5SiN_3 blev undersøgt detaljeret og fremviste at kunne lagre brint reversible ved relativt moderate forhold. Effekten af at dope et system med lithiumamid og silicium, $LiNH_2$+Si, med $TiCl_3$ blev også undersøgt, og det blev vist at øget dopingmængde giver væsentligt forbedrede desorptionsforhold.

Kapitel 8 omhandler den nylige publicerede ”brintpille”, hvilken i dette arbejde blev forsøgt at blive omdannet til en reel brintpille i forhold til en ammoniakpille. Resultaterne peger på muligheder for at kombinere materialet i ammoniakpillen med andre stoffer, som gør det muligt at opbevare brint reversibelt.

TABLE OF CONTENTS

1 INTRODUCTION

On January 28, 2003, President George W. Bush in his State of the Union address said:

"A single chemical reaction between hydrogen and oxygen generates energy, which can be used to power a car—producing only water, not exhaust fumes. With a new national commitment, our scientists and engineers will overcome obstacles to taking these cars from laboratory to showroom, so that the first car driven by a child born today could be powered by hydrogen, and pollution-free. Join me in this important innovation to make our air significantly cleaner, and our country much less dependent on foreign sources of energy.."[1]

These words carried a lot of weight especially because they were accompanied with a budget for $1.2 billion dollars over 5 years.

On April 27, 2004, as a first installment of the budget, $575 million dollars was set apart for four main areas: 1) Infrastructure research, 2) hydrogen storage research, 3) fuel cell research, 4) hydrogen technology education projects.[2]

Earlier that year, in March, an announcement from the EU showed that USA is not alone in its interest in the hydrogen economy. €100 million was set apart. Furthermore, Japan doubled its budget in 2003 to $268 million on hydrogen energy research compared to 2002.[3]

Since then with oil prices rising continually to a record high of $147 per barrel in July this year, green energy has been more often and more forcefully been publicized.

Why this attention?

One reason is that the fossil fuels, mined from the underground, emit CO_2 which is an unwanted addition to the global ecosystem. Pollution and the greenhouse effect are unwanted side-effects.

Second, the season of easy access to crude oil is believed to be over.[4] The arguments are that the greatest oil fields have already been discovered, new large findings are getting scarcer, and expenses to extract oil from the existing field are increasing as the oil is harder and harder to get to.[5]

Green energy is a term that embraces technologies of sustainable energy such as wind power, hydropower, geothermal energy, solar energy (meaning solar panels), and tidal power. Hydrogen may play a part in these as a carrier of energy, when excess electricity is created.

The use of hydrogen has the benefit of having water as its byproduct when it is being used as fuel:

$$2H_2 + O_2 \rightarrow \text{energy} + 2H_2O \qquad (1)$$

Hydrogen can be burned in internal combustion engines just like fossil fuels, but the thermal efficiency is limited by the thermodynamical carnot limit, which is about 25% for hydrogen-air

mixtures. Fuel cells in which the reaction above proceeds electrochemically, however, escape this limit: about 50-60% can be reached, twice as much as the thermal process.[6]

The four areas listed above receiving funding are fundamentals pillars in advancing the use of hydrogen as part of an advent of green energy in the world.

The second item—efficient and safe storage of hydrogen (especially in connection with on-board storage in cars)—is a major factor that is yet a very active research field. While many approaches show promise, all state-of-the art technology so far has disadvantages which disqualify them for economical use. The aim is to develop a system that will fulfill certain requirements such as weight limit, safety, and cost.

The present work reviews methods of hydrogen storage and focuses on storage in solid materials, particularly newer materials—the complex hydrides. Much experimental work was connected a study of complex hydrides including the construction of a high pressure microbalance for the precise characterization of hydrogen storage properties for new materials. Propositions for 3 new types of systems are given together with experimental results—common for them is that they utilize nitrogen as a component in various forms.

2 COMPACT HYDROGEN STORAGE: A BIG CHALLENGE

Storing hydrogen is not a challenge in itself and the technique is today fully developed. Just go to the laboratory and find a pressurized flask of hydrogen stored at 200 bar pressure. Using hydrogen in the laboratory for small-scale experiments is one thing. Another is to have a storage unit of hydrogen that will function as on-board fuel in a car. Mobile transport is of course a major constituent of modern infrastructure, and using a car as model system for obtaining a solution for hydrogen storage seems inevitable for hydrogen energy to have a great impact on society.

For cars, hydrogen storage must be

1) compact
2) quick reloading of hydrogen
3) safe for humans

It is estimated that a modern, commercially available car optimized for mobility with a range of 400 km burns about 24 kg of petrol in a combustion engine; if hydrogen is used as fuel in a combustion engine, only 8 kg is needed. Using a fuel cell, only 4 kg hydrogen is needed.[6]

At room temperature and atmospheric pressure, 4 kg of hydrogen takes up a volume of 45 m^3. This is the volume of a balloon of 4.5 m diameter. To store hydrogen on-board a car, the hydrogen must therefore be in a compact form.

Three types of storage are considered which all has hydrogen compacted in different ways. The three types are:

1) High-pressure storage (compressed hydrogen)
2) Cryostorage (liquid hydrogen)
3) Storage in solid materials (compacted hydrogen)

Another exists which is not considered in the present treatment, namely on-board reforming of liquid hydrogen containing fuels. Methanol is among potent candidates in this respect.[4] Hydrocarbon reforming is also possible, but this approach is now considered obsolete, and research in car companies has stopped within this field.[6]

2.1 High-pressure storage

The most straightforward and conventional way to store compact hydrogen is to compress it into metal vessels. This is simple solution and unfortunately even at a high pressure of 200 bar, 4 kg hydrogen takes up a lot of space. Figure 1 shows a comparison of how much volume 4 kg hydrogen takes up in different storage alternatives. It is obvious that storing the fuel at 200 bar is insufficient for use in a car. Hydrogen at higher pressures will take up smaller space, but at the same time the strength of the vessel that holds the hydrogen must be taken into consideration.

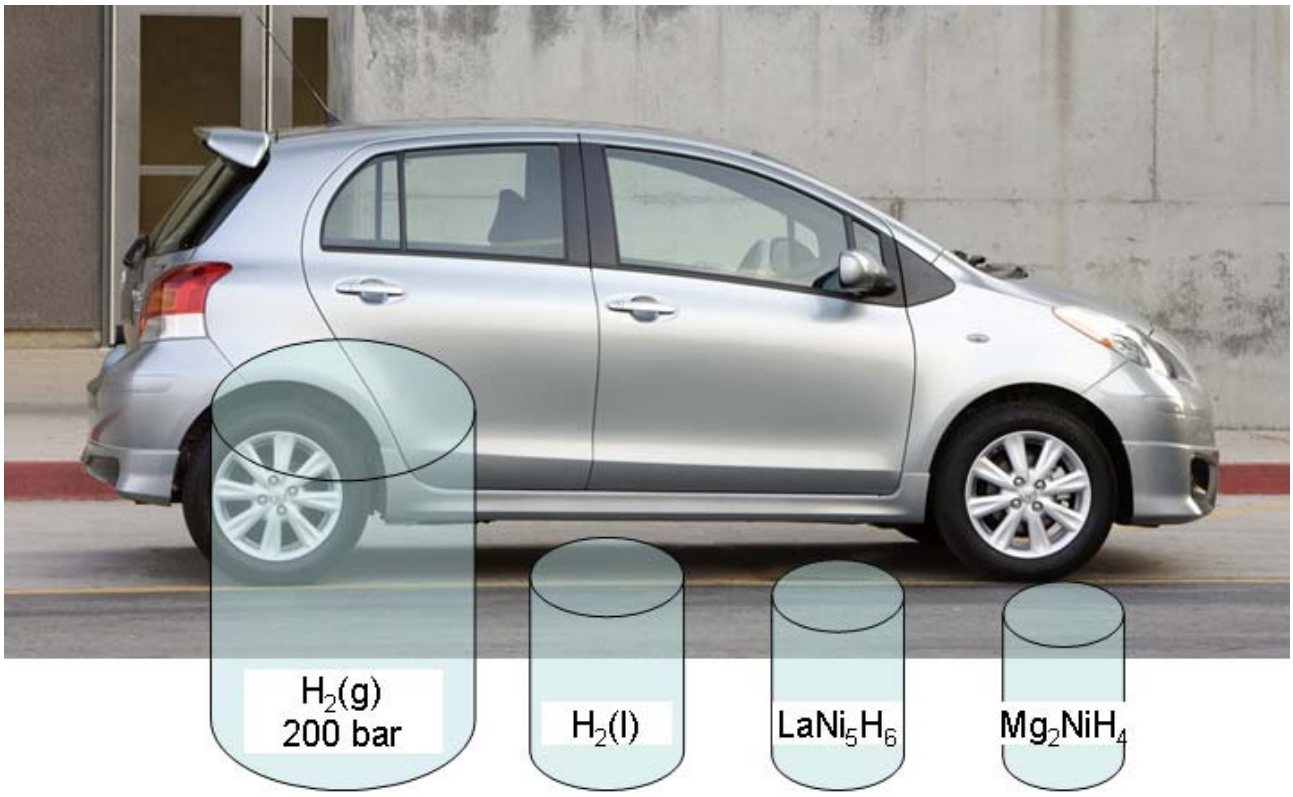

Figure 1 Volume of 4 kg hydrogen compacted in different ways with size relative to the size of a car. The large tank to the left represents high-pressure storage (after illustration in ref. 6).

2.1.1 Material strength

If hydrogen is stored at high pressure, the material used for the tank becomes important. One important property for the material is the tensile strength. Figure 2 shows a diagram of a cross-section of a cylindrical pressure vessel as seen from above. The gas presses equally on all wall elements with an effectual normal force. In the diagram, p is the gas pressure, r the inner radius of the vessel, and t is the thickness of the wall.

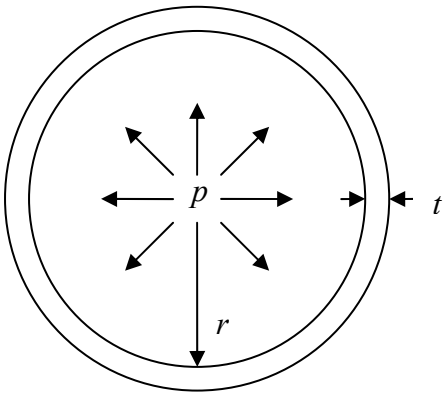

Figure 2 Schematic cross-section of a pressure vessel as seen from above.[7]

To ensure that no yield occur the following relationship must be fulfilled:

$$p * r / t < \sigma_y \quad (2)$$

where σ_y is the yield strength of the material (1500-1900 MPa for pressure vessel steel).[7] It is apparent that a higher pressure or a larger ratio of inner radius to wall thickness will require a material with proportionally higher yield strength.

By using materials reinforced by carbon fibers, up to 700 bar can be withstood. However, because hydrogen reacts with the materials at this pressure, an inert inner coating such as aluminium is put in the tank. Or the other way around: the tank would be made of aluminium and then strengthened by the carbon fiber reinforced material. This kind of tank has been tested to work for up to 700 bar, and in 2008 General Motors started a demonstration project of fuel cell cars using cylinders with hydrogen at this pressure. 4 kg hydrogen at 700 bar has a volume of about 115 L and if contained in a spherical tank, its diameter would only be 60 cm.[6]

2.1.2 Work of compression

A disadvantage in regard to using high-pressure storage is the energy that must be spent on the compression of the hydrogen gas:

Isothermal compression:

$$w = -nRT \ln (V_1/V_o) = p_o V_o \ln (p_1/p_o) \quad (3)$$

Adiabatic compression:

$$w = \frac{\gamma}{\gamma - 1} p_o V_o \left(\frac{p_1}{p_o} \right)^{\frac{\gamma - 1}{\gamma}} - 1 \qquad (4)$$

where w is the compression work, p_o the initial pressure, p_1 the final pressure, V_o the initial specific volume of hydrogen (11.11 m^3 kg^{-1} at STP), and γ the heat capacity ratio (C_p/C_v = 1.41 for H_2).[7]

Figure 3 shows the ratio between the compression work and the higher heating value (energy output as heat when hydrogen and oxygen are converted to steam) as a function of the final pressure for both isothermal and adiabatic compression.

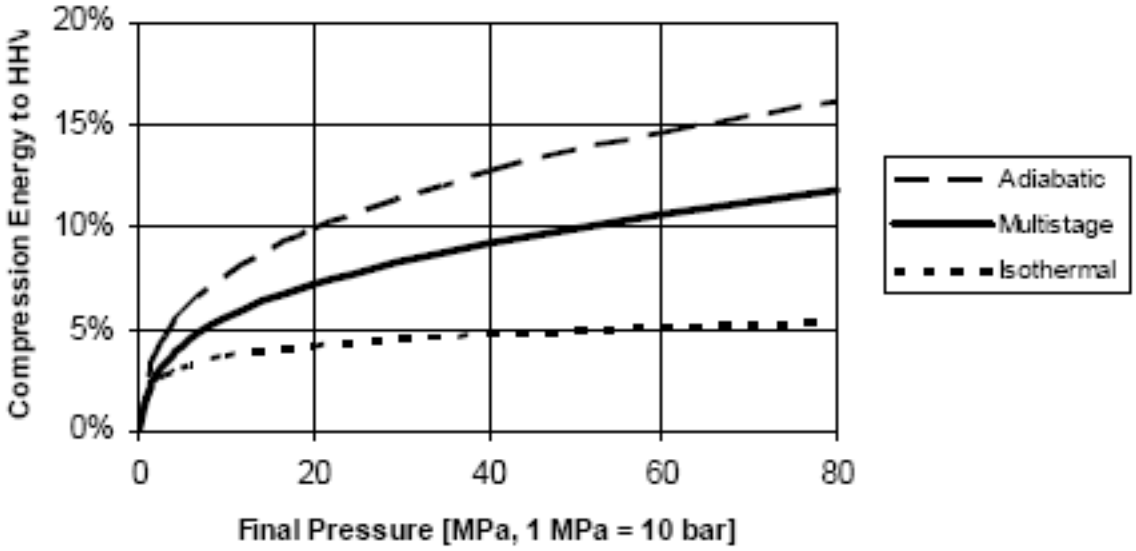

Figure 3 Relationship between the compression energy/HHV ratio and the final pressure.[8]

In practice, multi-stage compressors with intercoolers are used which operate somewhere between the two limiting cases (also shown in the figure).[8]

As can be seen, compressions to 700 bar use more than 10% of the higher heating value, which is a substantial loss in the overall efficiency.

Another disadvantage is the psychological impact of knowing that you are driving around with gas at extreme pressure in a container that can potentially explode, which is a big deterrent.

2.2 Cryostorage

Another approach is to store hydrogen at temperatures where it is liquid. Hydrogen takes up even less space if it exists as liquid (see Figure 1).

2.2.1 Density of hydrogen

Figure 4 shows the relationship between the density of hydrogen and pressure. It is evident that the density of liquid hydrogen far exceeds that of gas even if the pressure is above 1,000 bar. When the ideal gas approximation is used, there is a convergence at about 900 bar, but the compression factor of hydrogen at 1,000 bar and 300 K is in fact 1.636, signifying a great divergence from ideal gas behavior.[9]

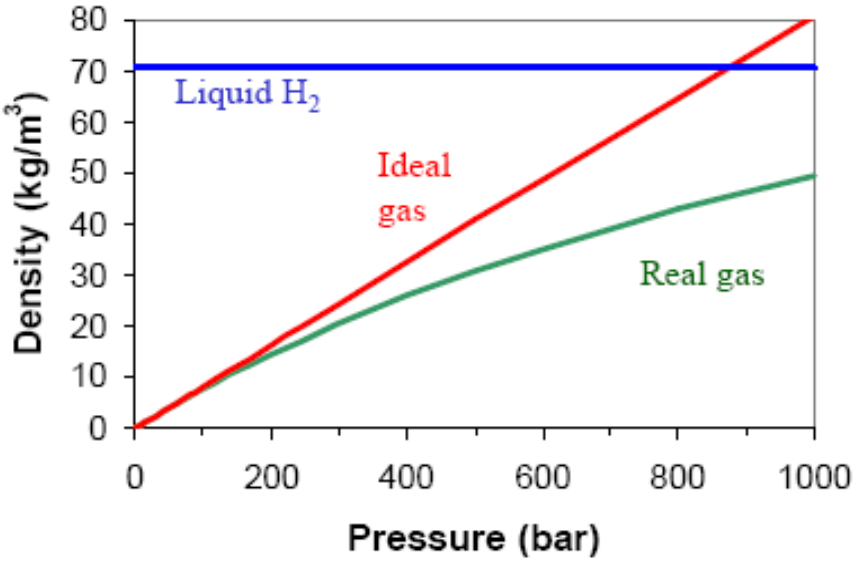

Figure 4 The density of hydrogen in liquid and gas state. The ideal gas approximation is insufficient at extreme pressures which are used for high-pressure storage.[9]

A problem associated with using liquid hydrogen is that its boiling point is extremely low, 20.3 K.[10] Even though hydrogen can be liquefied and kept stored in insulated vessel, heating inevitably occurs within the tank. The critical temperature lies at 33.23 K above which the liquid state of hydrogen does not exist. The result is that hydrogen eventually boils off and is lost. It is estimated that although the boil-off the first three days are negligible, it will amount to roughly 1% per day hereafter.[11]

This might not appear like a big problem for use in a car that is driven often, but if the fuel is not spent within a few days the loss due to evaporation is a disadvantage to the cryogenic storage solution indeed.

2.2.2 Work of liquefaction

Since significant energy must be spent to condensate the hydrogen gas, it puts limitations on where the condensation process can be performed. Figure 5 represents the ratio of the liquefaction energy to the higher heating value of hydrogen as a function of the hydrogen liquefaction plant capacity. It is seen that the plant must be significant in size in order to approach even 25%.

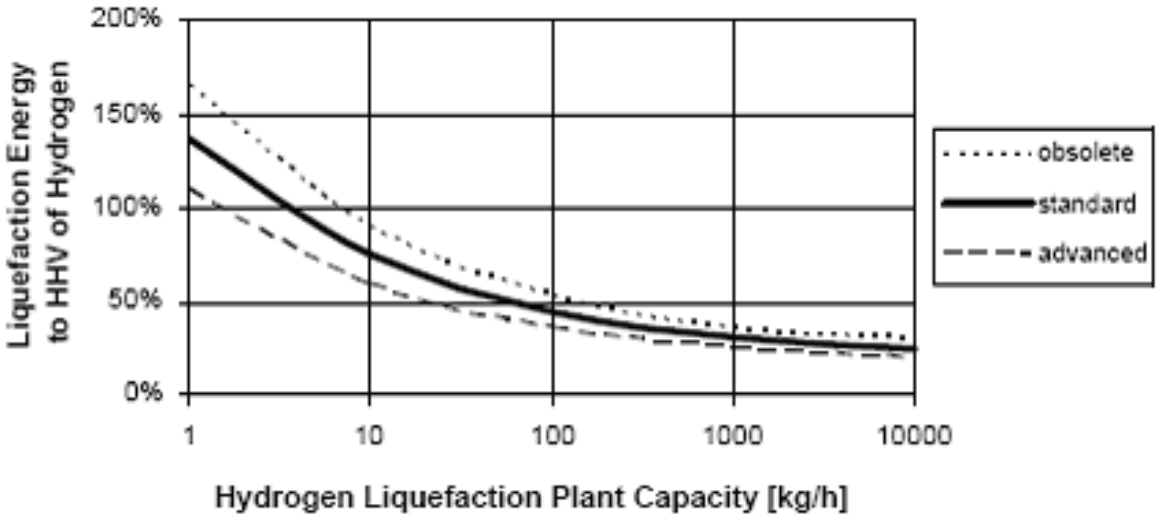

Figure 5 The relationship between liquefaction energy/HHV of hydrogen and the capacity of a hydrogen liquefaction plant. Three different standards for technology are represented.[8]

It is concluded that storage of hydrogen through high-pressure compression or liquefaction are both costly in terms of energy.

2.3 HYDROGEN STORAGE IN SOLID MATERIALS

In the previous section, two approaches to the challenge of storing hydrogen efficiently and safely have been reviewed namely high-pressure storage and cryostorage.

A third approach is to store hydrogen in solid materials. To appreciate some of the advantages by taking this route to answer the challenge of storing hydrogen efficiently and safely, it is useful to consider the data listed in Table 1, which contains values for essential parameters for hydrogen in relation to energy value and safety.

The lower heating value for hydrogen corresponds to liquid water being the product. If steam is the product, the value would be slightly lower (higher heating value).[12]

In terms of ignition, it is seen, that hydrogen very prone to catch fire. The minimal ignition energy is one tenth of that of petrol, and the ignition limit in air constitutes a broad range. Also, the quick

dispersion of hydrogen, whether burning or not, completes the picture of a subtle substance that calls for concern with regard to safety.

Table 1 Physical and chemical properties of hydrogen, methane and petrol. Values for methane (natural gas) and petrol are included for comparison to hydrogen.[11]

Property	Hydrogen (H_2)	Methane (CH_4)	Petrol ($-CH_2-$)
Lower heating value (kWh kg^{-1})	33.33	13.9	12.4
Self-ignition temperature (°C)	585	540	228-501
Flame temperature (°C)	2,045	1875	2,200
Ignition limits in air (Vol%)	4-75	5.3-15	1.0-7.6
Minimal ignition energy (mW s)	0.02	0.29	0.24
Flame propagation in air (m s^{-1})	2.65	0.4	0.4
Diffusion coefficient in air (cm^2 s^{-1})	0.61	0.16	0.05

Perhaps one of the major advantages of storage in solid materials is the safety issue because the hydrogen is stored inside the chemical structure of the material (which hopefully is not a safety concern in itself). This means that the fuel cannot be burned directly as a whole in contact with fire, and release from the material normally takes several hours. This and other essential issues are summarized in Table 2 based on the study of this author.

Table 2 Rough comparison of essential issues for the three main approaches to hydrogen storage

Issue	High-pressure storage	Cryostorage	Solid storage
Volume	Large	Medium	Small
Weight	Medium	Medium	Variable
Safety	Variable	High	Low
Establishment	Well-established	Medium to low	Low

The technology of storage in solid materials are not as mature as the other two which are more straight-forward. However, during the last decade or so there has been a surge in development, and the efforts seem to steadily increase.

2.3.1 Requirements for solid storage materials

It has been estimated that an acceptable weight and volume of a storage vessel in a car is around 100 kg and 100 L, respectively.[11] Based on these numbers and on other considerations[6], the data in Table 3 represent requirements for hydrogen storage systems as gathered by Schüth et al.[11] The US Department of Energy (DoE) have also set forth some milestones as goals for development of hydrogen storage systems, which are included. Note that the density values are for the entire system including tank etc.

Table 3 Requirements for solid materials for hydrogen storage[11]

Property	Schüth	DoE 2005	DoE 2010	DoE 2015
Gravimetric storage density (kg H_2 / kg system, wt%)	6.5	4.5	6.0	9.0
Volumetric storage density (kg H_2 / 100 L system)	6.5	3.6	4.5	8.1
Dehydrogenation kinetics (deliver)	3 h			
Rehydrogenation kinetics (refuel) (minutes)	5	8	3	2
Rehydrogenation conditions	< 50 bar	< 80 °C	< 80 °C	< 80 °C
Equilibrium pressure	Around 1 bar near room temperature			
Life cycles	500	500	1,000	1,500

One of the most important properties among the ones listed is the gravimetric storage. The volumetric storage density is easily fulfilled for many materials (refer to Figure 1—hydrogen is extremely compact in solid materials), but the material must either consist of light elements or be able to store many hydrogen atoms to be viable for storage medium.

The dehydrogenation refers to the release of hydrogen from the material. In a car, three hours has been deemed as enough to give enough time to empty the tank within a typical time period between refueling plus some safety margin to have sufficiently high hydrogen flow at almost empty tank and full energy demand. Rehydrogenation occurs when the material is being loaded with hydrogen. Car owners are not expected to spend more than a couple of minutes filling it up.[11]

More will be said about pressure and enthalpy in the following sections. With regard to the minimum number of cycles, the value of 500 is estimated from car fill-ups. If the storage system is used as part of an energy system in a house, however, one can expect loading of such a storage module during the day, when solar hydrogen is produced, and discharging during the night. This means in the extreme one cycle per day, and under the assumption that an energy system for a house has a lifetime of more than ten years, a cycle stability of many thousand cycles is expected.[11]

2.3.2 Materials based on adsorption

The multitude of solid materials that can contain hydrogen can be split up in various ways. In this report, a differentiation based on the underlying physical principle by which hydrogen is contained in the material is used:

1) Adsorption materials
2) Absorption materials

The first category which will be discussed in this section will be treated in terms of thermodynamical principles only. At the present no more than 2% in gravimetric storage density has been reached unless impractical temperatures far below 0 °C are used. Instead, focus will be directed at the second category.

2.3.3 Materials based on absorption

Many materials are capable of absorbing hydrogen gas. All of these materials involve metal atoms in some way—hydrogen is either bonded directly to the metal atom or indirectly as part of a non-metal ligand. Figure 6 represents a family tree of absorption materials, which with a single word are called *hydrides*.

When absorbed, hydrogen molecules are dissociated on the surface of the material surface and the atoms enter into the lattice:

$$H_2 \rightarrow 2H \tag{5}$$

The hydrogen atoms are positioned in interstitials in the structure. When the hydride, denoted M, is included in the reaction we get:

$$M + xH_2 \leftrightarrow MH_{2x} \quad (6)$$

Normally, this reaction is exothermic leading to heat evolvement, which is a problem that must be dealt with to get a stable storage system. Ideally, as included in Table 3, the enthalpy will be as close to zero as possible.

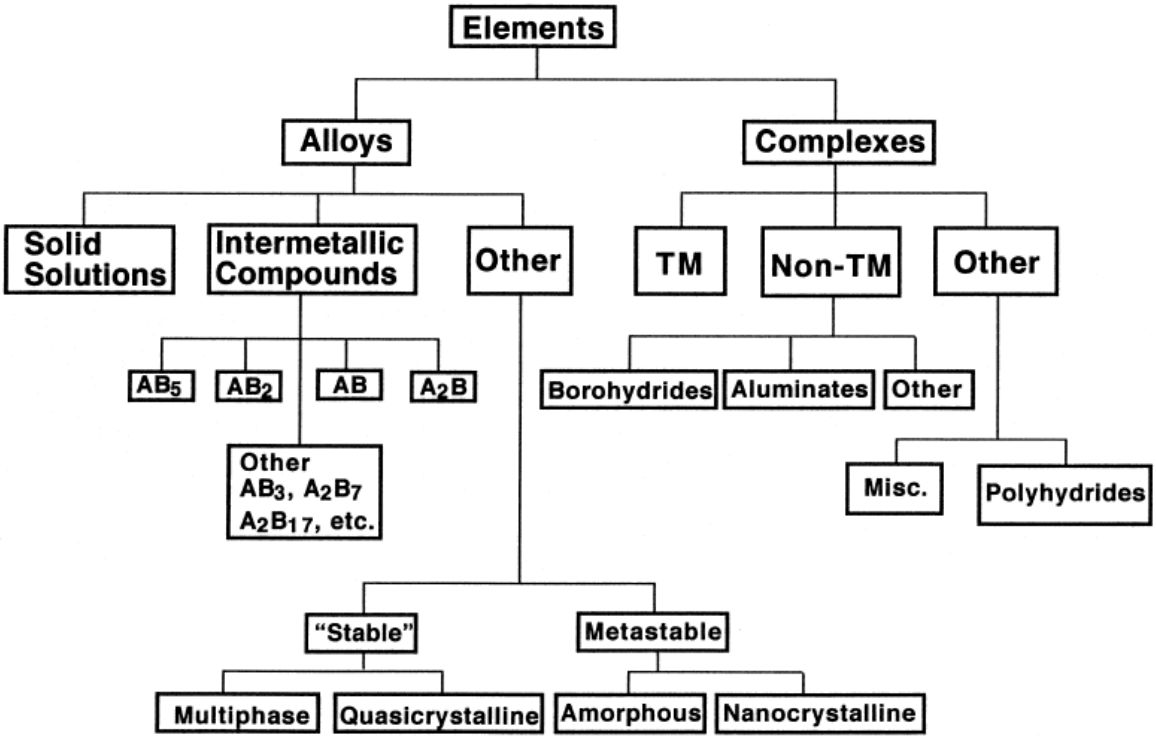

Figure 6 Family tree for hydrides. The elements and alloys are called metal hydrides, and the complexes are called complex hydrides[12]

Ways to characterize hydrides

When hydrogen is absorbed in the hydride, a mechanical equilibrium will be established between the ambient gas and the absorbed hydrogen. Figure 7 represents a pressure-composition isotherm (PCI) which is a useful tool in determining the storage capacity of a hydride.

A cycle of absorption and desorption follows the arrows along the curve. During absorption, relatively little hydrogen is absorbed at small pressures. At a certain pressure, the *plateau pressure*, the flux of hydrogen is drastically increased represented by the piece of the curve which ideally is horizontal. Small variations in pressure around the plateau pressure cause a large amount of hydrogen to be absorbed or released. This amount is proportional to the reversible capacity $\Delta(H/M)_r$, which can be read from the curve. H/M means the ratio between number of hydrogen atoms and the number of metal atoms in a formula unit. During engineering, based on the available

pressure and temperature ranges something between this quantity and the maximum possible storage, $(H/M)_{max}$, is reached. The capacity is usually calculated as weight% (wt%), but atomic H/M ratio or volume% is also used occasionally. In the latter case, it is useful to remember that only the density only considers the material itself and not the void volumes inherent in engineering containers.

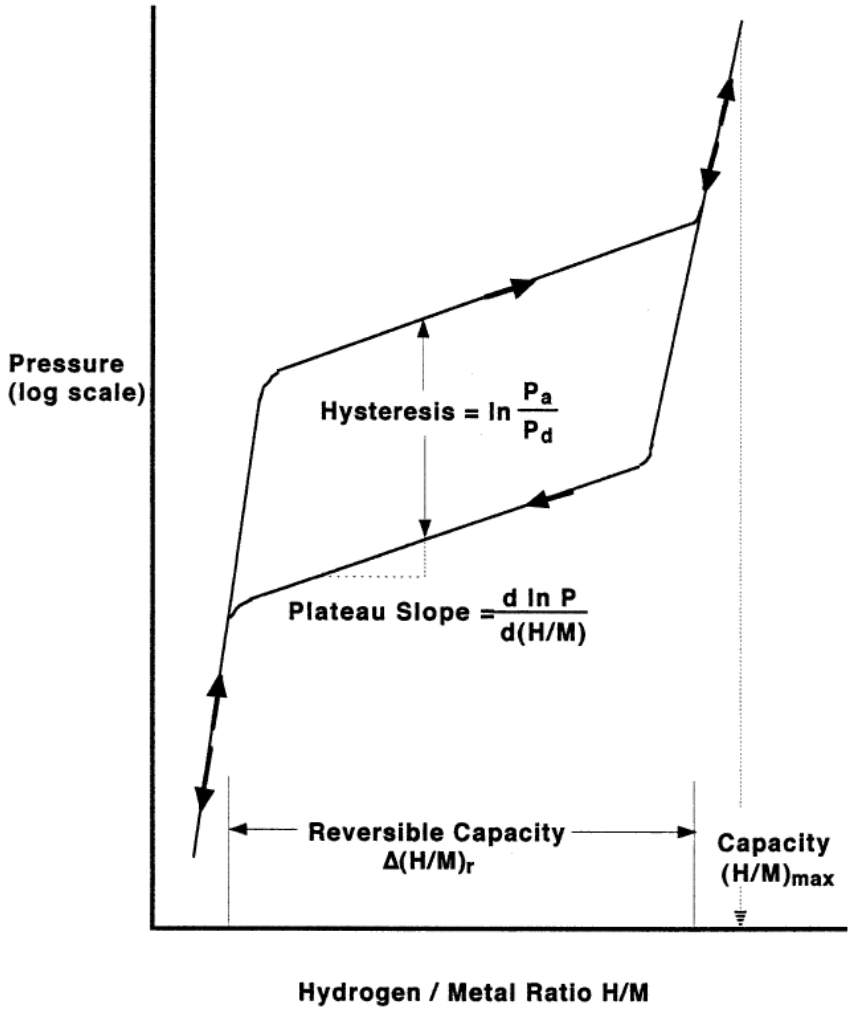

Figure 7 Pressure-concentration isotherm for hydrogen absorption/desorption in metal hydrides.[13]

Another essential way to characterize hydrides is with van't Hoff lines. These are based on the thermodynamic relationship between the hydrogen pressure and the temperature:

$$\ln p = \Delta H/RT - \Delta S/R \qquad (7)$$

Since the enthalpy and entropy changes are nearly constant and both *negative* as a rule, the pressure increases when the temperature increases. Figure 15 in Section 2.3.5 shows an example of this for

$CaNi_5$. ln p can be plotted as a function of $1/T$. A straight line with slope $\Delta H/R$ and intersection $-\Delta S/R$ will result. Figure 9 shows van't Hoff lines for a few metal hydrides.

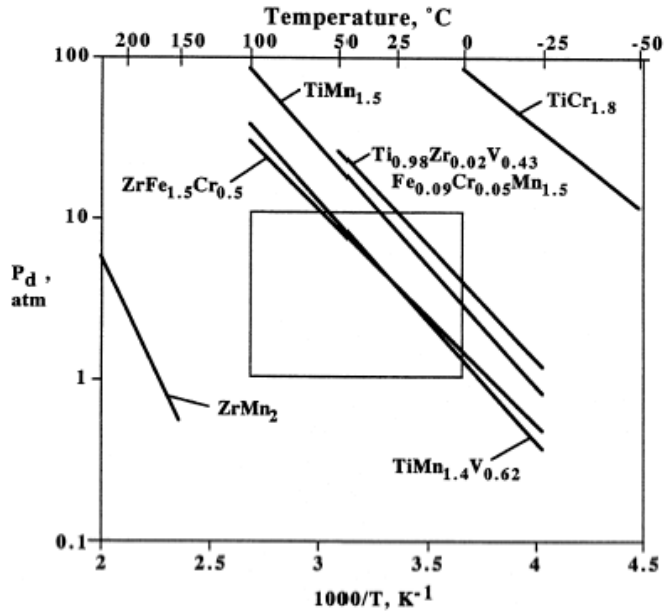

Figure 9 Van't Hoff diagram for the relationship of desorption pressure and temperature[12]

The box in the diagram is the boundaries for which the temperature is between 0 and 100 °C, and the pressure lies between 1 and 10 bar. Outside this box, the conditions are unreasonable to be present in a car, although temperatures up to 200 °C could exist with a system including a high temperature polymer electrolyte membrane fuel cell (HT-PEMFC).[14,15]

Absorption and desorption kinetics

Even though a given hydride has a van't Hoff line inside the box mentioned above, and its storage capacity is high, other properties must be fulfilled to qualify for a viable storage material. As listed in Table 3, the absorption (rehydrogenation) must take less than 5 minutes, and the desorption (dehydrogenation) less than 3 hours.

The kinetics of absorption and desorption are believed to adhere to the following reaction mechanism:[16]

(1) Physisorption of hydrogen molecules

(2) Dissociation of hydrogen molecules and chemisorption

(3) Surface penetration of hydrogen atoms

(4) Diffusion of hydrogen atoms through the hydride layer, either by an interstitial or a vacancy mechanism

(5) Hydride formation at the metal/hydride interface

It is assumed that the particles are spherical. The hydride phase grows from the metal/gas interface to the center according to Figure 10, because hydrogen first forms a solid solution (α phase) with a concentration gradient from the surface to the center, and saturation of the α phase (creation of the β phase) takes place first at the metal/gas interface. Also, the lattice expansion associated with the β phase requires less energy at the solid/gas interface than in the bulk of the solid.

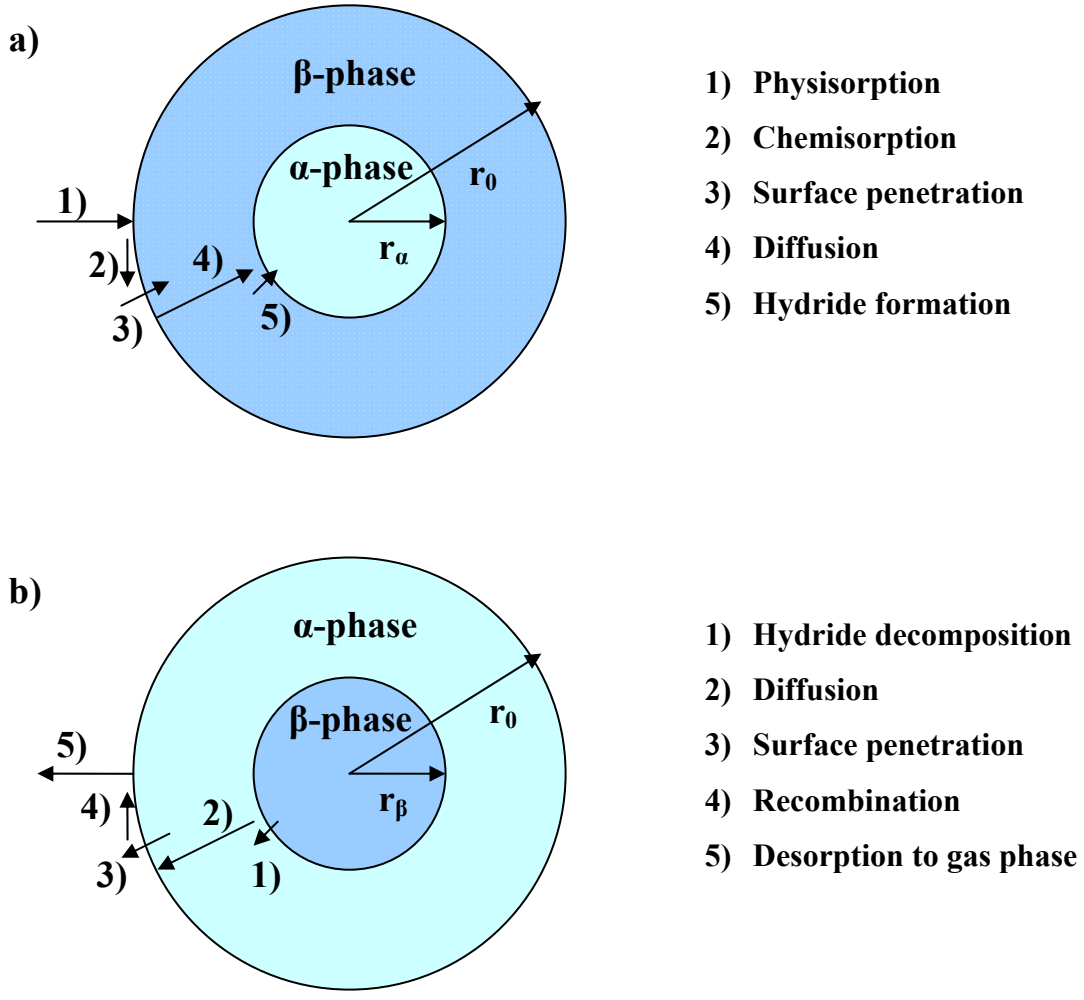

Figure 10 Reaction partial steps for the (a) absorption and (b) desorption of hydrogen by a spherical particle.[16]

The relation between the total amount of reacted hydride and the radius r_α of the α phase is given by

$$n(t) = n_M Z \, [1 - r_\alpha(t)^3 / r_o^3] \tag{8}$$

where $n(t)$ is the number of moles of reacted hydrogen atoms, r_o and r_α are the radii of the particle and the α phase core, n_M is the number of moles of the hydride sample, and Z the stoichiometric factor of hydrogen in the hydride MH_Z.

Using hydrogen in a closed reservoir and measuring the pressure change, called Sieverts' method, the following relationship is used

$$n(t) = 2[p_o - p(t)] \, V_{res} / (RT) \tag{9}$$

where V_{res} is the volume of the reservoir, p_o the initial hydrogen pressure and $p(t)$ the pressure as a function of the reaction time t.

Based on the above two equations an expression for $r_\alpha(t)$ as a function of $p(t)$ can be derived:

$$r_\alpha(t) = r_o \, [1 - 2(p_o - p(t)) \, V_{res} / (n_M Z R T)]^{1/3} \tag{10}$$

Also the rate $dn(t)/dt$ of hydrogen absorption is given by

$$dn(t)/dt = - 2 \, dp(t)/dt \, V_{res} / RT \tag{11}$$

Based on the above relationships, the following flux densities and coverages can be obtained for hydrogen molecules:[17]

Physisorption:	$\theta_{H2} \propto p(t) * \exp(-\Delta H_{ph} / kT)$	(12)
Chemisorption:	$j_{pc} \propto \theta_{H2} \, (1 - \theta_H)^2 \exp(-A_{ch}/kT)$	(13)
Surface penetration:	$j_{cm} \propto \theta_H * (1 - c_H/c_{H,max}) \exp(-A_M/kT)$	(14)
Diffusion:	$j_{diff} = - D \nabla c_H$	(15)

where θ_{H2} is the coverage for physisorption, θ_H the coverage for chemisorption, ΔH_{ph} the enthalpy change of physisorption, j_i refers to flux, c_i to concentration, A_i represents activation energies, and D is the diffusion coefficient.

As was seen earlier, the coverage will increase with increasing pressures. Therefore, the physisorption and chemisorption processes will both be faster, if the pressure increases. For temperature effects, it is seen that all processes increase in speed when the temperature increases.

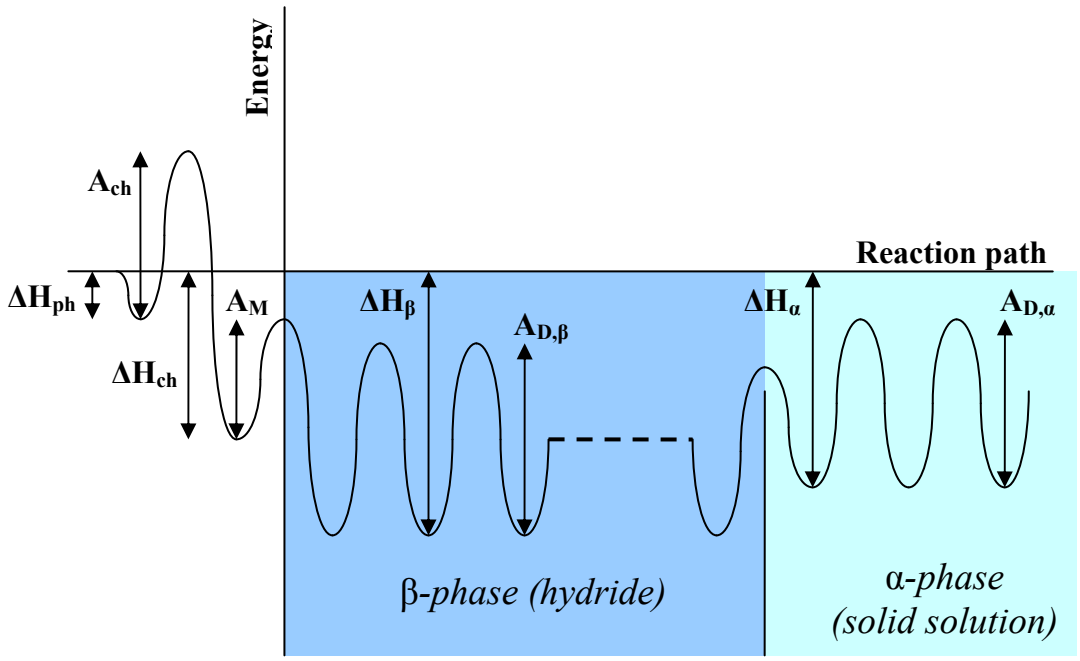

Figure 11 Energy levels of a hydrogen atom in the positions along the reaction path, schematic.[17]

Figure 11 shows the energy profile associated with the five steps. Inside the bulk metal, the hydrogen diffusion is characterized by the diffusion activation energies $A_{D\beta}$ and $A_{D\alpha}$. Therefore D is dependent on these: D increase as $A_{D\beta}$ and $A_{D\alpha}$ decrease, resulting in faster kinetics.

The equations for chemisorption and surface penetration apply only to absorption. For desorption the following apply:[17]

Chemisorption: $$j_{cp} = constant * \theta_H^2 \exp[(2\Delta H_{ch} - \Delta H_{ph} - A_{ch}) / kT] \quad (16)$$

Surface penetration: $$j_{mc} = constant * c_H (1- \theta_H) \exp[(\Delta H_{\alpha,\beta} - \Delta H_{ch} - A_M) / kT] \quad (17)$$

By these relationships it is seen that enthalpies of physisorption and chemisorption together with their activation energies play an important part in the kinetics of absorption and desorption.

2.3.4 Metal hydrides

Elemental metal hydrides

Hydrides from a single metal element, like LiH, are nonvolatile solids and are formed when H^- anions combine with metal cations.[18] Unfortunately, as Figure 12 shows, these hydrides, with the exception of vanadium, release hydrogen at conditions that are not appropriate for storage in a car.

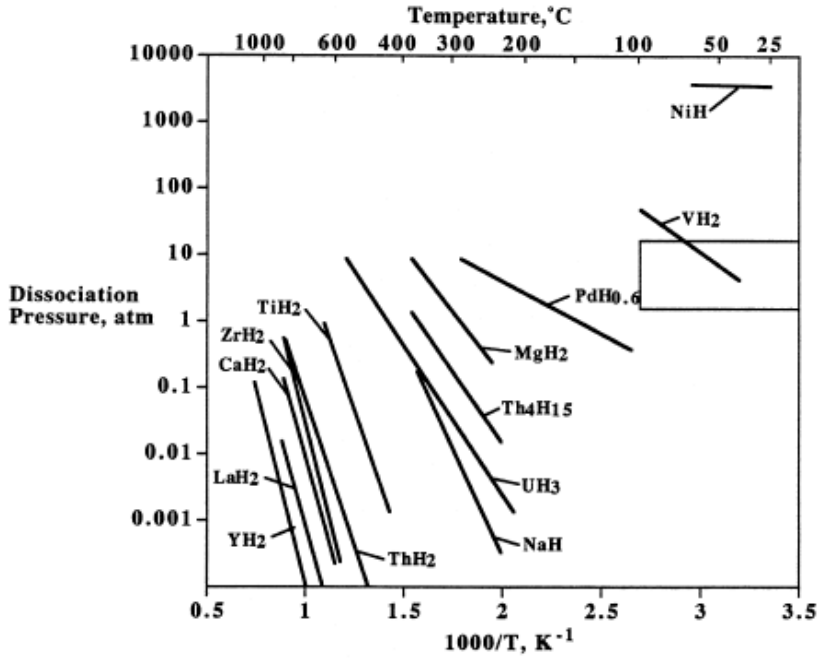

Figure 12 Van't Hoff lines for elemental metal hydrides[13]

However, by adding water they react readily to release the hydrogen. Table 4 gives a few examples.

Table 4 Hydrolyzation of selected elemental metal hydrides[11]

Hydride	Reaction	Storage capacity (wt%)
LiH	$LiH + H_2O \rightarrow LiOH + H_2$	7.7
NaH	$NaH + H_2O \rightarrow NaOH + H_2$	4.9
MgH_2	$MgH_2 + 2H_2O \rightarrow Mg(OH)_2 + 2H_2$	6.3

A system with NaH has already been commercialized (Powerball®), in which NaH coated with polyethylene in the form of small balls are broken down in the presence of water leaving the contents open to be hydrolyzed. Of course, as is the case with all single-metal hydrides, the reactions are irreversible, and the hydroxide must be removed, which is inconvenient. Filling up fuel consisting of hydrogen *and* metal will also make both the fuel and the filling process more expensive.

Alloys

By alloying metals together, van't Hoff lines lying in between the lines for the elemental hydrides are obtained. Figure 13 shows some lines for so-called AB_5 hydrides.

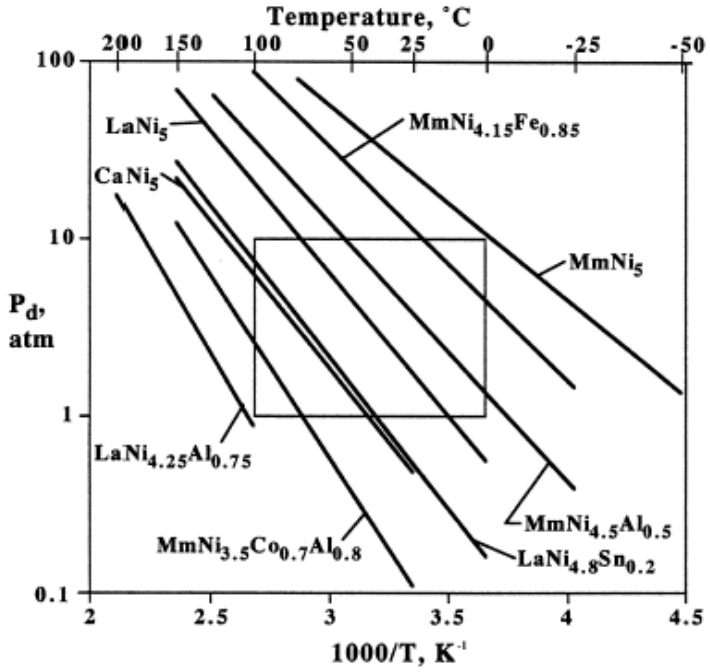

Figure 13 Van't Hoff lines for AB_5 hydrides[13]

In Figure 12 it is seen that the lines for lanthanum hydride and nickel hydride, for example, lies well outside the box. $LaNi_5$, seen here in Figure 13, on the other hand, lies inside the box. This is true for other alloys too, and in this way alloys can be engineered to conform to 'box conditions'.

Hydriding alloys are normally divided into the following subcategories: AB_5, AB_2, AB, and A_2B. More exist, but these are the common ones. 'A' represents a strongly hydriding metal, which includes the lanthanides, calcium, yttrium, zirconium, and titanium. 'B' represents a weakly hydriding metal, which often is nickel, but also manganese, iron, and aluminium.[13]

A representative selection of some of the best alloys found with respect to storage capacity, cost, and absorption/desorption temperature (at 1 bar) is given in Table 5.

Table 5 Characteristics for selected hydrided alloys. Prices are from 1999 and should be interpreted as approximate (see ref. 13).

Type	Alloy	$(H/M)_{max}$	weight%	T for 1 bar P_d /°C	Cost /\$ kg^{-1}
A_2B	Mg_2NiH_4	1.33	3.6	255	6.26
AB	$TiFeH_{1.95}$	0.975	1.86	-8	4.68
AB_2	$ZrMn_2H_{3.6}$	1.2	1.77	167	11.29
AB_5	$LaNi_5H_{6.48}$	1.08	1.49	12	9.87
AB_2	$TiV_{0.62}Mn_{1.4}H_{3.44}$	1.14	2.15	-5	29.40

It is clear that there are many differences among the different types of alloys. An alloy with good storage capacity may have other disadvantages. For instance, $LaNi_5$ and $CaNi_5$ are relatively good hydriding alloys. But unfortunately they disproportionate into more stable compounds after a number of cycles. $TiCr_{1.8}$ in its maximally hydrided form, $TiCr_{1.8}H_{3.5}$, has a weight% of 2.43. But the temperature for desorption at 1 bar is -91 °C. Alloys with a lot of Zr and Mn often burn in air.[13]

The potential of metal hydrides have been explored for a long time. Concerning the further development and research within metal hydrides, a front-person within research in hydrogen storage materials, Sandrock, gives this outlook:

"There are many gaps to be filled and particular areas of R&D to follow within the framework of [metal hydrides], to be sure. However, it must be argued that we are reaching a point of diminishing returns involving limits to the inherent thermodynamics and metallurgy of these conventional families of hydriding alloys. We need to explore new and different approaches."[13]

An example of a well-known metal hydride will be given in the next section, and following that, complex hydrides will be investigated.

2.3.5 Example of a metal hydride: $CaNi_5$

In Figure 13 is seen that an alloy, $CaNi_5$, lies well inside the box conditions. $CaNi_5$ is example of a metal hydride that has been studied extensively, since it shows good promise in its pure state. The range of studies that has been performed on $CaNi_5$, is exemplary of methods which have been generally used to "tweak" hydrides into better performance.

For $CaNi_5$, detailed studies have been made on:

- its reactions with components in air[19,20]
- phase diagrams[21,22]

- activation of reaction with hydrogen[23]
- changes in crystal structure after hydrogenation[24,25] or reaction with deuterium[26]
- PCI's[18,27-32]
- reaction kinetics[33,34] including the dependence of particle size[35]
- the effect of annealing[36]
- the effect of doping with palladium[37,38]
- stability of cycling[39-41] including under elevated temperatures[42-43]
- substitution of Ca or Ni with other elements such as Mg[44-47], La[48] including with Al[49-52], Ce, Mm, and Zn[53], Al, Cu, and Ni[54], Al, Cr, Mn, Fe, Co, Cu, Zn or Sn[47]
- applications in assisting in heat transfer[55] and as a catalyst for hydrogen transfer reactions in organic compounds.[56,57]

During this wide range of research comes from an extensive period of 1978 to 2006 (publication years), improvements have been seen in performance such as in the kinetic behavior. However, problems are prevalent with stability.

In its pure state, $CaNi_5$ is a good test material for testing a system for measuring hydrogen uptake, as it is well characterized, is easily activated and has reasonable kinetics at room temperature.

From a publication by Sandrock et al. on $CaNi_5$, he describes the activation as being done "easily at room temperature and pressures of <20 atm".[18]

Figure 14 shows an absorption/desorption cycle for $CaNi_5$ at room temperature.

The curve shows, that the plateau pressure is approximately 0.5 bar at room temperature.

As was described in Section 2.3.3, for elevated temperatures, the plateau pressure increases according to the equation

$$\ln p = \Delta H/RT - \Delta S/R \qquad (7)$$

Figure 15 shows the corresponding PCI's for different temperatures. It is seen that there is an approximately equal distance between the three plateaus at the highest temperatures separated by 20 degrees.

Further quantities is available from Sandrock et al.[13]: 0.16 for hysteresis, 0.19 for the slope, $(H/M)_{max} = 1.05$, and $(H/M)_{rev} = 0.55$.

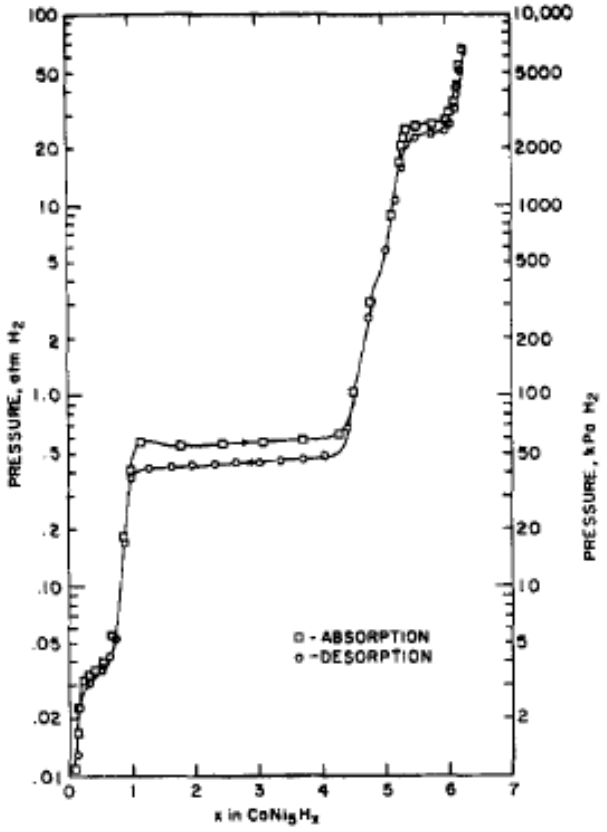

Figure 14 PCI for $CaNi_5$ alloy at 25 °C.[18]

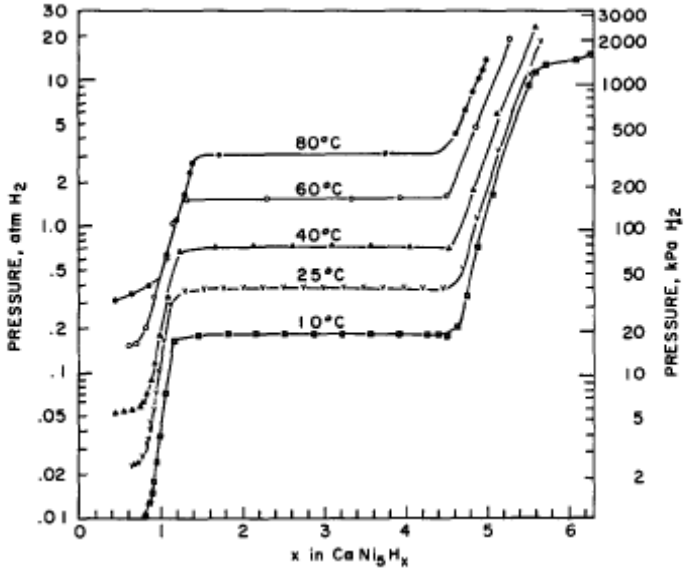

Figure 15 PCI's for $CaNi_5$ at different temperatures.[18]

2.3.6 Alanates

A breakthrough in the search for hydrogen storage materials happened in 1997 when Bogdanovic et al. published the results of doping sodium alanate, $NaAlH_4$, with titanium[58]. The results showed some considerable improvements for this material as a possible storage medium. Much research on alanates has been instigated through this.

Thermodynamics

It is known that $NaAlH_4$ has a rather high storage capacity according to the reactions:

$$3NaAlH_4 \rightarrow Na_3AlH_6 + 2Al + 3H_2 \quad (3.7 \text{ wt\% } H_2 \text{ content}) \quad (18)$$

$$Na_3AlH_6 \rightarrow 3NaH + Al + 1.5H_2 \quad (1.8 \text{ wt\% } H_2 \text{ content}) \quad (19)$$

This system is reversible, but the kinetics is so slow that practical considerations have originally been out of the question. With Bogdanovic as pioneer (although improved kinetics for $LiAlH_4$ with titanium has been known since 1951), it has been shown that by doping with titanium a van't Hoff line is located inside the 'box conditions' mentioned earlier. This is represented in Figure 16.[59]

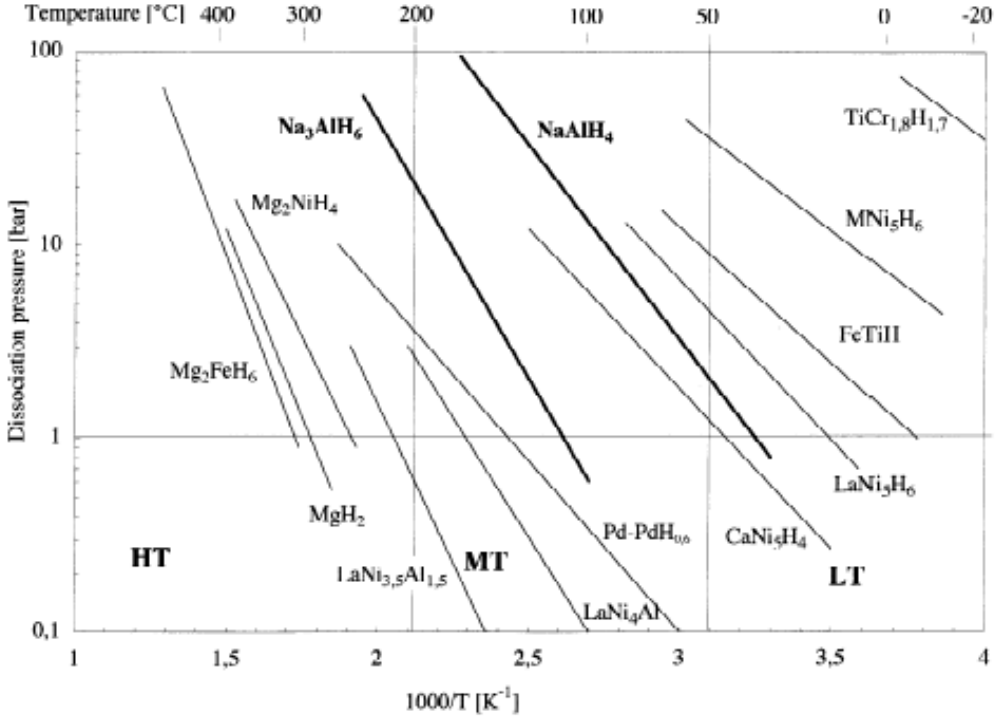

Figure 16 Van't Hoff plots for sodium alanate[59]

The location of the lines for $NaAlH_4$ and Na_3AlH_6 can be compared to metal hydrides in this region. The step above, the decomposition of $NaAlH_4$, is seen to have an equilibrium pressure of 20 bar at 200 °C, and the second step an equilibrium pressure of more than 100 bar at the same temperature.

These two steps are reflected in the PCI's represented in Figure 17. The first plateau corresponds to the first step and the second plateau to the second step.

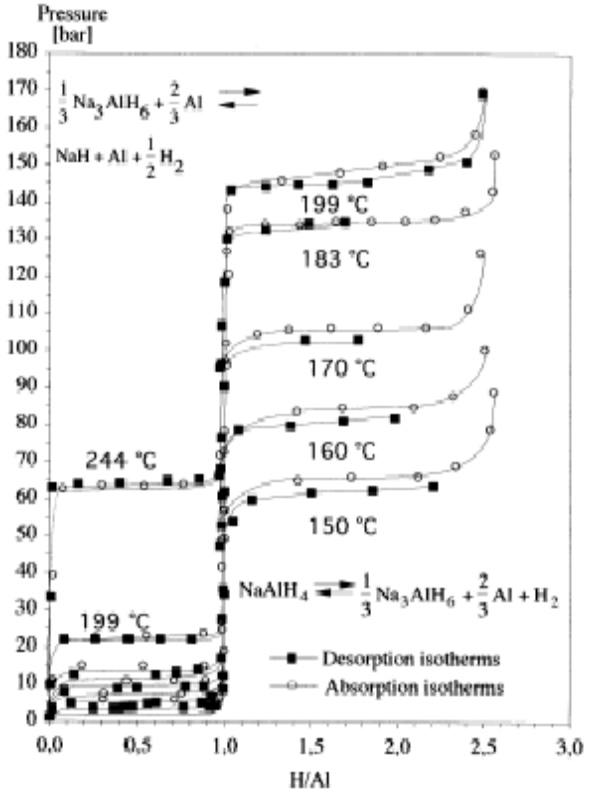

Figure 17 PCI's for sodium alanate at different temperatures[59]

Kinetics

The kinetics of the $NaAlH_4$ system as represented in Figures 18 and 19 show that both absorption and desorption although improved by titanium, are rather slow.

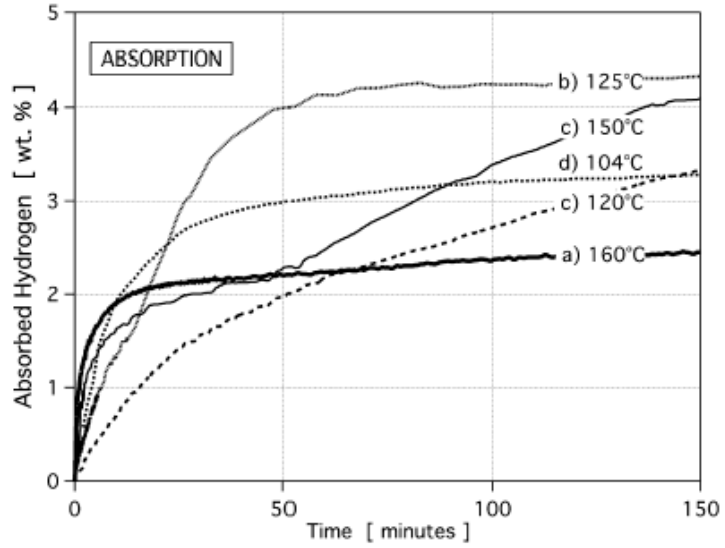

Figure 18 Hydrogen absorption with time for sodium alanate at various conditions (see details in ref. 60)

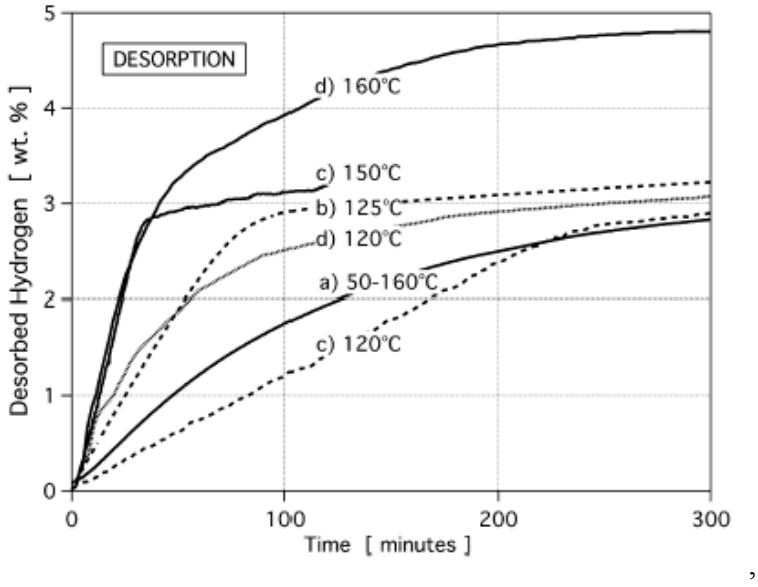

Figure 19 Hydrogen absorption with time for sodium alanate at various conditions (see details in ref. 60)

These data mean that although $NaAlH_4$ is a material with high storage capacity (about 5% in practice), the time for absorption, at the current stage of development, still has a long way to go to compare with the goal of 5 minutes for use in cars.

Much research has been done in attempting to improve the hydrogen storage properties of $NaAlH_4$, including doping with almost all transition metals and some of the rare earth elements[59,61] and with carbon.[62] A study was also made for a scale-up bed of 100 g $NaAlH_4$ to examine heat transfer

effects for an actual storage container, giving a more realistic picture of some of the challenges for solid state hydrogen storage.[63]

Other alanates than $NaAlH_4$ are under consideration for hydrogen storage, such as $LiAlH_4$[64-72] (releases hydrogen already during ball-milling at room temperature, but is irreversible), $Mg(AlH_4)_2$[73-77] (able to release 6.6 wt% hydrogen at 163 °C, but is irreversible) and $Ca(AlH_4)_2$.[78-81]

2.3.7 Complex hydrides containing nitrogen for hydrogen storage

Much progress in the search of new materials for hydrogen storage has been made since the discovery of catalyzed $NaAlH_4$. An important breakthrough is lithium nitride, Li_3N, beginning with a publication by Chen et al.[82] Since then, many articles have been published on systems based on Li_3N.

The reaction for lithium reacting with hydrogen is:

$$Li_3N + 2H_2 \leftrightarrow LiNH_2 + 2LiH \qquad \Delta H = -96.3 \text{ kJ/mol } H_2 \qquad (10.4 \text{ wt\%}) \qquad (20)$$

Theoretically, reversible hydrogen of 10.4 wt% can be stored in this reaction. However, Chen et al. claimed that the reaction followed a two-step reaction path:

$$Li_3N + H_2 \leftrightarrow Li_2NH + LiH \qquad \Delta H = -165 \text{ kJ/mol } H_2 \qquad (21)$$

$$Li_2NH + H_2 \leftrightarrow LiNH_2 + LiH \qquad \Delta H = -44.5 \text{ kJ/mol } H_2 \qquad (6.5 \text{ wt\%}) \qquad (22)$$

PCI's for this system show two plateaus where only the second one was reversible. This corresponds to the enthalpies of the two steps above, in which step one has a very high enthalpy difference (irreversible) and step two a moderate enthalpy difference (reversible).

It is theorized[83] based on the notion that hydrogen in LiH is negatively charged ($H^{\delta-}$) and hydrogen in $LiNH_2$ is positively charged ($H^{\delta+}$), that the presence of these two forms makes it easier to form molecular hydrogen. Simultaneously, $N^{\delta-}$ and $Li^{\delta+}$ combine to form Li_3N. The exact mechanism of this reaction is still being actively discussed. Realizing the interaction between metal amides ($LiNH_2$, $Mg(NH_2)_2$, and $Ca(NH_2)_2$ as a basis (see ref. 84 for a classical review on these amides)) and elementary hydrides (mostly LiH, MgH_2, and CaH_2) and this notion of destabilization of hydrogen containing species, was an offset to a large and fruitful field of research that has been ongoing, and is no where close to being exhausted. In Table 6 a wide overview is presented of systems that contain a metal amide as a component, serving as a significant group in the research of complex hydrides.

Table 6 Hydrogen storage systems based on metal amides. "0 bar" normally refers to dehydrogenation in a closed evacuated chamber and "1 bar" normally refers to an open system in which hydrogen is carried away in an argon stream.

Reaction	*Theor. wt% H_2*	*Exp. wt% H_2*	*Reaction conditions*	*Reversibility*	*Ref.*
$\mathbf{Li_3N} + 2H_2 \leftrightarrow LiNH_2+2LiH$	*11.5*	*~10*	*255 °C at 20 bar*	*5.5 wt% at 255 °C and 0.04 bar*	*82, 85-91*
$\mathbf{LiNH_2}+LiH \leftrightarrow Li_2NH+H_2$	*6.5*	*6.5*	*285 °C at 3 bar*	*6.5 wt% at 285 °C and 0 bar*	*92-100*
$2\mathbf{LiNH_2}+MgH_2 \rightarrow Li_2Mg(NH)_2+2H_2 \leftrightarrow Mg(NH_2)_2+2LiH$	*5.6*	*5.4*	*200 °C at 30 bar*	*5.2 wt% at 200 °C and <30 bar*	*92, 101-107*
$\mathbf{LiNH_2}+LiAlH_4 \rightarrow [Li_2AlNH]+2½H_2$	*8.2*	*~8*	*400 °C at 0 bar*	-	*108*
$\mathbf{LiNH_2}+2LiAlH_4 \rightarrow 2Al+Li_2NH+LiH+4H_2$	*8.1*	*8.1*	*320 °C at 1 bar*	-	*109*
$Li_3AlN_2+2Li_2NH+3LiH+Al+4H_2 \leftrightarrow 3\mathbf{LiNH_2}+7LiH+Al+AlN$	*4.2*	*3.6*	*200 °C at 100 bar*	*3.6 wt% at 0.04 bar*	*110*
$2\mathbf{LiNH_2}+LiBH_4 \rightarrow Li_3BN_2H_8$	*11.9*	*~10*	*350 °C at 0 bar*	-	*111-116*
$2\mathbf{LiNH_2}+LiAlH_4 \rightarrow Li_3AlN_2+4H_2 \leftrightarrow LiNH_2+2LiH+AlN+2H_2$	*9.5 / 5.1*	*5.1*	*500 °C at 80 bar*	*5.1 wt% at 500 °C and 0 bar*	*113, 117-118*
$\mathbf{NaNH_2}+LiAlH_4 \rightarrow NaH+2/3Al+LiAl_{0.33}NH+2H_2$	*5.2*	*5.1*	*120 °C at 0 bar*	-	*119*
$\mathbf{Mg(NH_2)_2}+8/3LiH \rightarrow 1/3Mg_3N_2+4/3Li_2NH+8/3H_2$	*6.9*	*6.9*	*275 °C at 0 bar*	*6.9 wt% at 200 °C and 30 bar*	*102, 120-127*
$\mathbf{Mg(NH_2)_2}+4LiH \leftrightarrow Li_2Mg(NH)_2+2LiH+2H_2$	*4.6*	*4.5*	*250 °C and 0.05 bar*	*4.5 wt% at 250 °C and 0.9 bar*	*102, 120, 128*
$Mg_3N_2+4Li_3N+12H_2 \leftrightarrow 3\mathbf{Mg(NH_2)_2}+12LiH$	*9.1*	*9.1*	*250 °C and 350 bar*	*~8 wt% at 400 °C and 1 bar*	*129-131*
$2Li_2MgN_2H_2+H_2 \leftrightarrow 3LiH+2\mathbf{Mg(NH_2)_2}$	*5.5*	*5.3*	*220 °C and 70 bar*	*4.1 wt% at 220 °C and 0.01 bar*	*132, 133*
$\mathbf{Mg(NH_2)_2}+LiH \rightarrow ½Li_2Mg_2N_3H_3+NH_3+2H_2$	*6.2*	*0.5*	*310 °C*	*0.5 wt% at 210 °C*	*134*
$\mathbf{Mg(NH_2)_2}+MgH_2 \rightarrow 2MgNH+2H_2$	*7.3*	*4.9*	*310 °C*	-	*135, 136*
$\mathbf{Mg(NH_2)_2}+LiAlH_4 \rightarrow 1/3Mg_3N_2+1/3Li_3AlN_2+2/3AlN+5H_2$	*8.5*	*7.9*	*350 °C*	*1.5 wt% at 350 °C and 80 bar*	*137*
$\mathbf{Mg(NH_2)_2}+xNaH \leftrightarrow ?$ *(x = 1, 1½, or 2)*	*N/A*	*1.8, 2.2, or 1.8*	*160 °C and 0.05 bar*	*~100 % at 160 °C and 6 bat*	*139*
$\mathbf{Mg(NH_2)_2}+CaH_2 \rightarrow MgCa(NH)_2+2H_2$	*4.1*	*3.9*	*350 °C at 80 bar*	-	*139*
$2\mathbf{Mg(NH_2)_2}+4CaH_2 \rightarrow CaMg_2N_2+Ca_2NH+CaNH+7H_2$	*5.0*	*4.9*	*510 °C at 1 bar*	-	*140*
$\mathbf{Mg(NH_2)_2}+\mathbf{Ca(NH_2)_2}+4LiH \leftrightarrow$	*5.0*	*3.0*	*280 °C and 1 bar*	*220 °C and 75 bar*	*141*

$Li_4MgCaN_4H_4+4H_2$					
$\mathbf{Ca(NH_2)_2}+CaH_2 \rightarrow 2CaNH+2H_2$	*3.5*	*3.3*	*60 ~ 500 °C and 1 bar*	-	*142*
$\mathbf{Ca(NH_2)_2}+3CaH_2 \rightarrow 2CaNH+2CaH_2+2H_2 \rightarrow 2Ca_2NH+4H_2$	*4.0*	*3.5*	*60 ~ 500 °C and 1 bar*	-	*142*
$\mathbf{Ca(NH_2)_2}+2LiH \rightarrow CaNH+Li_2NH+2H_2$	*4.5*	*4.5*	*260 °C*	-	*143*
$Ca_3N_2+2H_2 \rightarrow \mathbf{Ca_3(NH_2)_2} \rightarrow 2CaNH+CaH_2$	*2.6*	*2.4*	*550 °C and 30 bar*	-	*144*
$\mathbf{Ca(NH_2)_2}+NaH \leftrightarrow \mathbf{NaNH_2}+$*Ca-N-H (solid solution)* $+ ½H_2$	*1.1*	*~1.1*	*270 °C*	*1.0 wt% at 250 °C and 70 bar*	*145*

It is readily appreciated from the info in the table that compared to conventional, interstitial, metal hydrides, complex hydrides offer very high weight capacities. While many of them are irreversible, a good deal of them is reversible or partly reversible. However, problems with kinetics (not reviewed in the table) and especially operation conditions with sometimes very high temperatures and impractical pressure plateau levels (close to 0 bar in many instances) are abundant.

Nitrogen in molecular form, N_2, has very limited interaction with these systems, with the exception of the production of lithium. An interesting tidbit, observing the interaction between Li and N_2 by chance (lithium used to dope carbon nanotubes with was in a nitrogen glovebox for a couple of days and became interested in the purple Li_3N product), and trying to hydrogenate it was how the results for Li_3N in Ping Chen's group started.[146] The more stable nitrogen compound, NH_3, is often involved where metal amides are concerned. The production of ammonia is believed to proceed according to the reaction:[147-148]

$$2LiNH_2 \rightarrow Li_2NH + NH_3 \quad (23)$$

It has been shown that NH_3 reacts "ultrafast" (contact time < 25 ms) with LiH[86] according to the reaction:

$$NH_3 + LiH \rightarrow LiNH_2 + H_2 \quad (24)$$

In this way, while lithium amide is decomposed into lithium imide and ammonia, ammonia will react with lithium hydride to create more lithium amide that in turn can decompose further. The system can be said to be "ammonia mediated" (and can be catalyzed by the addition of $TiCl_3$, for example[149]). A problem occurs if ammonia leaves the system as the system eventually becomes nitrogen (and hydrogen) depleted, resulting in less and less capacity for containing hydrogen.

Some groups fully exploit ammonia as a carrier for hydrogen, and use metal chlorides as a reversible storage system exclusively for ammonia such as in hexammine magnesium chloride or octammine calcium chloride:[150-155]

$$Mg(NH_3)_6Cl_2 \leftrightarrow MgCl_2 + 6NH_3 \quad (25)$$

$$Ca(NH_3)_8Cl_2 \leftrightarrow CaCl_2 + 8NH_3 \quad (26)$$

Of course, to be usable, ammonia must be cracked at high temperature to hydrogen and nitrogen, even when catalyzed, in order to achieve H_2/N_2 streams sufficient free from ammonia. More is said about this in Chapter 8.

As with this example as it is with emission of ammonia in general for nitrogen-containing hydrogen storage systems, it is an important drawback with many nitride systems if used with fuel cells, since even traces of ammonia in hydrogen fuel is poisonous to most PEMFC's. NH_3 forms ammonium hydroxide inside certain types of cells which do permanent damage.[12]

For this reason, many researchers include tests for detecting ammonia in gas stream evolving from nitrogen-containing hydrogen storage systems. These include mass spectrometry, gas chromatography, Nessler's reagent, and various transition metal nitrate solutions, such as $Co(NO_3)_2(aq)$ which change color from pink to blue, when ammonia is dissolved. An indirect method is to lead the stream through a solution and determine the pH change.

It will be seen in the next section that an issue with complex hydrides is its stability to air. As a lone exception, and to this day unexplained, a very interesting development was seen with Weifang Luo et al. in 2007 with the system $2LiNH_2+MgH_2$. They showed that the capacity and kinetics of the system do not change after the desorbed sample ($\rightarrow Li_2Mg(NH)_2$) was exposed to water-saturated air at 220 °C for 21 h.[103]

2.3.8 Reactions with air

For many metal hydrides, stability in air is a concern. For the interstitial absorbing metal hydrides, the issue is generally present to a certain degree, and for the complex hydrides the issue is even more serious.

An example taken from personal experience from this author was related to $NaAlH_4$. In a prior project, purification of technical grade $NaAlH_4$ (containing for example Al) was attempted using the procedure described by Bogdanovic[58], dissolving in THF, filtering, extracting by pentane and subsequent drying. The attempt failed as the filter used was too fine, and the dissolved $NaAlH_4$ would not sieve through. The waste materials were then unwittingly left in the glassware in a plastic bucket in a fume cupboard over the weekend waiting to be taken care of. Coming Monday, when inspected all glassware and walls of the fume cupboard were covering in a black film, the plastic bucket had melted with remains lying here and there, and the vinyl table board had cracked in two. This is a, perhaps colourful, example of the volatility of a complex hydride, as they will often react spontaneously exothermically with components in the air releasing hydrogen, which evolves into a violent process causing explosion if enough material (aka. critical mass) is available.

Air consists mainly of nitrogen, oxygen, argon, carbon dioxide, and water. Of these, especially water is damaging to hydrides; it reacts quickly and produces hydroxides, hydrogen and heat. Reactions with some hydrides (especially those involved in nitrogen-containing systems) will be given here. Table 7 gives a summary of a literature study of the chemistry of these species.

Table 7 Reactivity of common species connected to hydrogen storage compounds involving nitrogen. Based on a literature study.

Compound	H_2O	O_2	N_2	CO_2
LiH	++	-	-	-
MgH_2	+	-	-	-
Li_3N	++	N/A	-	++
$LiNH_2$	++	+	-	N/A
$LiBH_4$	++	-	-	N/A

Key: ++ = very reactive, + = somewhat reactive, - = no reaction. All at room temperature and atmospheric pressure.

Lithium hydride:

Lithium is seen used very often in connection with hydrogen storage systems of metal amides and hydrides. Reactions with H_2O, O_2, N_2, and CO_2 are examined.

With water:

Lithium hydride, when exposed to slightly moist air will immediately form a thin fluid film of LiOH which crystallizes and protects the hydride from further rapid oxidation. When finely powdered, it can ignite spontaneously in air. Furthermore, it will react instantly with small amounts of liquid water or water vapour according to the reaction

$$LiH + H_2O \rightarrow LiOH + H_2 \quad (28)$$

This occurs sometimes with explosive violence, and the liberated hydrogen will ignite spontaneously.[156]

With oxygen:

If large crystalline lumps of LiH are heated in perfectly dry oxygen, no reaction will take place unless the hydride is heated very rapidly; then explosive combination can take place. The ignition temperature for lithium hydride is around 200 °C. LiH is stable to dry air and oxygen at 20 °C**,** but it can under certain conditions ignite spontaneously in the air if it is in a finely divided state (because of atmospheric humidity). At red heat, it ignites in oxygen with the formation of Li_2O (which leads to subsequent reaction with H_2O):[156, 157]

$$2LiH + O_2 \rightarrow Li_2O + H_2O \quad (29)$$

$$Li_2O + H_2O \rightarrow 2LiOH \quad (30)$$

With nitrogen:

Nitrogen reacts with lithium hydride at elevated temperatures to form lithium nitride:[156]

$$6LiH + N_2 \rightarrow 2Li_3N + 3H_2 \quad (31)$$

With carbon dioxide:

At elevated temperatures, carbon dioxide reacts with lithium hydride to give the formate:[156]

$$LiH + CO_2 \rightarrow HCOOLi \quad (32)$$

Magnesium hydride:

Magnesium hydride obtained from the elements is markedly inert to air, and reacts slowly with water, in contrast to MgH_2 prepared by pyrolysis. The difference can be ascribed satisfactorily to the different grain size and the crystalline nature.[156]

Lithium nitride:

Lithium nitride reacts with water to yield lithium hydroxide and ammonia. It is ultimately converted to lithium carbonate in the air. The compound readily reacts with water and carbon dioxide**.** It is also flammable, particularly when it is finely divided.[156-158]

$$Li_3N + 3H_2O \rightarrow 3LiOH + NH_3 \quad (33)$$

The reaction of Li_3N with CO_2 has not been found in the literature, but this reaction is suggested:

$$2Li_3N + 3CO_2 + 3/2O_2 \rightarrow 3Li_2CO_3 + N_2 \quad (34)$$

Lithium amide:

With water:

Lithium amide is hydrolyzed by water to yield lithium hydroxide and ammonia.[157]

$$LiNH_2 + H_2O \rightarrow LiOH + NH_3 \quad (35)$$

With oxygen:

Lithium amide is readily oxidized. For example, the substance may be oxidized with dinitrogen oxide to yield lithium azide. Amides of the alkali metals in general must be guarded against air oxidation to prevent the formation of potentially explosive substances.[157]

Lithium borohydride:

With water:

With water, alkali metal tetrahydroborates hydrolyse slowly at pH > 7 and rapidly at pH < 7. $LiBH_4$ is initially rapidly hydrolysed by water at 20 °C but the rate diminishes during hydrolysis because of the increase in pH.[157]

$$LiBH_4 + 2H_2O \rightarrow LiBO_2 + 4H_2 \quad (36)$$

With oxygen:

Alkali metal tetrahydroborates all ignite in air at elevated temperatures, the final product of combustion being the metal borate MBO_2. For the sodium and potassium compounds reaction commences at about 300 and 350 °C respectively but it is not complete until well above 400 °C. [157]

2.3.9 Synthesis of metal hydrides: The ball-milling process

Several times so far, *ball-milling* has been mentioned as a way of treating starting materials to produce an alloy or other compounds. Ball-milling or *mechanical alloying* is a common and straight forward technique to produce new materials based on metals. In principle, metal chips or powder is ground together by steel balls. Figure 20 shows a jar with balls and Figure 21 shows an in-house machine in which two jars of that type is positioned. When started, the jars are rotated around their own center axis while the jars are moved around in a circular motion around an axis between the jars. Inside, the balls experience two centrifugal forces: 1) the local one according to the jar rotating about itself, and 2) one for the result of the circular motion of the jar.

Figure 20 A typical ball-milling jar. The main container+lid+balls are made of stainless steel. The bottom piece and top piece (shown below the jar) are made of brass. The lid to the right has an O-ring which insulates when the lid is placed on top of the jar. The top piece is then places on top of the lid.

Figure 21 Typical ball-milling equipment (Fritsch Pulverisette 7 planetary mill). Two jars are each placed in a holder and fastened, after which the milling process can be started.

Optimization

Experience with the ball-mill shown in the pictures above has proved that the following factors play a role in the result:[159]

- Starting materials (powder or chips)
- Sample size (balls/materials mass ratio)
- Number of balls
- Size of balls
- Rotation speed
- Milling time
- Temperature

The optimization of these parameters has been made for certain materials, but it would be necessary to re-optimize the process for new starting materials. One factor, for example, that is sought to be avoided is a premature soldering of the materials, because this results in an uneven distribution of the starting materials in the product. Optimizing the mass ratio balance can help this problem.

2.4 Measurement of hydrogen uptake

At this point several data of thermodynamic and kinetic relationships for hydrogen storage materials have been under consideration. In this section, considerations in regard to measurements of hydrogen uptake will be discussed.

In a progress report for the Department of Energy (USA) for 2004 in the section called 'III.E Testing'[160] two types of analytical equipment are being reviewed: 1) a Sieverts P-V-T (pressure-volume-temperature) system, which performs volumetric measurements based on variations in hydrogen pressure, 2) a microbalance placed in a pressure chamber for direct gravimetric measurements.

A high pressure microbalance for measurement of hydrogen uptake was developed in this project and is described in Section 3.

2.4.1 Sieverts' method

Although the Sieverts' method is not used for this project, it is a method often seen used when measuring hydrogen uptake. This is probably due to its simple and straightforward construction compared to the high pressure microbalance. It will only be discussed here in brief with the intent to see the relation of the high pressure microbalance to this widely used system.

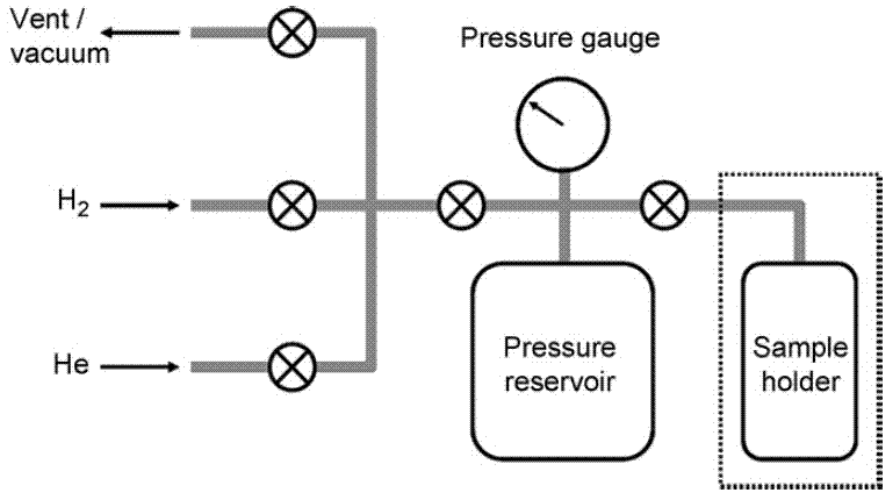

Figure 22 Principle of Sieverts' apparatus for volumetric measurement of hydrogen uptake by samples (after ref. 161).

Figure 22 shows the principle of a Sieverts' system. Hydrogen enters into a reservoir container with a relatively large and known volume. A valve separates the container from the reactor in which the sample is placed. A furnace around the reactor is used to heat the sample and gas in the reactor. This system can be evacuated or flushed with helium (although any inert gas can be used).

The uptake of hydrogen in the reservoir container can be calculated (taking into account that the valve to the reactor is open) by using the ideal gas equation:

$$n = pV / RT \tag{37}$$

The number of moles of H_2, n, is relatively smaller when the pressure, p, is smaller assuming that the temperature, T, is held constant. By calculating the difference in number of moles, the hydrogen uptake can be directly calculated in terms of mass, weight percent, and so forth.

For higher pressures, other state equations, like the van der Waals equation should be used.

An issue that makes the Sieverts' system a challenge to construct is that it must be totally tight. Any leak will be confused with hydrogen uptake, and thereby give an inaccurate result.

Also, in obtaining a PCI, any inaccuracies in the hydrogen uptake measurement will accumulate as points on the isotherm for higher and higher pressures (for absorption) are made. The following example illustrates this:

1) Hydrogen is let in until the pressure is 1.0 bar

2) As the sample absorbs hydrogen, the pressure drops to 0.9 bar

3) The amount of hydrogen uptake is calculated from the drop in 0.1 bar

4) However the volume determination is unknowingly inaccurate and the amount of hydrogen uptake calculated is 10% too large, for instance.

5) Hydrogen is let in until the pressure is 1.5 bar

6) The sample absorbs hydrogen and another value for the amount of hydrogen uptake is calculated

7) The amount of hydrogen uptake for this new equilibrium pressure on the PCI will be the sum of the two values calculated, but since they are both 10 % too large, the sum will also be 10 % too large.

Even though it appears that these complications should be fairly straightforward to overcome, experience from several groups has shown that it is not so easy in practice. They are having problems still after several years of development.

The Sieverts' apparatus is commercialized. An example from Hy-Energy, now acquired by Setaram Instruments, is shown in Figure 23.

Figure 23 Automated commercial Sieverts' apparatus from Hy-Energy[38]

3 NEW EQUIPMENT: HIGH PRESSURE MICROBALANCE FACILITY FOR DETERMINING CHANGE IN HYDROGEN CONTENT

A high pressure microbalance was constructed especially for characterizing hydrogen storage properties for new materials. In order to have a controlled and protected system, an extensive microbalance facility was built. Some part of this work was already made in a prior project (in particular making large metal components for the assembly). The components in this facility include:

1 Microbalance:
   - Cahn electromagnetic microbalance
   - Setup for a light emitting diode located opposite a photodiode (sensor)
   - Electronic control
   - "Hangdown" wires from each end of the beam of the microbalance
2 Sealed environment for microbalance to operate in high pressure hydrogen:
   - Steel block with cavity to fit the balance
   - Tubes for hangdown wires
   - Removable sample and counterweight chambers
   - Counterweights and sample packages
3 Heating system:
   - Heating elements for sample and counterweight chambers
   - Thermocouples next to heating elements, inside sample and counterweight chambers, and in microbalance cavity
4 Glove box with inert gas environment:
   - Glove box frame and support for microbalance
   - Security flask
   - Gas inlet and foot control
   - Purification column with fan and particle filter
   - Regeneration system for purification column using PLC
5 Gas supply system:
   - Tubing with pressure controller, mass flow controller, magnet solenoid valves, pressure transducers, etc.

- Vacuum pump and vent
- Communication box with data acquisition modules
- Special relay box

6 Computer operating system for the facility:

- General LabVIEW software for operating facility

Items 1-5 on this list are described in sections 3.1 trough 3.6. Tests and issues related to the components are discussed together with the descriptions. The LabView software under item 6, however, is described separately in chapter 4.

3.1 Microbalance

3.1.1 Cahn Electromagnetic Microbalance

The heart of the system is a Cahn microbalance from the 60's as shown in Figure 101. It has a beam that can rotate about the center of balance. The axis of the beam is held by an electromagnet. On the right arm of the beam (according to Figure 101) a thin rectangular piece of aluminium foil is attached. This foil serves as to shield a ray of light coming from a light source (a light emitting diode, LED) just in front of the foil (the ray is horizontal and parallel to the axis the beam rotates about). A light sensor (a photodiode) on the other side of the foil outputs a voltage proportional to the magnitude of the light that gets past the foil. The balance uses the null balance principle using the photodiode as null detector.[162] When weight is applied on the left arm, the right arm moves upward and shields more of the light (because the foil at equilibrium position covers the lower part of the ray). The voltage of the null detector is read by an external controller, which then sets a voltage change in the electromagnet, which moves the beam back towards equilibrium. The voltage over the electromagnet, when the beam is in equilibrium, is proportional to the weight of the sample, and thus the weight can be directly obtained.[163]

The microbalance is rated to measure up to a maximum of 200 mg. By using a counterweight of 800 mg, samples up to 1 g can thus be used. Another specification of the balance is, that the beams should not be loaded with more than 1 g each.[163] In practice, we can then have a sample of minimum 800 mg in which mass increases can be measured to up to 1000 mg. Likewise a sample of maximum 1000 mg can be measured to lose mass down to 800 mg.

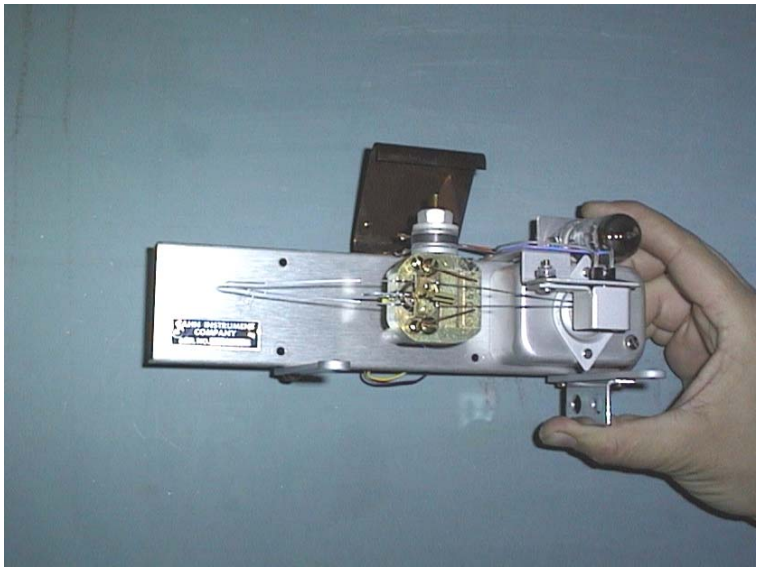

Figure 24 The original Cahn microbalance setup. The balance has been removed from the metal support. A box for the light emitter and opposing box containing the light sensor is seen at the end of the right arm of the beam.

3.1.2 Setup for a light emitting diode located opposite a photodiode (sensor)

A holder was designed and made for the LED and photodiode, seen in Figure 25.

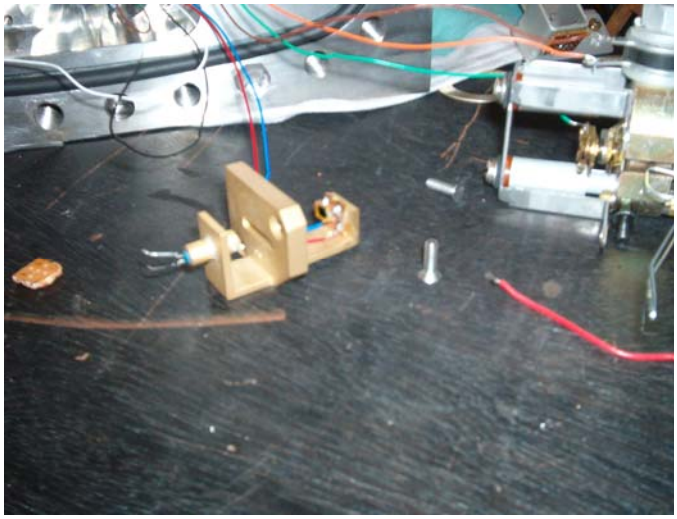

Figure 25 Brass holder for a LED and a photo diode. The arm with foil will cut off the beam of light (focused by the little pipe the LED is fastened in). The holder is to be fastened in the right end of the cavity in the microbalance pressure chamber which has a hole, the protrusion holding the photodiode can fit into. The back of the electromagnetic balance is seen to the right. The visible aluminum frame is electrically isolated from the round supports of the microbalance.

The holder, made of brass (which is easy to form and weld during manufacture), was designed so it could be screwed in place inside the cavity of the steel block (see Section 3.2), so the flag from the microbalance beam shields half the light beam from the LED, when in equilibrium.

The LED emits light in the near-infrared range at 800-950 nm. The photodiode is sensitive to light in the range 400-1100 nm, but peaks at 850 nm. False light from external sources (visible light being in the 400-700 nm range) is not an issue, since the chamber is sealed off (see Section 3.2).

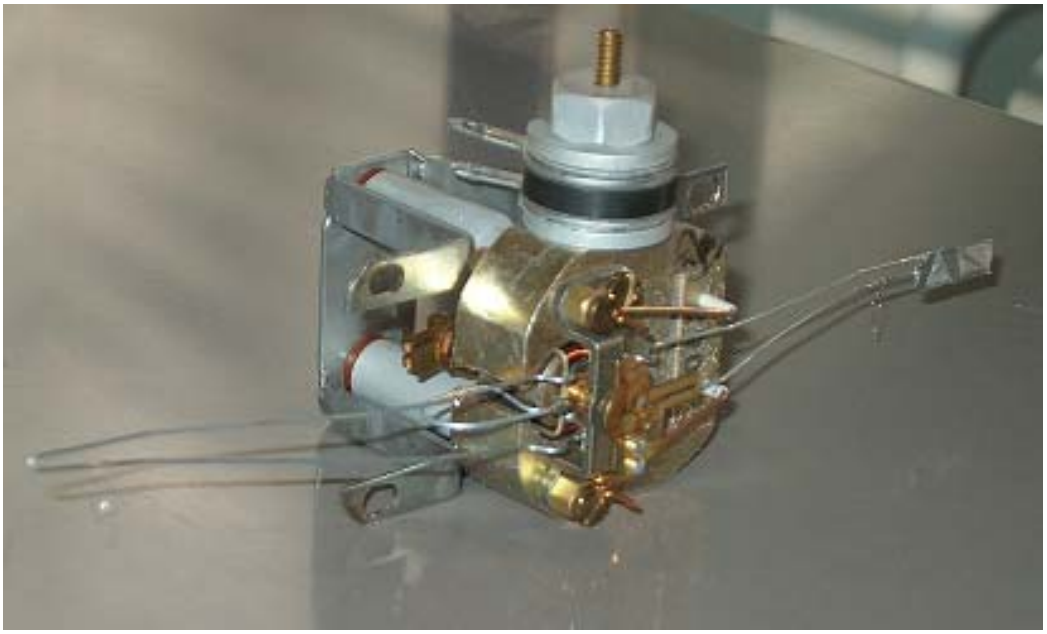

Figure 26 Cahn microbalance with attached aluminum frame for fixture in the cavity of the microbalance pressure chamber. The frame is electrically isolated from the bulk of the electromagnet of the microbalance. The foil on the right beam is visible, as are the small loops on each end of the beam. The round thermistor on top of the electromagnet was originally used for temperature correction, but was unused in the new facility.

3.1.3 Electronic controller

The function of the microbalance controller, which is shown in Figure 27, is to read the light intensity, deliver correction voltage to the balance and an external output signal with voltage proportional to the one delivered to the balance, which is therefore proportional to the weight exerted on the left beam of the balance from which the sample hangs.

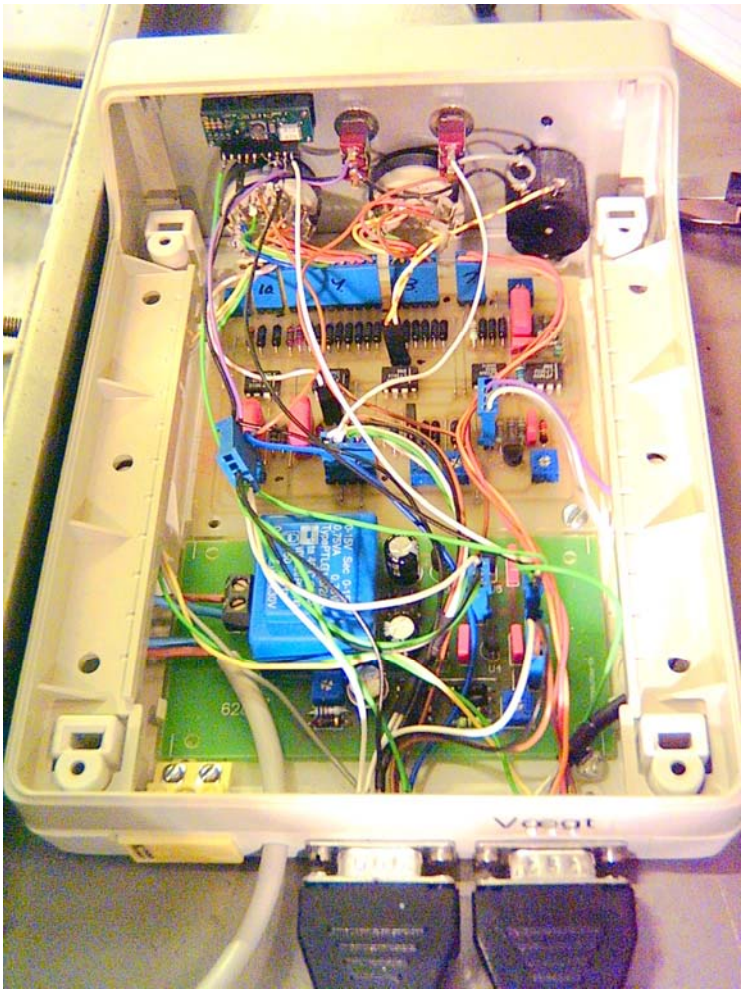

Figure 27 The inside of the microbalance controller. Refer to Appendix 11.1 for electronic circuit diagrams. The green board is the "628" circuit and the beige upper board is the "640" circuit which is the heart of the controller.

The controller, including electronic circuits and so forth, was made by an electrical engineer, especially for the use of this microbalance, based on the design specifications given him.

It is beyond the scope of this work to explain the electronic circuits of the controller. However, in order to understand the integration of the controller in the system, some details must be accounted for.

Appendix 11.1 contains electronic circuit diagrams for the controller. The first diagram shows a top-level circuit. The rectangle named "640" represents the primary circuit, which is shown in the second diagram. The ports J1-J10 (except J6) each have an individual number of pins, and the equivalent pins are seen in the diagram for "640". Also, in the top-level circuit, there are two 9-pin ports, B1 and B2. B1 is the output to a computer and B2 is the connection to the microbalance. Table 8 shows the values for the individual pins of B1.

Table 8 Specification of port B1, which contains output to be read by a computer

Pin	Voltage	Notes
1	+15 V	
2	+10 V	
3	0	Ground
4	-10 V	
5	-15 V	
6	variable	There is a display on the front panel of the controller, which can be used instead of a PC. Dials on the front panel change a number on a display, which goes from approx. -1400 to +1400. 10 V corresponds to 1000 on the display.
7	variable	This is the voltage used to balance the beam. It is proportional to the sample mass. 200 mg corresponds approx. to 10 V.
8	not used	
9	not used	

Table 9 lists the specifications for the pins of port B2.

Table 9 Specification of port B2. This is connected to the microbalance, LED, and photodiode.

Pin	Voltage	Notes
1	Not used	
2		To the electromagnet, connection 1
3		To the electromagnet, connection 2
4	Not used	
5	Not used	
6	+5 V	To the LED anode
7		To the photodiode cathode
8		To the photodiode anode
9		To the LED cathode

Pins 2 and 3 in port B2 to the electromagnet can be interchanged, so the direction of the current is reversed. This will reverse the direction in which the beam is rotated as a response to the light intensity received by the photodiode.

Potentiometer P3, shown in the second diagram of Appendix 11.1, is of particular interest, since it is used to change the output voltage (pins 6, 7 in port B1). It can be adjusted (with a screwdriver), so 200 mg corresponds to slightly over 10 V or slightly below 10 V. In practice, this will normally be set to maximum, so the resolution will be as good as possible.

The third diagram of Appendix 11.1 shows the location of P3 on the print board.

3.1.4 Hangdown wires

From each end of the beam of the microbalance platinum wire of thickness 0.1 mm were tied. This procedure was carried out after the microbalance was in place in the cavity of the steel block (pressure chamber), described in the next section, and tubes for the hangdown wires were in place. The procedure for putting the wires in place is not straight-forward and is therefore reviewed here.

The platinum wires come typically from a curled-up state on a wheel, and they must be straightened. This was done by heating over a Bunsen burner. Two separate wires were made and inserted and tied to the beam of the microbalance in the following manner:

A piece of sewing thread was tied to a little metal piece in one end for weight. The metal piece was dropped down into one of the holes from inside the steel block down through the connecting tube. The thread was held in place over the hole and the metal piece entered all the way down through the other end of the tube. Here the metal piece was cut off and the thread was tied to one end of one of the straightened platinum wires. By gently pulling the thread up from the top, the platinum wire was moved up into the steel block. When there, the thread was cut off, and a delicate procedure of tying the wire to one of the loops hanging from the beam was made using a forceps and a needle. This procedure was made for both wires.

Tiny hooks of 0.1 mm NiCr wire were made and tied to the lower ends of the platinum wires, one hook for each wire. NiCr is stiffer than Pt and suitable for repeated use when samples are put on and removed from the hook.

This procedure of inserting and tying the hangdown wires to the microbalance and to the hooks was extremely difficult to execute. During operation of the microbalance, special care must therefore be taken so the wires are not accidentally broken by accidently pulling of the wire. A replacement of wires or hooks will require both skill and dexterity.

3.1.5 List of equipment and materials

Name	Brand and model	Material	Additional info
Electromagnetic Microbalance	Cahn RG		
Infrared emitter	Siemens SFH 487	GaAlAs, Clear blue tinted plastic lens	Operating temperature range: -55 to +100 °C Reverse voltage: 5 V Forward current: 100 mA (at 25 °C), 25 mA (at 80 °C) Power dissipation: 200 mW Spectral emission: 775 – 1000 nm (peak 880 nm)
Photodiode	Siemens BPW 34	Silicon-PIN	Operating temperature range: -40 to +85 °C Reverse voltage: 32 V Power dissipation: 150 mW Spectral sensitivity: 400 – 1100 nm (peak 880 nm)

3.2 Sealed environment for microbalance to operate in high pressure hydrogen

3.2.1 Steel block with cavity to fit the balance

The Cahn microbalance was originally designed to occupy a glass chamber. However, for samples at high pressure and temperature the balance had to be used in a more fitting place.

Figure 28 shows a specially designed block of austenitic stainless steel (type 316, 18% chromium and 8% nickel) with cavities made to hold the microbalance. This block is interchangeably called “steel block” and “microbalance pressure chamber” throughout this chapter, designating its composition and use, respectively.

The block was pressure-tested with oil and proven to be resistant to up to 250 bar pressure.

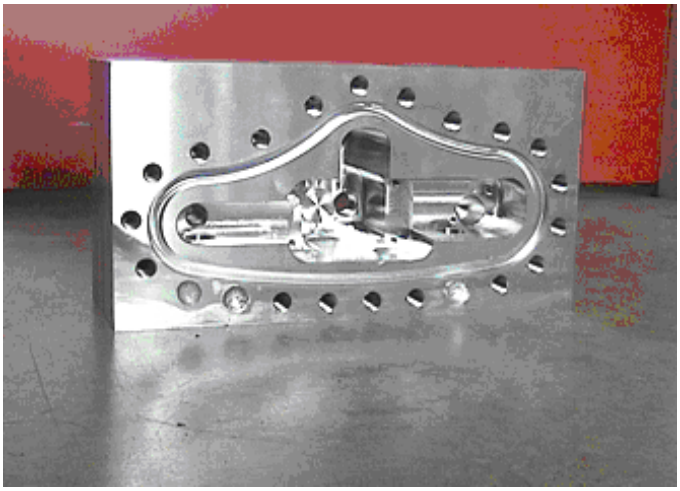

Figure 28 Pressure chamber with cavity to fit the microbalance. The curvy profile around the cavity is designed to hold an O-ring. The holes around this profile are places for bolts, so a plate can be screwed on to seal off the pressure chamber.

The microbalance and LED/photodiode setup were carefully transported and fitted into the chamber following wiring of the components. The wires were combined through a fitting in the back of the chamber, secured with an O-ring. The isolation of the wires was removed at the place where they went through the fitting, and epoxy glue was used to seal the wires in place with subsequent test that the wires did not short-circuit.

Figure 29 shows the microbalance and LED/photodiode setup in place in the chamber.

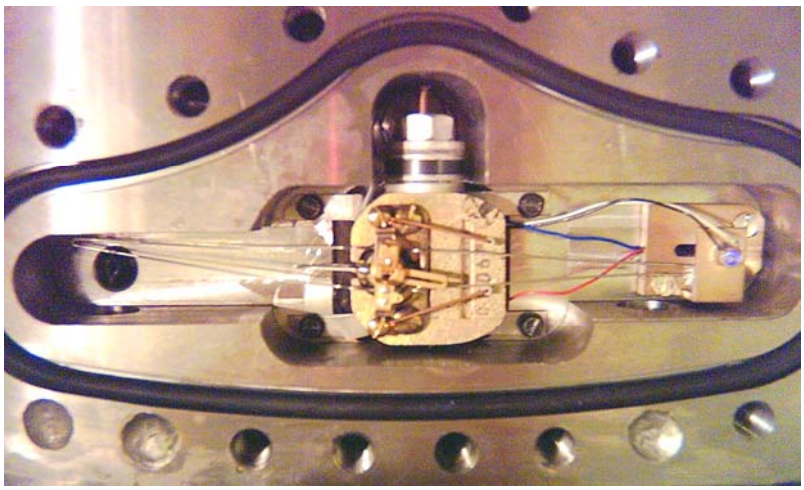

Figure 29 The microbalance and LED holder positioned in the pressure chamber. The violet object on the brass holder is the LED. The *black* and *white* wires are connected to the LED cathode and anode, respectively. The *blue* and *red* wires are connected to the photodiode cathode and anode, respectively. A thin loop can be distinguished hanging from the end of the left beam. A platinum hangdown wire was subsequently tied to this loop.

3.2.2 Positioning of the pressure chamber

An important issue is to have the pressure chamber positioned securely and unmovable inside the glovebox. A steel support was designed and manufactured and screwed in place from one side of the glovebox to the opposite side, see Figure 30. To solve this problem, three metal pieces were made so they could be placed on the underside of the bench. Each piece had a hole where a bolt with a washer could go through and end in the bottom of the pressure chamber. Threaded holes were made so the bolts could have a grip in the pressure chamber. Figure 31 shows a diagram of this setup.

Figure 30 Glovebox used for the site of the microbalance. The pressure chamber went on top of the metal bench seen fastened on opposite sides near the ceiling.

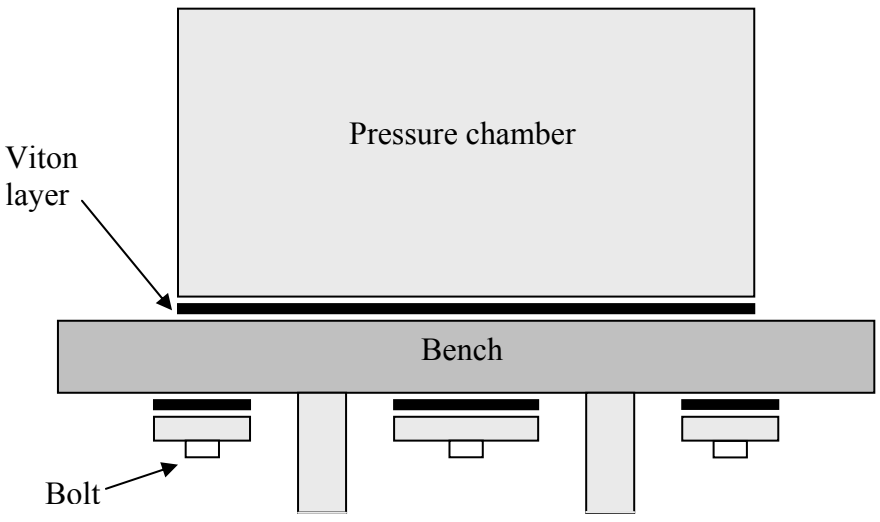

Figure 31 Diagram of how the pressure chamber was fastened to the bench by using pieces of Viton and stainless steel.

Layers of Viton (0.5 mm thick) were cut out (with holes for the tubes with hangdown wires) to lie between the metal pieces, bench, and steel block.

With the bolts fastened, the steel block was totally fixed to the bench and the tubes could be centered (see Section 3.2.3). At this point the tubes were simply screwed into the bottom of the pressure chamber using a big wrench with a lot of torque, so the joints would be gas tight. Figure 32 shows the metal pieces screwed tight.

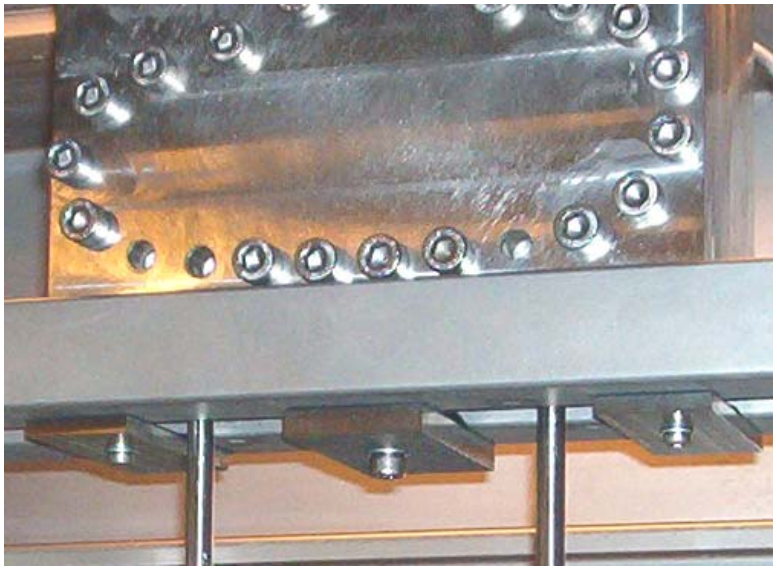

Figure 32 Underside view of how the steel block is fastened by using metal pieces and bolts. The block is seen here with the front plate screwed in place. Tubes for the hangdown wires are also seen in place.

3.2.3 Tubes for hangdown wires

In the bottom of the pressure chamber, two holes were drilled, thread was etched, and tubes were attached, see Figure 32 and 33. O-rings were used as seals between the fitting and the pressure chamber.

Two “positioners” were constructed in the lower part of the bench, see Figure 34. The function of these is to adjust the position of the tubes when fitted in the steel block. The wires from the microbalance cannot touch the tubes at any point or it will cause disturbances in the measurements, so adjustments using these positioners help the wires become free from contact.

Figure 33 One sample/counterweight chamber and tube out of the pair. The chamber is fitted on the end of the fitting of the tube, in the right bottom corner, using a brass gasket, which is replaced after each use (the counterweight chamber need not be removed). The other end is fitted in the steel block, using an O-ring as gasket. The T-fitting serves as inlet/outlet for gas from the external gas supply (see Section 3.5).

Figure 34 The bench seen from below. The two positioners have screws from four sides that can slightly adjust the orientation of the tubes that go through them.

Figure 35 shows the tubes fitted through the positioners in the bench and the hangdown wires with weights in place.

Figure 35 Tubes with hangdown wires in place through the positioners of the bench. Tubes are fitted on the T-fittings and combined for a single gas inlet/outlet for the whole volume of the microbalance pressure chamber and sample/counterweight chambers.

3.2.4 Removable sample and counterweight chambers

In Figure 33 was shown a sample/counterweight chamber. By using replaceable brass gaskets, these chambers can be removed and reattached during sample transfer, e.g. It was important, that the chambers were large enough to allow for a sample of around 1 gram mass. They were constructed by an in-house workshop.

Figure 36 provides a diagram of a sample chamber with dimensional data to give an impression of the allowed volume of the sample to be used with the balance.

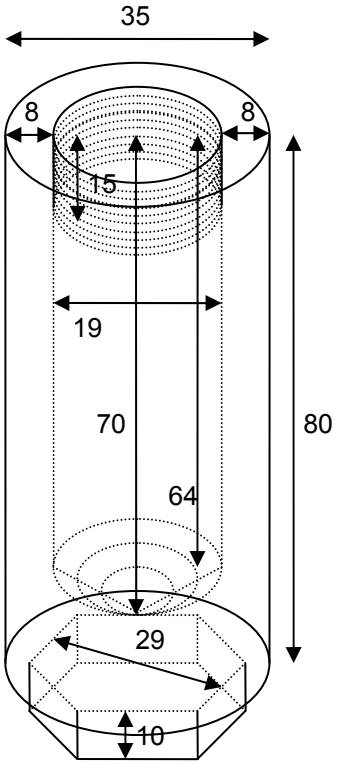

Outer diameter:	35
Inner diameter:	19
Outer disc area:	
$\pi/4 * 35^2 =$	962.1
Inner disc area:	
$\pi/4 * 19^2 =$	283.5
Inner depth (excl. fitting):	
Min. (64-15) =	49
Max. (70-15) =	55
Inner volume (excl. fitting):	
283.5 * (49 + 55)/2 =	14742
=	14.74 mL

Figure 36 Diagram of a sample chamber with dimensions. Numbers are in mm, mm^2, or mm^3. The nut in the bottom are used for screwing the chamber on a fitting with a wrench.

3.2.5 Counterweights and sample packages

While counterweights could be made simply from an aluminum rod with a drilled hole in the top, samples would need a special container to hold it. From prior experience[164] it has been observed that powder particles often "jump" out of containers during hydriding if there is nothing to hinder it. For the purpose of this microbalance, sample "packages" were made from metal foil (usually aluminum) folded around a cylinder (such as a pencil) and closed off at one end (being the bottom of the package). The sample powder would be poured into the container, which would then be shut off, by folding the foil in the top end. A hole for the NiCr hook would be made with a needle in the top, and several holes (4-8) would be punched in around the top part to allow for gas inlet/outlets.

3.2.6 The relationship between mass and voltage at room temperature

In order to calibrate the microbalance with regard to the relationship between sample mass and output voltage, calibration weights were made. The calibration weights were made in various manners:

- Sawing a small piece off an aluminum rod and filing it until the mass was right – making the hole for the hook by drilling
- Covering a screw with aluminum foil and using a needle to make a hole

Most weights were weighed on 3 different laboratory microbalances to obtain the right mass. Table 10 lists the measurements.

Table 10 The masses of the calibration weights were measured on 3 different scales. Balance 3 had an extra digit compared to the other two.

Weight	Bal. 1	Bal. 2	Bal. 2	Bal. 3	Bal. 3	Average
I (800 mg)				800.00	800.00	800.00
II (800 mg)	799.9	800.2	799.9	799.96	799.90	799.97
III (900 mg)	899.9	900.2	899.9	899.99	899.90	899.98
IV (950 mg)	950.4	950.7	950.3	950.35	950.27	950.40
V (1000 mg)	999.7	1000.1	999.8	999.86	999.86	999.86

Specifically, the weights were made of the following materials:

I: 100 % aluminum from rod

II: Aluminum foil around a stainless steel screw

III: Aluminum foil around a stainless steel screw

IV: Aluminum foil around a stainless steel screw

V: 100 % aluminum from rod

Voltages for the maximum and minimum loads, i.e. 1000 mg and 800 mg (keeping the 800 mg as counterweight) were measured.

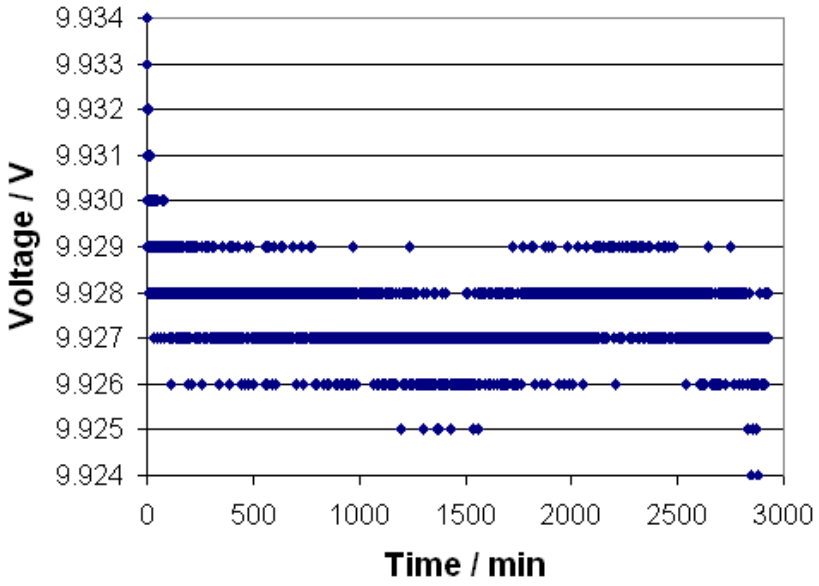

Figure 37 Raw data for measurements of 1000 mg calibration weight. The resolution of the data are seen to be 1 mV.

Figure 37 shows the measurements for the 1000 mg calibration weight in vacuum over almost 50 hours. It is seen, that the resolution to which the voltages are picked up are with 3 decimals. Also, the noise seems to occur over a 2 mV range. Since 10 V is approx. equivalent to 200 mg, this means a noise of 40 μg.

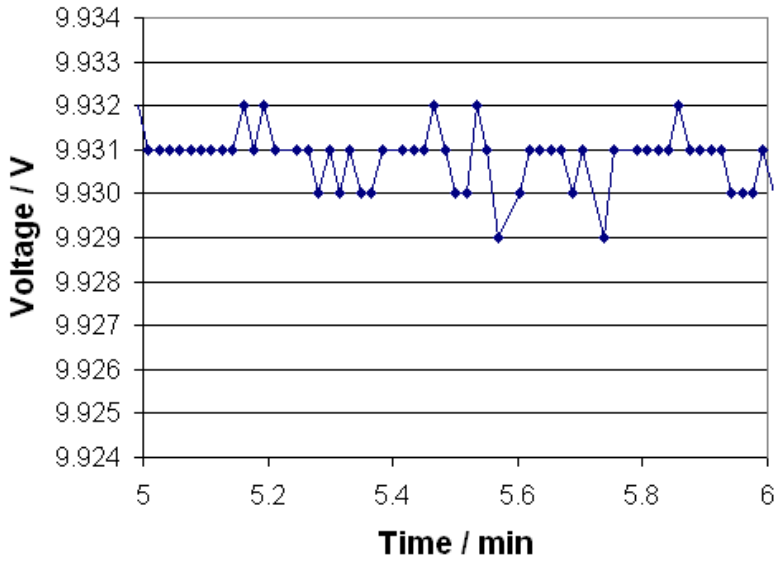

Figure 38 Close-up at raw data for 1000 mg calibration weight

Figure 38 shows the noise over a short time range. It gives an impression of how "vigorous" the noise is.

To get an approximation of the quantity for the "degree" of the noise, the standard deviation can be used:

$$\sigma = \sqrt{\frac{\Sigma (x - \mu)^2}{N - 1}} \tag{38}$$

where x is a data, μ is the average value of all data, and N is the number of data considered.

For 800 mg (really 799.97 mg), the equilibrium voltage reached -0.182 V.

The standard deviation in the data for 800 and 1000 mg was calculated to:

$$\sigma(800 \text{ mg}) = 4.83 * 10^{-4}$$
$$\sigma(1000 \text{ mg}) = 9.27 * 10^{-4}$$

From these values, it would seem that the noise increases with increasing mass.

Measurements were made for the 900 mg (really 899.98 mg) and 950 mg (really 950.40 mg) calibration weights as well showing equilibrium voltages of 4.866 V and 7.408 V, respectively.

It is expected that the voltage is proportional to the sample mass. If this is truly the case, it is straightforward to determine its function.

Since the line through two distinct points (x_1, y_1) and (x_2, y_2) is given by

$$f(x) = y_1 + [(y_2 - y_1) / (x_2 - x_1)] * (x - x_1) \tag{39}$$

the function for the voltage for a line going through (799.97 mg, -0.182 V) and (999.86 mg, 9.9273 V) would be

$$U(m) = -0.182 + [(9.9273 + 0.182) / (999.86 - 799.97)] * (m - 799.91)$$
$$= 0.05057 \text{ V/mg} * m - 40.637 \text{ V} \tag{40}$$

The opposite function is:

$$m(U) = (U + 40.637 \text{ V}) / 0.05057 \text{ V mg}^{-1} \tag{41}$$

The first function predicts the following values:

U (899.98 mg) = 4.875 V

U (950.40 mg) = 7.425 V

These values are 9 mV and 18 mV off, respectively. This is equal to about 180 μg and 360 μg, which is 0.02 % and 0.04 % of the total masses, respectively.

Based on these values there are a clear linear proportionality between the mass and the voltage.

Also, it is seen that 200 mg is corresponds to

0.05057 V/mg * 200 mg = 10.114 V

Since 200 mg ~ 10.114 V:

1 mV ~ 200 mg / 10114 = 19.77 μg

3.2.7 The relationship between voltage and pressure

For microbalances, buoyancy effects are easily observed, that is, the pressure in the system affects the mass the balance measures. If the right-hand side of the balance (designated beam + foil + hangdown wire + NiCr hook + counterweight) does not have the same buoyancy coefficient as the left-hand side of the balance (beam + hangdown wire + NiCr hook + sample package), there will be an observable change in measured mass when the pressure changes.

Measurements were carried out for weight II (refer to Table 10) at pressures in the range 0 – 42 bar hydrogen. Figure 39 shows the result.

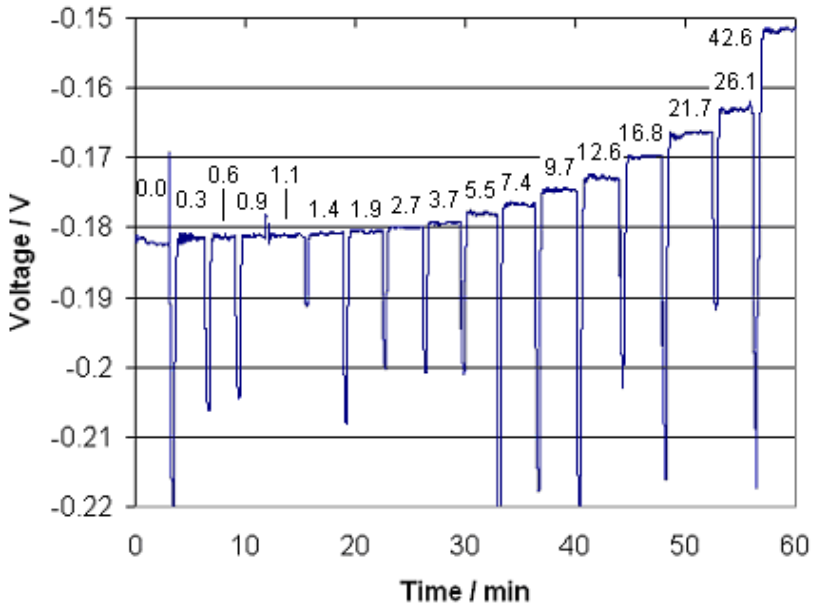

Figure 39 Voltage rise as an effect of increased pressure. Each sharp peak corresponds to a burst of pressure increase. The numbers above the curve correspond to the pressure at that time of measurement.

For each time extra hydrogen was let in to increase the pressure in the system a disturbance is seen as a large (relative) drop in voltage/mass. Approx. 3 minutes were given for the system to relax after each pressure "burst". The measurements were carried out an extra time to see the reproducibility.

Figure 40 shows the values for two series of measurements made plotted as voltage vs. pressure.

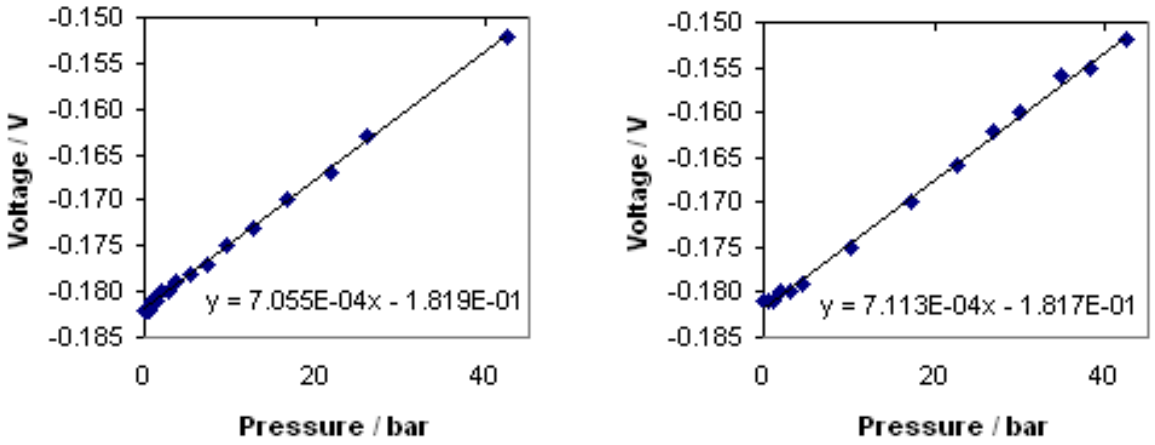

Figure 40 Relationship between pressure and measured voltage in the microbalance for a 800 mg Al reference weight.

The equations for the lines in the plots are made by linear regression and show that there is a clear linear relationship between the pressure and the voltage/effective mass.

As for the degree of noise, the standard deviations are:

$$\sigma(0 \text{ bar}) = 4.83 * 10^{-4}$$

$$\sigma(42 \text{ bar}) = 5.89 * 10^{-4}$$

The difference is negligible. Therefore, the pressure is concluded to have no determinable effect on the degree of noise in the measurements.

3.3 Heating system

In order to be able to heat the sample during an experiment, a thermocontroller unit was set up with two individual temperature controllers (CAL 3300 Autotune Temperature Controller). Each controller had a thermocouple (Omega KTIN 116 Ungrounded, Type K) plugged in and would give power to heating elements according to the temperature programmed. These controllers were also able to ramp the temperature using heating rate (in units of degrees per minute) and an optional soak temperature (the temperature that is kept constant at the end of the ramp).

3.3.1 Heating elements for sample and counterweight chambers

The heating elements were manufactured according to the specifications given of power and diameter. They are of 375 W each. One unit is seen in Figure 41.

Figure 41 Heating element. The element is made of stainless steel and has a power of 375 W. The time to heat a 430 g sample chamber (heat capacity of 0.45 J g^{-1} K^{-1}) up from 25 to 300°C (at 100% efficiency) is calculated to 2 minutes and 20 seconds.

The diameter of the heating elements is bigger than the outer diameter of the sample chambers even when clamped all together. A sheet of flexible graphite (Papyex®, 1 mm thick) was cut out and rolled around the sample chamber into a double layer. The material being easily deformed and highly thermally conductive served as a very appropriate layer between the heating elements and sample chambers. To obtain as low a temperature gradient as possible between the heating elements and the thermocouples, the thermocouples were squeezed down between to the flexible graphite layers and the heating elements, so the thermocouples would touch the surface of the heating elements. The thermocouples would sink into the material. Figure 42 shows the setup.

Figure 42 Heating element around sample chamber using flexible graphite sheet as buffer. A thermocouple can be seen coming out from the left side of the picture.

3.3.2 Thermocouples in microbalance system

Apart from the thermocouples used next to the heating elements, it was desirable to have thermocouples inside the system, in the volume the gas would occupy. For example, it would be important to have a measurement as good as possible of the temperature of the sample of a given experiment. The closest reading would be, if a thermocouple could be placed in the middle of the powder sample, but due to the nature of the setup, this was not possible. Instead, it was designed that the thermocouple should be located as close to the sample package as possible.

This was achieved by drilling a hole through the side of the fitting located above the brass gasket (refer to Figure 42). A thin and flexible thermocouple was inserted through the hole and bent downwards and pushed toward the side of the inner surface of the fitting, so it would interfere as little as possible in the area used by the hangdown wire. An 8 mm long cylindrical brass tube was squeezed up in the mouth of the fitting to fix the thermocouple in place. The drilled hole, through which the thermocouple put, was sealed by silver welding in order to keep the fitting gas tight. This whole procedure was made for both fittings, the one above the sample chamber and the one above the counterweight chamber.

It was also important to determine to what degree the heat would transfer to the pressure chamber and microbalance. The following are the temperature limits for various components:

- O-rings: 100 °C (See ref. 165 under 'Chloroprene')
- LED: 100 °C
- Photodiode: 80 °C

Therefore, it was important to make sure, that the temperature in the microbalance pressure chamber did not exceed 80 °C.

A 3.5 mm thick thermocouple was fixed in a fitting (Swagelok), which was set in a threaded hole in the back of the steel block. In this way the end of the thermocouple would be located inside the microbalance pressure chamber and be able to measure the temperature of the gas.

3.3.3 Changes in temperature of the microbalance pressure chamber

Figure 43 gives a diagram of a microbalance setup in a pressure chamber with sample chambers.

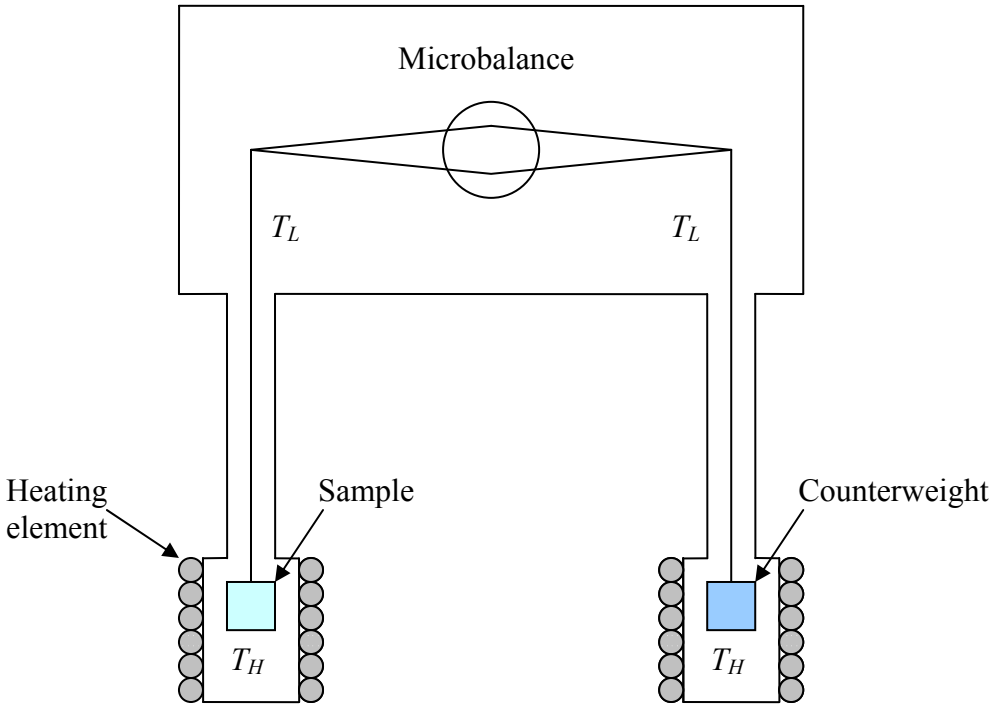

Figure 43 Diagram of the heating in the microbalance setup. T_H represents high temperatures and T_L low temperatures.

As noted it is essential as energy is transferred as heat from the heating elements to the sample/counterweight chambers to the gas inside and the hangdown wire tubes up into the microbalance pressure chamber, that the microbalance will not get too hot, because it might get damaged.

Figure 44 shows the result of an experiment where the sample chamber was heated to different temperatures and the equilibrium temperature in the microbalance pressure chamber was recorded. The measurements show what seems to be a linear relationship between the temperature in the sample chamber and the pressure chamber.

There obviously is a high degree of cooling of the gas/metal as the heat is transferred upwards. During the experiment the metal was touched to get an idea of how the heat was transferred through the steel. While all the fittings near the sample chamber were very hot for values of T_1 above 250 °C, the temperature would drop significantly up along the tube to the pressure chamber. At the topmost part of the tube it was almost not warm. Therefore, a high degree of heat transfer must have occurred to the air around the tubes.

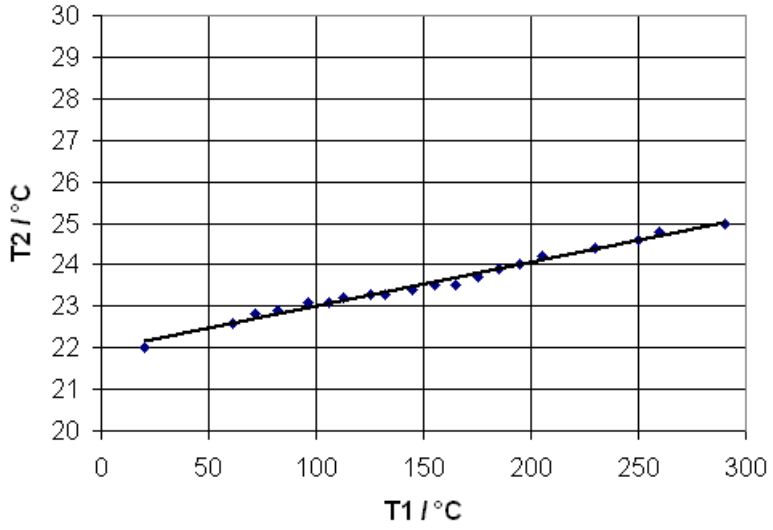

Figure 44 Temperature in pressure chamber as function of temperature in sample chamber. T1 is the temperature of the sample chamber, and T2 is the temperature inside the pressure chamber.

3.3.4 Convective flow of gas affecting the mass readings because of differences in temperature

For normal use of the microbalance facility, measurements are made while the system (extending to the valve that directly opens up for gas to the sample chamber etc.) is closed, i.e. no gas exchange with the surroundings occurs. This means that there is no gas flow in the system. However, when the gas is heated it will expand locally where the heating occurs, which will mean a decrease in local density of the gas. This leads to free convective movement by which energy is removed from the volume immediately close to the boundary surface.[166]

The free convection implies a flow upwards, which originates in the sample/counterweight chambers in the volume directly up against the metal surface. As the gas moves up and gradually cools down, it will increase in density, adjust vertically and flow downwards in the middle of the tubes and chambers. At the bottom of the chambers the gas will be heated again and move to the metal surface and upwards, thus completing a flow cycle. This will result in a downward force to act on the sample and the counterweight (because they are located in the middle of the chambers). If these forces are equal at all temperatures, this convection effect will not influence on the mass reading of the balance. However, in practice, differences in morphology and density between the counterweight and the sample package will result in differences in the mass measurement from the microbalance with different temperatures.

This convective effect is observed clearly when the relationship between the mass reading and temperature is examined in the cases of when only one heating element is used and when both heating elements are used heating at the same temperatures. Figure 45 shows the voltage reading of the microbalance for a 1 g aluminum reference weight when only the sample chamber is heated, and

Figure 46 shows the voltage reading when both the sample chamber and the counterweight chamber are heated synchronously.

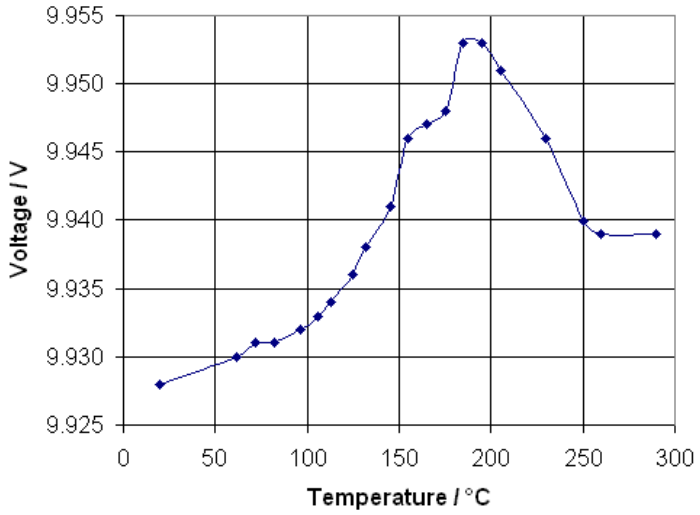

Figure 45 Voltage as function of the temperature in the sample chamber. A 1 g Al reference sample is used, and only the sample chamber is heated. The range on the voltage axis, 50 mV, corresponds to 0.6 mg or 0.06 wt% of the reference sample.

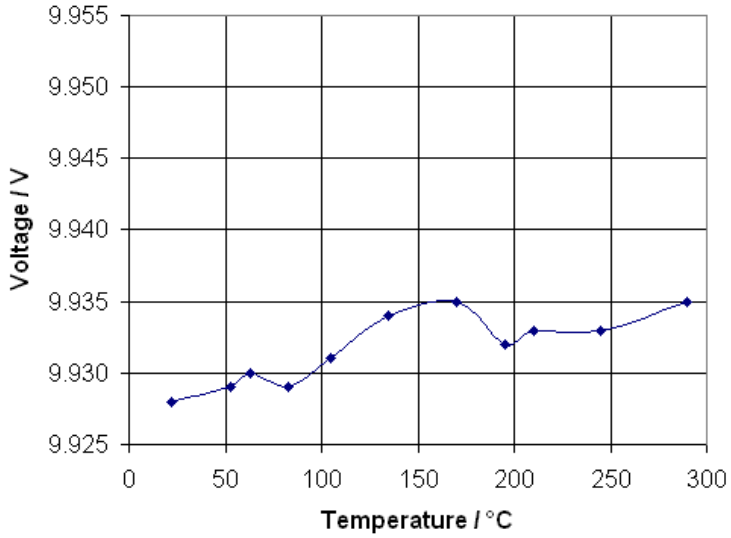

Figure 46 Voltage as function of the temperature in the sample chamber. A 1 g Al reference sample is used. The sample chamber and the counterweight chamber are to the same temperature. The range on the voltage axis, 50 mV, corresponds to 0.6 mg or 0.06 wt% of the reference sample.

A clear distinction is observed when both heating elements are used, and the maximum deviation from the value at room temperature is about 0.015 wt%, occurring at 170 °C and 285 °C.

3.3.5 Noise in mass readings at different temperatures

A study on aerodynamic forces in thermogravimetry using a Cahn microbalance (the same type used here) showed that at 100 °C there was "noise" showing itself as seemingly random fluctuations in a range over 40 µg. At 300 °C it had increased to 60 µg. The noise thus increased with increasing temperature.[167]

It would be expected that higher temperatures cause more aerodynamic noise than at lower temperatures. Higher temperatures mean more vigorous motion and more forceful battering into the sample of gas molecules in the atmosphere around the sample.

It was found with the experiments in the previous discussion under convection effects, that the degree of noise did not extend above 40 µg even at higher temperatures up to 300 °C. Figure 47 shows the standard deviation of the mass readings at various temperatures using only the sample chamber heating element.

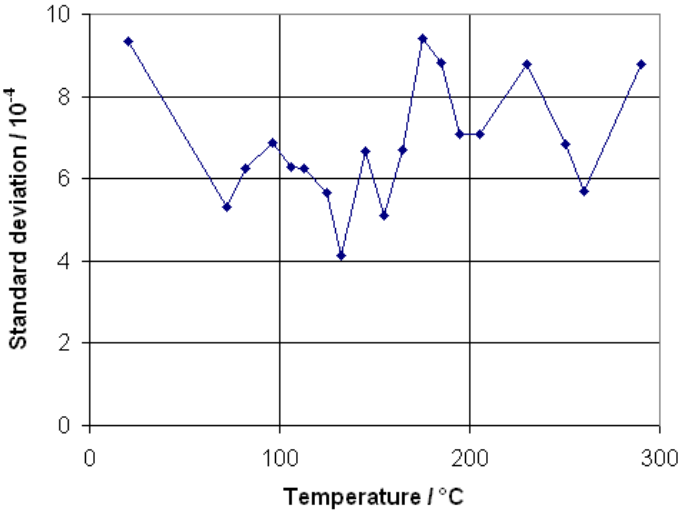

Figure 47 The degree of noise as expressed by the standard deviation of the measured voltage as function of the temperature. 1 g Al reference sample was heated using only the heating element on the sample chamber.

For the experiment in which both heating elements were used, the standard deviation of the data was $8.2*10^{-4}$ at 50 °C and $8.4*10^{-4}$ at 290 °C.

From these observations, it is concluded that the degree of noise do not increase with temperature in the microbalance facility.

3.4 Glovebox with inert gas environment

The microbalance system was integrated in a glovebox in order to protect samples from reacting with air during transfer from its container to the hook on the hangdown wire on the microbalance. It was seen in Section 2.3.8 that many typical materials for hydrogen storage are susceptible to spontaneous reaction with components in air, especially oxygen, water, and carbon dioxide.

Typical gases used in gloveboxes are dry air, argon, and nitrogen (helium can also be used, but is normally more expensive than the others). Dry air is avoided for the use of hydrogen storage materials, and nitrogen, although cheap, reacts spontaneously with lithium, which has proved to be a problem for certain experiments. For this microbalance, argon was chosen.

As the working standard for air sensitive materials is < 1 ppm O_2, it was necessary to make a purification column to continually purify the gas in the glovebox. Even though the glovebox can be made reasonably tight, there will be contamination as samples are transferred through the antechamber (transfer tube on the side of the glovebox), and because of diffusion of outside air through materials (especially the rubber gloves are susceptible). Even the smallest leaks at various places in the glovebox are significant as very small amounts of air are enough to contaminate the atmosphere at these purity levels. Slight overpressure in the glovebox can reduce the rate of contamination, but not completely.

3.4.1 Components for and the setup of the glovebox

The glovebox was custom-made from scratch. This included the construction and/or installation of the following components:

- Bench support for microbalance block with “positioners”
- Front window with neoprene gloves
- Foot control for inlet/outlet of argon
- Security flask for overpressure
- Oxygen meter
- Overhead light
- Centrifugal pump (fan)
- Purification column (with control for regeneration)
- Particle filter

Figure 48 shows a diagram for the setup of the glovebox and its connected components.

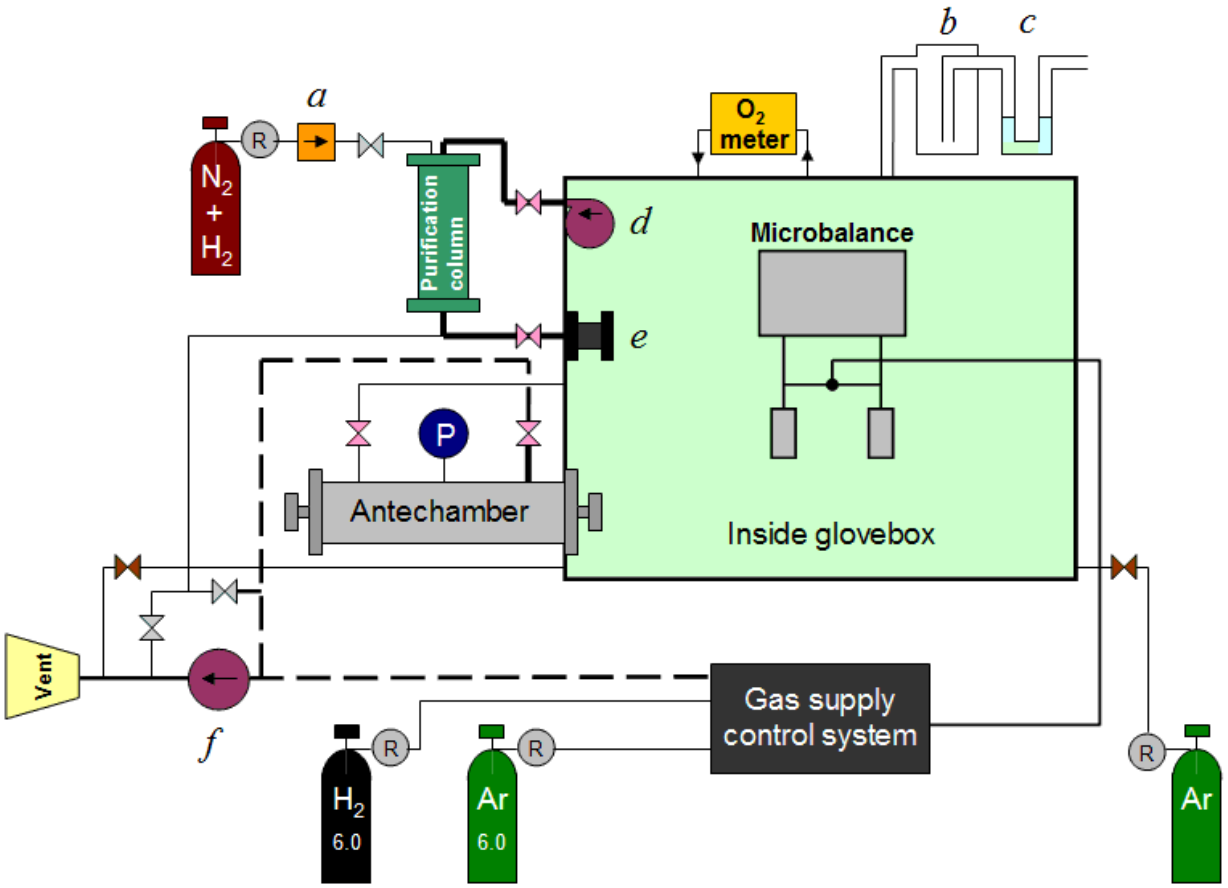

Figure 48 Diagram of the glovebox with various components in the microbalance facility. The microbalance is shown in the inside of the glovebox. Lines are generally of 4 types, all representing tubes: 1) Thin line is 6 mm stainless steel tube (inner diameter = 4 mm), 2) Thick line is 10 mm stainless steel tube (inner diameter = 8 mm), 3) Thickest line is 35 mm tube, 4) Dashed thickest line is a flexible 35 mm aluminium vacuum tube. Letters correspond to: a) Flow meter, b) security flask, c) U-tube with silicone oil, d) centrifugal pump (fan), e) particle filter, f) vacuum pump. Circles with 'R' are reduction valves. Valve symbols (2 opposed triangles) correspond to: Light blue = Controlled by regeneration control box, Pink = Controlled manually, Brown = Controlled by foot control.

3.4.2 Gas in and out of the glovebox

Initially the glovebox was flushed through with argon for several minutes in order to get as oxygen free an atmosphere as possible. The oxygen meter measured the level of oxygen inside the glovebox. Only the oxygen level was measured (water and carbon dioxide assumed to be of proportional amounts to oxygen and of course of much less magnitude). The oxygen meter had a pump, which could take out gas from the glovebox, analyze it (limit was below 1 ppm), and deliver it back to the glovebox. The gas was taken out from the top of the glovebox, which was the best place, since oxygen would be more concentrated towards the top than the bottom of glovebox as a cause of the lower molecular mass of oxygen compared to the atomic mass of argon. Therefore, the

measured O_2 level corresponded to the worst level of impurity in the main bulk of the atmosphere of the glovebox.

The gas was continually pumped to the purification column by a centrifugal pump and delivered back while passing through a particle filter (to keep particles from the column outside the glovebox). The gas was taken from the top of the glovebox (containing the most impure parts) and blown out in the bottom of the box.

Extra argon gas could be added to the glovebox by stepping on an electronic foot control, which manipulated the magnet valve on the tube between the argon flask and the glovebox. Likewise, gas could be taken away from the glovebox by the foot control, which could open a magnet valve that led the gas to ventilation (outside the building).

A security flask on top of the glovebox served as overpressure ventilation. An attached U-tube with silicone oil (having a very low vapour pressure[168]) regulated at which pressure limit, the gas would be ventilated.

Samples were transferred to the glovebox through the antechamber. To do this, the innermost lid of the chamber was sealed manually from inside the glovebox. The sample was put inside the chamber, which was thereafter sealed by the outer lid. The vacuum valve was opened and the chamber evacuated for about 15 minutes. Occasionally the chamber was flushed with argon (taken from the box) to more thoroughly clean the chamber from air. The vacuum valve was closed, and the valve to the argon opened, so the chamber was filled with gas until the pressure of the chamber and the glovebox was equal. The argon valve was closed, and the lid to the chamber opened from the inside of the box, and the sample was transferred to the inside of the box.

Figure 48 includes a representation of a gas supply control system for the microbalance. This unit controlled the gas coming into and out of the microbalance, and is discussed in Section 3.5. Figure 49 shows the actual setup of the system.

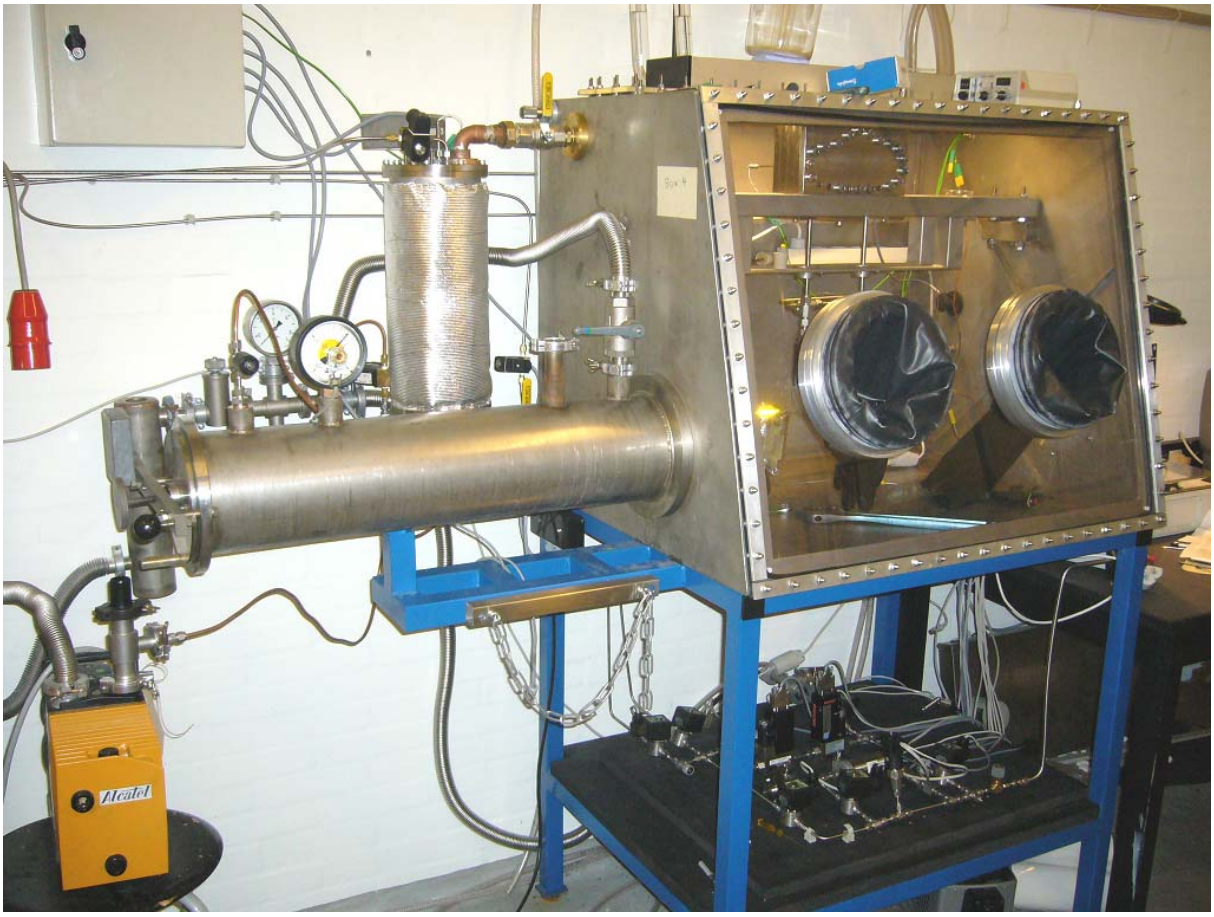

Figure 49 Glovebox with microbalance installed. The gas supply control system is seen in on the black plate below the box. The purification column is in place on the left of the box. The antechamber (transfer tube) has valves for vacuum and for argon gas taken from inside the glovebox. A control box for regeneration of the purification column is seen on the wall in the upper left part of the picture. An Alcatel vacuum pump for the system is seen in the lower left corner.

3.4.3 Safety in connection to working with the microbalance and glovebox

When working with gasses at high pressure (the microbalance facility being rated to 100 bar) in a contained environment, especially hydrogen, safety is a natural concern.

The concern is that a failure in the hydrogen containing components occurs, which results in hydrogen coming out. For all tubes, connections, valves etc. outside the glovebox, a failure will result in hydrogen coming out in the room, where people are present when operating the system. Since all components are rated for use with gases at least 100 bar violent failures or fractures should not occur. More likely, a connector would start leaking slowly, which would be visible as a pressure drop.

A possible dangerous scenario is if the person working with the system, accidently unscrews the sample chamber, while there is pressurized hydrogen inside. It was calculated that the pressure

increase in the glovebox would amount to about 200 mbar if all hydrogen inside at 100 bar (at room temperature) came out. This is enough to be of concern.

However, drawing on experience in working with gloveboxes including accidents herewith[109], it is known that the gloves themselves can act as a significant buffer for pressure increase. The flexibility of the neoprene material is sufficient, that they can expand largely in surface area, creating extra volume for the gas inside, and thus releasing stress from the surfaces inside the glovebox. Gas will be immediately vented through the security flask, and the buffer of the gloves will serve to give time to vent enough gas, so the pressure will drop to normal.

The degradation of the stainless steel used throughout the system because of hydrogen embrittlement might be a valid concern[169]. However, no evidence of hydrogen embrittlement was observed even after lengthy exposure to hydrogen at high pressures and temperatures. This is in agreement with a model by Shih and Johnson and experimental Nelson curves[170], which have shown that for plain carbon steel a safe area of operation at 300 °C for 100 h was up to at least 350 bar hydrogen pressure. At 100 bar for 100 h it was safe up to 350 °C. Embrittlement primarily stems from the formation of methane in the material, so plain carbon steel provides a worse scenario than austenitic stainless steel, which was used for the microbalance facility, with a maximum carbon of 0.15 % compared to a maximum carbon content of 2.1 % for plain carbon steel.

3.4.4 Purification column and regeneration

As noted earlier, it was essential that the gas in the glovebox be purified continually, as contaminants from outside unavoidably entered into the box atmosphere. Therefore, a purification column was made for the job. It has already been described how the column was integrated in the setup for the glovebox: gas from the glovebox was continually pumped through the column.

The design for the column was based on a purification column on a commercial glovebox (Vacuum Atmospheres Company). The specifications in Table 11 was found in the manual for the glovebox or measured directly on the commercial column.

Table 11 Specifications for a commercial purification column from Vacuum Atmospheres Company

Parameter	Value
Height of cylinder	400 mm
Diameter of cylinder	150 mm
Mass of upper layer packing material: zeolite	0.80 kg
Mass of middle layer packing material: Cu catalyst	2.30 kg
Mass of lower layer packing material: zeolite	1.80 kg
Capacity of zeolite	0.031 g H_2O / g zeolite Total = 80.6 g H_2O
Flowrate of gas through cylinder	9.5 L / min

The way the column works, is that it removes oxygen and water from the gas stream. The zeolite removes water (water molecules being adsorbed in the many pores of the molecular framework) and oxygen combining with copper on the catalyst, which consists of copper on an alumina matrix. These processes occur spontaneously at room temperature and atmospheric pressure (or slightly above as is the case in the glovebox).

At a certain point, the capacity of the zeolite and copper catalyst (combined called 'packing material') is reached, which is evidenced by the oxygen meter starting to measure a relative higher oxygen content. At this point it is necessary to regenerate the packing material.

The regeneration cycle for the new column was based on the one for the commercial column. It is specified in Table 12.

Table 12 Regeneration cycle based on commercial glovebox with purification column from Vacuum Atmospheres Company.

Step	Name of step	Length of time	Explanation
1	Close off to glovebox		The 2 valves to the glovebox are manually closed, so the gas stream is stopped
2	Heating of column	4 hours	The heating element is powered and heats the packing material to 425 °C
3	Passing Formier gas through column	1 hour	Formier gas (10% H_2/90% N_2) reduces copper oxide to copper. Heat is still on.
4	Evacuation	8 hours	With the reduced pressure and raised temperature, water molecules are desorbed from the zeolite bed. The heating element is turned off, so the temperature falls gradually.
5	Open again to glovebox		The 2 valves to the glovebox are manually opened again

Under step 2, a thermocouple was put in the commercial column (in the center) and it was observed that the temperature reached 425 °C during the passing of Formier gas. It was specified that the material itself should have a temperature of more than 200 °C to be regenerated, however, to ensure that the temperature would be high enough even in the sides of the constructed column, a temperature of 350 °C was used.

During the regeneration cycle, copper oxide in the catalyst is reduced by the hydrogen in the Formier gas. The water trapped in the zeolite bed is released at lowered pressure (and elevated temperature).

Figure 50 shows different parts of the column during the building of it.

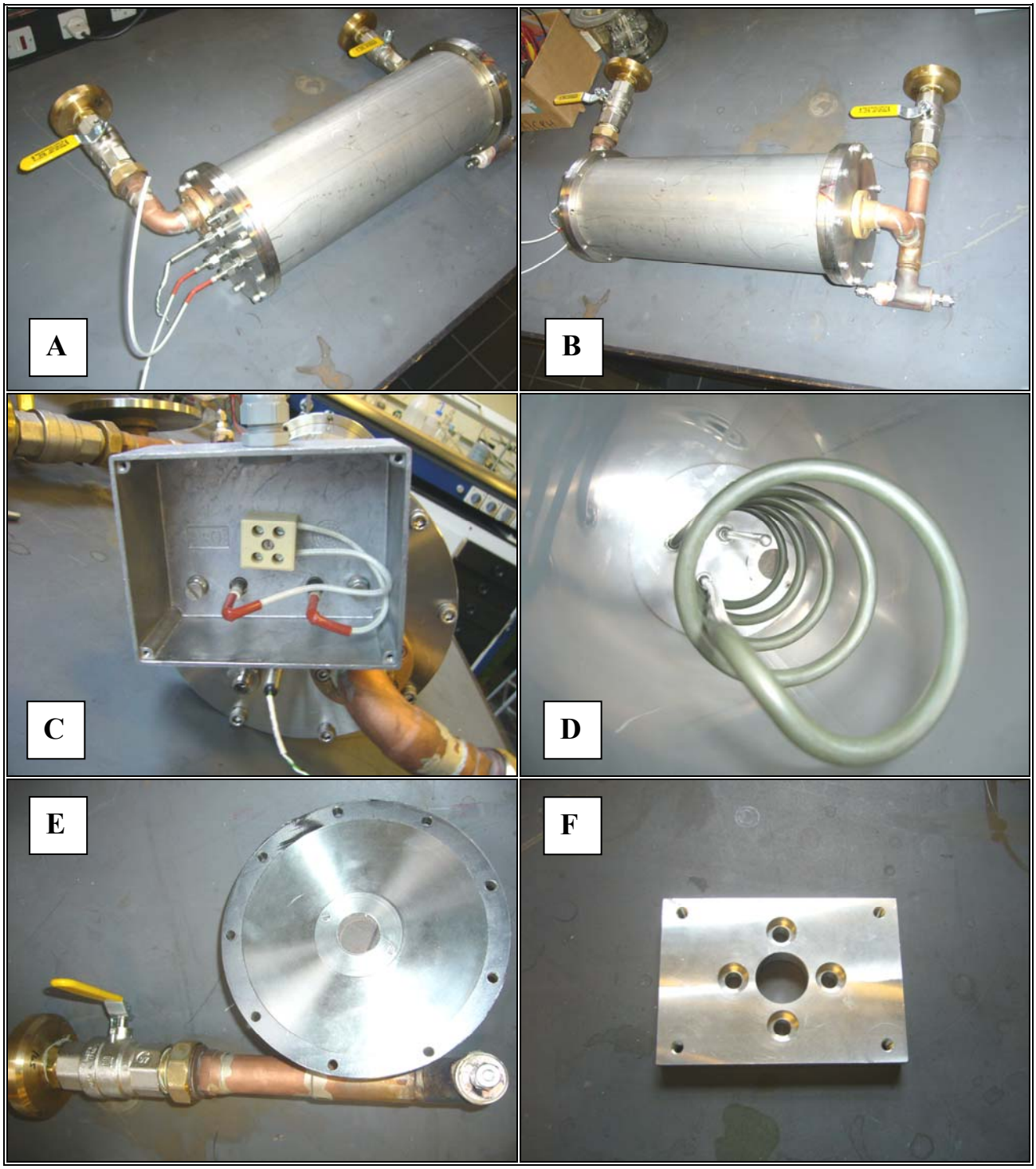

Figure 50 Purification column with various parts. A) The column with top and lower lids in place. The end to the left is the upper part, and has connections to the heating element inside. The two manual valves are vacuum tight. B) Column from a different angle. C) Top part of column with box for electrical connection to the heating element. Under the box a thermocouple is visible coming out from the lid. D) Shot taken from inside from below. The heating element is spiral. The thermocouple is visible and is located close to the center of the column cylinder. A particle filter (thread grate) is also seen in the top lid, through which the inlet gas from the glove box enters. E) The bottom lid. A particle filter like the one in the top lid is seen in the center. On the circumference of the lid is a gasket of 0.5 mm thick Papyex® flexible graphite sheet cut out to fit. The brass connector on the other side of the valve has a groove with an O-ring to seal against the side wall of the glovebox. F) Detail of a fastening

board of aluminium for the inside of the glovebox wall opposite the upper and lower brass connectors. The gas goes through the center large hole. The 4 holes around it are places for bolts that enter into the brass connectors. The four small holes in the corners are threaded and used for fastening the centrifugal pump in the top and particle filter in the bottom.

In order to insulate the column when it was warm, a glass cloth with aluminium coating was prepared for the column as seen in Figure 50 (A).

A Moeller Easy412-AC-R PLC (Programmable Logic Controller) was used to control the series of steps of the regeneration of the column. The PLC had 4 relays that could be switched on and off automatically according to the program made. During heating a thermo controller CAL 3200 with a thermocouple in the middle of the column would be switched on set for 350 °C and keeping the temperature at this level. Table 13 shows the principle of the program.

Table 13 Relays operated by program on PLC during regeneration cycle on a home-made purification column for the glovebox. It was found that 2 hours was enough to heat the packing material and column up to 350 °C. The 'Q'-s are codes for Moeller PLC's designating a relay. 'MV' means magnet solenoid valve. These are clearly visible in Figure 128.

Relay	Name of control	Time: 0-2 hours	Time: 2-3 hours	Time: 3-11 hours
Q1	Heat	ON	ON	
Q2	MV 1: Formier gas		ON	
Q3	MV 2: Venting		ON	
Q4	MV 3: Vacuum			ON

Figure 51 (B and C) shows the PLC with thermo controller and cooler in a box, which was also seen in Figure 49 from the front being closed. Figure 51 (A) shows the complete purification column with all connections in place.

Figure 51 Purification column integrated with glovebox and regeneration apparatus. A) Tubes are connected with magnet valves to the column. The magnet valve in the top is for Formier gas. The two in the bottom to the left of the column are for venting and evacuation. The PLC in the regeneration control box operates these valves via its relays and program. B) Panel in regeneration control box showing the Moeller PLC, an ON/OFF button for initiating the regeneration program, and a CAL 3200 temperature controller (from CAL Controls). This controller was set to 350 °C at default, so it would begin heating to 350 °C when it was turned on. C) Back of the panel showing the temperature controller and a solid state relays glued with cooling glue on an aluminum cooling block. The 4 holes above the temperature controller are entrances for the wires to the Q1-4 relay connectors also visible in the bottom of the PLC in picture B.

A complete diagram over the regeneration control box is given in Figure 52.

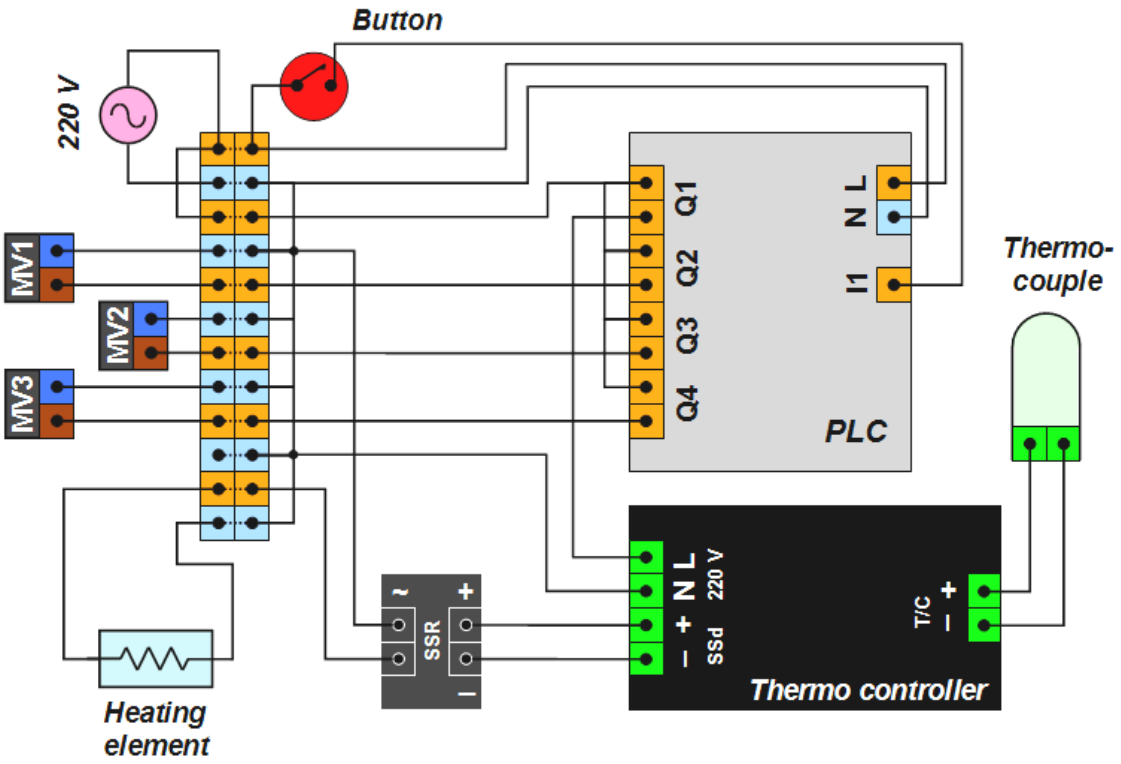

Figure 52 Diagram over units and connections related to the regeneration box for the purification column of the glovebox and of which Figure 51 showed the actual setup. The main unit "PLC" was set to initiate the regeneration cycle program when "I1" was powered by switching the button on. "MV1"-"MV3" represents magnet valves referred to in Table 13. The thermo controller utilized a solid state relay (connected to "SSd" (solid state drive) on the thermo controller) on a cooler, which could tolerate higher currents than the internal relay in the thermo controller itself. The heating element shown was the one inside the purification column

3.4.5 Purification of glovebox atmosphere

In normal operation, the purification column will continually purify the atmosphere in the glovebox by having the gas flowing through it by the force of the fan.

However, as a first purification, when there is initially air inside (or in another case, when there has come a major contaminant into the glovebox), the glovebox is flushed through with argon (inlet by use of the footswitch and outlet through the security flask and U-tube). This was done in the glovebox, and after approximately 40 minutes of flushing (the flow through the inlet was rather slow) the reading of the O_2-meter had reached 3%. In the meantime the purification column had been regenerated a first time after packing (the packing material being already contaminated by species from the air) at 250 °C. The flushing was stopped, and the fan was turned on and the valves to the purification column opened. Figure 53 show the effect of the first purification process, resulting in a decrease from about 3% to 1% oxygen.

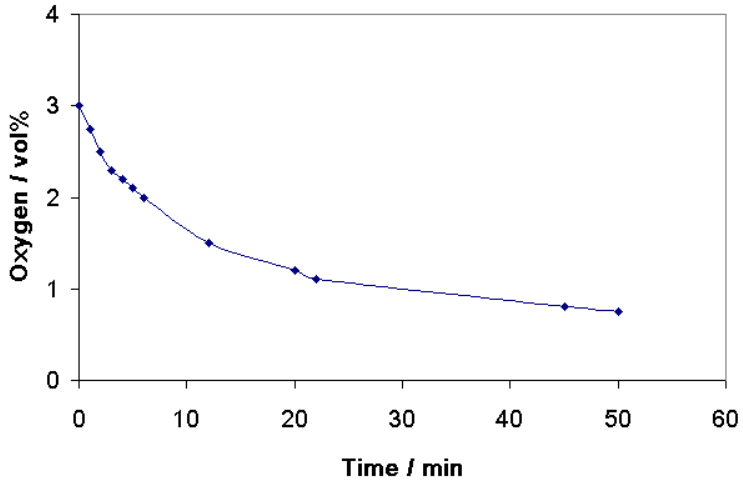

Figure 53 Measurement of oxygen content in the glovebox atmosphere by the O_2-meter during operation of the purification column.

Since it looked like the column had reached its capacity for picking up oxygen, the column was regenerated again. However, a temperature of 325 °C was used, since the sides of the column were not really warm at 250 °C. Figures 54 and 55 show the result of subsequently purifying the glovebox atmosphere. The result was that down to 3 ppm O_2 could be reached within 226 minutes. After several hours of operation the level was below 1 ppm O_2, which was the level hoped for.

During use of the glovebox, it was shown that the atmosphere would stay at < 1 ppm for about a week. It would then slowly go up to 1-10 ppm for a few days. It was noted that for normal use, that the column should be regenerated one or twice every month, depending on the purity level desired. If the system was used on a daily basis, the glovebox should preferably be left with some overpressure (buffered by the gloves) at the end of the day, as this helped keep contaminants from leaking into to box.

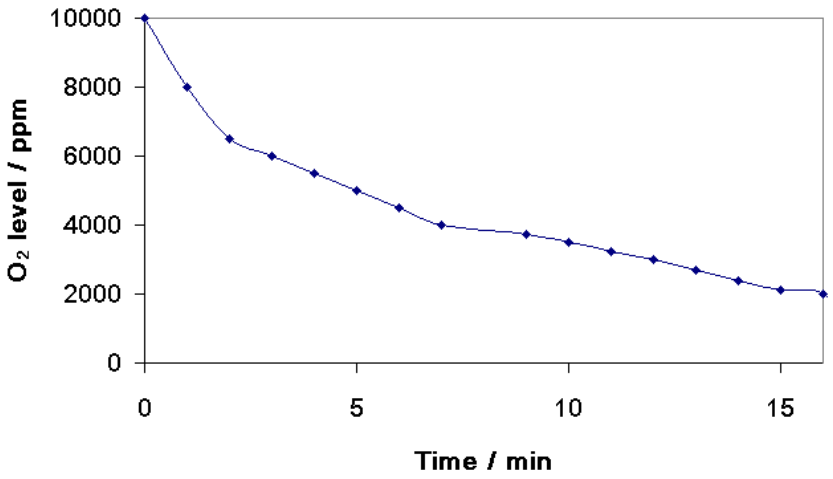

Figure 54 Second purification of the glovebox atmosphere. 10,000 ppm corresponds to 1%.

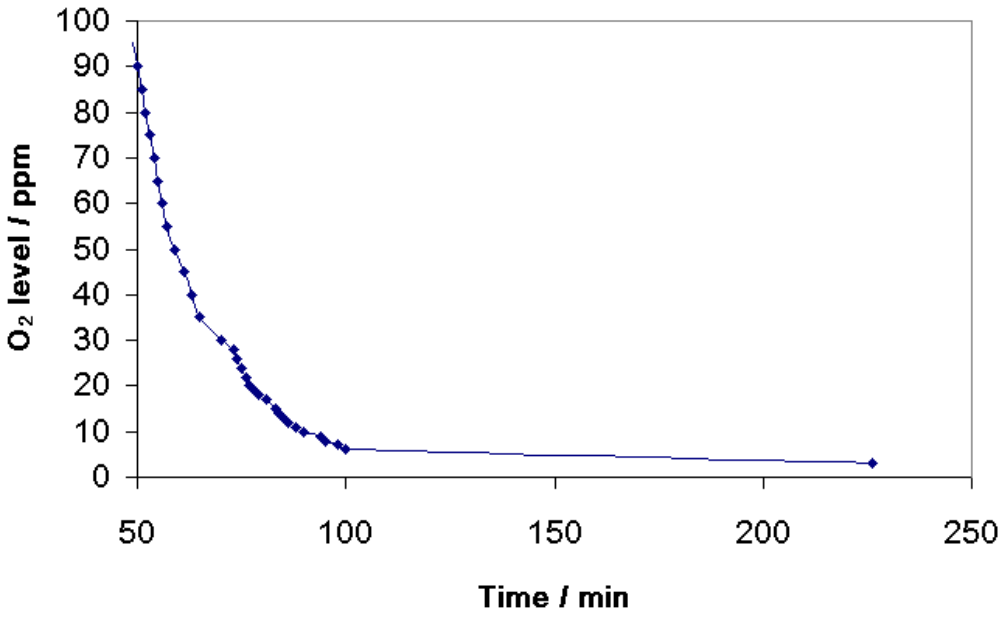

Figure 55 Second purification of the glovebox atmosphere continued from Figure 54, but using a smaller scale for the O_2 level.

3.5 Gas supply control system

The microbalance system was designed to primarily work with hydrogen. However, it would also be necessary to be able to flush the system with argon and of course to evacuate it.

When conducting an experiment, in which a pressure-composition isotherm is measured, it is essential that the pressure can be controlled stringently. The mass of the sample is measured for a series of pressure steps, and the inlet (in case of increasing pressure) or outlet (in case of decreasing pressure) must be controlled to such a degree that even small steps, e.g. a 0.02 bar change in the 0-1 bar range, are possible.

Figure 56 shows the flow diagram that was designed for the microbalance facility.

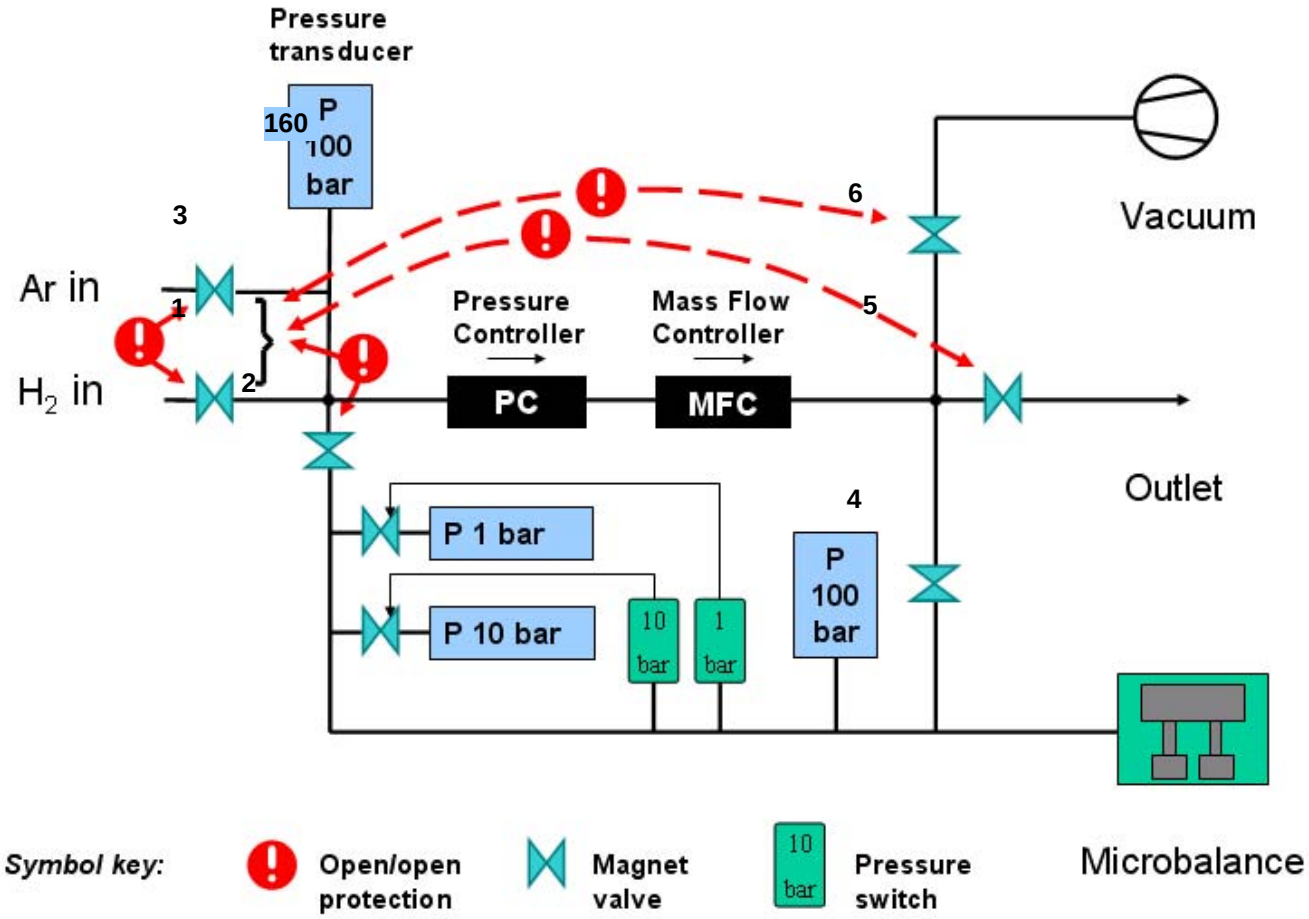

Figure 56 Flow diagram for gas supply control to the microbalance. Argon and hydrogen were supplied to microbalance through a pressure controller and mass flow controller. Transducers measured the pressure at points where the gases entered the system and in the open system including the microbalance in ranges of 0-1, 1-10 and 1-100 bar to achieve a good resolution. The pressure switches were connected to magnet valves in order to shut them off, if the pressure exceeded the maximum rated pressure of the transducers. The open/open protection designations were made for the pairs of magnet valves that should not be able to be open at the same time, in order to avoid accidents. The numbered magnet valves were operated by a computer system, see Section 4.

When gas is let into the microbalance, gas first enters from the inlet of either the argon or the hydrogen flask (using reduction valves). It then passes through the pressure controller and mass flow controller. The mass flow controller is rated to be used with a maximum of 5 bar difference between its inlet and outlet, so the pressure controller is used to set the pressure to 5 bars above the desired outlet pressure to the microbalance.

Figure 57 shows the actual setup of the gas supply control system.

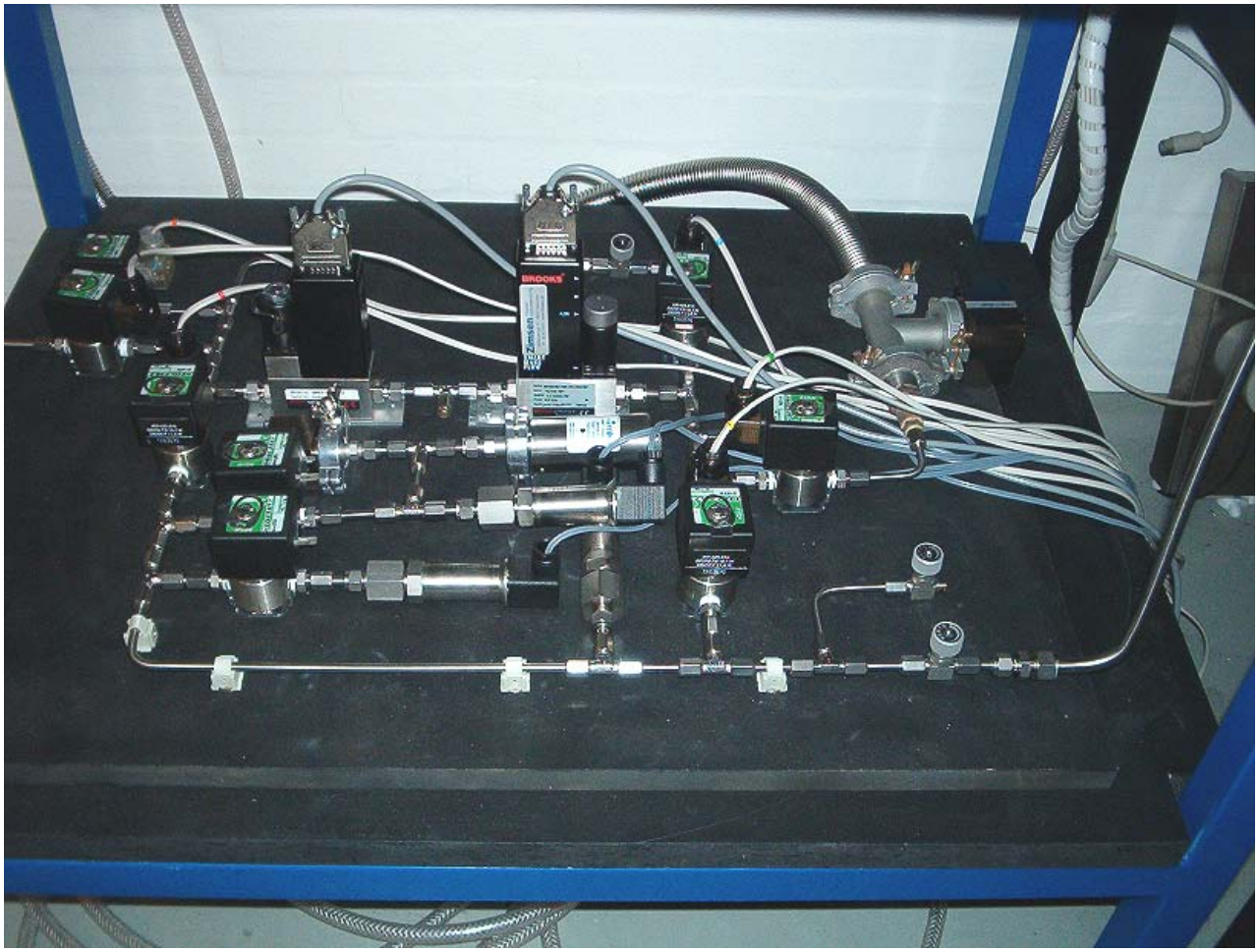

Figure 57 Setup of the gas supply control system. The system was located underneath the glovebox in which the microbalance resided (see Section 3.5). All units were connected to a control box (see Section 3.6.1). Overpressure valves are visible in the 0-1 bar department, just in front of the pressure controller, and at the vacuum outlet. At this stage of development the pressure switches were not included and an extra Pirani transducer was included in the 0-1 bar department to be able to measure vacuum levels.

3.5.1 List of equipment and materials

Name	Brand and model or type	Material/contents	Additional info
Hydrogen 6.0	Strandmøllen	$H_2 > 99.9999\%$ $O_2 \leq 0.1$ ppm $H_2O \leq 0.5$ ppm $CO_2 + CO \leq 0.05$ ppm $C_nH_m \leq 0.05$ ppm $N_2 \leq 0.5$ ppm	In flask of 200 bar (10 Nm^3), using reduction valve Lab Line SL225 N2 (high purity valve)
Argon 6.0	Strandmøllen	$Ar > 99.9999\%$ $O_2 \leq 0.1$ ppm $H_2O \leq 0.5$ ppm $CO_2 + CO \leq 0.05$ ppm $C_nH_m \leq 0.05$ ppm $N_2 \leq 0.3$ ppm	In flask of 200 bar (10 Nm^3)

Digital mass flow controller	Brooks 5850S/BC-1H-A-1-A-C-2-B-A-1-B-1	Stainless steel, Viton seal	Power supply input: +24 V DC Set point input: 0-5 V DC Output: 0-5 V DC and 0-20 mA Upstream pressure : 5-100 bar Downstream pres.: 0-95 bar Range : 0-2 NL/min
Upstream pressure controller	Brooks 5866/A1-A-1-B-7-B-E-2	Stainless steel, Viton seal	Power supply input: +24 V DC Set point input: 0-5 V DC Output: 0-5 V DC Upstream pressure: 100 bar Downstream pres.: 0-100 bar
Flow meter to Formier gas	Sho-rate 50 M	Stainless steel fittings	65 mm = 640 NL/h N_2
Pressure switch (0.5 – 5 bar)	Suco 0184457032	Stainless steel, EPDM membrane	Adjustment range: 0.5 – 5 bar Max. over pressure: 300 bar
Pressure switch (1 – 10 bar)	Suco 0184458032	Stainless steel, EPDM membrane	Adjustment range: 1 – 10 bar Max. over pressure: 300 bar
Pressure transmitter (0 – 1 bar)	Bourdon E913-33-B15A	Stainless steel, NBR (nitril) seal	Pressure range: 0-1 bar Output signal: 4-20 mA Max. over pressure: 4 bar Burst pressure: 7 bar
Pressure transmitter (0 – 10 bar)	Bourdon E913-33-B22A	Stainless steel, NBR (nitril) seal	Pressure range: 0-10 bar Output signal: 4-20 mA Max. over pressure: 21 bar Burst pressure: 31 bar

3.6 Data acquisition and communication interface

All electronical units (magnet valves, mass flow and pressure controller, and pressure tranducers) were operated by a LabVIEW program. A communication interface using data acquisition modules were made, see Figure 58. During testing it was found, that the relays in the relay module (ICP-DAS i-7066) were not rated high enough to handle the initial current used in the magnet valves, whenever they were manipulated. Therefore, high-current relay interfaces were used between the relay module and the magnet valves, see Figure 59.

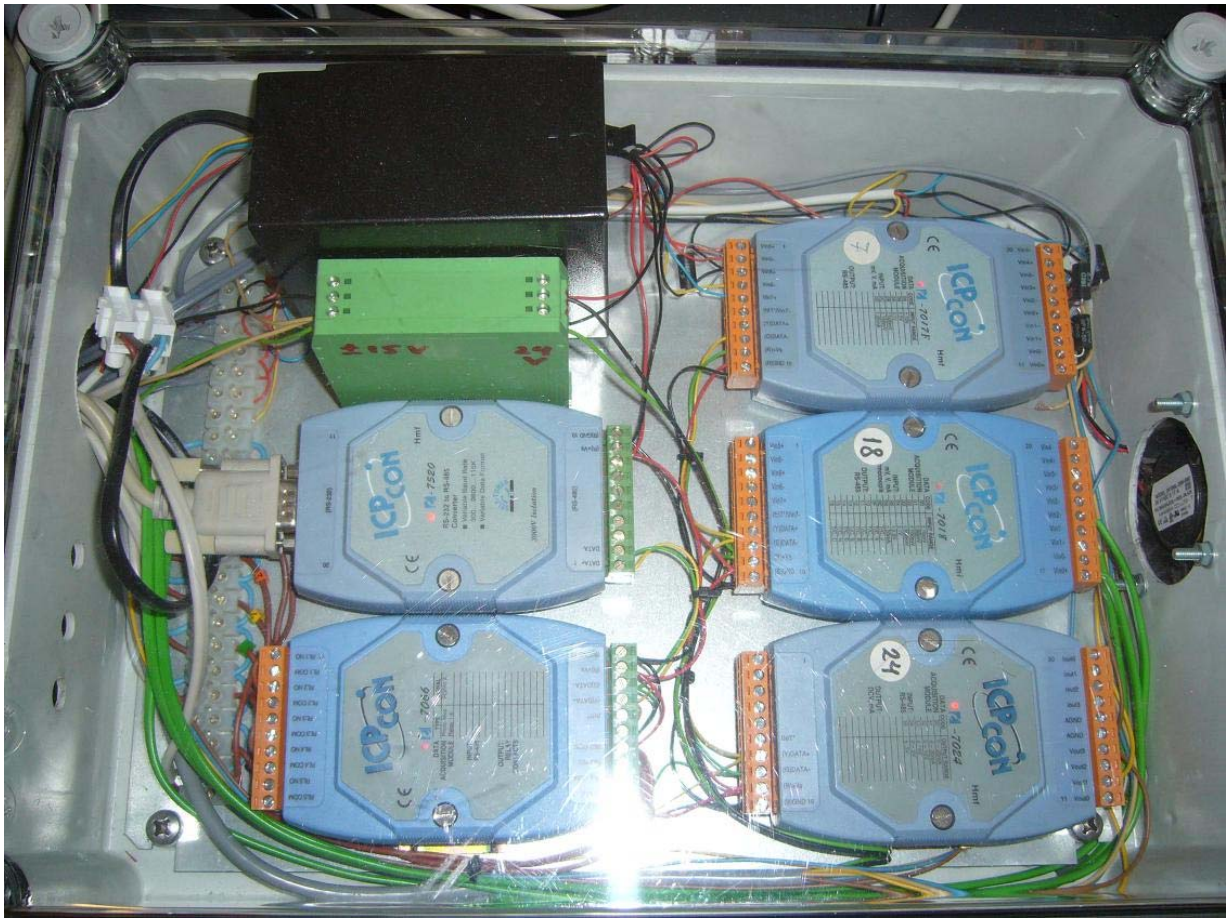

Figure 58 Box with data acquisition modules. From the top left, going anti-clockwise: The black unit is a 24 V power source, the green box a DC-DC converter from 24 V to ±15 V (for the microbalance controller, refer to Table 8), RS-232 to 485 converter (protocols of modules vs. computer), relay module (i-7066), analogue output module (i-7024, sets voltages for controlling the mass flow and pressure controller), thermocouple input module (i-7018), and analogue input module (i-7017, reads voltages microbalance, pressure transducers, mass flow and pressure controller). The box was cooled by a fan seen in the right wall.

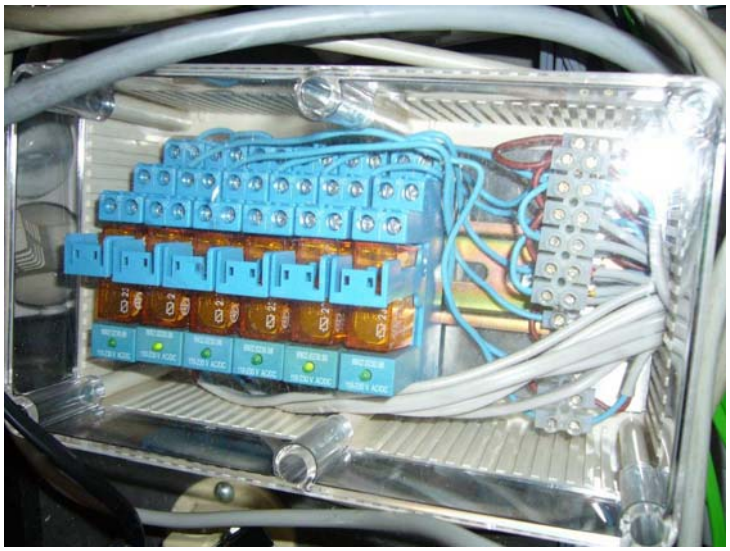

Figure 59

Relay box with 6 relay interfaces to serve as bridge between the relay module (i-7024) and the magnet valves.

3.6.3 List of equipment and materials

Name	Brand and model	Material/contents	Additional info
DC/DC converter	Traco TEP 2423		Power supply input: 24 V DC Output: ±15 V DC
Relay interface	Finder 48.51.8.230.0060	Contact material : AgNi	Max 10 A (up to 20 A peak), 230 V AC, 0.7-1.2 W (without load - full load)
Analog input module	ICP-DAS i-7017F		Channels: 4 (16 bit resolution) Input range: ±150 mV, ±500 mV, ±1 V, ±5 V, ±10 V, ±20 mA Power consumption: 1.4 W
Thermocouple input module	ICP-DAS i-7018		Channels: 8 Power consumption: 1.2 W
Analog output module	ICP-DAS i-7024		Channels: 4 (14 bit resolution) Output range: 0~20 mA, 4~20 mA, 0~5 V, 0~10 V, ±10 V Power supply: +10~30 V DC Power consumption: 2.4 W
Photo MOS Relay Out Module	ICP-DAS i-7066		Channels: 7 Current: 0.4 A Power consumption: 0.8 W
RS-232 to RS-485 converter	ICP-DAS i-7520		Input: RS-232 protocol Output: RS-485 protocol Power consumption: 2.2 W

4 COMPUTER OPERATING SYSTEM FOR THE FACILITY

The high pressure microbalance described with all supporting auxiliary equipment, described in Section 3, was made to be controlled by a computer.

An application was developed for operating the units in LabVIEW. LabVIEW is known to use virtual instruments which have graphical user interfaces connected to underlying block diagrams that give the relationships and virtual wiring between various elements such as number variables (shown by text fields, sliders etc.), buttons, charts etc. For the purpose of this thesis, the LabVIEW application can be seen as a methodology developed in order to obtain PCI's for hydrogen storage materials

The main function of the application was:

1) Initialize data modules (i/o)
2) Provide graphical user interface to manipulate magnet valves and mass flow controller
3) Run an automatic PCI acquiring cycle based on values for pressures entered in
4) Record data to file

The following sections will give an overview of the user panels and describe the underlying methodology.

4.1 Main operation panels overview

Figure 60 shows the main operating panels. This screen contains several smaller panels which give information about and provides options to control the microbalance system. In the top left corner, the information about the sample being measured on is entered, and subsequently included in a file together with data on the measurements. The top middle panel provides key information about the sample measurement, such as current total wt% uptake, pressure in the system, and so forth. The unit just beneath is a control for how often data is saved to the file (right now it saves every 5 seconds). The large panel to the right contains here a chart on which already measured (wt%, pressure)-points are shown making up a PCI. The large panel in the lower left is a status snapshot of the gas supply control system and the microbalance. Here, a diagram of the tubing is shown together with buttons for manipulating magnet valves. Values for pressure are updated as obtained by pressure transducers. Also, info from the pressure controller and mass flow controller is seen. The flow in the mass flow controller can be set directly from the control "set flow". In the square showing the microbalance (green), info about mass measured and temperatures in different compartments are seen.

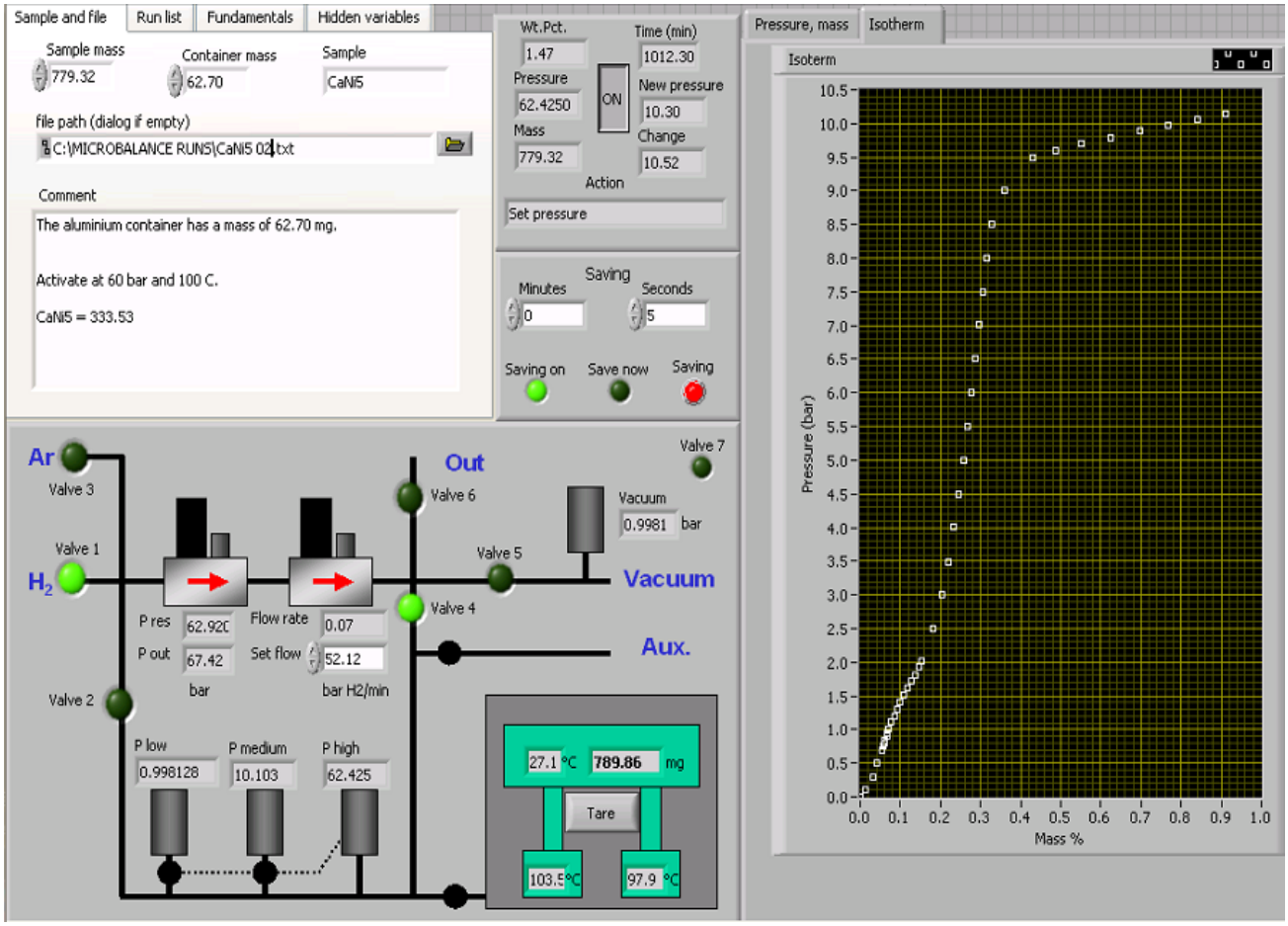

Figure 60 Main user panel of application for operating the microbalance and gas supply control system. The system pressure is chosen from the pressure values, 'P low', 'P medium' and 'P high', according to the range the value 'P high' lies in. 'P res' is the pressure measured in the "reservoir", which is the term used for the volume up against the inlet of the pressure controller, 'P out' being the desired pressure set to be 5 bar above the value on the right side of the mass flow controller (since this is a requirement for the operation of the mass flow controller).

Figure 61 shows a few different panels in the main screen, which have been selected by choosing different "flags" shown in the top of some panels.

In the "Run list" the list of pressure values desired to measure on are entered in together with the time for each step. To the right (under the flag "Pressure, mass") charts are visible for updated mass of the sample as measured by the microbalance and the system pressure.

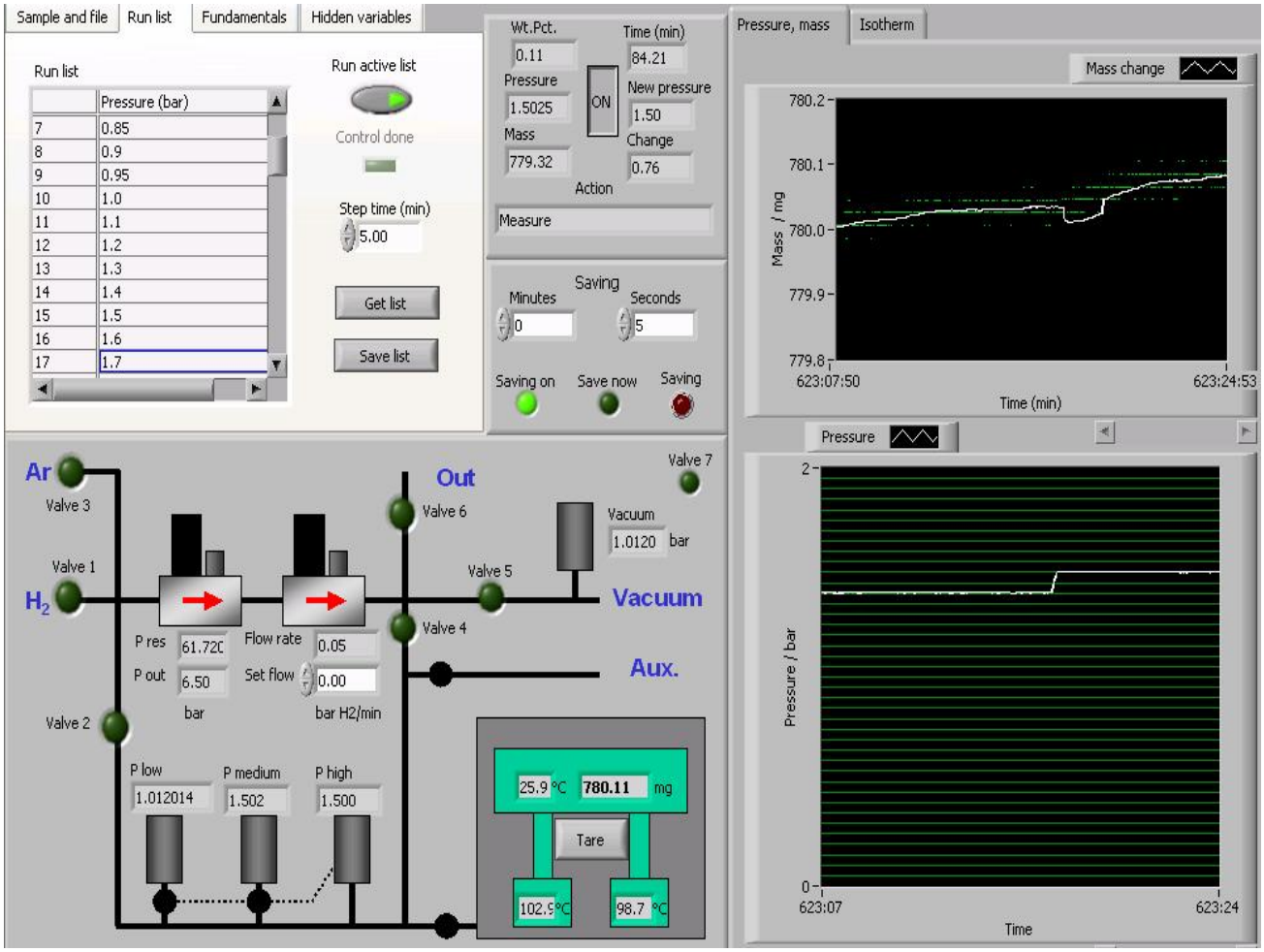

Figure 61 Main user panel of application for operating the microbalance and gas supply control system with other flags chosen. The chart for the mass shows both actual readings (in green) and a smoothed value, which is an averaged value based on the preceding 100 values.

4.2 Methodology of automatic PCI acquiring

A newer version of the 'Run list' panel is shown in Figure 62. From this place it was possible to obtain PCI's automatically based on the values entered in.

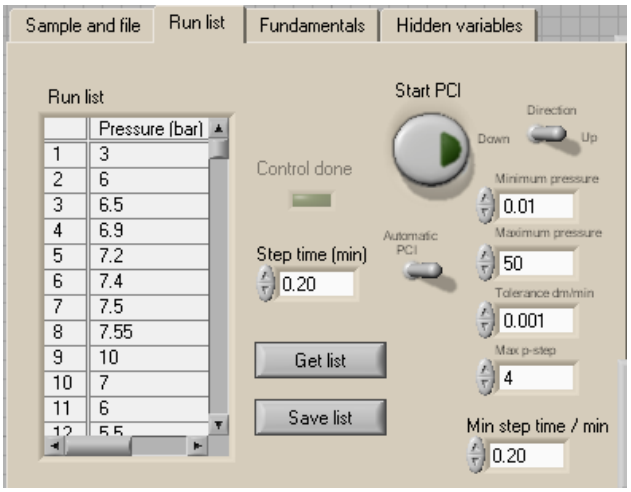

Figure 62 Control panel for automatic PCI acquiring. The series of pressure values for which the PCI is based on is written in either the 'Run list' or defined through the variables on the right for the application to automatically select steps.

A run-through of the principles in how the system obtains a PCI is found in Table 14.

Table 14 Methodology for the algorithm that records a PCI.

Step	Name of step	Action
1	Decide which pressure value to set for next measurement	If the selector 'Automatic PCI' (see Fig. 62) is not set, the next value in the 'Run list' is selected. Otherwise the next step is based on an algorithm, and the 'Run list' is not used at all (step 2)
2	Automatic PCI pressure	Algorithm which uses 'Minimum pressure', 'Maximum pressure', 'Max p-step', and 'Min step time/min' to intelligently calculate the next step based on if a plateau point seems to have been reached (detected from a relatively large wt% increase during preceding step).
3	Control reservoir	At the beginning of a PCI cycle, it makes sure that the difference between the pressure in the reservoir and the pressure in the microbalance is small (less than 0.1 bar) to avoid large disturbances when valve 2 (see Fig. 61) is opened during lowering of pressure in the microbalance.
4	Set pressure	Opens for inlet of hydrogen to the microbalance or the outlet to vacuum based on whether the pressure is supposed to be increased or decreased in the microbalance. The flow set for the mass flow controller is based on an algorithm, which makes the flow slow down in proportion to how close the microbalance pressure is to the target pressure. Flow limits are enforced for max. and min. flows.

5	Check reservoir for mass flow controller fail	Sometimes the mass flow controller will leak tiny amounts even though the flow is set to zero. This happens even for top grade equipment and has to do with wear on an O-ring in the controller. This becomes a problem during a PCI cycle in which the pressure is stepwise increased, because the pressure in the volume between the mass flow controller and valve 4 (refer to Fig. 61) may be suddenly higher than the next target pressure. The volume in this case is emptied together with the reservoir and new gas is slowly introduced to reach the target pressure.
6	Measure	All valves are closed and the system is left "quiet" to measure on the mass of the sample. The system keeps measuring either for a set 'Step time' (see Fig. 61) or based on whether the change in mass during the step was sufficiently small compared to the time at the end of the preceding step (tolerance was set in "Tolerance dm/min" seen in Fig. 62).
7	Write PCI	At the end of measuring for a point, data is stored as (wt% and pressure) in a list which makes out the PCI for the sample. The data is updated on the PCI chart (Fig. 60). The algorithm starts over from step 1 if the last point has not been reached (last value on the 'Run list' or, alternatively, if 'Automatic PCI' is used, the next calculated pressure value in step 2 exceeds the 'Maximum pressure' that has been set.

The main text of the thesis will not be devoted to details in the application. However, Appendix 11.2 documents the diagrams, which are mostly self-explanatory for LabVIEW users, true to the nature of LabVIEW virtual instruments.

5 TEST OF THE HIGH PRESSURE MICROBALANCE ON $CaNi_5$

In Section 2.3.5, the alloy $CaNi_5$ was described as being easy to activate and having reasonable kinetics at room temperature. In this section, testing was performed on this well characterized metal hydride. The alloy was activated with hydrogen and PCI's were measured on it.

5.1 Test for leaks in the system

A large issue for the newly built equipment was that the system was tight enough, so a vacuum would be sustained. There will always be diffusion through walls and leaks to some very small degree. But the goal was to make this influx of molecules small enough that it was of no consequence.

The whole system was systematically made tight using O-rings with fittings in connections. Figure 63 shows the change in pressure in the system after evacuating for a couple of hours and closing for the vacuum pump, allowing time for adsorbed species on inner walls to also leave the system.

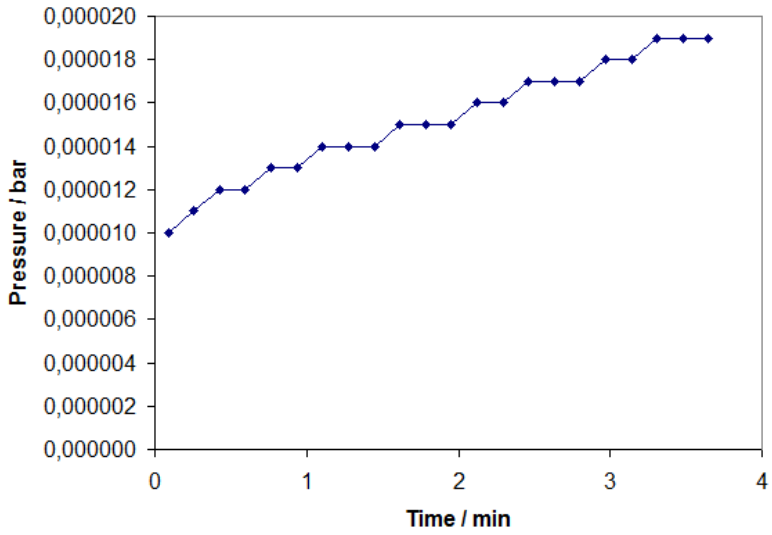

Figure 63 Test for leaks in microbalance system after evacuating for many hours and shutting for access to the vacuum pump.

This magnitude of pressure increase (about 0.3 Pa/min.) is considered very good, and is acceptable, comparable to commercial systems (e.g. evacuated glovebox antechamber from Vacuum Atmospheres Company). This result serves as a validation of the system, that its construction was vacuum tight, and that any increases in mass by the microbalance (on a scale of milligrams at least) would stem from hydrogen, and not from species in the air.

5.2 Activation of commercial $CaNi_5$ sample

From the literature it is known, that $CaNi_5$ can be activated somewhat easily even at room temperature (see Section 2.3.5).

$CaNi_5$ was acquired from Aldrich Corp. (produced by Ergenics and denoted HY-STOR 201). The material, which was a silvery gray powder with particles of about 1-3 mm in diameter, was introduced into a sample package of aluminum foil in a glovebox with inert atmosphere (Ar, $O_2 < 1$ ppm). The package was transferred to the microbalance in the specially prepared glovebox and the system was evacuated for about 15 minutes. The system was then pressurized with hydrogen up to 70 bar, then evacuated, in a series of 3 cycles. Figure 65 shows the result of this activation process.

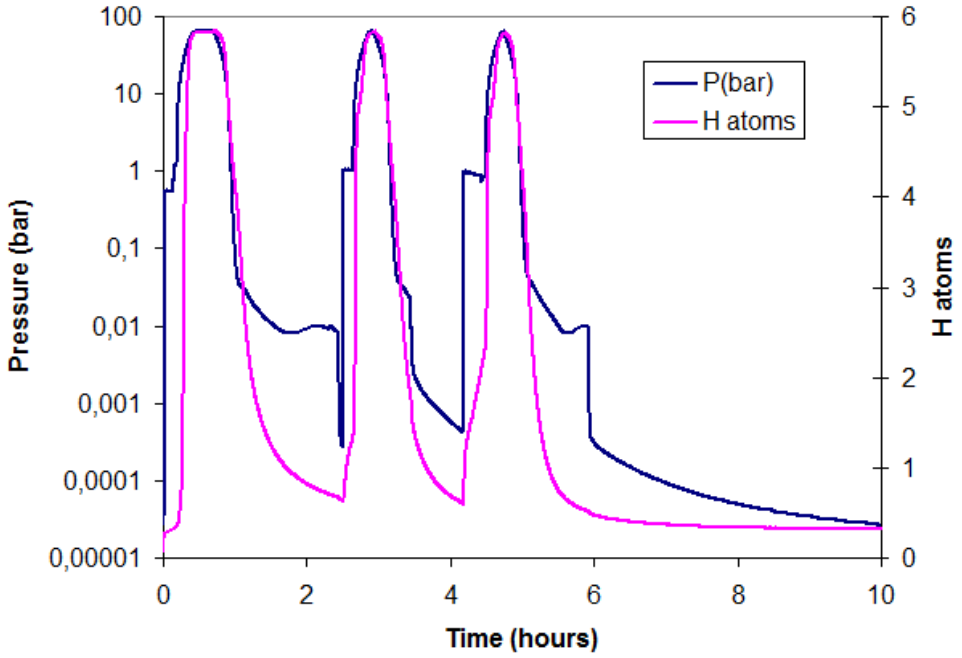

Figure 65 Activation of commercial $CaNi_5$ sample at room temperature by cycling hydrogen up to 70 bar in and out of the system and the sample.

It is seen that up to 5.8 atoms per formula unit ($CaNi_5$) were absorbed. This was somewhat less to what was achieved in a pure $CaNi_5$ for Sandrock et al. (about 6.1 wt%). It is assumed that this stemmed from impurities in the sample (Ni for example).

Figure 66 shows the relation between the absorption of hydrogen in the sample and the temperature as measured by the thermocouple located close to the sample package. It is observed that the response in temperature change was quick when hydrogen was absorbed. This exothermic reaction heated up the hydrogen atmosphere fast. Notably, the temperature quickly dropped again after the initial absorption, which indicates, that the heat was quickly dissipated in the system. This is important for argument that the system will reasonably quickly go to thermal equilibrium in the volume close to the sample, leading to a slightly more accurate measurement of the temperature as reactions occur in the sample.

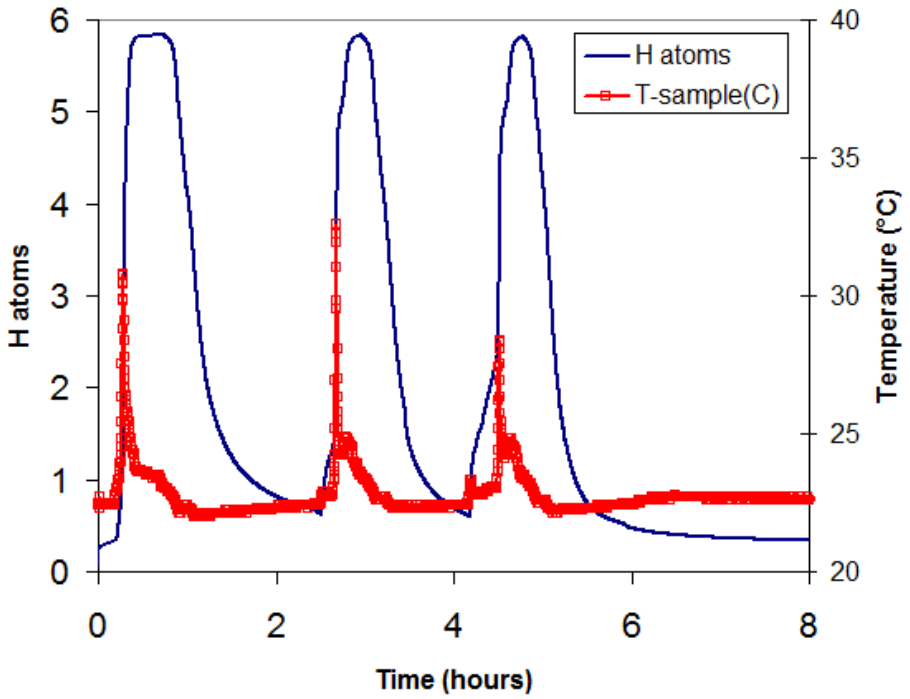

Figure 66 Activation of commercial $CaNi_5$ sample at room temperature. The temperature is measured by a thermocouple located close (within 1 cm) to the sample.

5.3 Acquiring of PCI's for $CaNi_5$

Following activation of the $CaNi_5$ sample, PCI's were recorded at different temperatures, 25 °C, 50 °C and 80 °C.

5.3.1 PCI for $CaNi_5$ at room temperature

The system was programmed to record measurements for a series of pressures based on the observed plateaus in the literature. I.e. points were concentrated between 0 and 1 bar and 20 and 50 bar. The experiment was set up to have a measuring time of 1 hour per point.

Figure 67 shows the result, which shows a PCI for $CaNi_5$ at about 25 °C (not heated externally). It is seen that the sample failed to reflect the plateau at around 0.5 bar, both at absorption and desorption, showing large hysteresis. At the end of the series (desorption at 0.1 bar) the system was left for a longer time after the measurement of 1 hour, and it was seen that the mass was still dropping, although slowly. This means that the system was not in equilibrium yet, and suggests that both hydrogenations and dehydrogenations at these low pressures and/or this low temperature are very slow, a key piece of information that you do not find in the literature.

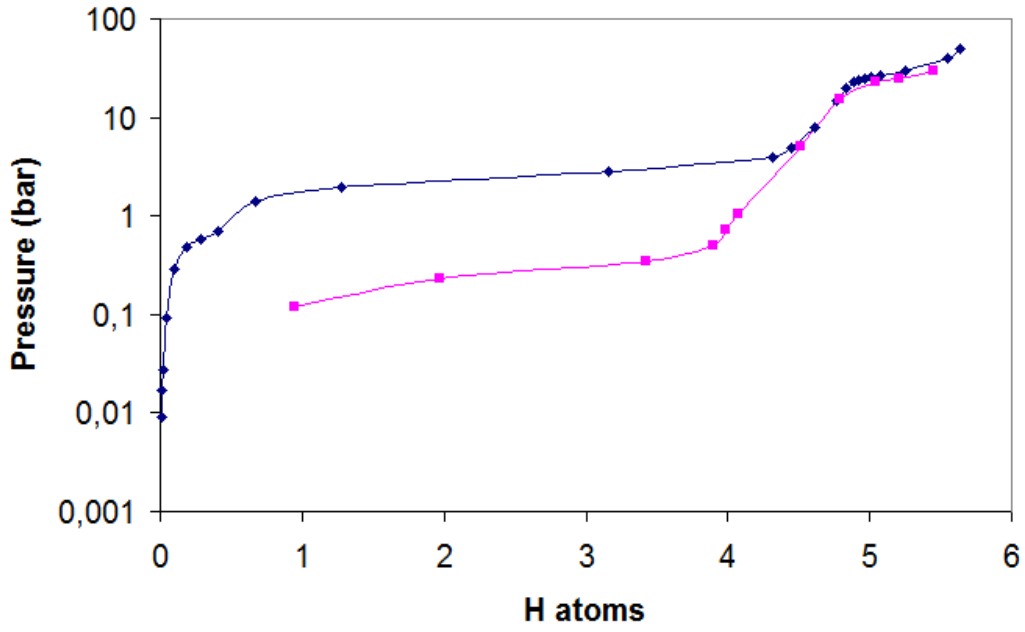

Figure 67 PCI at 25 °C for commercial $CaNi_5$ sample activated at room temperature. Each point is the measurement after measuring for 1 hour following changing the pressure between points.

An analysis was made on the degree of hydrogenation and dehydrogenation as a function of time and pressure from the data obtained during the experiment. Figure 68 shows the result for the hydrogenation and Figure 69 the results for the dehydrogenation.

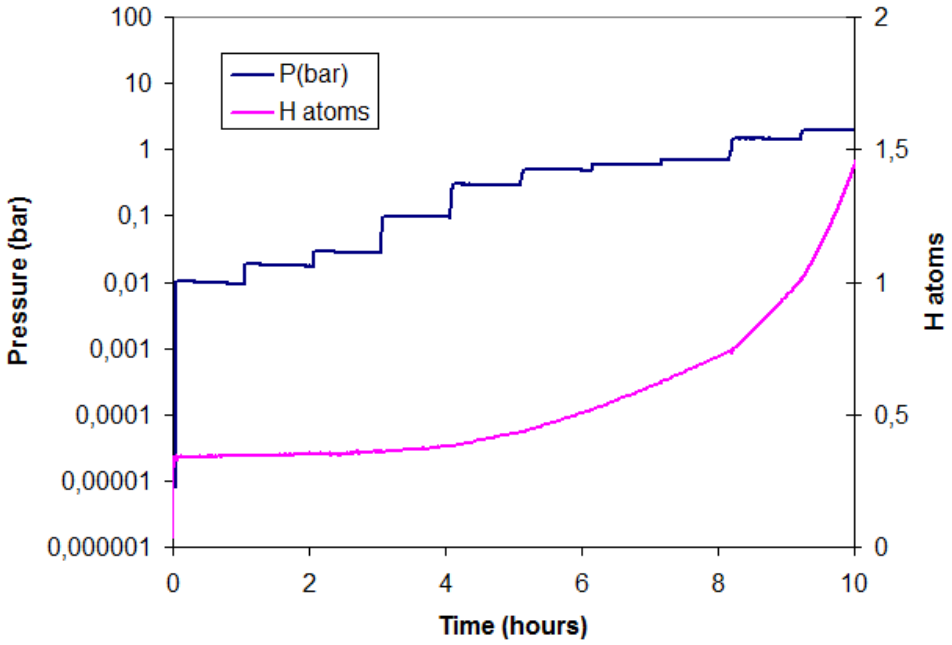

Figure 68 Hydrogen absorption in $CaNi_5$ at room temperature as a function of time and pressure (hydrogen).

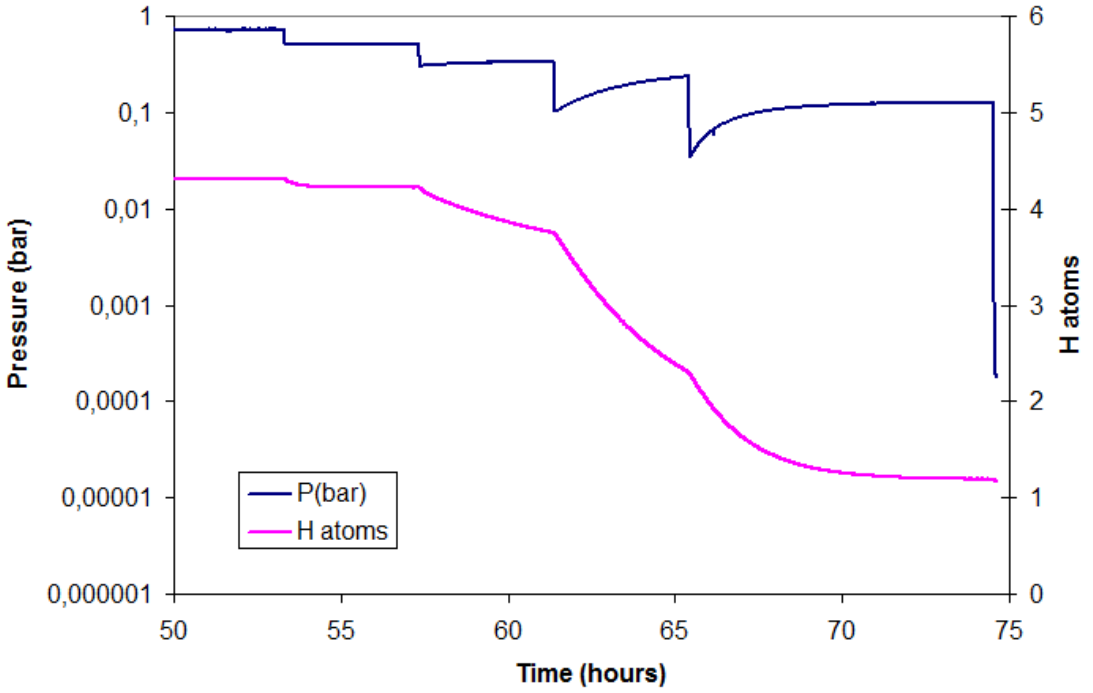

Figure 69 Hydrogen desorption in $CaNi_5$ at room temperature as a function of time and pressure (hydrogen).

From these measurements it is clear, that the sample did not reach equilibrium during critical steps where the plateaus are reached. From Figure 69 it is seen, that an excess of 10 hours for one step is required for that particular point. This slow desorption rate is also the reason for the lack of a full dehydrogenation of the sample within the time allotted to the measurement.

5.3.2 PCI for $CaNi_5$ at 50 °C

Commercial $CaNi_5$ was activated and a PCI was recorded at 50 °C as shown in Figure 70. Here two plateaus show themselves nicely and the hysteresis at the main plateau is rather low.

Figures 71 and 72 show analyses of the experiment on the hydrogenation and dehydrogenations rates, respectively. At this temperature, the rates were faster, although some steps did not reach equilibrium within 1 hour of measurement per point.

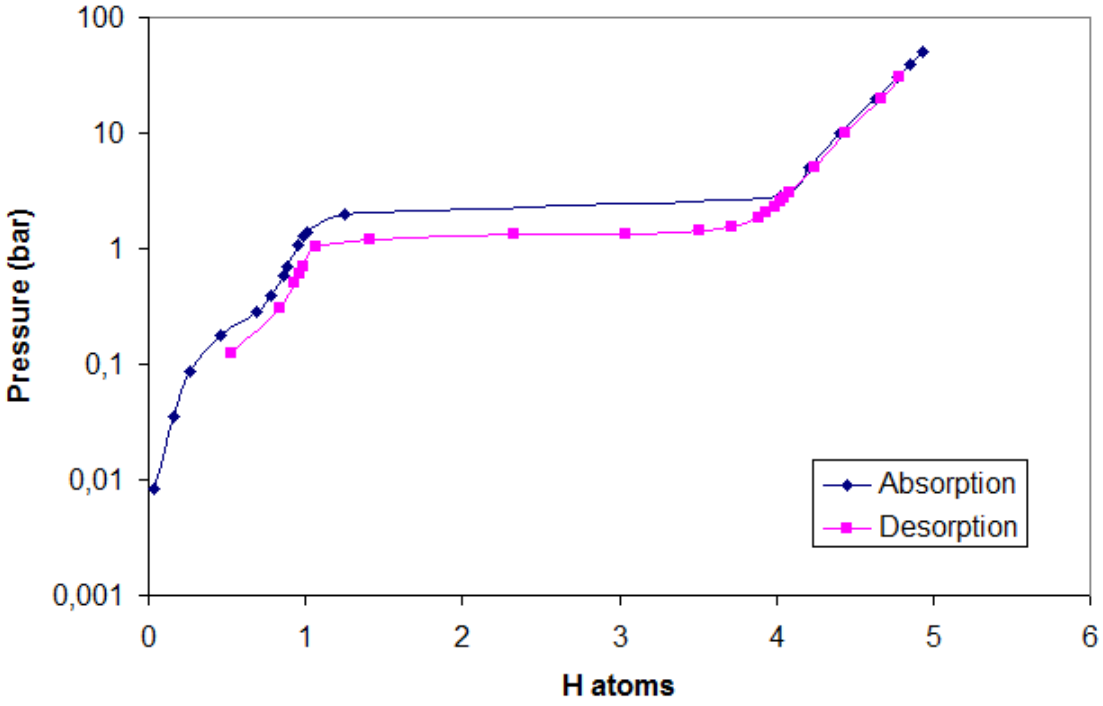

Figure 70 PCI at 50 °C for commercial $CaNi_5$ sample activated at 25 °C

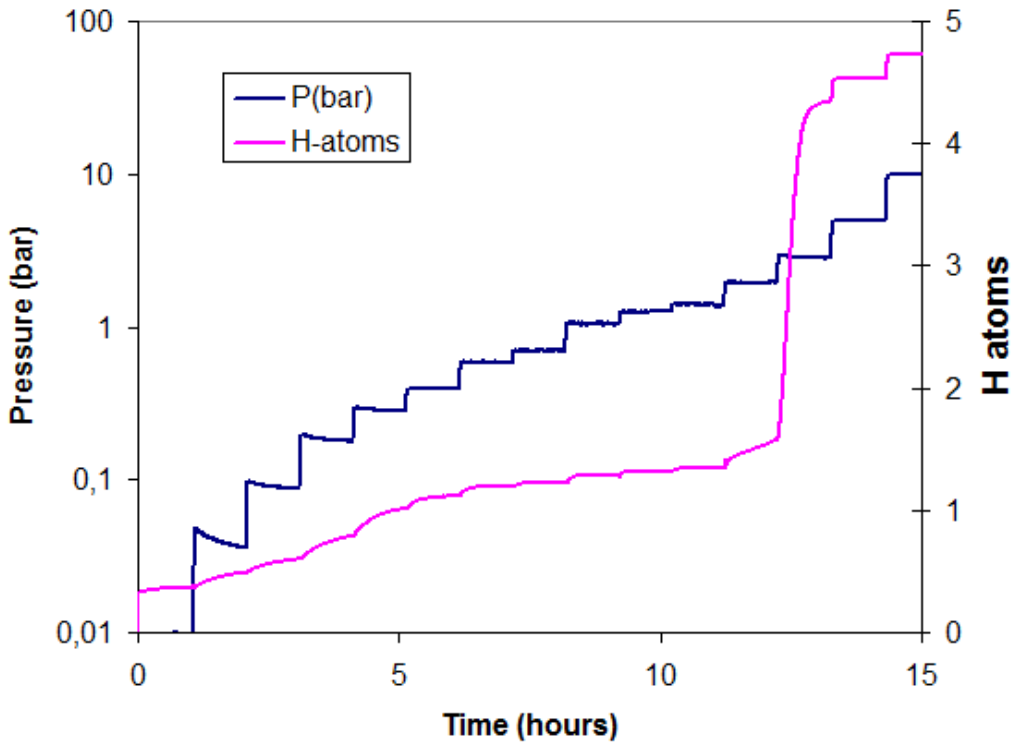

Figure 71 Hydrogen absorption in $CaNi_5$ at 50 °C as a function of time and pressure (hydrogen).

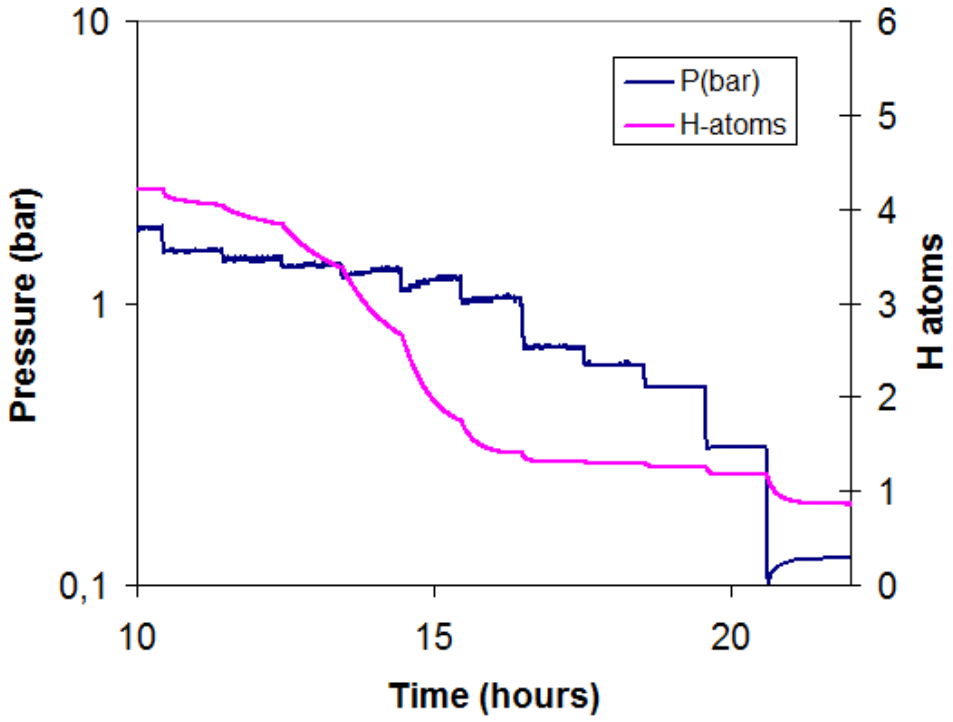

Figure 72 Hydrogen desorption in $CaNi_5$ at 80 °C as a function of time and pressure (hydrogen).

5.3.3 PCI for $CaNi_5$ at 80 °C

A PCI was also obtained in the same way as earlier but at 80 °C using the same sample that had been used for the isotherm at 50 °C. Figure 73 shows the P-C isotherm, and here it is seen that there are some hysteresis still. During absorption, the main plateau is missed by the points programmed (concentrated around the plateau value in the literature). Also, during desorption, the sample is not fully reversible. An analysis of the reaction rates (Fig. 75 in Section 5.3.5) show that the system has reached equilibrium. A reason for the irreversibility of the system may be decomposition. It has been suggested in the literature that $CaNi_5$ disproportionates into CaH_2 and Ni according to the reaction

$$CaNi_5 + H_2 \rightarrow CaH_2 + 5Ni \qquad (42)$$

with possible intermediates stages of $Ca_2Ni_7H_x$.[42]

J.O. Jensen et al. have shown that the disproportionation rate increases with temperature.[42] It is very likely that decomposition was the cause for this irreversibility, especially when using measuring times as long as 1 hour for every step.

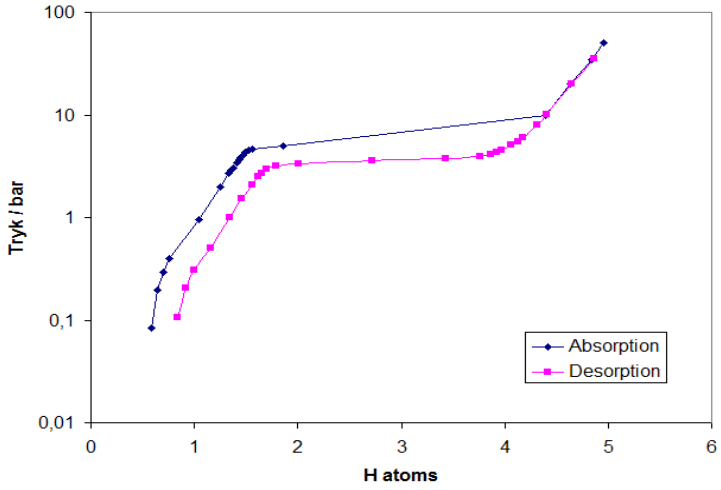

Figure 73 PCI at 80 °C for commercial $CaNi_5$ sample activated at 25 °C

5.4 Van't Hoff Plot for $CaNi_5$

With desorption plateau pressures from isotherms from several temperatures, a Van't Hoff plot (see Section 2.3.3) is obtained in order to find the enthalpy of hydridring for the reaction between $CaNi_5$ and H_2. Figure 74 contains the plot. From the slope of the line between the 3 points, an enthalpy of -31.4 kJ/mol H_2 is calculated. The entropy is calculated from the intercept to be 0.100 kJ/(mol·K) Sandrock et al. recorded -31.8 and -33.5 kJ/mol H_2 for the enthalpy and 0.101 kJ/(mol·K) for the entropy.[18,171] The experimental values obtained with this commercial $CaNi_5$ in the new high pressure microbalance facility are close enough to validate the use of the equipment to obtain accurate PCI's for metal hydrides.

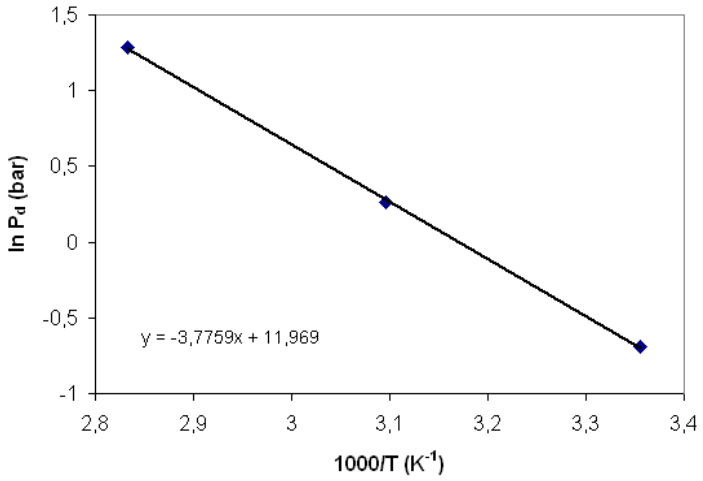

Figure 74 Van't Hoff plot for desorption plateau pressures of commercial $CaNi_5$ sample obtained from PCI's at 25, 50 and 80 °C.

5.5 Analysis of rest times for steps in a pressure series

Since an issue with the recording of the $CaNi_5$ PCI's was that it was unforeseen how long the measuring times were for each point. Also, for a set constant measure time per step that is long enough to include equilibrium for the slowest points, much waste of time will result from the points that are quick to achieve equilibrium.

From this reasoning, an analysis was made on how much the mass changes per time for a given experiment. This was implemented in the LabVIEW program (see Section 4.7.6) and resulting in Figure 75 for $CaNi_5$ at 80 °C.

In these measurements, it is observed at what value of change (in about a minute), equilibrium is satisfactorily reached. A threshold value is chosen by the operator (0.0001 µg was chosen) on basis on the judgment of the user from curves like these.

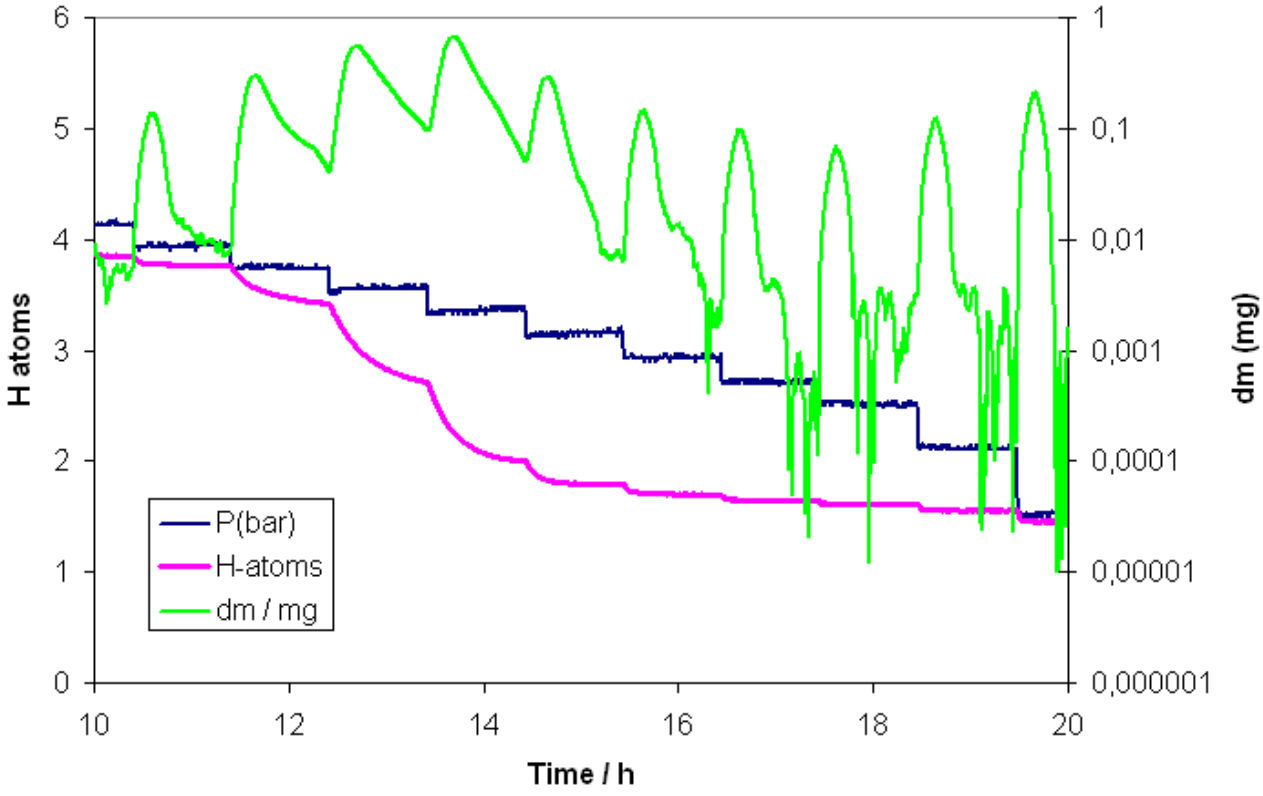

Figure 75 Analysis of rest times for desorption of commercial $CaNi_5$ sample at 80 °C. The curve named "dm" is the difference in mass over about 1 minute taken from averages of mass values at these two points (each averaged over values from the past ~1 minute).

6 NEW SYSTEMS FOR HYDROGEN STORAGE I: Li-Al-N-H

It was reviewed in Section 2 that combinations of complex hydrides can yield destabilized systems, in which hydrogen can be released under more moderate conditions in terms of temperature.

In 2005 Lu and Fang[109] published results for a Li-Al-N-H system using $LiNH_2$ and $LiAlH_4$ together in molar ratio 2:1. While $LiAlH_4$ alone desorbs 6.4 wt% in two steps below 200 °C and the system $LiNH_2$+2LiH desorbs 6.0 wt% below 220 °C, this new system, $2LiNH_2$+$LiAlH_4$, could desorb 8.1 wt% in 3 steps below 300 °C. In the paper, however, information about the composition of the gaseous products which can be attributed to both hydrogen and ammonia was absent, and it was assumed that the product was pure hydrogen.

Around the same time, in 2006, Nakamori et al.[113] showed by mass spectrometry that the gaseous product from the reactants consists only of hydrogen, however they were not able to confirm more than a 4.1 mass% hydrogen release below 577 °C, using 5 K/min in a TPD experiment. This should be compared to the 2 K/min used in Lu and Fang's experiment. In both instances, 1 bar argon was used as atmosphere.

Ping Chen's group at National University of Singapore subsequently published a couple of papers, on the Li-Al-N-H system[108,117-118] in which they prove that the system of lithium amide and lithium alanate actually turns into lithium aluminum nitride, Li_3AlN_2 with desorption of hydrogen according to

$$2LiNH_2 + LiAlH_4 \rightarrow Li_3AlN_2 + 4H_2 \quad (42)$$

However, they found that when reversed, the following reaction occured:

$$Li_3AlN_2 + 2H_2 \rightarrow LiNH_2 + 2LiH + AlN \quad (43)$$

This reaction was found to be reversible and thus able to store 5.2 wt%. However, the temperature range was rather broad: 50-500 °C.

In this chapter, it will be described how lithium aluminum nitride was synthesized by the process of ball milling lithium nitride and aluminum under nitrogen pressure,

$$Li_3N + Al + \tfrac{1}{2}N_2 \rightarrow Li_3AlN_2 \quad (44)$$

which is a process that has not been described in the literature so far.

The material was characterized by experiments in the high pressure microbalance to determine its potential for hydrogen storage below 300 °C.

6.1 Synthesis of Li_3AlN_2

Li_3N and Al were ball-milled under 12 bar nitrogen at 600 rpm using a Fritsch P7 planetary ball-mill and 5 steel balls in a steel milling jar with a home-made lid for adding pressurized gas (up to ~15 bar). The lid had a channel in the center in the bottom which led up and to one side of it, ending out in an opening with fitting that could be connected to an external tube. A threaded valve with O-rings was placed in it to be able to seal off the channel by twisting the valve with a screwdriver. To the end of being able to ball-mill under gas pressure, a filling station was set up with a pressure gauge and calibrated in such a way that the pressure in the jar could be measured before and after milling. This was done by first filling the station with connected jar (valve open) with nitrogen. The pressure in the system was read on the gauge and recorded. The valve in the lid was then closed off after which the filling station was evacuated by a vacuum pump. A valve to the pump was turned to block access to the pump and the valve in the lid was opened. The pressure read on the gauge could now be tied directly to the pressure in the jar before releasing the enclosed gas into the rest of the system. By doing this procedure for a series of pressure values, tabulation was made for the relationship, which was linear as expected.

Li_3N and Al were thus milled for 4 hours. The product was a fine grey powder, and it was analyzed by XRD. Figure 76 shows the result.

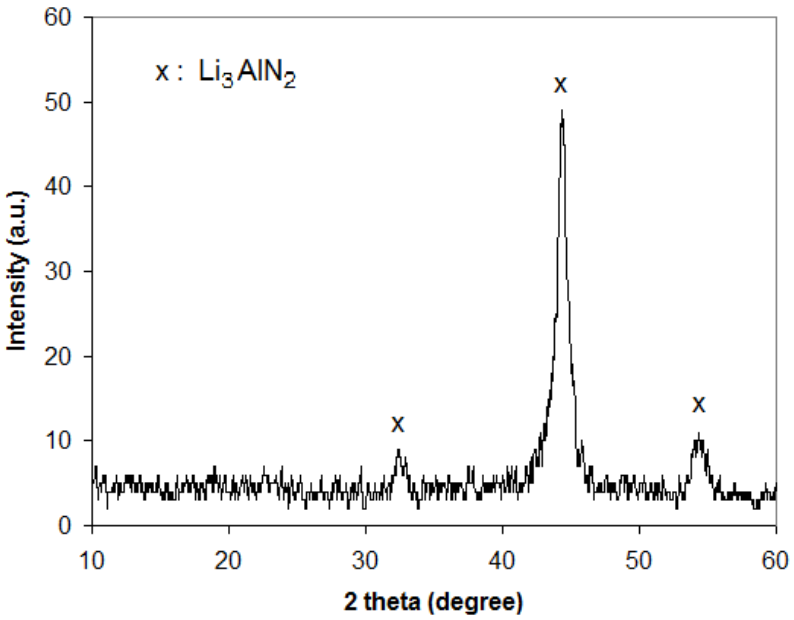

Figure 76 XRD of ball-milled sample of Li_3N and Al under nitrogen pressure according to the stoichiometry in (1)

It is seen that the product detected was single phase Li_3AlN_2. Hence, it is shown that lithium aluminium nitride can be synthesized according to (44). Interestingly, this process is able to break the triple bond in molecular nitrogen.

Further samples were also made to check the amount of nitrogen spent during ball milling. It was shown in each instance, by measuring the pressure before and after milling, that approximately the stoichiometric amount (using an estimate for the volume of the milling jar with balls and powder) according to reaction (44) was used in the reaction. Also, single phase Li_3AlN_2 was observed by XRD in each instance.

6.2 Interaction between Li_3AlN_2 and hydrogen

The reaction of the first sample above with hydrogen was investigated in the high pressure microbalance. The following sections review the results.

6.2.1 Absorption and desorption of hydrogen in Li_3AlN_2

The Li_3AlN_2 sample was transferred to the microbalance and hydrogen was introduced to 1.45 bar at a steady temperature of 150 °C. Under these conditions the mass increased slowly over the first 100 minutes by a total 0.26 wt% of the sample mass, shown in Figure 77. At this point a PCI program was started measuring for 15 minutes after each step of pressure change (generally 0.5 bar during absorption). Figure 78 shows the resulting PCI.

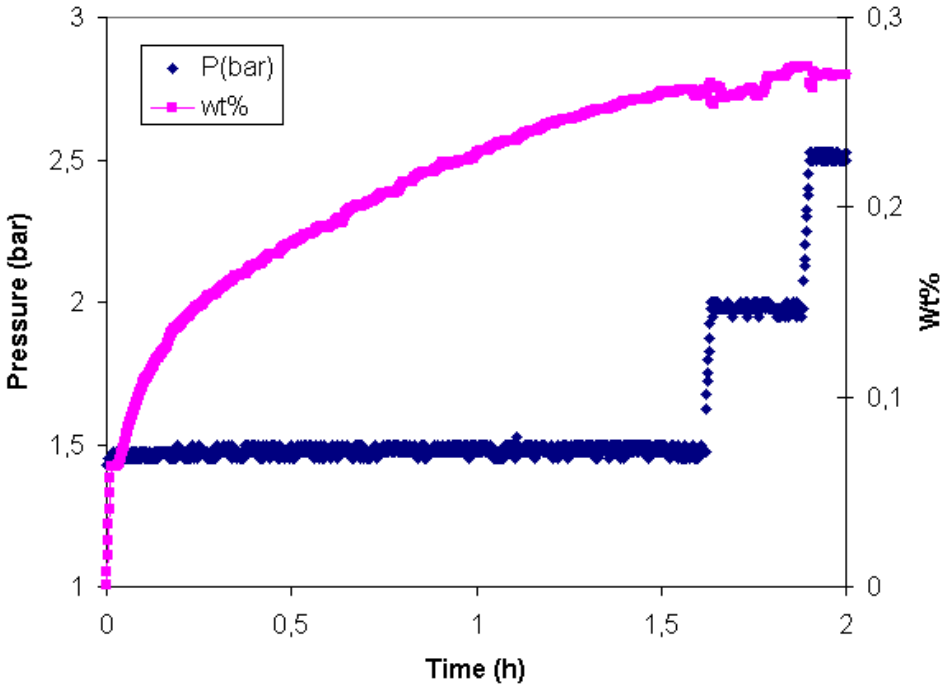

Figure 77 Absorption of hydrogen in Li_3AlN_2 sample at 150 °C and initially 1.5 bar. The PCI step measurements were started after about 100 minutes, which are shown by the pressure steps.

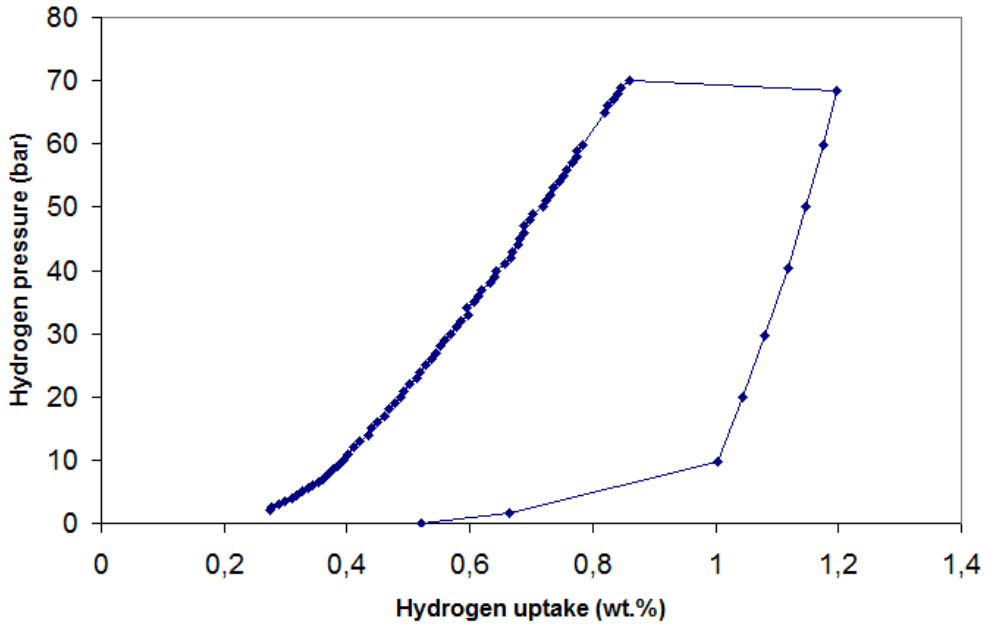

Figure 78 PCI recording of Li_3AlN_2 sample at 150 °C. The step time was 15 minutes.

At reaching 70 bar, a total of 1.19 wt% had been taken up. However, while the sample was left for many hours during these conditions, more hydrogen was taken up. This is shown in Figure 79. It is seen that the pressure drops in response to the uptake, which is a cause of the closed system and hydrogen being absorbed by the sample. Not shown here, the sample continued to absorb up to 1.2 wt%.

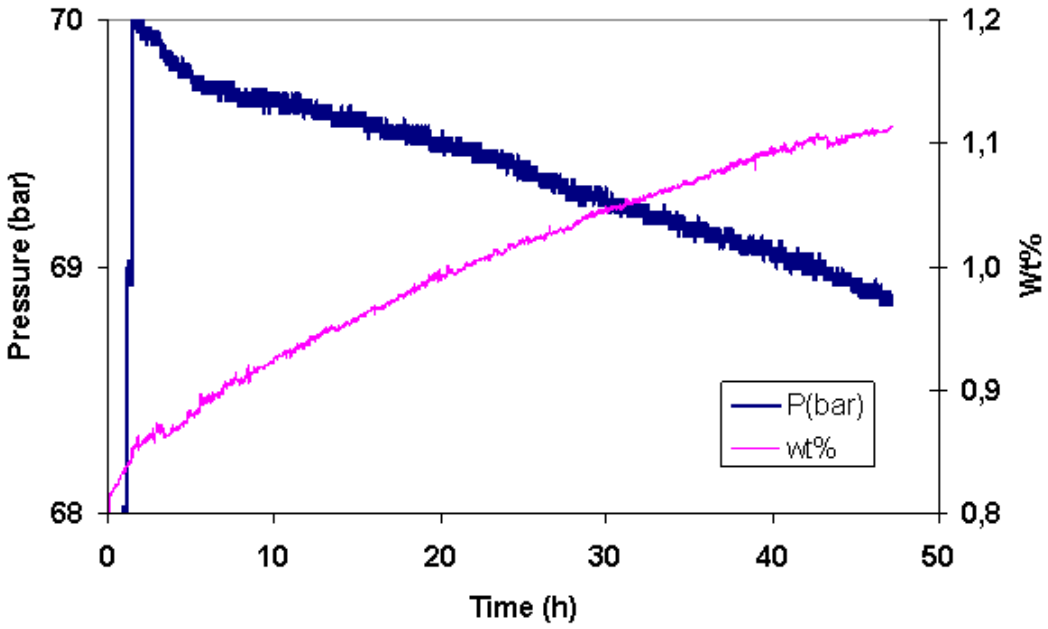

Figure 79 Long term uptake by Li_3AlN_2 sample at ~70 bar hydrogen and 150 °C.

During the desorption half-cycle (refer to Fig. 78), about 0.7 wt% was desorbed. The curves for pressure and wt% in Figure 80 illustrate that the desorption at this temperature was rather fast, as equilibrium was reached very quickly as a response to the pressure changes.

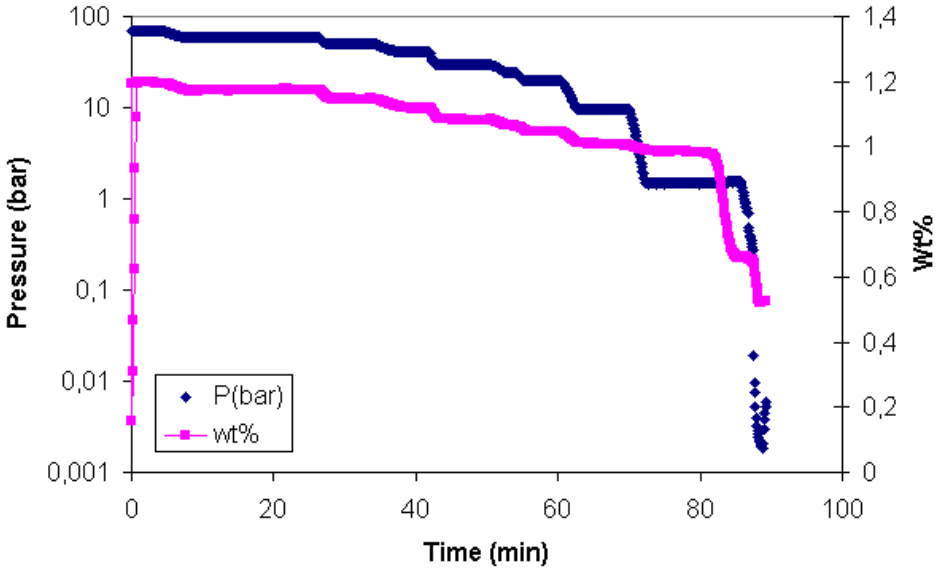

Figure 80 PCI recording of Li_3AlN_2 sample at 150 °C. The step time was 15 minutes.

Using the same sample the temperature was subsequently raised to 300 °C, and hydrogen was introduced at 1.2 bar. The uptake reached 0.8 wt% after which the pressure was increased in steps, see Figure 81. The pressure was increased further to 65 bar, not shown here.

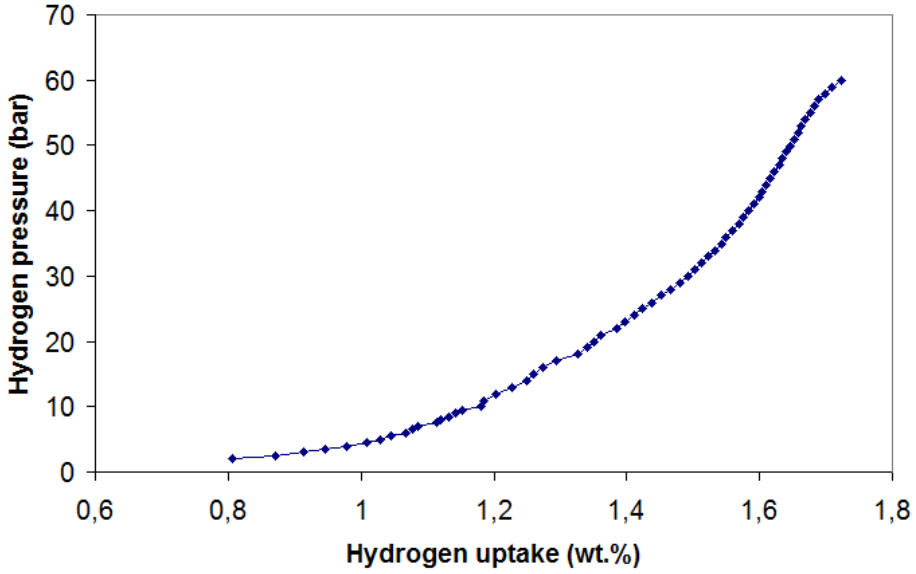

Figure 81 Hydrogen uptake in Li_3AlN_2 sample at 300 °C at various hydrogen pressures. For each point, the sample was left for 10 minutes.

The pressure was afterwards dropped fast to 40 bar and to 2.65 bar to get a sense of the kinetics. During this dehydrogenation at 300 °C, as seen in Figure 82, close to 1 wt% was desorbed within 1 hour. Afterwards the pressure was dropped to vacuum level and down to 0.7 wt% was desorbed.

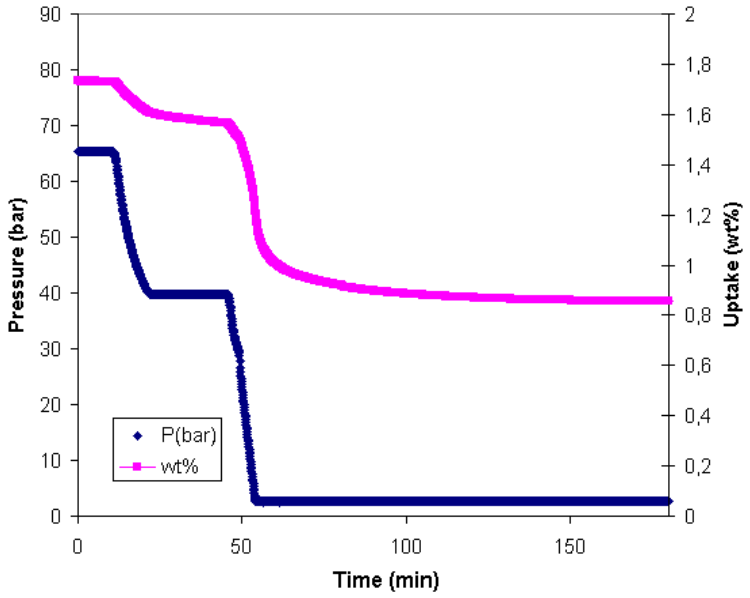

Figure 82 Desorption of hydrogenated Li_3AlN_2 sample at lowered pressures at 300 °C as measured by TGA in high pressure microbalance.

To see if this same fast kinetics would apply for absorption, the pressure was increased with maximum flow in the microbalance to a total of 75 bar. As Figure 83 shows, an increase from 0.7 to 2.1 wt%, i.e. a total of 1.4 wt% within 1 hour was recorded.

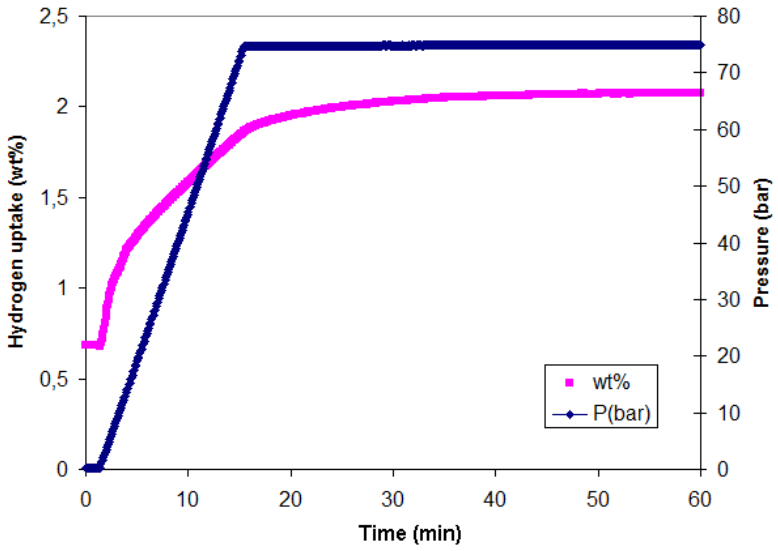

Figure 83 Hydrogen uptake in Li_3AlN_2 sample at 300 °C. After the initial absorption and desorption at 300 °C.

As the experiment shown in Figure 83 was continued keeping the temperature constant and not opening for externally changing the pressure, the sample would start losing mass down to 1.36 wt% within a time frame of 18 hours. This is further described and discussed in Section 6.2.2.

Hereafter another desorption experiment was made dropping the pressure as fast as possible down to 1.5 bar. As shown in Figure 84, the sample again lost ~1 wt%, this time within 30 minutes.

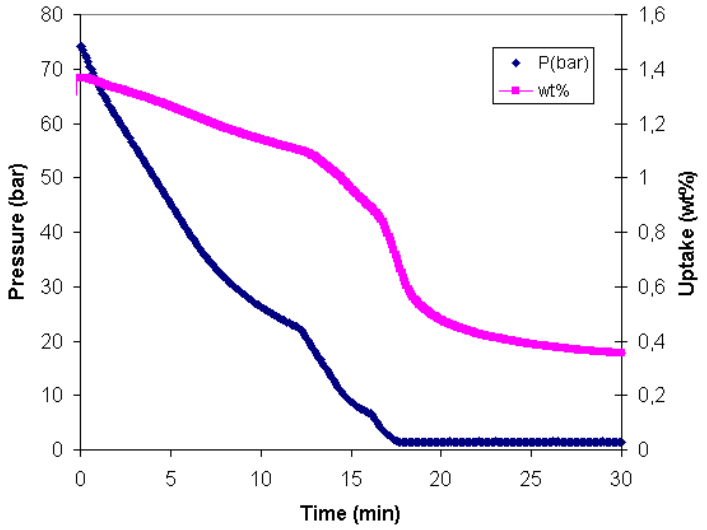

Figure 125 Second desorption run for hydrogenated Li_3AlN_2 sample at 300 °C.

Another absorption and desorption cycle was run at 300 °C, showing quick absorption of ~1 wt% and quick desorption of ~1 wt%.

The results for these experiments are listed in Table 15.

Table 15 Summary of experiments for hydrogen interaction with Li_3AlN_2.

Type	Temperature (°C)	Time (h)	Change in pressure (bar)	Absolute change in mass (wt%)	Relative change in mass (wt%)
Absorption	150	20	0 → 70	0 → 0.8	+0.8
Absorption	150	40	70 → 68	0.8 → 1.1	+0.3
Desorption	150	1½	68 → 0	1.2 → 0.5	-0.7
Absorption	300	18	0 → 60	0.8 → 1.7	+0.9
Desorption	300	3	65 → 2.7	1.7 → 0.9	-0.8
Absorption	300	1	0 → 74	0.7 → 2.1	+1.4
Desorption	300	½	74 → 1.5	1.4 → 0.4	-1.0
Absorption	300	½	1.5 → 74	0.4 → 1.4	+1.0
Desorption	300	1	74 → 2	1.3 → 0.3	-1.0

The conclusion of these experiments is that 0.7 wt% hydrogen can be reversibly stored in Li_3AlN_2 at 150 °C and 1.0 wt% at 300 °C. 1.0 wt% represents about 1 hydrogen atom. Figure 84 shows an XRD measurement for the sample at the end of the A-D cycles. From this it is clear, that Li_3AlN_2 was still present, and had not been turned into a different species completely. Aluminum nitride, AlN, was also present. This evidence will be used in the next section to confirm reaction 43 for the hydrogenation of the sample used in this series of experiments.

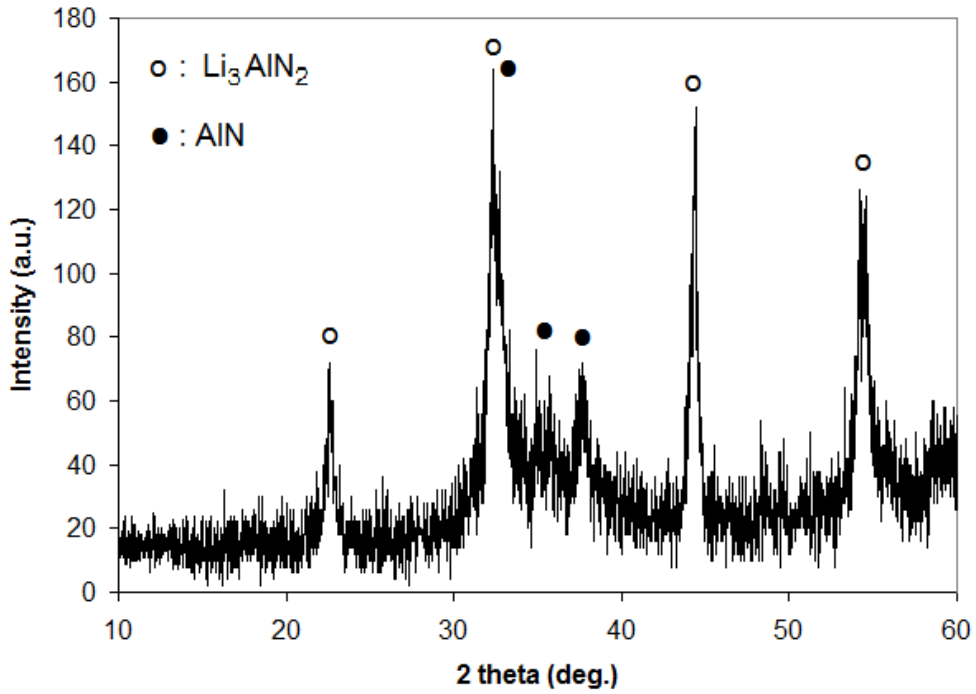

Figure 84 XRD of Li_3AlN_2 sample after 3 hydrogenations and dehydrogenations at 300 °C.

6.2.2 Decomposition of hydrogenated Li_3AlN_2 sample at high pressure hydrogen

At 300 °C and under about 60 bar hydrogen, Li_3AlN_2 would continue to absorb hydrogen to a limit, and then start to lose mass. Figure 85 shows this tendency. At 150 °C no loss in mass could be detected for at least 40 hours under 70 bar hydrogen, although the decomposition may be so slow, that it was overridden by a slow but steady absorption of hydrogen.

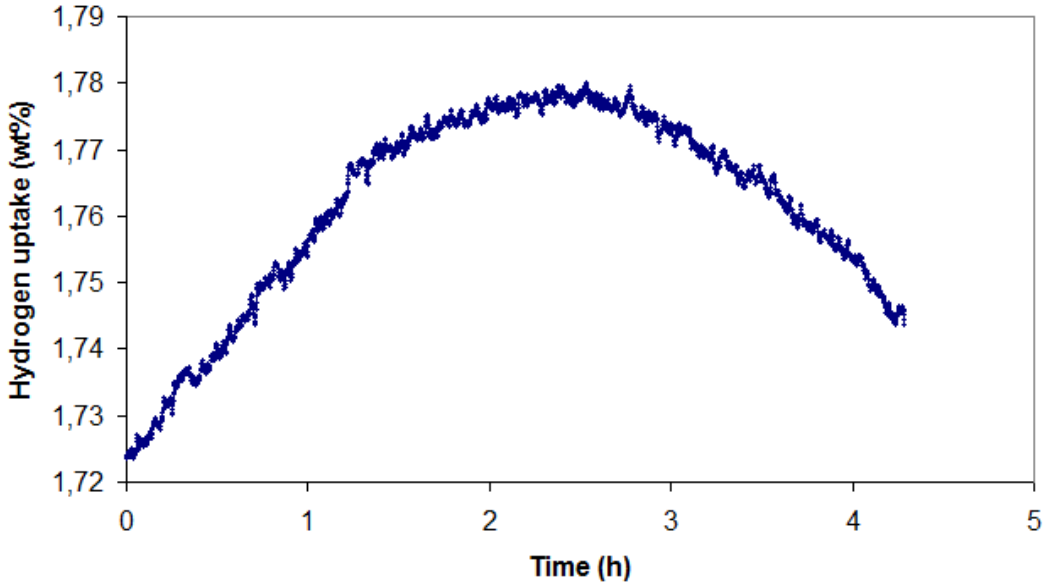

Figure 85 Hydrogen uptake in Li_3AlN_2 sample at 300 °C and 60 bar.

At a subsequent experiment, and over many hours, the clear trend of decomposition was evidenced. Shown in Figure 86, the limit of 2.1 wt% absorption was reached, after which a mass loss of about 0.7 wt% occurred over a time of 18 hours. This gives an average weight loss of 0.04 wt%/h.

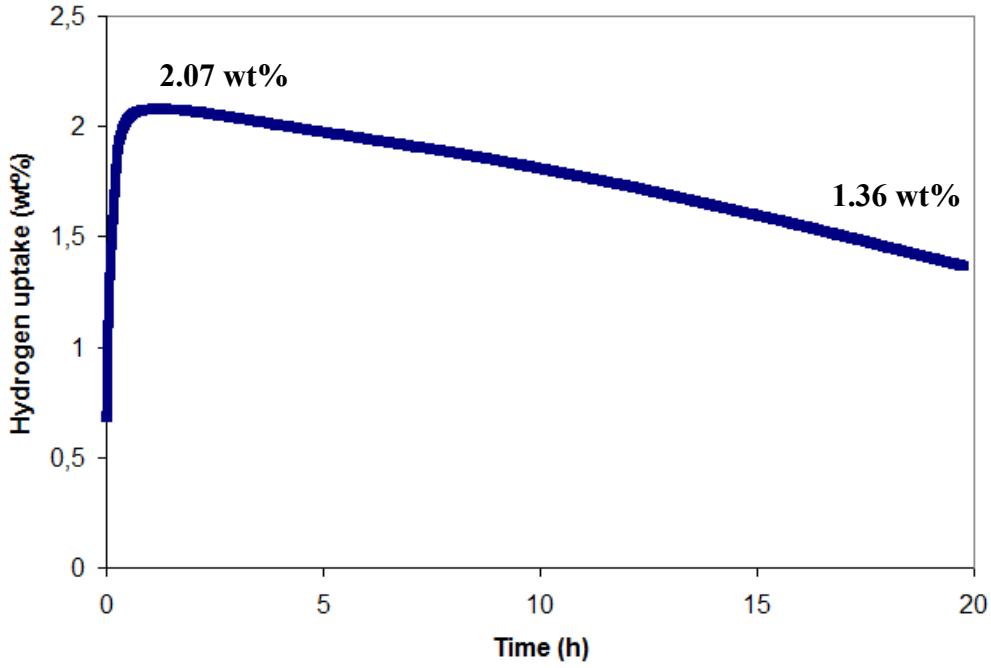

Figure 86 Decomposition of hydrogenated Li_3AlN_2 sample at 300 °C and 67 bar hydrogen.

The only gaseous species conceivable to be a decomposition product from the sample is ammonia. The reaction considered in Section 2.3.7,

$$2LiNH_2 \rightarrow Li_2NH + NH_3 \quad (23)$$

is a possibility. Pinkerton showed that this reaction proceeds at temperatures above 200 °C. Furthermore, when in the presence of high pressure hydrogen (above 50 bar) the reaction occurs at rates comparable to the ones seen here for Li_3AlN_2. [172]

Based on this evidence, it is indicated that Li_3AlN_2 interacts with hydrogen to, in part, produce $LiNH_2$. In the previous section it was seen that AlN was part of the sample after dehydrogenation. It is suggested that during hydrogenation, reaction (43) occurred:

$$Li_3AlN_2 + 2H_2 \rightarrow LiNH_2 + 2LiH + AlN$$

However, while decomposition of $LiNH_2$ occurred, a like molar amount of AlN was left unable to go back to a Li_3AlN_2 phase.

It is concluded from these experiments and observations, that Li_3AlN_2 can be synthesized by ball-milling Li_3N and Al under moderate nitrogen pressure, and that up to 2 wt% hydrogen can be absorbed under 70 bar hydrogen and 300 °C . Evidence was seen, especially in the observation loss of mass at 300 °C and hydrogen pressure indicating the presence of $LiNH_2$, that the hydrogenation reaction proceeded to equation (43). In total, about 1 wt% was seen to be reversible, although some of the capacity was likely lost due to decomposition of $LiNH_2$ into lithium imide and ammonia.

7 NEW SYSTEMS FOR HYDROGEN STORAGE II: Li-Si-N-H

In chapter 2, the development in the research of complex hydrides for hydrogen storage was reviewed. It has been seen that the horizon for possible hydrogen storage systems with high weight capacity of hydrogen and favorable thermodynamics has been consirable broadened with the research led by Bogdanovic et al.[58] and Chen et al.[82], inviting researchers to investigate many possible combinations of compounds.

In 2006, Alapati, Johnson and Sholl published a work[173], in which they examined over than 100 reactions of combinations of compounds including LiH, MgH_2, CaH_2, $Ca(AlH_4)_2$, $LiBH_4$, Li_3N, Mg_3N_2, and Si. They calculated the theoretical wt% hydrogen that could be desorbed and used density functional theory to calculate the enthalpy of the reaction. Using the criteria for a potentially good hydrogen storage stystem that ΔH should be between 30 and 60 kJ/mol H_2 and the wt% at least 6.5, they found several applicable systems. Since the beginning of the research in the present work, Alapati et al. have continued developing their model[174-176], predicting new systems out of over 2 million examined systems[177], yielding many new interesting avenues for investigation, none-the-least for experimentalists.

Table 16 Systems for hydrogen storage for which the theoretical wt% H_2 is calculated and density functional theory used to calculate the reaction enthalpy, denoted here as ΔU_o.[173]

Reaction	wt% H_2	ΔU_0
$3\ LiNH_2 + 2\ LiH + Si \rightarrow Li_5N_3Si + 4\ H_2$ (10/11 Si atoms)	7.16	34.2/23.3[a]
$LiBH_4 + 2\ LiNH_2 \rightarrow Li_3BN_2 + 4\ H_2$	11.9	24.3 (o) 20.2 (h)
$MgH_2 + 2\ LiBH_4 \rightarrow 2\ LiH + MgB_2 + 4\ H_2$	11.56	66.8 (o) 58.6 (h)
$LiNH_2 + MgH_2 \rightarrow LiMgN + 2\ H_2$	8.19	31.9
$4\ LiBH_4 + MgH_2 \rightarrow 4\ LiH + MgB_4 + 7\ H_2$	12.46	69.2 (o) 59.9 (h)
$7\ LiBH_4 + MgH_2 \rightarrow 7\ LiH + MgB_7 + 11.5\ H_2$	12.99	71.5–75.5 (o) 61.5–65.5 (h)
$CaH_2 + 6\ LiBH_4 \rightarrow CaB_6 + 6\ LiH + 10\ H_2$	11.69	62.7 (o) 52.9 (h)
$ScH_2 + 2\ LiBH_4 \rightarrow ScB_2 + 2\ LiH + 4\ H_2$	8.91	49.7 (o) 41.6 (h)
$TiH_2 + 2\ LiBH_4 \rightarrow 2\ LiH + TiB_2 + 4\ H_2$	8.63	22.2 (o) 14.1 (h)
$LiBH_4 + C \rightarrow LiBC + 2\ H_2$	11.95	45.1 (o) 37.0 (h)
$2\ LiNH_2 + C \rightarrow Li_2CN_2 + 2\ H_2$	6.97	31.4
$ScH_2 + 2\ LiBH_4 + C \rightarrow ScB_2C + 2\ LiH + 4\ H_2$	7.86	52.9 (o) 44.8 (h)
$ScH_2 + 2\ LiBH_4 + 2\ C \rightarrow ScB_2C_2 + 2\ LiH + 4\ H_2$	7.04	52.4 (o) 44.3 (h)
$MgH_2 + 2\ LiBH_4 + 2\ C \rightarrow MgB_2C_2 + 2\ LiH + 4\ H_2$	8.59	55.3 (o) 47.2 (h)
$CaH_2 + 2\ LiBH_4 + 2\ C \rightarrow CaB_2C_2 + 2\ LiH + 4\ H_2$	7.35	59.7 (o) 51.6 (h)

One of the systems described in the initial work, see Table 16, was based on lithium, nitrogen and silicon:

$$3LiNH_2 + 2LiH + Si \rightarrow Li_5SiN_3 + 4H_2 \qquad (45)$$

This system has a theoretical wt% of 7.16 and an enthalpy of reaction of +34.2 kJ/mol H_2. It was an straight-forward system to investigate, as Li_5SiN_3 is fairly analogous to Li_3AlN_2, of which experiments had already been conducted in our laboratory (see chapter 6). It would be interesting to

see, whether the method of synthesis could be extended from Li_3AlN_2 directly to Li_5SiN_3 and characterize the material with regard to hydrogen storage.

In the present work, it was thus planned to examine the reaction

$$Li_5SiN_3 + 4H_2 \rightarrow 3LiNH_2 + 2LiH + Si \quad (46)$$

7.1 Synthesis of Li_5SiN_3 and reaction with hydrogen

Lithium silicon nitride in the form Li_5SiN_3 has been described to be a grayish white solid. It is not a very common compound as evidenced by the little literature found on it.

There are 3 ways for the synthesis of Li_5SiN_3 found in the literature as follows:

1) Addition of silicon and nitrogen to liquid lithium.[178,179] Lithium is heated to 450 °C, and silicon is added producing a Li-$Li_{22}Si_5$ solution. By adding nitrogen, lithium nitride, Li_3N, is formed, and the subsequent reaction occurs

$$15Li_3N + Li_{22}Si_5 \rightarrow 5Li_5SiN_3 + 42Li \quad (47)$$

of which lithium silicon nitride is precipitated.

2) Calcination of Li_3N and silicon nitride, Si_3N_4.[180,181] Li_3N and Si_3N_4 are typically mixed together and pressed into a pellet and calcinated at 800 °C under nitrogen flow for 20 minutes. The following reaction occurs

$$5Li_3N + Si_3N_4 \rightarrow 3Li_5SiN_3 \quad (48)$$

3) Ball milling of Li_3N and Si_3N_4.[182] In the single study found using this technique, the reactants were ball milled under nitrogen for 20 h at a speed of 500 rpm using 12 balls of 10 mm diameter. Iron and iron nitride were found together with Li_5SiN_3. The impurities from iron were believed to stem from the ball milling jar and balls, which were all of stainless steel.

Evidence in our lab points to indeed the presence of iron impurities during ball milling with our equipment. However, using shorter milling times, lower speed and/or fewer/smaller balls are all expected to limit the amount of impurities.

An alternative for synthesis of Li_5SiN_3 is proposed in this study as follows:

4) Ball milling of Li_3N and Si under nitrogen pressure and subsequent calcination. The product is pelletized and calcinated under nitrogen pressure at high temperature, and thereafter ground to a powder.

Apart from Li_5SiN_3, other forms of lithium silicon nitride exist. Yamane et al.[180] achieved pure phases of Li_2SiN_2, Li_5SiN_3, $Li_{18}Si_3N_{10}$, $Li_{21}Si_3N_{11}$, Li_8SiN_4 by using ratios between the reactants Li_3N and Si_3N_4 of 0.6, 5.1, 6.0, 7.1, and 8.2, respectively, all at 800 °C. Anderson et al.[183] showed that Li_2SiN_2 could be synthesized by a novel method using a household microwave oven! They ground Li_3N, $LiNH_2$ and NH_4Cl in an agate mortar and transferred it to a quartz vial to which $SiCl_4$ were added. The vial was fitted with a pressure relief valve. In a microwave oven they then applied microwaves to the reactants. By washing the product with water, Li_2SiN_2 was solubilized. The solution was centrifuged and solid Li_2SiN_2 was obtained.

Experimental studies of the reaction of Li_5SiN_3 with hydrogen have been described nowhere in the literature to this author's knowledge.

In this study, methods 3-4 were used. In addition, lithium nitride was synthesized from the elements to have a pure starting product.

7.1.1 Synthesis of Li_3N

Lithium reacts—as the sole element under standard conditions—spontaneously with nitrogen. However, the reaction is slow, although this condition is changed by raising the pressure and/or temperature. The reaction is often carried out in the laboratory by using fairly high temperature, above 100 °C. The reaction is as follows:

$$3Li + ½N_2 \rightarrow Li_3N \qquad (49)$$

and has an enthalpy of reaction of -197 kJ/mol.

Experimental

3.007 g Li (99% granule < 3mm) was transferred to a reactor (see Figure 87), in a glovebox with Ar (< 1 ppm O_2).

Figure 87 Reactor for solid-gas reactions. The reactor (which is sealed in the lid with an O-ring) is placed in a pocket that contains a heating element with a thermocouple and a blanket of quartz wool for insulation. There is an approximate temperature difference of 70 °C between the measured temperature and the internal temperature of the reactor. The pressure gauge reads in psi units, so the 302 psi that can be seen would be approximately 20 bars.

10 bar purified N_2 was added to the reactor, and it was heated slowly to 130 °C (internal temperature about 60 °C), while observing the pressure. At 130 °C, the pressure starting falling slowly, and the temperature would rise spontaneously. When the pressure was below 1 bar, more nitrogen was added, and the reaction continued. In the end, the temperature would stop rising. Up to 20 bar nitrogen was added and the temperature was increased by the heater to 170 °C. After 30 minutes no more pressure drop was observed, and the reaction was taken to be finished. The overpressure of nitrogen was removed, and the product was transferred in glovebox to a milling jar with a single steel ball of a Retsch MM 301 SPEX vibrating mill, see Figure 88.

Figure 88 Product of the lithium reacted with nitrogen in a SPEX milling jar. There is a single stainless steel ball for the operation.

The product was crushed in the SPEX for 30 minutes at a frequency of 18 Hz, see Figure 89.

Figure 89 SPEX vibrating mill. The milling jars are moved rapidly sideways back and forth in the horizontal plane resulting in the single steel ball transferring its kinetic energy to the powder in the jars and crushing it into a fine powder.

A pellet of the product, which was a fine purple powder, was pressed in glovebox, and XRD was performed on it, see the result in Figure 90. It shows a mixture of two polymorphs of Li_3N, α-Li_3N and β-Li_3N, which both have a hexagonal crystal structure. The yield of the product was 98.5%.

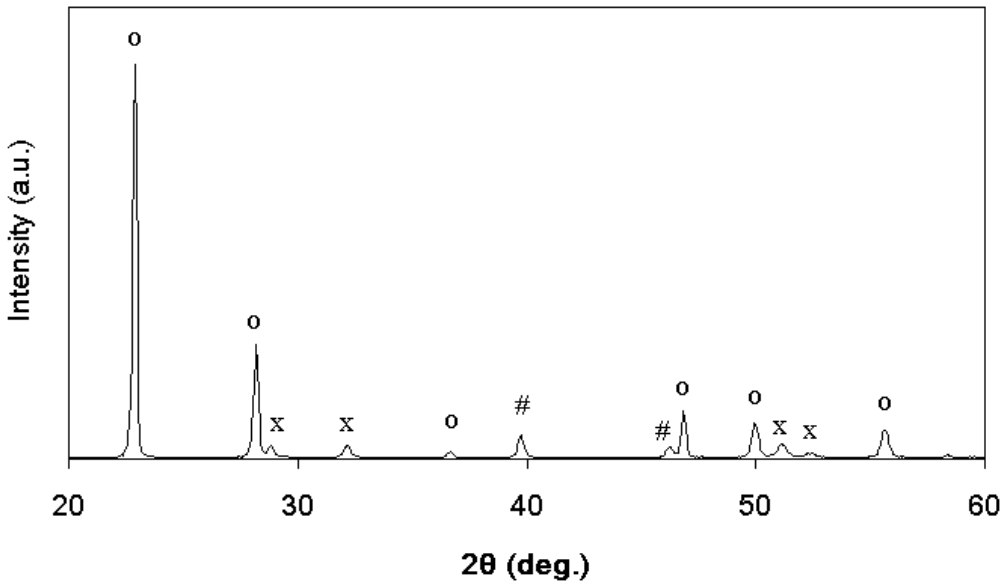

Figure 90 XRD of lithium reacted with nitrogen. The key is: o = α-Li_3N, x = β-Li_3N, # = Pt. Pt is an artifact from the sample holder in the XRD apparatus, which is visible when the pellet sample is not thick enough to absorb all X-rays. No impurities are observed (Li, Li_2O, for example).

Another synthesis of Li_3N was made in the same manner, but with the difference that no external heat was supplied. 14 bar N_2 was applied. After 3 hours the pressure was close to 0 bar. 14 bar N_2 was applied again, and a drop to 12 bar was observed after 1 hour. 20 bar N_2 was applied, and no drop was observed for 5 minutes. External heat was now supplied, and the temperature was raised to 170 °C (100 °C internal). Apart from that attributed to temperature rise, no difference in pressure was observed, meaning that no more reaction took place. The product showed a virtually identical XRD result to the first. The yield was 99.0%, estimated gravimetrically.

This second result shows that Li_3N can be synthesized readily from the elements by only having a pressure of 14 bar N_2. No external heat supply was necessary.

7.1.2 Synthesis of Li_5SiN_3 by calcination using Li_3N, Si and N_2 as reactants and its reaction with hydrogen

In this synthesis the following reaction was hypothesized:

$$5Li_3N + 3Si + 2N_2 \rightarrow 3Li_5SiN_3 \qquad (50)$$

To make a sample of 1.5 g Li_5SiN_3, 0.83 g of Li_3N (from in-lab synthesized Li_3N, see previous section) and 0.40 g Si (Alfa Aesar, 99.999%, 1-5 μm) were ball milled in a Retsch PM 400 planetary mill under 42 bar N_2 at 250 rpm in this way: 50 s in clockwise direction, 15 s pause, 50 s in anti-clockwise direction, 15 s pause, and repeat for 16 h. This method was used in order to give time to dissipate heat from the milling jar, so the temperature stayed around room temperature, thus giving a temperature-controlled environment. The lids for the ball milling jars were custom-made in such a way, that it had a valve to allow for admission of pressurized gas to the jar.

The product was a gray powder with a shade of yellowish brown. Figure 91 shows the XRD of the powder. It shows that Li_5SiN_3 was formed. However, a broad diffuse peak around 20° is present. This comes possible from an amorphous phase. To see if this could stem from an amorphous phase of silicon, Si was ball milled alone under the same conditions as before, and a XRD was made. This showed no such broad peak. It is therefore not possible to attribute the broad peak to amorphous silicon at this point.

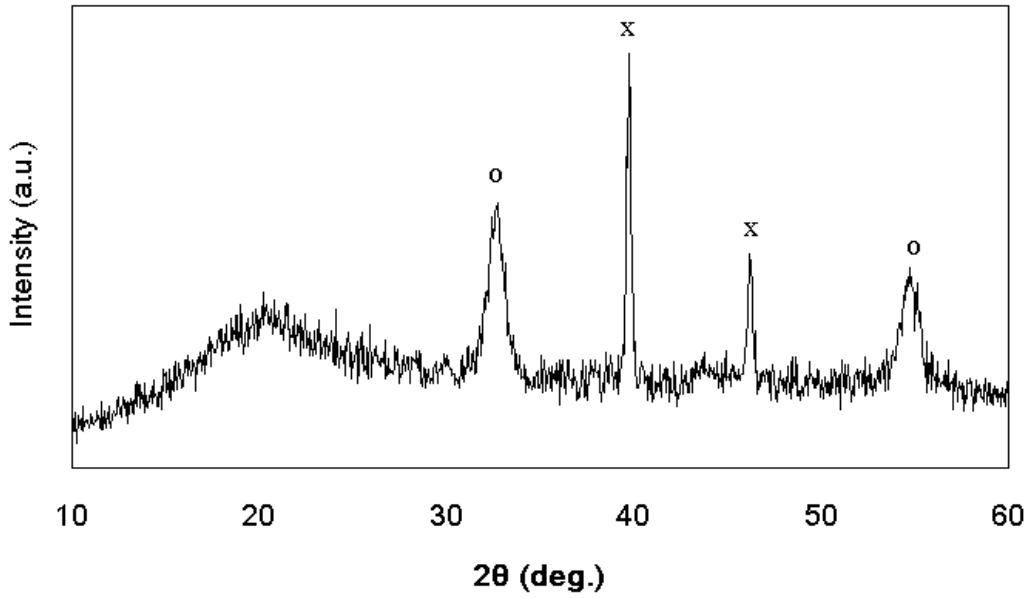

Figure 91 XRD of ball milled Li_3N and Si under N_2 pressure. Key: o = Li_5SiN_3, x = Pt. Pt is an artifact from the sample holder in the XRD apparatus, which is visible when the pellet sample is not thick enough to absorb all X-rays. The broad peak around 20° could not be identified.

In an attempt to remove the apparant amorphous phase and to crystallize the Li_5SiN_3 phase, some of the powder was pressed into a pellet and calcinated under 40 bar N_2 at 500 °C (reaction temperature; the external temperature was 600 °C and there was about a 100 degree difference between the inside of the reactor and the heating element where the thermocouple resided). Figure 92 shows the setup of the calcination procedure.

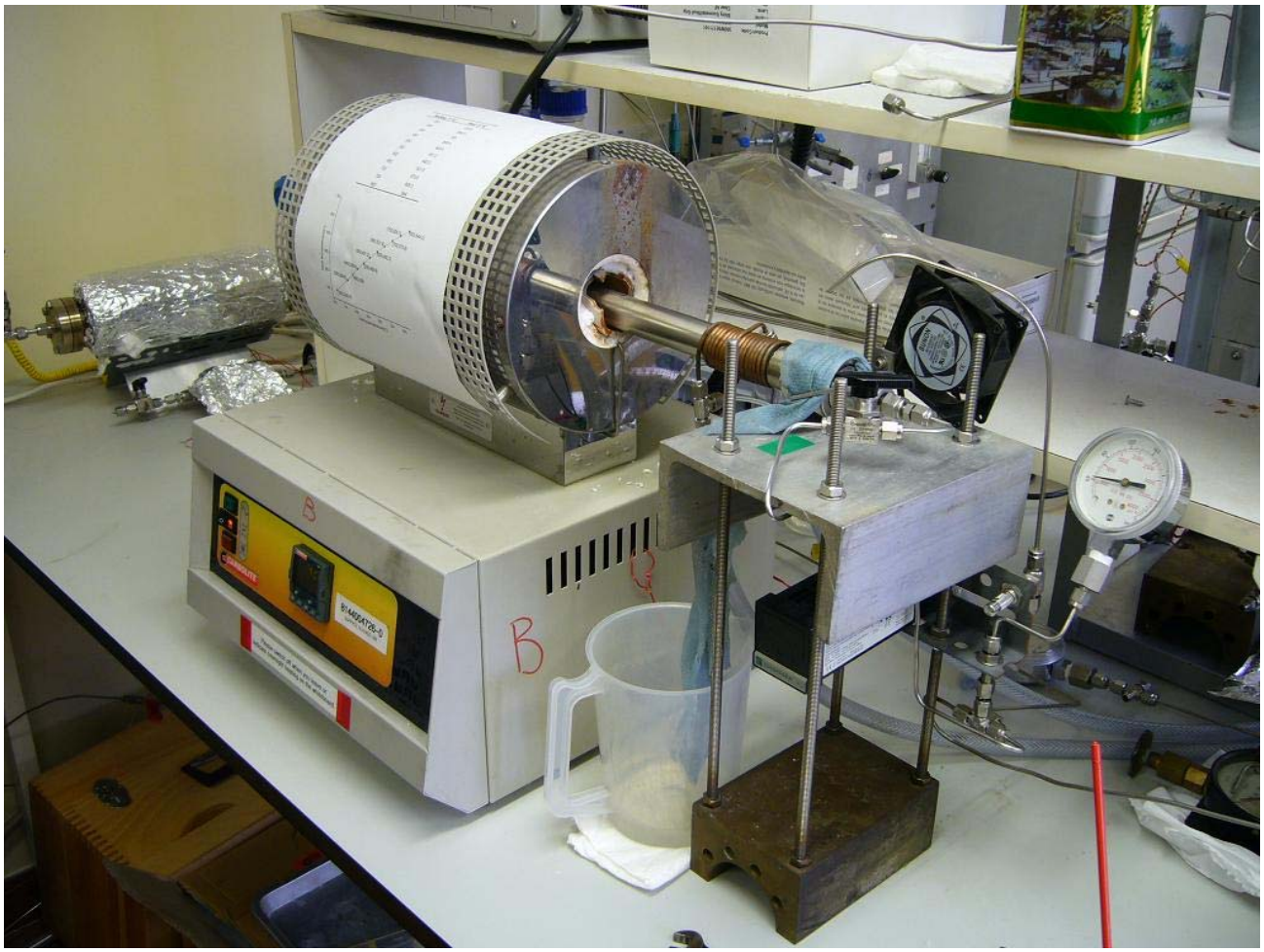

Figure 92 Calcination in reactor sealed with O-ring. The wound copper tube cooled the reactor with flowing water. The blue cloth cooled the metal close to the O-ring and was continually wetted with water. The reaction tube was also cooled by the fan.

The calcination did not remove or change the broad peak around 20° as the X-ray diffractogram was unchanged except for the inclusion of a Li_2O phase. Li_5SiN_3 was therefore not crystallized any further under these calcination conditions.

The powder from before the calcination was put into an Advanced Materials Gas Reaction Controller (Sieverts' apparatus) in order to test for reactivity with hydrogen. Figure 93 shows the result of the hydrogenation.

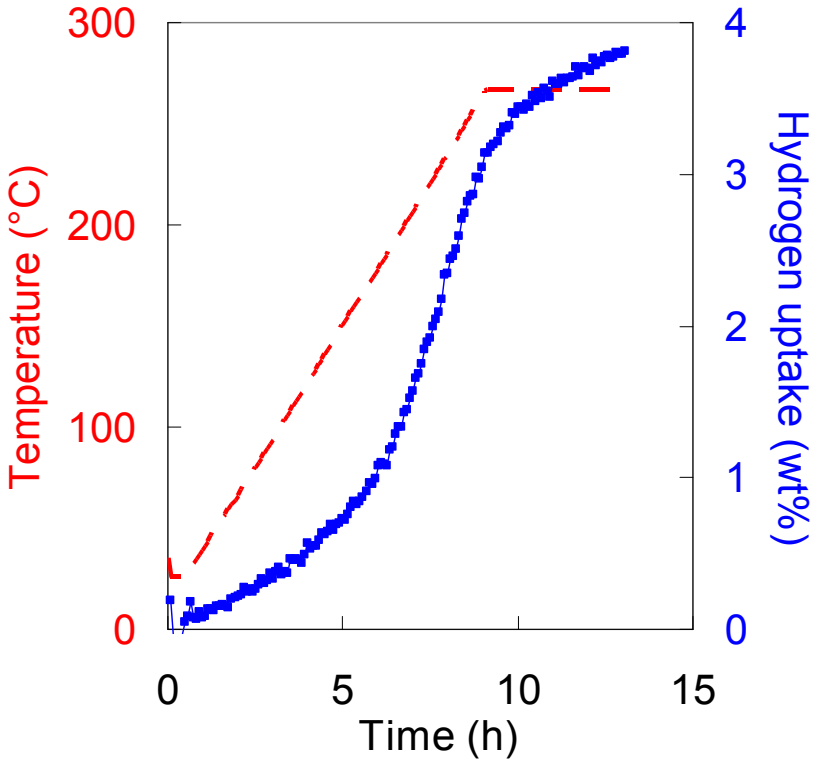

Figure 93 Li_5SiN_3 reacting with hydrogen. The pressure of hydrogen was 67 bar and the temperature was increased at 0.5 K/min up to 270 °C after which it was kept steady.

Under the hydrogenation conditions a total of 3.8 wt% could be taken up by the sample. The hydrogenated sample was taken to XRD and showed virtually no change except for miniature peaks identified as lithium hydride, LiH. Also, the peaks for Li_5SiN_3 had not shifted, so no expansion of the crystal lattice could be detected for Li_5SiN_3 after hydrogenation.

A second batch was made in same manner and was hydrogenated at 75 bar hydrogen and 335 °C. This showed an uptake of 3.8 wt% just like the first sample.

The hydrogenated sample was treated under temperature programmed desorption (TPD) in a homemade setup in order to test for hydrogen desorption (and verifying the uptake of hydrogen in the sample). Figure 94 shows the setup of the TPD.

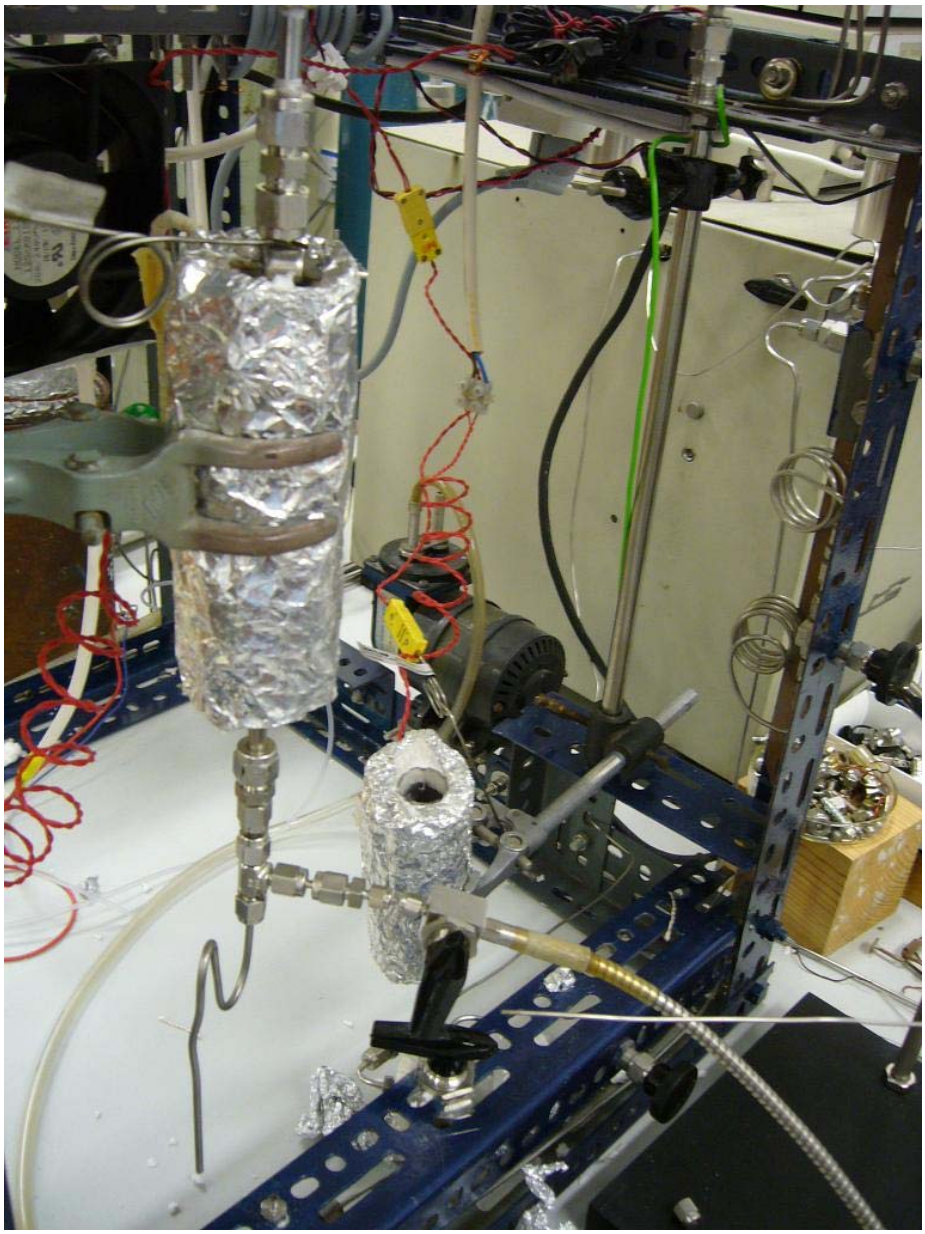

Figure 94 Setup for temperature programmed desorption. The sample was transferred in a glovebox to a stainless steel reactor tube and a piece of quartz wool was put in the bottom to keep it the sample from falling out of the tube. The wool was set it place with a piece of metal that was held in place inside the tube. The reactor tube was fitted as shown in the picture and a heating element was placed around it. A stream of argon was allowed to flow through the reactor. In the bottom, a take-out of the stream was made and led to a mass spectrometer. The rest of the gas was vented and could be tested for ammonia content, e.g. by passing it through a $Co(NO_3)_2$ solution.

The TPD, seen in Figure 95, shows that hydrogen begins to be desorbed from the sample at around 170 °C and peaking at 260 °C. Importantly, from a more practical point of view, no desorption of ammonia was detected. As described in Chapter 3, it is essential with regard to practical uses in combination with a PEM fuel cell to avoid ammonia in the desorption product.

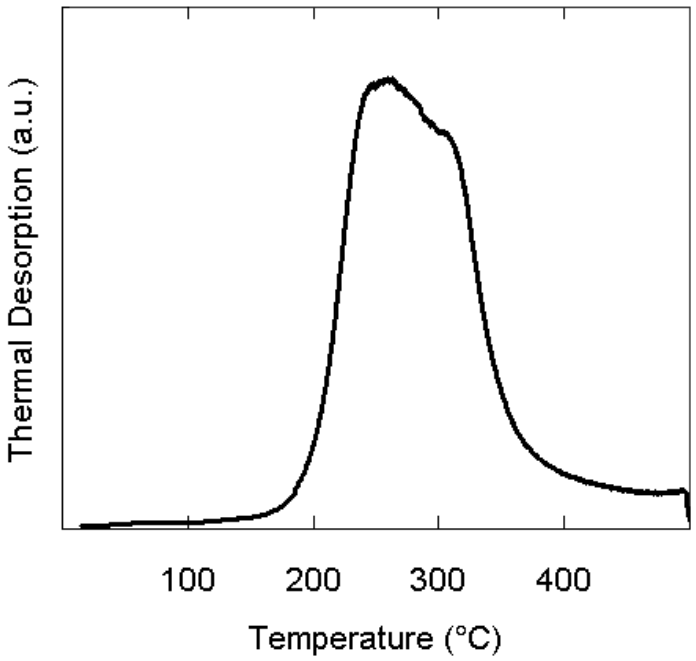

Figure 95 Temperature programmed desorption of the hydrogenated Li_5SiN_3 sample. The temperature was increased from room temperature to 500 °C at 2 K/min, and a flow of Ar carried the gaseous products to a mass spectrometer. The curve shows the measured levels of hydrogen. No levels of ammonia were discernable within the limit of detection.

A sample from the hydrogenated Li_5SiN_3 was taken to the Gas Reaction Controller to get a measure of the weight percent that could be desorbed.

Figure 96 shows the result of the procedure. 2.5 wt% could be desorbed at temperatures below 335 °C. As the TPD showed no ammonia and only hydrogen desorption, it is assumed that the 2.5 wt% corresponds only to hydrogen.

Hence, the hydrogenation of Li_5SiN_3 was shown to be partly reversible and involving no gaseous ammonia products.

It was also shown that ball milling Li_3N and Si under N_2 with subsequent calcination at 500 °C created a phase of Li_5SiN_3, however not pure. Another sample was made, pelletized with as much force as the pellet apparatus would allow, and calcinated at 700 °C for 13 hours, but with the same XRD result, although with an iron phase present (probably impurity from the reaction tube).

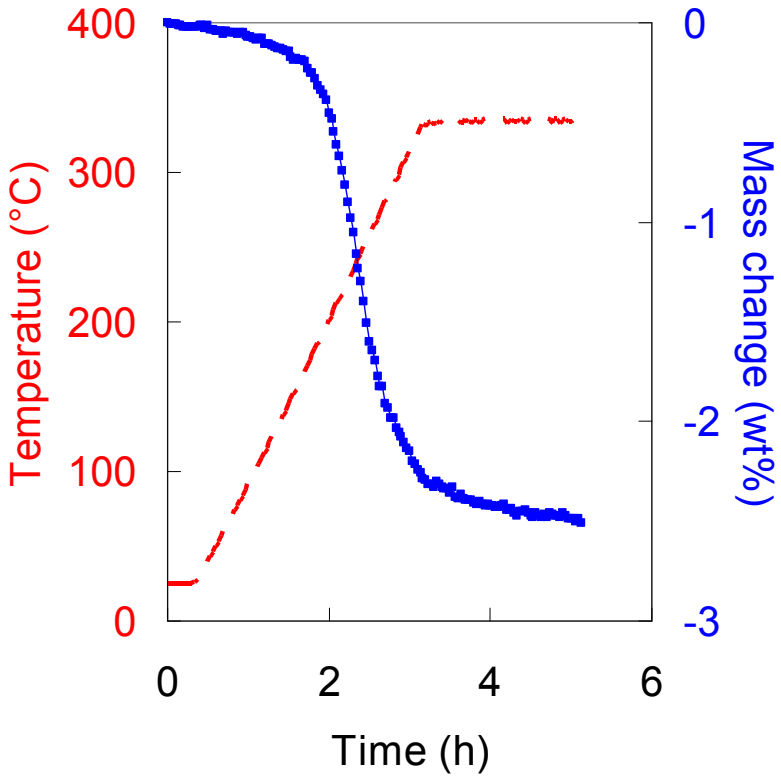

Figure 96 Gas (hydrogen) release of the hydrogenated Li_5SiN_3 sample at ~0.01 MPa hydrogen. The temperature was raised at 2 K/min. and was kept constant at 334 °C. The broken line shows the temperature, and the thick line shows the change in mass.

7.1.3 Li_2SiN_2 and reaction with hydrogen

As described in Section 7.1, Yamane et al.[180] showed that Li_5SiN_3 can be synthesized from Li_3N and Si_3N_4 at 800 °C, and that Li_2SiN_2 could also be synthesized under the same conditions, but by varying the ratio in the equivalents of the reactants.

In an attempt to produce a crystalline phase of Li_5SiN_3 a pellet pressed sample of ball milled Li_3N and Si was calcinated under 30 bar N_2, all similar to the procedure described in 7.1.2. However, as for heating, the reaction tube was heated quickly to 570 °C after which the temperature was raised gradually at a rate of 2 K/min. to 800 °C and left at this temperature for about 35 hours. The reason for this slow increase of temperature was to allow any phase changes to proceed to completion before the temperature was raised unduly high, perhaps causing other changes such as melting or evaporation of some of the components, causing the onset phase change to not be complete.

On inspection after the heating was finished, the reactor tube was found to have a small hole through which the gas had leaked through. The product, however, which was now light gray, was put in XRD. The result is shown in Figure 97.

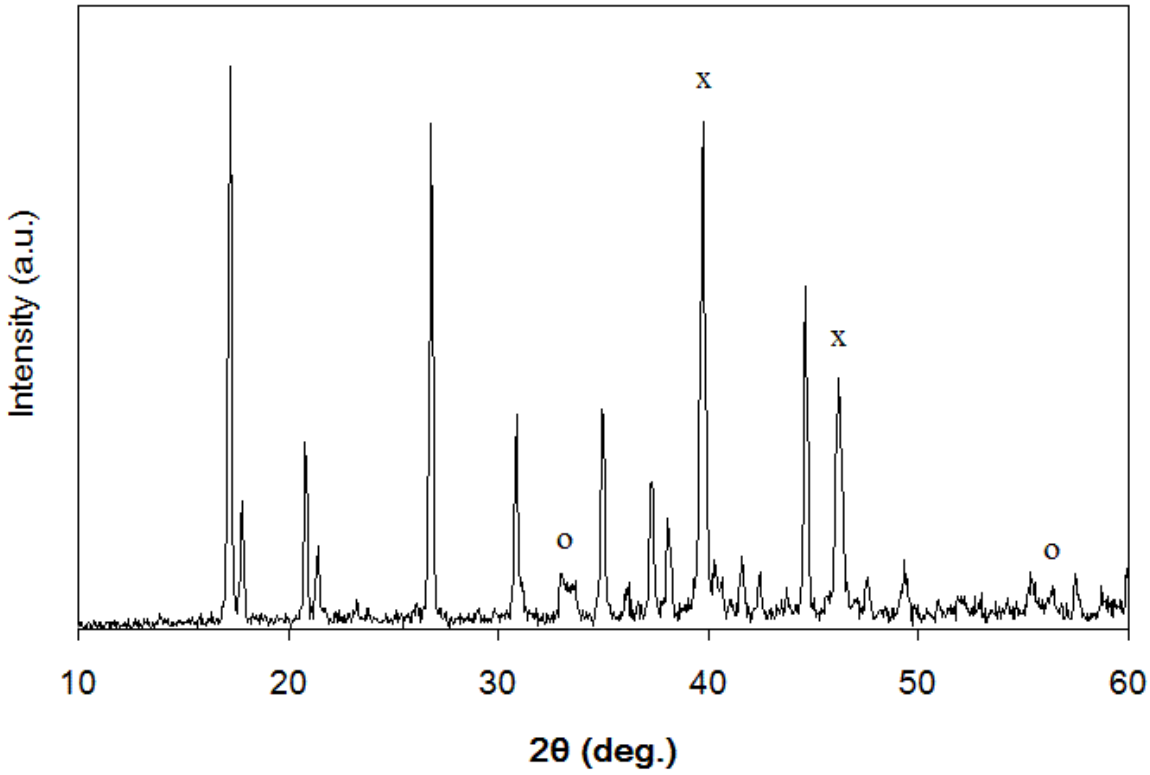

Figure 97 XRD of ball milled Li_3N and Si under 30 bar N_2 heated to 800 °C with pressure relief. Key: o = Li_2O, x = Pt. Pt is an artifact from the sample holder in the XRD apparatus, which is visible when the pellet sample is not thick enough to absorb all X-rays. All other peaks: Li_2SiN_2.

The result shows a clear phase of Li_2SiN_2, with what seems like a phase of Li_2O.

On further inspection of the hole in the reactor tube, it looked melted some places, and it is assumed that perhaps lithium had evaporated from the sample and reacted with the side of the tube, made of stainless steel, somehow etching its way through creating a hole. This removal of lithium would account for the lack of other Li products in this more lithium deficient form of lithium silicon nitride, Li_2SiN_2, compared to Li_5SiN_3.

While having obtained an almost pure phase of Li_2SiN_2, the pellet was crushed in the SPEX mill, and put in the Gas Reaction Controller to check for reaction with hydrogen. As Figure 98 shows, it was possible to absorb up to 4.8 wt% hydrogen in the sample at temperatures under 360 °C and at 80 bar hydrogen.

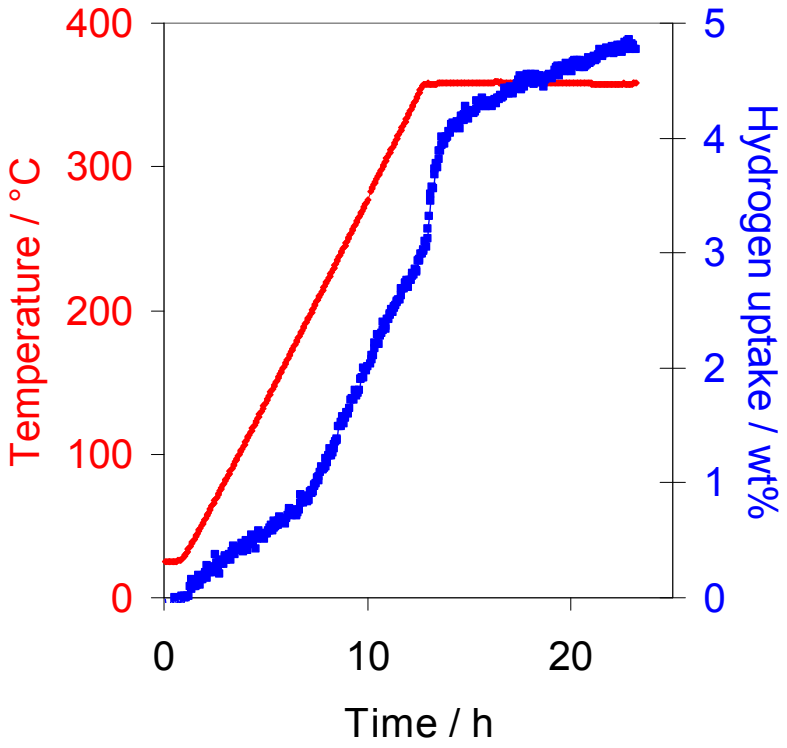

Figure 98 Li_2SiN_2 reacting with hydrogen. The pressure of hydrogen was 80 bar and the temperature was increased at 0.5 K/min up to 360 °C after which it was kept steady.

It was later attempted to produce Li_2SiN_2 based on both of these tentative reaction equations:

$$2Li_3N + Si_3N_4 \rightarrow 3Li_2SiN_2 \quad (51)$$

$$2Li_3N + 3Si + 2N_2 \rightarrow 3Li_2SiN_2 \quad (52)$$

Both were milled in a Fritsch Pulverisette 7 planetary mill with small milling jars and 5 stainless steel balls. For the second case involving reaction (52) a custom made lid with a valve for use of pressurized gas (as described earlier in Chapter 6) was used with the milling jar.

In all attempts, using the stoichiometry from (51) and (52) employing various milling times and various milling speeds, no trace of Li_2SiN_2 could be observed through XRD. It can thus be concluded that it is not possible—if not just very elusive for discovery—to synthesize Li_2SiN_2 through ball milling, but that it can be made by calcination at 800 °C, which was also described in the literature.[180]

7.1.4 Synthesis of Li_5SiN_3 by ball milling Li_3N and Si_3N_4 and investigation of the reversibility of reaction with hydrogen

It was desired to examine the reaction of Li_5SiN_3 more fully and to verify the reversibility of reaction (46).

Li_5SiN_3 was synthesized from Li_3N and Si_3N_4 according to (48) by ball milling reactants of a total of 1.2 g in a Fritsch Pulverisette 7 planetary mill with 5 steel balls for 4 hours at 600 rpm. The sample was hydrogenated at 70 bar at 300 °C and thereafter dehydrogenated in vacuum at 400 °C and 600 °C. After each step an X-ray diffractogram was recorded. The result is seen in Figure 99.

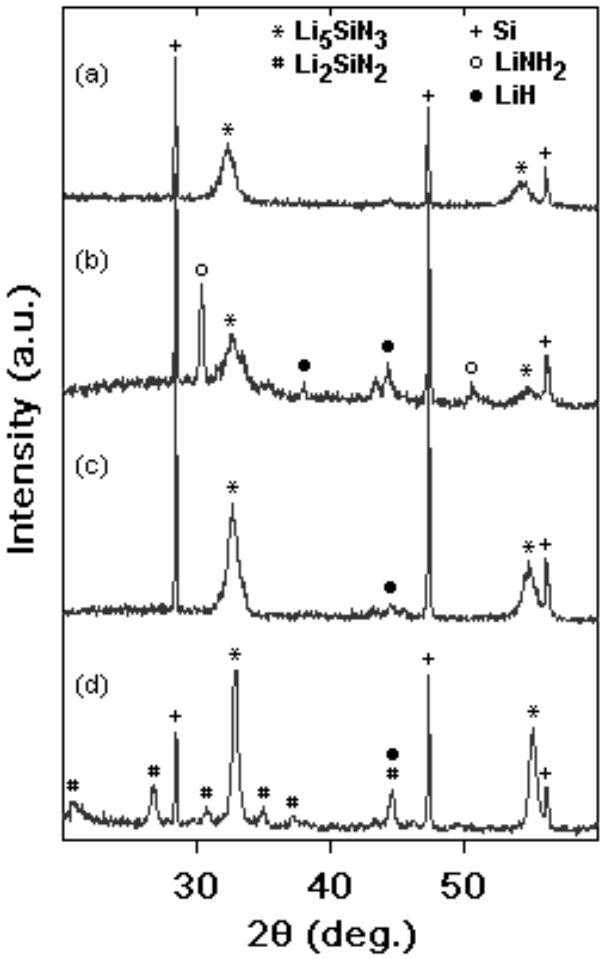

Figure 99 XRD recordings for hydrogenation and dehydrogenation of Li_5SiN_3. (a) The ball-milled sample, (b) after hydrogenation at 300 °C and 70 bar hydrogen, (c) after dehydrogenation at 400 °C and vacuum, (d) after dehydrogenation at 600 °C and vacuum. The recurrent Si phase stems from an inherent Si calibration piece in the XRD apparatus.

From these results it is seen that:

(1) Li_5SiN_3 could be synthesized from Li_3N and Si_3N_4. Unlike results in the literature[182] no impurities were found in this instance.

(2) Lithium amide, $LiNH_2$, and lithium hydride, LiH, were created during hydrogenation at 70 bar hydrogen.

(3) The $LiNH_2$ peaks disappeared during dehydrogenation at vacuum and 400 °C. The LiH was still present, although only identified by a very small peak.

(4) At heating to 600 °C under vacuum, a clear Li_2SiN_2 phase was created.

It is seen that this experiment confirms both (45) and (46), or in other words the reversible reaction

$$Li_5SiN_3 + 4H_2 \leftrightarrow 3LiNH_2 + 2LiH + Si \quad (53)$$

even though it does run to completion in both directions under these reaction conditions.

Observation (4) above shows that Li_2SiN_2 was created at a much lower temperature, 600 °C, than earlier observed (800 °C). The applied vacuum can account for loss of lithium in the sample caused by evaporation.

Reaction (45) was investigated to see if it was possible to let the reaction proceed to completion and in order to investigate the products.

A mixture of $LiNH_2$ (Aldrich, 95%), LiH (Aldrich, 95%), and Si (Alfa Aesar, 99.999%, 1-5 µm) in ratio 3:2:1 was ball milled for 17 hours at 450 rpm. The sample was heated to various temperatures under vacuum and it was taken out for XRD in between. Figure 100 shows the results.

From the XRD, the following is observed:

(1) Li_5SiN_3 was created at 300 °C, but $LiNH_2$ and LiH were still present. The peaks identified as $LiNH_2$ might actually be lithium imide, Li_2NH, as they are so close to each other, that it is not possible to discern them by XRD.

(2) The peaks for Li_5SiN_3 got sharper at rising temperatures up until the maximum temperature of 600 °C.

(3) The peaks for $LiNH_2$/Li_2NH disappeared at 600 °C.

This experiment confirms reaction (45), that Li_5SiN_3 is created from the reactants, although the reaction did not proceed to completion.

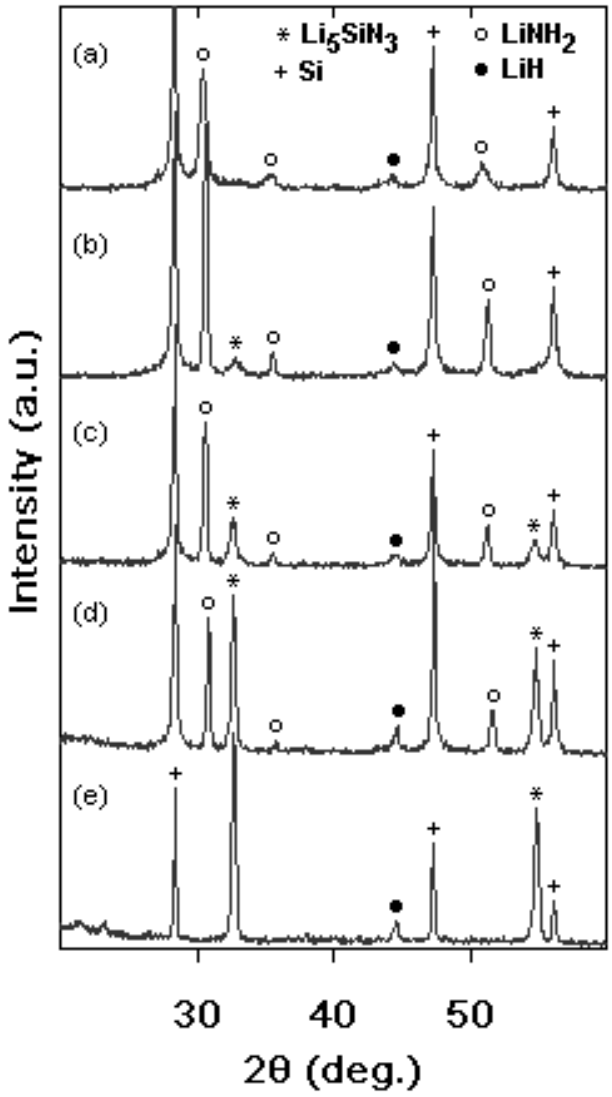

Figure 100 XRD results for $3LiNH_2+2LiH+Si$ heated to various temperatures in vacuum: a) Room temperature after ball-milling, b) 300 °C, c) 450 °C, d) 500 °C, e) 600 °C.

It was attempted to help the reaction proceed faster in two ways:

(a) Pre-mill the Si reactant in order to reduce the particle size. The silicon was milled for 17 hours at 450 rpm and is hereafter denoted Si*.

(b) Doping the sample with $TiCl_3$. 1 mol% was used.

A sample with variation (a) was compared to the normal mixture using TPD, shown in Figure 101.

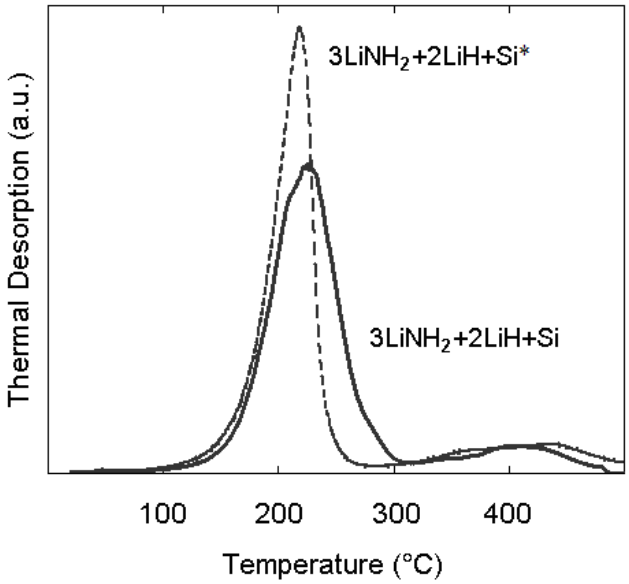

Figure 101 Temperature programmed desorption of $3LiNH_2+2LiH+Si$ and $3LiNH_2+2LiH+Si^*$. The temperature was increased from room temperature to 500 °C at 2 K/min, and a flow of Ar carried the gaseous products to a mass spectrometer. The line shows the detection levels of hydrogen. The recorded levels for ammonia were below the limit of detection.

It can be seen that the smaller particles of silicon do improve the kinetics of the reaction, as a more pronounced peak is observed with completion at about 50 degrees lower under these reaction conditions.

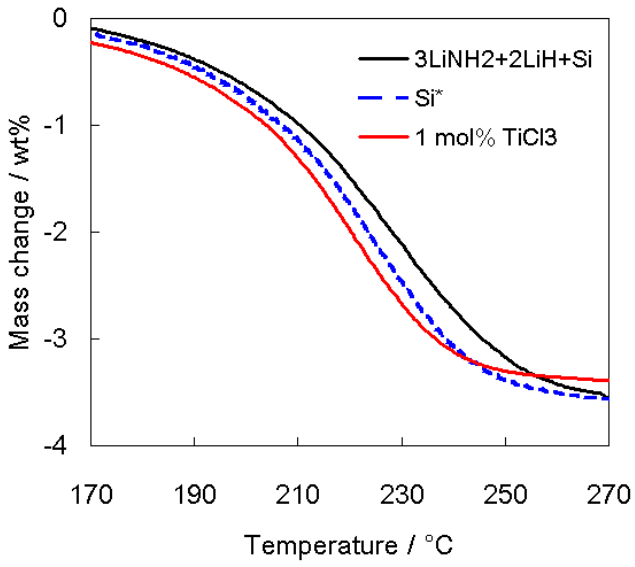

Fig 102 Thermal gravimetric analysis for $3LiNH_2+2LiH+Si$, with variations of pre-milling Si for 17 hours to decrease particle size, and doping with 1 mol% $TiCl_3$. The temperature was increased at a rate of 2 K/min.

The samples were subjected to TGA in the microbalance (described in Chapter 4), see Figure 102. The loss in wt% is about 3.5 for all below 270 °C. Slight improvements in desorption temperatures, up to 10 degrees, are observed for the samples using the variations.

The sample doped with $TiCl_3$ was tested with XRD at various temperature steps, see Figure 103.

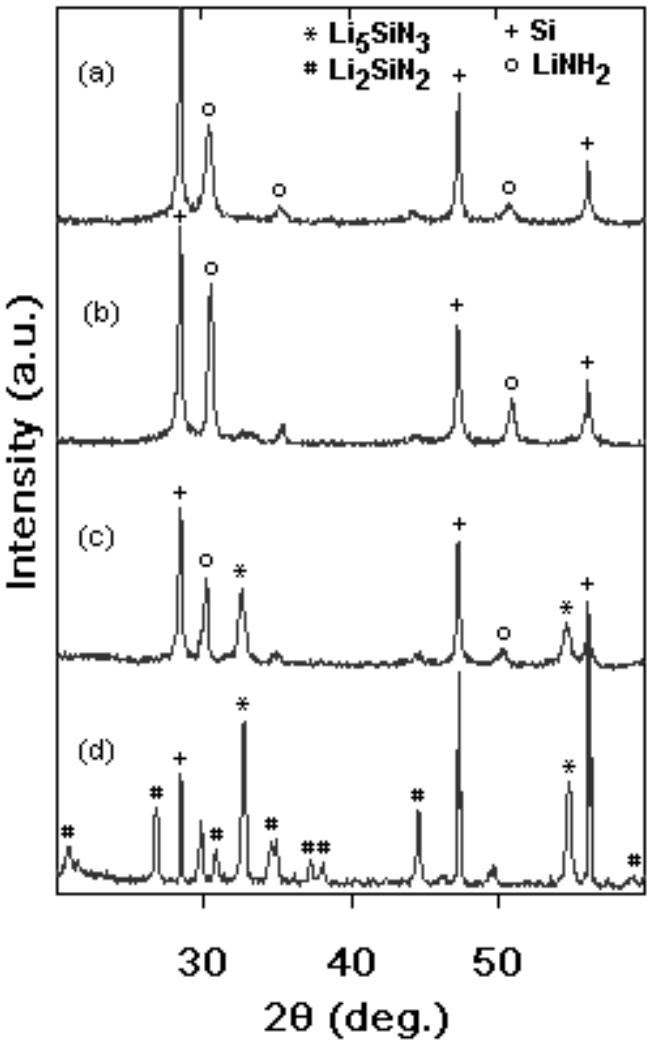

Figure 103 XRD results for $3LiNH_2+2LiH+Si$ doped with 1 mol% $TiCl_3$ heated to various temperatures: a) Room temperature after ball-milling, b) 300 °C, c) 450 °C, d) 600 °C

It is interesting to note here that Li_5SiN_3 is not observed in the XRD pattern until at least 450 °C. Therefore, the desorption seen in Figure 102 does most likely not stem from reaction (45). It is possible instead that the well-known reaction occurs:

$$LiNH_2 + LiH \rightarrow Li_2NH + H_2 \quad (54)$$

In fact, this hydrogen product in this reaction corresponds to 3.5 wt% of the sample mass.

Also, Li_2SiN_2 was formed at 600 °C, which is interesting, since it was not created in the sample without $TiCl_3$ doping. It is unclear why the difference in products occurred.

These experiments with smaller silicon particles and $TiCl_3$ doping point to, that using smaller particles increases the kinetics for the reaction, but not to such a degree, that a big change is taking place. Doping with $TiCl_3$ does not promote the formation of Li_5SiN_3, more the opposite. However, it would seem that perhaps it promotes the formation of Li_2SiN_2.

7.2 Desorption of $LiNH_2$ and Si

In Section 7.1.3, Li_2SiN_2 was seen to be able to take up hydrogen up to 4.8 wt%. As an analogue to Li_5SiN_3, this reaction can be thought to take place:

$$Li_2SiN_2 + 2H_2 \rightarrow 2LiNH_2 + Si \quad (55)$$

In this section reaction (55) is examined from the other direction, i.e. the desorption of hydrogen from lithium amide and silicon, which is proposed as:

$$2LiNH_2 + Si \rightarrow Li_2SiN_2 + 2H_2 \quad (56)$$

for which there is a theoretical 5.4 wt% H_2 desorption.

As it was seen in the experiments described in Section 7.1.4 that $TiCl_3$ seems to be promoting the formation of Li_2SiN_2 so the effect of doping with $TiCl_3$ will also be considered.

7.2.1 Desorption behavior of $2LiNH_2$ + Si and effect of doping with $TiCl_3$

Many samples were experimented upon in order to test the desorption behavior for the system $2LiNH_2$ + Si. Factors such milling speed, milling time and doping level were changed. The pressure inside the milling jar after milling was measured with a calibrated measuring system with pressure gauge and pump (described earlier in Chapter 6).

Interestingly, for many samples doped with $TiCl_3$, a pressure increase was often seen already after the ball milling. As an example, the pressure in the jar for a sample doped with 1 mol% $TiCl_3$ milled for 22 h at 600 rpm was 7 bar. General trends were that higher doping level, longer milling time, and faster milling speed all point to greater desorption (as evidenced by pressure increase in the jar after milling). A standard for which the pressure would not be raised higher than to 2 bar (including the initial 1 bar of Ar during loading) was settled for, so samples could be compared directly to each other. A milling time of 1 hour and a milling speed of 450 rpm became the standard.

Figure 104 shows the mass change measured by the microbalance for different doping levels of $2LiNH_2$ + Si. A reference of $LiNH_2$ is also included. It was considered in Chapter 6, that $LiNH_2$ undergoes decomposition close to 200 °C in vacuum according to:

$$2LiNH_2 \rightarrow Li_2NH + NH_3 \quad (23)$$

wherefore, the mass change for $LiNH_2$ would correspond to desorption of ammonia.

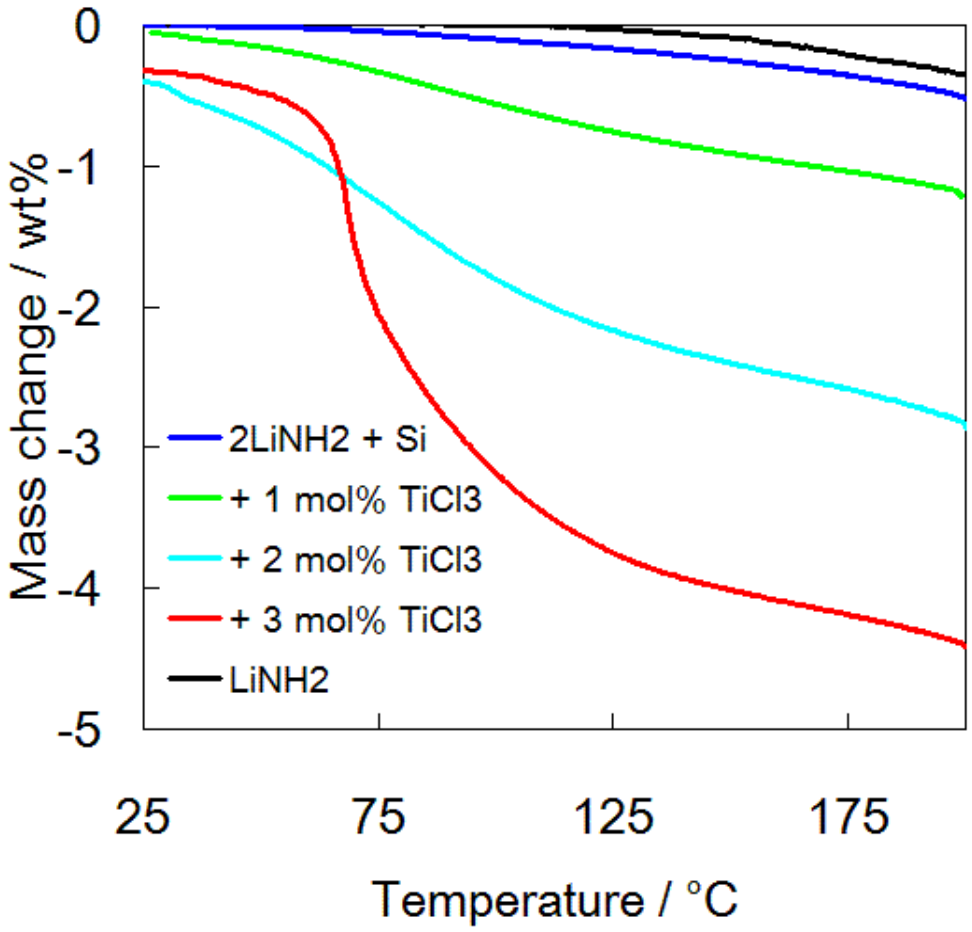

Figure 104 Mass change for samples of $2LiNH_2$ + Si milled for 1 hour at 450 rpm at different doping levels. A reference of $LiNH_2$ is included. The samples were heated at a rate of 2K/min in vacuum. All curves are standardized, i.e. the mass of the dopant is not included in the calculation of wt%, and for $LiNH_2$ the mass change is calculated as the wt% of a $2LiNH_2$ + Si system. The initial drops for the 2 mol% and 3 mol% happened so fast, that they occurred before the heating could be started.

It is seen clearly, that $TiCl_3$ had a great catalyzing effect for the reaction in $2LiNH_2$ + Si. For high doping levels, the desorption happened even more rapidly at room temperature.

It is of great interest to observe, whether the desorption product for these samples was hydrogen or ammonia or a mixture of these.

For the experiments in Figure 104, the temperature was kept steady at 200 °C. For the samples, the curve for the mass change converged into a straight line, and for the higher level doped samples (where the rate was higher), they achieved a mass loss of well over 7 wt%, straight to 19.4 wt%. If the mass loss was from pure ammonia desorption according to (81), a mass loss would be 23 wt%. However, assuming that some of the lithium amide were consumed to produce hydrogen, this mass loss would indeed be less than 23 wt%.

Figure 105 shows the mass change for the samples for the first 20 hours or so.

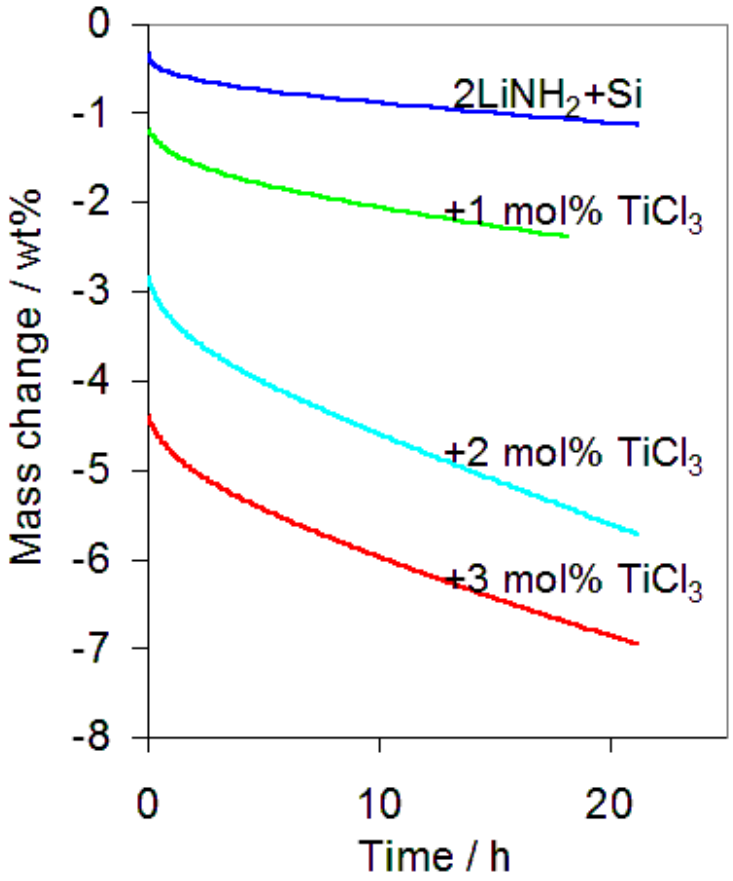

Figure 105 Decomposition of samples of $2LiNH_2$ + Si with different doping levels in vacuum. The temperature was first raised at 2K/min from room temperature to 200 °C (Figure 104) at which point it was kept steady. The access to vacuum was open, so products would be continually removed.

The desorption rates were equal to the slopes of the straight lines that the curves in Figure 105 converge into, and are depicted in Figure 106.

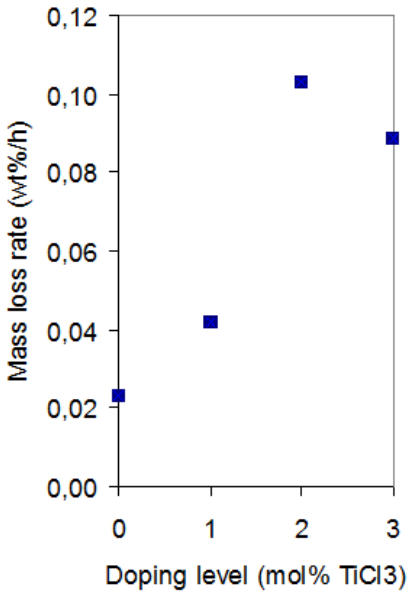

Figure 106 Decomposition rates for $2LiNH_2$ + Si samples at different doping levels of $TiCl_3$ when kept steady at 200 °C in vacuum.

It is seen from this, that 3 mol% $TiCl_3$ did not raise the decomposition rate compared to 2 mol% $TiCl_3$. So from these examined doping levels, it would seem that 2 mol% is best (if interested in NH_3 from this system).

For the 2 mol% system, the rate of decomposition was checked at different temperatures, see Figure 107. From this, it is observed that the rate of decomposition increased with temperature, and that it dropped close to 0 when approaching down to 180 °C. This indicates that there would be no ammonia decomposition below 180 °C, at least not as a result of (23).

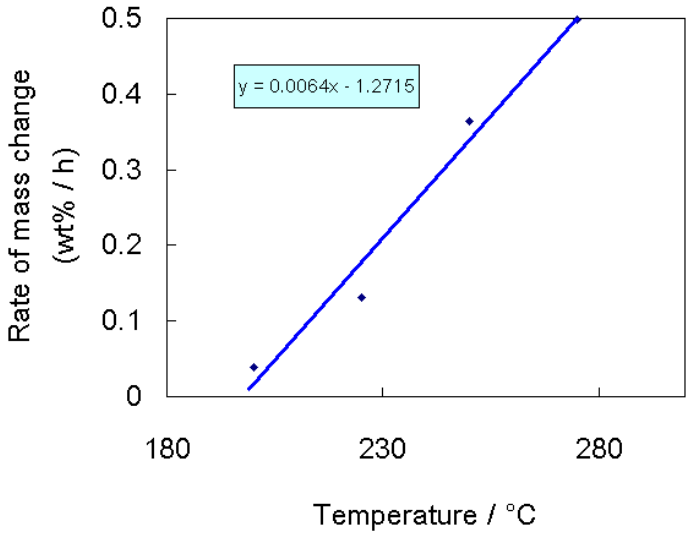

Figure 107 Decomposition rate for $2LiNH_2$ + Si with 2 mol% $TiCl_3$ as a function of temperature in vacuum.

In order to check whether the whole range of mass loss below 180 °C could come from ammonia desorption, the temperature was kept steady at 180 °C after heating up to 180 °C. See Figure 108 for the result.

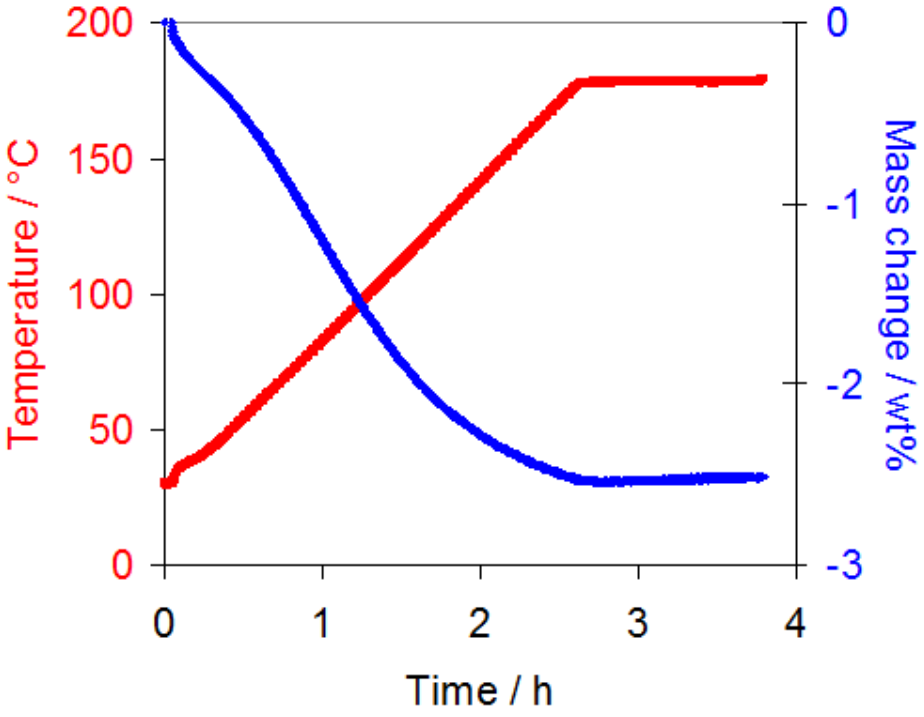

Figure 108 TGA for $2LiNH_2$ + Si with 2 mol% $TiCl_3$ heated at 2K/min and kept steady at 180 °C.

The mass loss stopped, when the temperature reached 180 °C and was kept steady. This means that no ammonia was released at this point, and it seems very improbably that the mass loss occurring as the temperature was raised to 180 °C comes from ammonia. The argument is that there is no reason for the reaction to stop at 180 °C, when much more $LiNH_2$ would be available for decomposition.

The reaction occurring, leading to the mass loss up to 180 °C, also seems to be in equilibrium, at least close to 180 °C, since there was no delay in the mass loss after 180 °C was reached. The reaction had finished at this point.

In order to further verify, whether there was ammonia released during temperatures up to 180 °C, an experimental setup (see Figure 109) was made to allow for TPD combined with a conical flask with distilled water, through which He flow from the TPD would run through. A pH-meter was used in the flask to measure the pH at different points, as the temperature in the reactor tube was increased. By using standardized parameters (flowrate of He, heating rate) for each experiment, the amount of ammonia desorbed from each sample could be compared against each other.

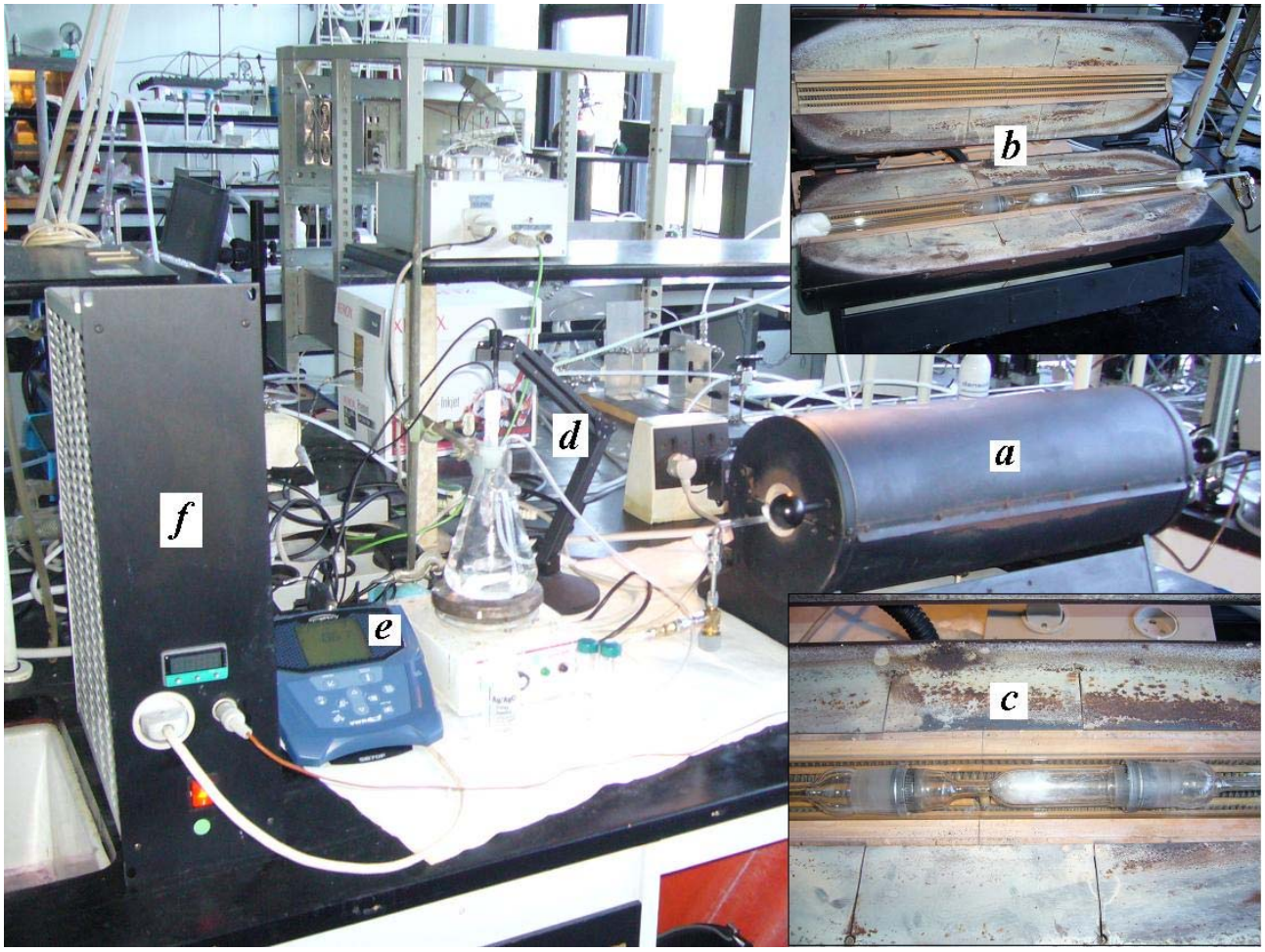

Figure 109 Experimental setup for determining NH_3 desorption profiles of samples: a) Oven, b) quartz tube with reactor inside, c) quartz reactor with graphite tape as gasket in connections, quartz wool for keeping the powder (on top of the wool) from following He flow through tubes, and thermocouple for oven right under the narrow neck of tube, d) conical flask with distilled water on a magnet stirrer and pH electrode in top, e) pH meter, f) temperature controller (CAL 3300) with ramping function.

Figure 110 shows results from TPD of $2LiNH_2$ + Si doped with 2 mol% $TiCl_3$ as well as the undoped system and from $LiNH_2$ as a reference. It is seen that $TiCl_3$ did improve the desorption of ammonia, but not to any large degree. This is appreciated when taken into account the low mass loss of $LiNH_2$ seen in Figure 104 (which occurred even at vacuum conditions). Taken together this means that little mass loss came from ammonia in $2LiNH_2$ + Si doped with 2 mol% $TiCl_3$.

An interesting observation from Figure 110 is that silicon seemed to depress the evolution of ammonia. It is not clear why this is so. There are examples of other stable compounds involving Si, N and H, such as $Si(NH)_2$ which reacts with ammonia to produce $Si(NH_2)_4$. Also, $SiCl_4$ can hold NH_3.[157] It is possible that Si acts in $2LiNH_2$+Si to hold on to NH_3 while the products are formed.

From XRD taken of some of the sample doped with $TiCl_3$ after desorption, no Li_2SiN_2 phases were seen. Phases of $LiNH_2$/Li_2NH and Si were visible.

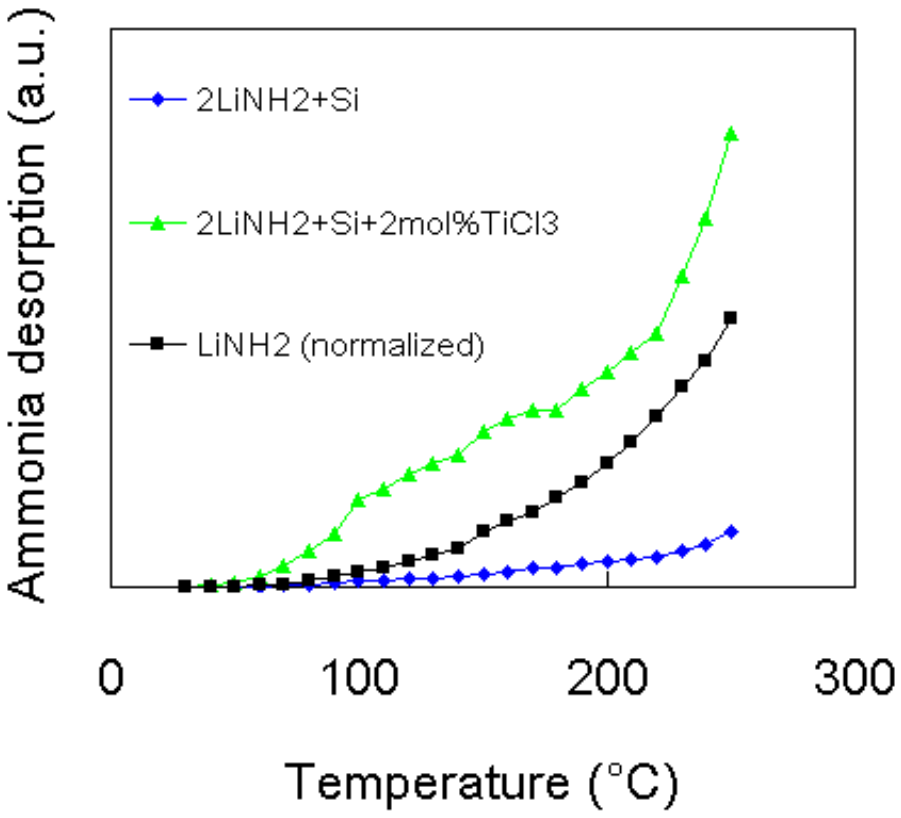

Figure 110 TPD of $2LiNH_2$ + Si, doped and undoped, and of $LiNH_2$ for reference. The curve for $LiNH_2$ is normalized to be directly comparable to the $LiNH_2$ amount in the other two systems. The temperature was increased at a rate of 10 K/min. Helium was used as gas flow. The ammonia desorption was measured by pH in water through which the outlet gas stream flowed.

In conclusion, although the reaction products for $2LiNH_2$ + Si are not fully unresolved, it was shown that hydrogen was desorbed at temperatures up to 180 °C. Ammonia was desorbed at higher temperatures to a large degree. Furthermore, doping with $TiCl_3$, the desorption rates were increased largely, both for hydrogen and for ammonia.

So far, attempts to rehydrogenate the samples have shown no positive results.

8 HYDROGEN STORAGE FROM SOLID AMMONIA STORAGE

In autumn 2005, an invention was given much attention in the media in Denmark.[150] It was named the "hydrogen pill", and it was called out to be the solution to problems of hydrogen storage. Based on the reaction

$$MgCl_2 + 6NH_3 \leftrightarrow Mg(NH_3)_6Cl_2 \quad (57)$$

the proposed solution was, that

1) hydrogen would first be used to produce ammonia,

2) then be stored at ambient conditions in anhydrous magnesium chloride

3) when desired for use it was heated to above 200 °C for the release of ammonia

4) ammonia was cracked at temperatures above 400 °C to attain a H_2/N_2 stream, from which hydrogen could be used.

An advantage of this system was that it offered very desirable low weight (9.1 wt% H_2 in terms of NH_3) and high density (0.11 kg H/L). Furthermore, the system was safe to handle, which is in contrast to the complex hydrides, for instance.

Unfortunately, a drawback was that the energy demands and high temperature for achieving a sufficiently pure H_2/N_2 stream rendered the solution less practical. Another issue was that the apparent safety benefit for working in atmospheric air does not translate when the system is actually in operation. $MgCl_2$ is highly hygroscopic, and even small amounts of water react with $MgCl_2$ when heated to produce hydrochloric acid. This would be a source of a corrosion problem in the system:

$$MgCl_2 \cdot H_2O \rightarrow MgO + 2HCl \quad (58)$$

In this chapter, a novel method of using the material of the "hydrogen" pill to turn it into a proposed real hydrogen pill, i.e. absorbing and releasing actual hydrogen is discussed. Experimental work was performed and preliminary results are given.

8.1 A bridge between ammonia storage and hydrogen storage

In experimental work on the Li-N system it was observed by Ruckenstein and Hu[87] that ammonia reacts exothermically with lithium hydride to produce lithium amide and hydrogen according to

$$LiH + NH_3 \rightarrow LiNH_2 + H_2 \quad (59)$$

In addition, they confirmed that $LiNH_2$ combines reversibly with LiH in an endothermic reaction to produce lithium imide and hydrogen:

$$LiNH_2 + LiH \leftrightarrow Li_2NH + H_2 \quad (60)$$

Under the assumption that reaction (59) is reversible, ammonia herein can function as a link between $MgCl_2$ and LiH, making out a reversible storage system: Ammonia is desorbed from $MgCl_2$ and reacts with LiH, creating $LiNH_2$, which in turn reacts further with LiH. The latter two steps produce hydrogen in the process.

This model should in principle be able to be used with any ammonia containing salt ($CaCl_2$, $CaSO_4$, and many other being examples) combined with a hydride that produces hydrogen upon reaction with ammonia. If the reactants of the system are mixed to such a degree, that there close contact on an atomic level, a combined enthalpy of reaction can be calculated on the basis for each step involved. Table 17 contains 5 systems based on this principle and gives the total enthalpies of reaction for each. These systems are candidates for which results of calculations for a set of systems were made, in that the criteria was that the wt% should be at least above 6 and the enthalpy of reaction should be between +5 and +50 kJ/mol H_2. Reaction 1 was examined experimentally.

Table 17 Proposed reactions (5 overall systems with each 3 intermediate reactions) for hydrogen storage in a combination of ammonia and hydrogen containing compounds

Overall reaction / intermediate reactions	Enthalpy of reaction / kJ/mol H_2	Theoretical wt% of hydrogen	Ref.
1. **$MgCl_2$*6NH_3 + 12LiH ↔ $MgCl_2$ + 6Li_2NH + 12H_2**	**+20.7**	**8.3**	
A. $MgCl_2$*6NH_3 ↔ $MgCl_2$ + 6NH_3	+18.1		*[94, 95, 185]*
B. 6LiH + 6NH_3 ↔ 6$LiNH_2$ + 6H_2	-21.4		
C. 6$LiNH_2$ + 6LiH ↔ 6Li_2NH + 6H_2	+24.0		
2. **$MgCl_2$*6NH_3 + 3MgH_2 + 8LiH ↔ $MgCl_2$ + Mg_3N_2 + 4Li_2NH + 14H_2**	**+6.7**	**8.3**	
A. $MgCl_2$*6NH_3 ↔ $MgCl_2$ + 6NH_3	+15.5		*[121]*
B. 3MgH_2 + 6NH_3 ↔ 3$Mg(NH_2)_2$ + 6H_2	-26.9		
C. 3$Mg(NH_2)_2$ + 8LiH ↔ Mg_3N_2 + 4Li_2NH + 8H_2	+18.1		
3. **$MgCl_2$*6NH_3 + 3MgH_2 + 12LiH ↔ $MgCl_2$ + Mg_3N_2 + 4Li_3N + 18H_2**	**+38.2**	**9.8**	
A. $MgCl_2$*6NH_3 ↔ $MgCl_2$ + 6NH_3	+12.1		*[121, 128]*
B. 3MgH_2 + 6NH_3 ↔ 3$Mg(NH_2)_2$ + 6H_2	-20.9		
C. 3$Mg(NH_2)_2$ + 12LiH ↔ Mg_3N_2 + 4Li_3N + 12H_2	+47.0		
4. **$CaCl_2$*8NH_3 + 16LiH ↔ $CaCl_2$ + 8Li_2NH + 16H_2**	**+16.1**	**8.6**	
A. $CaCl_2$*8NH_3 ↔ $CaCl_2$ + 8NH_3	+13.5		*[94, 95, 185, 186]*
B. 8LiH + 8NH_3 ↔ 8$LiNH_2$ + 8H_2	-21.4		
C. 8$LiNH_2$ + 8LiH ↔ 8Li_2NH + 8H_2	+24.0		
5. **$CaCl_2$*8NH_3 + 4MgH_2 + 16LiH ↔ $CaCl_2$ + 4/3Mg_3N_2 + 16/Li_3N + 24H_2**	**+35.1**	**10.1**	
A. $CaCl_2$*8NH_3 ↔ $CaCl_2$ + 8NH_3	+9.0		*[121, 128, 186]*
B. 4MgH_2 + 8NH_3 ↔ 4$Mg(NH_2)_2$ + 8H_2	-20.9		
C. 4$Mg(NH_2)_2$ + 16LiH ↔ 4/3Mg_3N_2 + 16/3Li_3N + 16H_2	+47.0		

8.1.1 Synthesis of $Mg(NH_3)_6Cl_2$

Magnesium chloride normally comes as the hexahydrate and the typical anhydrous version comes with only 98.0 % purity (not giving the possible content of water). There are two conventional ways of removing water from hydrated metal chloride. One way is to use thionyl chloride using the reaction

$$SOCl_2 + H_2O \rightarrow 2HCl + SO_2 \quad (61)$$

The reaction is performed under inert gas (e.g. nitrogen) in a flask heated to above 150 °C.

The other way is to pass hydrochloric acid in gas form through a reactor with filter while heating to around 450 °C, whereby water is removed. Hereafter, the temperature is increased to above 714 °C, which is the melting point of $MgCl_2$, and the material runs through the filter and down into a ampoule. The ampoule is then sealed, and the material is stored until used.

Both these methods were attempted for magnesium chloride hexahydrate, but they were found to not be as straightforward as believed. Volhard tests for chloride content proved that not all water was removed. Instead, a sample was found in-house reading anhydrous magnesium chloride. XRD showed that it contained single phase magnesium chloride and no hydrated phases, so it was assumed that the material had been successfully been purified earlier in one of the two procedures mentioned.

A sample of $MgCl_2$ was crushed with mortar and pestle in an argon glovebox and transferred to a Schlenk flask. The flask was then transferred to a setup with a vacuum line, see Figure 111. In the figure, flask ‘b’ was evacuated and filled with nitrogen (using the needle in the septum to normalize the pressure to 1 atm), after which the valve to flask ‘e’ with magnesium chloride was opened, allowing nitrogen to flow in. The cap on flask ‘e’ (not shown) was removed and the adaptor with a line to the two safety flasks were plugged in, allowing nitrogen to flow through the whole system and keep under inert conditions. Ammonia was then introduced from a cylinder (through ‘a’). Since ammonia is kept in the cylinder in liquefied form, heat is consumed in the process of delivering NH_3 in gaseous form, which resulted in making all tubes including flask ‘b’ very cold, down below the condensation point of ammonia (-33 °C at 1 atm). Hence flask ‘b’ was used to collect liquefied ammonia.

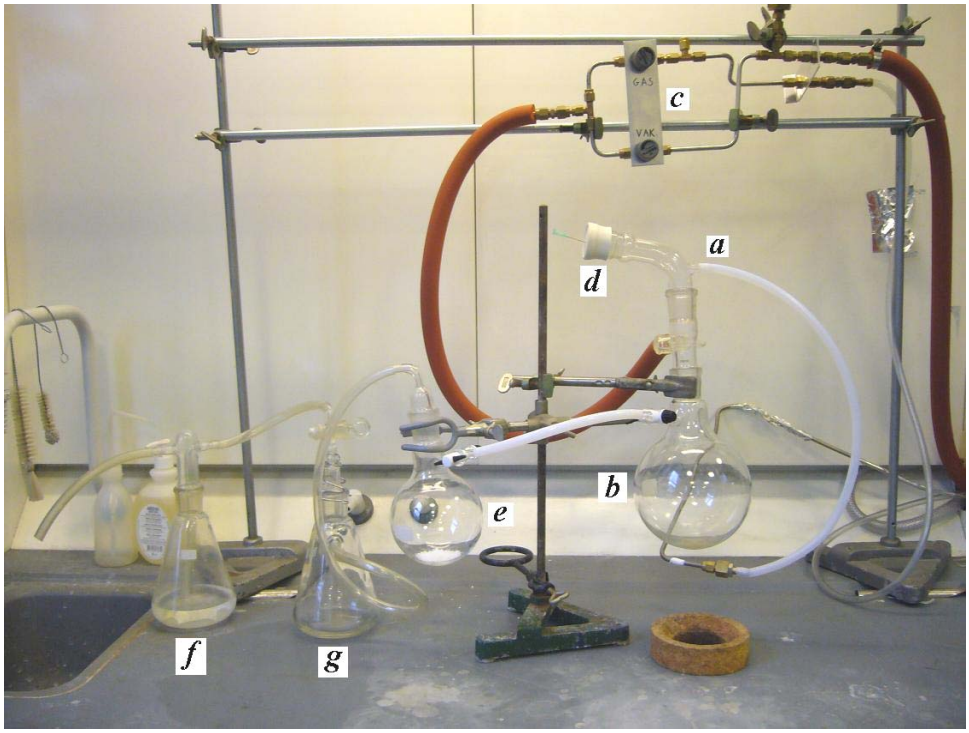

Figure 111 Experimental setup for adding NH_3 gas to a powder ($MgCl_2$ in this instance) at ambient conditions. The annotations are as follows: a) Inlet of ammonia from cylinder, b) flask for collection of liquefied ammonia, c) control for evacuation and inlet of nitrogen, d) septum with needle as pressure relief, e) Schlenk reaction flask with reactant powder, f) safety flask with silicone oil, g) safety flask to secure against backflow of silicone oil in case of under-pressure.

Flask 'e' was periodically capped and weighed to check for progress in the absorption of ammonia to the sample. Figure 112 shows the mass of the powder in terms of equivalents of ammonia added to $MgCl_2$. A little over 2 hours was used to get a 99 % saturation of the sample.

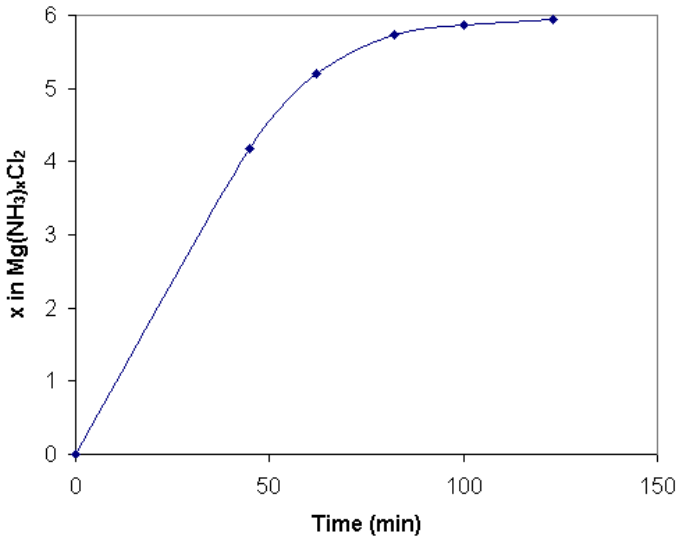

Figure 112 Addition of ammonia to a sample of $MgCl_2$ at 1 atm.

The sample was analyzed by TGA in the microbalance giving the result in Figure 113. The sample started to desorb ammonia already at room temperature when the system was evacuated. Around 70 °C the desorption sped up ending at 125 °C resulting in a total of 4 units of ammonia being desorbed:

$$Mg(NH_3)_6Cl_2 \leftrightarrow Mg(NH_3)_2Cl_2 + 4NH_3 \quad (62)$$

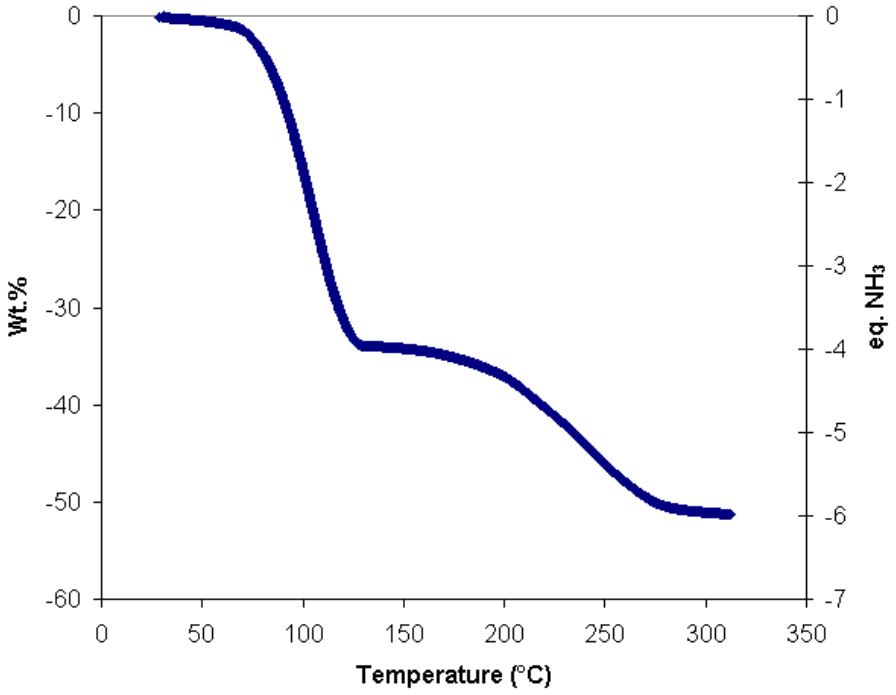

Figure 113 TGA of $Mg(NH_3)_6Cl_2$ in microbalance with a heating rate of 2 K/min. and open vacuum.

Starting at around 150 °C and ending at 300 °C the desorption of the last two units of NH_3 are desorbed fully, corresponding to

$$Mg(NH_3)_2Cl_2 \leftrightarrow MgCl_2 + 2NH_3 \quad (63)$$

Sørensen[184] made TPD on $Mg(NH_3)_6Cl_2$ at 1 bar and found a peak for 4 units at 190 °C, one for a 5th unit at 320 °C, and for the 6th unit at 400 °C. In comparison, using vacuum conditions therefore it was not possible to differentiate between desorption of the 5th and 6th unit.

8.1.2 TGA of $Mg(NH_3)_6Cl_2$ + 12LiH

A sample of $Mg(NH_3)_6Cl_2$ was mixed with 12 equivalents of LiH by mortar and pestle for 10 minutes in an argon glovebox. TGA in the microbalance gives the result shown in Figure 114.

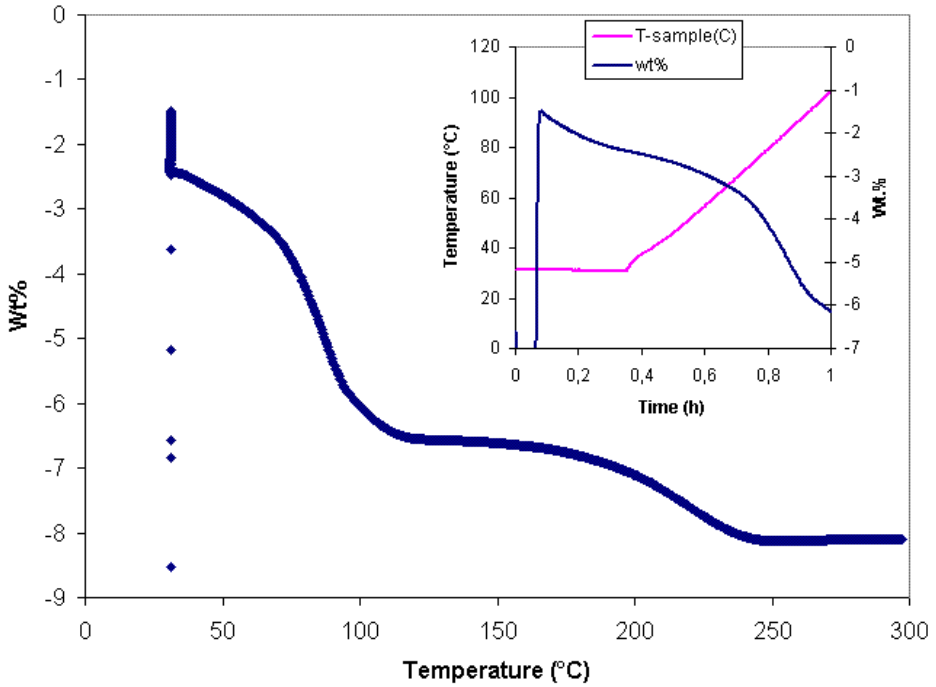

Figure 114 TGA of $Mg(NH_3)_6Cl_2$ + 12LiH in microbalance under open vacuum. The heating rate was 2 K/min. In the beginning of the measurement, the microbalance was initializing for 5 minutes (giving the false points between -9 and -3 wt% shown). The inset gives the mass loss as a function of time, showing that a significant desorption occurred at room temperature.

It is seen that desorption occurred already at room temperature under vacuum condition unlike for $Mg(NH_3)_6Cl_2$ alone. This is an indication that a chemical reaction was going on, most likely NH_3 reacting with LiH, producing H_2. The temperature was not seen rising at this point, which could also indicate that the heat developed by this reaction was consumed in releasing more NH_3 and possibly driving a reaction of $LiNH_2 + LiH \rightarrow Li_2NH + H_2$.

6.5 wt% was released up to 120 °C and another 1.6 wt% to a total of 8.1 wt% was released between 130 and 250 °C. The first step corresponds to ~80 % of the total and the second step to ~20 %.

The similarity of the curvatures of the curves in Figure 113 and 114 leads to assume that the release of ammonia directly led to going through all steps of the intermediate reactions, including $LiNH_2 + LiH \rightarrow Li_2NH + H_2$, which was simply driven by the heat released in $NH_3 + LiH \rightarrow LiNH_2 + H_2$. It would thus seem that 5 units of NH_3 (equivalent to 83 %) was released under 120 °C and the last unit was released up to 250 °C.

It has thus been shown that the 3 reactions can occur as one at rather low temperature, making the proposed model for bridging ammonia and hydrogen storage systems an interesting venue for research.

It would seem that there is a potential for much research among the lines of the model systems proposed.

9 CONCLUSION AND OUTLOOK

This thesis has focused on experimental work with especially complex hydrides containing nitrogen. An overview of current hydrogen storage techniques and "traditional" hydrogen storage in alloys, in which hydrogen is stored in interstitial sites in the metal lattice were given. Also, a broad and detailed overview over the current research within complex hydrides, especially those containing nitrogen (involved as ammonia, amide or imide) was also given.

For the examination of hydrogen storage properties of complex hydrides specialized equipment is needed, since most of these materials are susceptible to reaction with the atmosphere. Therefore, analytical equipment normally used in air or even made for fast sample transfers, are not applicable. Often, equipment has to be rebuilt or bought especially for the purpose of doing research on development on hydrogen storage materials.

In the line of this thinking, a specialized piece of facility was constructed and described in the present work. A high pressure microbalance with all needed auxiliary units was made in a glovebox, permitting samples to be transferred without being exposed to air at any time. $CaNi_5$, being a well-described hydrogen storage alloy and easy to activate, was used as a test alloy, in which the microbalance was shown to function well and according to its purpose.

Experimental work was done on 3 new systems, as follows.

9.1 Li-Al-N-H system

This system is called new, since the system was not described in the literature at the start of research on this system in connection with this work. However, work was done from an undescribed angle, using Li_3AlN_2 as a starting material and characterizing it for hydrogen storage. The material was successfully synthesized using ball milling of Li_3N and Al under moderate nitrogen pressure. As for hydrogen storage, the material was shown to be able to store a maximum of ~2 wt% under limit conditions of 70 bar and 300 °C. About 1 wt% was reversible, which confirms that Li_3AlN_2 can store hydrogen reversibly. As for practicality, this material however fails badly in terms of weight capacity, kinetics, and decomposition with ammonia desorption.

9.2 Li-Si-N-H systems

Samples of Li_5SiN_3 were successfully synthesized using 2 different reaction ways: 1) Ball milling of Li_3N with Si under nitrogen pressure, and 2) Ball milling Li_3N with Si_3N_4. For (1) a seemingly amorphous phase was observed, which could not be removed by calcinating the sample at temperatures up to 800 °C . Up to ~4 wt% hydrogen was observed to be taken up by this material, and about 2.5 wt% could be dehydrogenated afterwards. Detailed XRD analysis for steps at various temperatures confirmed that the material reacts reversibly with hydrogen, although its full reaction

mechanism was not resolved. This stemmed in part, it is believed, from the fact that the kinetics are slow and a long time must proceed for the reaction to go to completion.

Li_2SiN_2 was seen to be able to absorb up to ~5 wt%. Furthermore, the system $2LiNH_2$ + Si was examined with regard to desorption behavior. This system was seen to be able to desorb more than 4 wt% when doped with 3 mol% $TiCl_3$. Increasing the level of doping increased the amount desorbed. At temperatures above 180 °C, ammonia was released according to the decomposition reaction of $LiNH_2$ into Li_2NH and NH_3. Reversibility was not observed. Nevertheless, this system remains an interesting example of how doping with $TiCl_3$ can greatly catalyze reactions among the complex hydrides materials as was the case for $NaAlH_4$.

9.3 $Mg(NH_3)_6Cl_2$ + 12LiH

Five systems were proposed based on results in the literature from two "worlds": Those of storage of hydrogen in complex hydrides and those of storage of hydrogen in the form of ammonia in magnesium chloride. By using ammonia as the link and calculating combined enthalpies for subreactions for these systems, promising numbers for theoretical wt% hydrogen and enthalpy of reaction was attained to.

Preliminary experiments on one of these systems, mentioned above, showed desorption at low temperatures in amounts corresponding to the theory, indicating that these systems hold much promise for future research.

9.4 Outlook

It was found in the work for this thesis that Li_3AlN_2 from a practical standpoint would seem to be a poor hydrogen storage material. The hydrogen storage capacity is low under 300 °C, and there is the problem of desorption of ammonia. The results for the Li-Si-N-H systems, however, were surprisingly good as these new materials was shown to be able to store hydrogen in rather large weight capacities and reversibly. The large desorption amounts of catalyzed $2LiNH_2$+Si were furthermore unexpected, and proved to be an interesting avenue for further research—this includes determining the nature of the way $TiCl_3$ interacts with the species involved to produce this improvement in kinetics. This is an issue that has been investigated much for $NaAlH_4$, yet has eluded to be understood. $TiCl_3$-catalyzed $2LiNH_2$+Si is the only other system to the knowledge of this researcher, that improved the kinetics to this large degree, and it is therefore an obvious subject for further research.

The proposed systems for combining solid ammonia storage with Li/Mg-N-H systems also seem to hold much promise. Many more variations are possible, in that there exists a large range of salts that absorb ammonia reversibly, and that they can be combined with a variety of amide-containing systems. The thermodynamics for the reaction of many metal chlorides with ammonia is well-described by Lepinasse and Spinner[186] and can serve as a source for values from which to calculate the enthalpy of reaction for a combined hydrogen storage system. As a further example for the versatility, this modeling brings, is that it is known that $LiBH_4$ can absorb ammonia.[157] Therefore,

$LiBH_4$ (and perhaps other metal borohydrides) could perhaps serve as the carrier for ammonia instead of $MgCl_2$. There is ample opportunity to tailor systems that reach desired values of enthalpy of reaction and weight capacity.

10 REFERENCES

[1] Official website for the White House, USA, <http://www.whitehouse.gov/news/releases/2003/01/20030128-19.html>, visited in November 2008

[2] Official website for the Department of Energy, USA, <http://www.energy.gov/news/1793.htm>, visited in November 2008

[3] *Hydrogen posture plan—an integrated research, development, and demonstration plan*, Department of Energy, USA, Feb. 2004

[4] G.A. Olah, A.Goeppert, G.K.S. Prakash, *Beyond Oil and Gas: The Methanol Economy*, Wiley-VCH (2006)

[5] J. Rifkin, *The Hydrogen Economy,* Penguin (2003)

[6] L. Schlapbach, A. Züttel, *Hydrogen-storage materials for mobile applications*, Nature 414 (2001) 353-358

[7] M.F. Ashby, D.R.H. Jones, *Engineering Materials 1—An introduction to their properties & applications*, 2nd edition, Butterworth-Heinemann (1996)

[8] U. Bossel, B. Eliasson, G. Taylor, *The future of the Hydrogen Economy: Bright or Bleak?*, *Fuel Cell Seminar* (2003)

[9] R.H. Perry, D.W. Green, *Perry's Chemical Engineers' Handbook*, McGraw-Hill (1984)

[10] P. Atkins, J. de Paula, *Physical Chemistry*, 7th edition, Oxford University Press (2002)

[11] F. Schüth, B. Bogdanovic, M. Felderhoff, *Light metal hydrides and complex hydrides for hydrogen storage*, Chem. Commun. (2004) 2249-2258

[12] J. Larmine, A. Dicks, *Fuel Cell System Explained*, 2nd edition, John Wiley & Sons Ltd (2003)

[13] G. Sandrock, *A panoramic overview of hydrogen storage alloys from a gas reaction point of view*, J. Alloys Comp. 293-295 (1999) 877-888

[14] J.O. Jensen, Q. Li, C. Pan, A.P. Vestbø, K. Mortensen, H.N. Petersen, C.L. Sørensen, T.N. Clausen, J. Schramm, N.J. Bjerrum, *High temperature PEMFC and the possible utilization of the excess heat for fuel processing*, Int. J. Hydrogen Energy 32 (2007) 1567-1571

[15] J.O. Jensen, Q. Li, R. He, C. Pan, N.J. Bjerrum, *100-200 °C polymer fuel cells for use with $NaAlH_4$*, J. Alloys Comp. 404-406 (2005) 653-656

[16] M. Martin, C. Gommel, C. Borkhart, E. Fromm, *Absorption and desorption kinetics of hydrogen storage alloys*, J. Alloys Comp. 238 (1996) 193-201

[17] F. Schweppe, M. Martin, E. Fromm, *Model on hydride formation describing surface control, diffusion control and transition regions*, J. Alloys Comp. 261 (1997) 254-258

[18] G.D. Sandrock, J.J. Murray, M.L. Post, J.B.Taylor, *Hydrides and deuterides of $CaNi_5$*, Mater. Res. Bull. 17 (1982) 887-894

[19] M.P.S. Kumar, *Interaction of carbon monoxide with the hydrogen storage alloy, $CaNi_5$—kinetic and surface studies*, React. Solid. 7 (1989) 157-166

[20] P. Selvam B. Viswanathan, V. Srinivasan, *Evidence for the formation of surface carbonates on some hydrogen storage intermetallic compounds: an XPS study*, J. Hydrogen Energy 15 (1990) 133-137

[21] M. Notin, D. Belbacha, M.Rahmane, J. Hertz, *Experimental diagram and numerical optimization of the Ca-Ni system*, J. Less-Common Met. 162 (1990) 221-229

[22] D. Uremovich, F. Islam, M. Medraj, *Thermodynamic modeling of the Ca-Ni system*, Sci. Technol. Adv. Mater. 7 (2006) 119-126

[23] P. Selvam, B. Viswanathan, V. Srinivasan, *Some comments on modes of activation of $LaNi_5$ and $CaNi_5$ alloys for hydrogen storage*, Int. J. Hydrogen Energy 14 (1989) 687-689

[24] Y.K. Cho, R. Yamamoto, M. Doyama, S. Ono, K. Imanari, T. Tabata, *The phase transformations of $CaNi_5$ in a hydrogen atmosphere*, J. Less-Common Met. 88 (1982) 125-131

[25] L.D. Calvert, J.J. Murray, G.J. Gainsford, J.B. Taylor, *Crystal structure of $CaNi_5H$ using x-ray diffraction with in situ hydriding*, Mat. Res. Bull. 19 (1984) 107-113

[26] A. Yoshikawa, Y. Uyenishi, H. Iizumi, T. Matsumoto, N. Takano, F. Terasaki, *Determination of the position and occupancy of deuterium in $CaNi_5$ deuterides by neutron diffraction*, J. Alloys Comp. 280 (1998) 204-208

[27] J.J. Murray, M.L. Post, J.B. Taylor, *The thermodynamics of the system $CaNi_5$-H_2 using differential heat conduction calorimetry*, J. Less-Common Met. 90 (1983) 65-73

[28] M.L. Post, J.J. Murray, J.B. Taylor, *Metal hydride studies at the National Research Council of Canada*, Int. J. Hydrogen Energy 9 (1984) 137-145

[29] K. Yagisawa, A. Yoshikawa, T. Matsumoto, *Thermodynamic analysis of absorption pressure-composition isotherms of $CaNi_5H_x$ and $CaNi_5D_x$ (x = 0-1.1)*, J. Less-Common Met. 99 (1984) 205-213

[30] J.J. Murray, D.M. Grant, E. Akiba, M.L Post, *The gamma phase of $CaNi_5$+H_2*, Mat. Res. Bull. 21 (1986) 515-521

[31] L.G.I. Bennett, S.D. Arguner, J.S. Hewitt, *Investigation of hydriding processes in low-temperature/low-pressure metal hydrides*, Int. J. Hydrogen Energy 11 (1986) 577-582

[32] S. Langer, *Master's Thesis,* (2008)

[33] M.P.S. Kumar, B. Viswanathan, C.S. Swamy, V. Srinivasan, *High temperature interaction of hydrogen with intermetallic compound $CaNi_5$*, Mater. Chem. Phys. 20 (1988) 245-253

[34] K.S. Nahm, W.B. Jung, W.Y. Lee, *The reaction kinetics of hydrogen storage in $CaNi_5$*, Int. J. Hydrogen Energy 15 (1990) 635-640

[35] J. Murray, H. Miller, P. Bird, A.J. Goudy, *The effect of particle size and surface composition on the reaction rates of some hydrogen storage alloys*, J. Alloys Comp. 231 (1995) 841-845

[36] Z.P. Li, S. Suda, *The annealing effect on the durabilities of La-substituted $CaNi_5$-type alloys*, J. Alloys Comp. 231 (1995) 835-840

[37] X. Shan, J.H. Payer, J.S. Wainright, *Increased performance of hydrogen storage by Pd-treated $LaNi_{4.7}Al_{0.3}$, $CaNi_5$ and Mg_2Ni*, J. Alloys Comp. 426 (2006) 400-407

[38] X. Shan, J.H. Payer, J.S. Wainright, *Improved durability of hydrogen storage alloys*, J. Alloys Comp. 430 (2006) 262-268

[39] M.S. Bawa, E.A. Ziem, *Long-term testing and stability of $CaNi_5$ alloy for a hydrogen storage application*, Int. J. Hydrogen Energy 7 (1982) 775-781

[40] P.D. Goodell, *Stability of rechargeable hydriding alloys during extended cycling*, J. Less-Common Met. 99 (1984) 1-14

[41] Z.P. Li, S. Suda, *Electrochemical durability of Ca-based alloys*, Eletrochim. Acta 40 (1995) 467-471

[42] J.O. Jensen, T.S. Møller, N.J. Bjerrum, *Stability of $CaNi_5H_x$ stored at temperatures between 20 and 150 °C*, J. Alloys Comp. 330-332 (2002) 215-218

[43] M.P. Pitt, H.W. Brinks, J.O. Jensen, B.C. Hauback, *An in-situ neutron diffraction study of the ageing of $CaNi_5D_x$ at 80 °C and 9 bar*, J. Alloys Comp. 372 (2004) 190-196

[44] G. Liang, R. Schulz, *Phase structures and hydrogen storage properties of Ca-Mg-Ni alloys prepared by mechanical alloying*, J. Alloys Comp. 356-357 (2003) 612-614

[45] E.Y. Lee, K.S. Jung, K.S. Lee, *Synthesis of composite Mg-Ni-Ca metal hydride by mechanical alloying*, J. Alloys Comp. 446-447 (2007) 129-133

[46] D. Liu, X. Liu, Y. Zhu, L. Li, *Hydriding combustion synthesis of Mg-$CaNi_5$ composites*, J. Alloys Comp. 458 (2008) 394-397

[47] J.O. Jensen, N.J. Bjerrum, *Systematic B-metal substitution in $CaNi_5$*, J. Alloys Comp. 293-295 (1999) 185-189

[48] J. Shinar, D. Shaltiel, D. Davidov, A. Grayevsky, *Hydrogen sorption properties of the $La_{1-x}Ca_xNi_5$ and $La(Ni_{1-x}Cu_x)_5$ systems*, J. Less-Common Met. 60 (1978) 209-219

[49] X.-L. Wang, H. Hagiwara, S. Suda, *Surface properties of the fluorinated calcium-based AB_5 alloys*, J. Alloys Comp. 231 (1995) 376-379

[50] Z.P. Li, S. Suda, *Effects of hydriding-dehydriding cycling on* P-C-T *and electrochemical properties of La-Ca-Ni-Al alloys*, J. Alloys Comp. 231 (1995) 594-597

[51] Z.P. Li, S. Suda, *A new family of hydride electrode materials based on $CaNi_5$-type alloys*, J. Alloys Comp. 231 (1995) 751-754

[52] Z.P. Li, T. Matsuoka, S. Suda, *An investigation of Ca-based hydride electrode materials*, Vacuum 47 (1996) 893-897

[53] G. Liang, J. Huot, R. Schulz, *Mechanical alloying and hydrogen storage properties of $CaNi_5$-based alloys*, J. Alloys Comp. 321 (2001) 146-150

[54] E. Tuscher, P. Weinzierl, O.J. Eder, *Porous metal hydride compacts: preparation, properties and use*, Int. J. Hydrogen Energy 8 (1983) 199-203

[55] I. Yonezu, K. Nasako, N. Honda, T. Sakai, *Development of thermal energy storage technology using metal hydrides*, J. Less-Common Mat. 89 (1983) 351-358

[56] H. Imai, T. Tagawa, M. Kuraishi, *Acceleration effect of hydrogen storage alloys for the catalytic dehydrogenation of cyclohexane*, Mat. Res. Bull. 20 (1985) 511-516

[57] H. Imamura, T. Tanaka, Y. Sakata, S. Tsuchiva, *Catalytic transfer hydrogenation on a hydrogen-absorbing alloy ($CaNi_5$) using hydriding-dehydriding properties*, Catal. Lett. 56 (1998) 65-67

[58] B. Bogdanovic, M. Schwickardi, *Ti-doped alkali metal aluminium hydrides as potential novel reversible hydrogen storage materials*, J. Alloys Comp. 253-254 (1997) 1-9

[59] B. Bogdanovic, R.A. Brand, A. Marjanovic, M. Schwickardi, J. Tölle, *Metal-doped sodium aluminium hydrides as potential new hydrogen storage materials*, J. Alloys Comp. 302 (2000) 36-58

[60] K.J. Gross, G.J. Thomas, C.M. Jensen, *Catalyzed alanates for hydrogen storage*, J. Alloys Comp. 330-332 (2002) 683-690

[61] D.L. Anton, *Hydrogen desorption kinetics in transition metal modified $NaAlH_4$*, J. Alloys Comp. 356-357 (2003) 400-404

[62] A. Zaluska, L. Zaluski, J.O. Ström-Olsen, *Sodium alanates for reversible hydrogen storage*, J. Alloys Comp. 298 (2000) 125-134

[63] G. Sandrock, K. Gross, G. Thomas, C. Jensen, D. Meeker, S. Takara, *Engineering considerations in the use of catalyzed sodium alanates for hydrogen storage*, J. Alloys Comp. 330-332 (2002) 696-701

[64] V.P. Balena, J.W. Wiench, K.W. Dennis, M. Pruski, V.K. Pecharsky, *Titanium catalyzed solid-state transformation in $LiAlH_4$ during high-energy ball-milling*, J. Alloys Comp. 329 (2001) 108-114

[65] J. Chen, N. Kuriyama, Q. Xu, H.T. Takeshita, T. Sakai, *Reversible hydrogen storage via titanium-catalyzed $LiAlH_4$ and Li_3AlH_6*, J. Phys. Chem. B 105 (2001) 11214-11220

[66] D. Blanchard, H.W. Brinks, B.C. Hauback, P. Norby, *Desorption of $LiAlH_4$ with Ti- and V-based additives*, Mater. Sci. Eng. B 108 (2004) 54-59

[67] D.S. Easton, J.H. Schneibel, S.A. Speakman, *Factors affecting hydrogen release from lithium alanate ($LiAlH_4$)*, J. Alloys Comp. 398 (2005) 245-248

[68] O.M. Løvvik, *Adsorption of Ti on $LiAlH_4$ surfaces studied by band structure calculations*, J. Alloys Comp. 373 (2004) 28-32

[69] M. Resan, M.D. Hampton, J.K. Lomness, D.K. Slattery, *Effects of various catalysts on hydrogen release and uptake characteristics of $LiAlH_4$*, Int. J. Hydrogen Energy 30 (2005) 1413-1416

[70] A. Andreasen, T. Vegge, A.S. Pedersen, *Dehydrogenation kinetics of as-received and ball-milled $LiAlH_4$*, J. Solid State Chem. 178 (2005) 3672-3678

[71] J.-W. Jang, J.-H. Shim, Y.W. Cho, B.-J. Lee, *Thermodynamic calculation of $LiH \leftrightarrow Li_3AlH_6 \leftrightarrow LiAlH_4$ reactions*, J. Alloys Comp. 420 (2006) 286-290

[72] Y. Suttisawat, P. Rangsunvigit, B. Kitiyanan, N. Muangsin, S. Kulprathipanja, *Catalytic effect of Zr and Hf on hydrogen desorption/absorption of $NaAlH_4$ and $LiAlH_4$*, Int. J. Hydrogen Energy 32 (2007) 1277-1285

[73] M. Fichtner, O. Fuhr, *Synthesis and structures of magnesium alanate and two solvent adducts*, J. Alloys Comp. 345 (2002) 286-296

[74] M. Fichtner, J. Engel, O. Fuhr, A. Glöss, O. Rubner, R. Ahlrichs, *The structure of magnesium alanate*, Inorg. Chem. 42 (2003) 7060-7066

[75] M. Fichtner, O. Fuhr, O. Kircher, *Magnesium alanate—a material for reversible hydrogen storage?*, J. Alloys Comp. 356-357 (2003) 418-422

[76] R.A. Varin, C. Chiu, T. Czujko, Z. Wronski, *Mechano-chemical activation synthesis (MCAS) of nanocrystalline magnesium alanate hydride [$Mg(AlH_4)_2$] and its hydrogen desorption properties*, J. Alloys Comp. 439 (2007) 302-311

[77] M.S.L. Hudson, D. Pukazhselvan, G.I. Sheeja, O.N. Srivastava, *Studies on synthesis and dehydrogenation behavior of magnesium alanate and magnesium-sodium alanate mixture*, Int. J. Hydrogen Energy 32 (2007) 4933-4938

[78] M. Fichtner, C. Frommen, O. Fuhr, *Synthesis and properties of calcium alanate and two solvent adducts*, Inorg. Chem. 44 (2005) 3479-3484

[79] O.M. Lövvik, *Crystal structure of $Ca(AlH_4)_2$ predicted from density-functional band-structure calculations*, Phys. Review B 71 (2005) 144111: 1-5

[80] C. Wolverton, V. Ozolins, *Hydrogen storage in calcium alanate: First-principles thermodynamics and crystal structures*, Phys. Review B 75 (2007) 64101: 1-15

[81] H. Kabbour, C.C. Ahn, S.-J. Hwang, R.C. Bowman, Jr., J. Graetz, *Direct synthesis and NMR characterization of calcium alanate*, J. Alloys Comp. 446-447 (2007) 264-266

[82] P. Chen, Z. Xiong, J. Luo, J. Lin, K.L. Tan, *Interaction of hydrogen with metal nitrides and imides*, Nature 420 (2002) 302-304

[83] S.-I. Orimo, Y. Nakamori, J.R. Eliseo, A. Züttel, C.M. Jensen, *Complex hydrides for hydrogen storage*, Chem. Rev. 107 (2007) 4111-4132

[84] R. Juza, *Amides of the alkali and the alkaline earth metals*, Z. Anorg. Allg. Chem. 231 (1937) 121-135

[85] Y. Nakamori, S. Orimo, *Li-N based hydrogen storage materials*, Mater. Sci. Eng. B 108 (2004) 48-50

[86] G.P. Meisner, F.E. Pinkerton, M.S. Meyer, M.P. Balogh, M.D. Kundrat, *Study of the lithium-nitrogen-hydrogen system*, J. Alloys Comp. 404-406 (2005) 24-26

[87] Y.H. Hu, W. Ruckenstein, *Ultrafast reaction between LiH and NH_3 during H_2 storage in Li_3N*, J. Phys. Chem. *A* 107 (2003) 9737-9739

[88] Y.H. Hu, E. Ruckenstein, *H_2 storage in Li_3N. Temperature-programmed hydrogenation and dehydrogenation*, Ind. Eng. Chem. Res. 42 (2003) 5135-5139

[89] Y.H. Hu, E. Ruckenstein, *Highly effective Li_2O/Li_3N with ultrafast kinetics for H_2 storage*, Ind. Eng. Chem. Res. 43 (2004) 2464-2467

[90] Y.H. Hu, N.Y. Yu, E. Ruckenstein, *Effect of the heat pretreatment of Li_3N on its H_2 storage performance*, Ind. Eng. Chem. Res. 43 (2004) 4174-4177

[91] Y.H. Hu, E. Ruckenstein, *High reversible-hydrogen storage capacity with ultrafast kinetics of $LiNH_2/Li_3N$*, Ind. Eng. Chem. Res. 44 (2005) 1510-1513

[92] W. Luo, E. Rönnebro, *Towards a viable hydrogen storage system for transportation application*, J. Alloys Comp. 404-406 (2005) 392-395

[93] P. Chen, Z. Xiong, J. Luo, J. Lin, K.L. Tan, *Interaction between lithium amide and lithium hydride*, J. Phys. Chem. B 107 (2003) 10967-10970

[94] T. Ichikawa, S. Isobe, N. Hanada, H. Fujii, *Lithium nitride for reversible hydrogen storage*, J. Alloys Comp. 365 (2004) 271-276

[95] T. Ichikawa, N. Hanada, S. Isobe, H. Leng, H. Fujii, *Mechanism of novel reaction from $LiNH_2$ and LiH to Li_2NH and H_2 as a promising hydrogen storage system*, J. Phys. Chem. B 108 (2004) 7887-7892

[96] S. Isobe, T. Ichikawa, N. Hanada, H.Y. Leng, M. Fichtner, O. Fuhr, H. Fujii, *Effect of Ti catalyst with different chemical form on Li-N-H hydrogen storage properties*, J. Alloys Comp. 404-406 (2005) 439-442

[97] T. Ichikawa, N. Hanada, S. Isobe, H.Y. Leng, H. Fujii, *Hydrogen storage properties in Ti catalyzed Li-N-H system*, J. Alloys Comp. 404-406 (2005) 435-438

[98] S. Isobe, T. Ichikawa, S. Hino, H. Fujii, *Hydrogen desorption mechanism in a Li-N-H system by means of the isotopic exchange technique*, J. Phys. Chem. B 109 (2005) 14855-14858

[99] S. Isobe, T. Ichikawa, Y. Kojima, H. Fujii, *Characterization of titanium based catalysts in the Li-N-H hydrogen storage system by X-ray absorption spectroscopy*, J. Alloys Comp. 446-447 (2007) 360-362

[100] S. Isobe, T. Ichikawa, H. Leng, H. Fujii, Y. Kojima, *Hydrogen desorption processes in Li-Mg-N-H systems*, J. Phys. Chem. Solids 69 (2008) 2234-2236

[101] W. Luo, *$(LiNH_2$-$MgH_2)$: a viable hydrogen storage system*, J. Alloys Comp. 381 (2004) 284-287

[102] M. Aoki, T. Noritake, Y. Nakamori, S. Towata, S. Orimo, *Dehydriding and rehydriding properties of $Mg(NH_2)_2$-LiH systems*, J. Alloys Comp. 446-447 (2007) 328-331

[103] W. Luo, J. Wang, K. Stewart, M. Clift, K. Gross, *Li-Mg-N-H: Recent investigations and development*, J. Alloys Comp. 446-447 (2007) 336-341

[104] W. Luo, S. Sickafoose, *Thermodynamic and structural characterization of the Mg-Li-N-H hydrogen storage system*, J. Alloys Comp. 407 (2006) 274-281

[105] W. Lohstroh, M. Fichtner, *Reaction steps in the Li-Mg-N-H hydrogen storage system*, J. Alloys Comp. 446-447 (2007) 332-335

[106] Z. Xiong, J. Hu, G. Wu, P. Chen, W. Luo, K. Gross, J. Wang, *Thermodynamic and kinetic investigations of the hydrogen storage in the Li-Mg-N-H system*, J. Alloys Comp. 398 (2005) 235-239

[107] Z. Xiong, G. Wu, J. Hu, P. Chen*, Ternary imides for hydrogen storage*, Adv. Mater. 16 (2004) 1522-1525

[108] Z. Xiong, G. Wu, J. Hu, P. Chen, *Investigation on chemical reaction between $LiAlH_4$ and $LiNH_2$*, J. Power Sources 159 (2006) 167-170

[109] J. Lu, Z.Z. Fang, *Dehydrogenation of a combined $LiAlH_4/LiNH_2$ system*, J. Phys. Chem. B 109 (2005) 20830-20834

[110] Y. Kojima, M. Matsumoto, Y. Kawai, T. Haga, N. Ohba, K. Miwa, S. Towata, Y. Nakamori, S. Orimo, *Hydrogen absorption and desorption by the Li-Al-N-H system*, J. Phys. Chem. B 110 (2006) 9632-9636

[111] F.E. Pinkerton, G. P. Meisner, M.S. Meyer, M.P. Balogh, M.D. Kundrat, *J. Phys. Chem. B* 109 (2005) 6-8

[112] M. Aoki, K. Miwa, T. Noritake, G. Kitahara, Y. Nakamori, S. Orimo, S. Towata, *Appl. Phys. A* 80 (2005) 1409-1412

[113] Y. Nakamori, A. Ninomiya, G. Kitahara, M. Aoki, T. Noritake, K. Miwa, Y. Kojima, S. Orimo, *J. Power Sources* 155 (2006) 447-455

[114] F.E. Pinkerton, M.S. Meyer, G.P. Meisner, M.P. Balogh, *J. Phys. Chem. B* 110 (2006) 7967-7974

[115] G.P. Meisner, M.L. Scullin, M.P. Balogh, F.E. Pinkerton, M.S. Meyer, *J. Phys. Chem B* 110 (2006) 4186-4192

[116] F.E. Pinkerton, M.S. Meyer, G.P. Meisner, M.P. Balogh, *Improved hydrogen release from $LiB_{0.33}N_{0.67}H_{2.67}$ with metal additives: Ni, Fe, and Zn*, J. Alloys Comp. 433 (2007) 282-291

[117] Z. Xiong, G. Wu, J. Hu, Y. Liu, P. Chen, W. Luo, J. Wang, *Adv. Funct. Mater.* 17 (2007) 1137-1142

[118] P. Chen, Z. Xiong, G. Wu, Y. Liu, J. Hu, W. Luo, *Scr. Mater.* 56 (2007) 817-822

[119] Z.T. Xiong, J.J. Hu, G.T. Hu, Y.F. Liu, P. Chen, *Catalysis Today* 120 (2007) 287-291

[120] M. Aoki, T. Noritake, G. Kitahara, Y. Nakamori, S. Towata, S. Orimo, *Dehydriding reaction of $Mg(NH_2)_2$-LiH system under hydrogen pressure*, J. Alloys Comp. 428 (2007) 307-311

[121] H.Y. Leng, T. Ichikawa, S. Hino, N. Hanada, S. Isobe, H. Fujii, *J. Phys. Chem. B* 108 (2004) 8763-8765

[122] T. Ichikawa, K. Tokoyoda, H. Leng, H. Fujii, *Hydrogen absorption properties of Li-Mg-N-H system*, J. Alloys Comp. 400 (2005) 245-248

[123] H.Y. Leng, T. Ichikawa, S. Isobe, S. Hino, N. Hanada, H. Fujii, *Desorption behaviours from metal-N-H systems synthesized by ball milling*, J. Alloys Comp. 404-406 (2005) 443-447

[124] T. Ichikawa, H.Y. Leng, S. Isobe, N. Hanada, H. Fujii, *J. Power Sources* 159 (2006) 126-131

[125] T. Nakagawa, T. Ichikawa, R. Iida, H. Leng, N. Takeichi, T. Kiyobayashi, H. Takeshita, H. Fujii, *Observation of hydrogen absorption/desorption reaction processes in Li-Mg-N-H system by in-situ X-ray diffractmetry*, J. Alloys Comp. 430 (2007) 217-221

[126] K. Okamoto, K. Tokoyoda, T. Ichikawa, H. Fujii, *A process for synthesizing the Li-Mg-N-H hydrogen storage system from Mg and $LiNH_2$*, J. Alloys Comp. 432 (2007) 289-292

[127] Y. Nakamura, S. Hino, T. Ichikawa, H. Fujii, H.W. Brinks, B.C. Hauback, *Dehydrogenation reaction of Li-Mg-N-H systems studied by in situ synchrotron powder X-ray diffraction and powder neutron diffraction*, J. Alloys Comp. 457 (2008) 362-367

[128] Y. Nakamori, G. Kitahara, S. Orimo, *J. Power Sources* 138 (2004) 309-312

[129] Y. Nakamori, G. Kitahara, K. Miwa, S. Towata, S. Orimo, *Appl. Phys. A* 80 (2005) 1-3

[130] H. Leng, T. Ichikawa, H. Fujii, *J. Phys. Chem. B* 110 (2006) 12964-12968

[131] S. Isobe, T. Ichikawa, K. Tokoyoda, N. Hanada, H. Leng, H. Fujii, Y. Kojima, *Thermochim. Acta* 468 (2008) 35-38

[132] J. Hu, Y. Liu, G. Wu, Z. Xiong, P. Chen, *J. Phys. Chem. C* 111 (2007) 18439-18443

[133] Y. Liu, J. Hu, G. Wu, Z. Xiong, P. Chen, *J. Phys. Chem. C* 112 (2008) 1293-1298

[134] Z. Xiong, G. Wu, J. Hu, P. Chen, W. Luo, J. Wang, *Investigation on hydrogen storage over Li-Mg-N-H complex—the effect of compositional changes*, J. Alloys Comp. 417 (2006) 190-194

[135] J. Hu, Z. Xiong, G. Wu, P. Chen, K. Murata, K. Sakata, *J. Power Sources* 159 (2006) 120-125

[136] J. Hu, G. Wu, Y. Liu, Z. Xiong, P. Chen, *J. Phys. Chem. B* 110 (2006) 14688-14692

[137] Y. Liu, J. Hu, G. Wu, Z. Xiong, P. Chen, *J. Phys. Chem. C* 111(2007) 19161-19164

[138] Z. Xiong, J. Hu, G. Wu, P. Chen, *Hydrogen absorption and desorption in Mg-Na-N-H system*, J. Alloys Comp. 395 (2005) 209-212

[139] Y. Liu, J. Hu, Z. Xiong, G. Wu, P. Chen, K. Murata, K. Sakata, *Investigations on hydrogen desorption from the mixture of $Mg(NH_2)_2$ and CaH_2*, J. Alloys Comp. 432 (2007) 298-302

[140] J. Hu, Z. Xiong, G. Wu, P. Chen, K. Murata, K. Sakata, *J. Power Sources* 159 (2006) 115-119

[141] Y. Liu, Z. Xiong, J. Hu, G. Wu, P. Chen, K. Murata, K. Sakata, *J. Power Sources* 159 (2006) 135-138

[142] S. Hino, T. Ichikawa, H. Leng, H. Fujii, *Hydrogen desorption properties of the Ca-N-H system*, J. Alloys Comp. 398 (2005) 62-66

[143] K. Tokoyoda, S. Hino, T. Ichikawa, K. Okamoto, H. Fujii, *Hydrogen desorption/absorption properties of Li-Ca-N-H system*, J. Alloys Comp. 439 (2007) 337-341

[144] Z. Xiong, G. Wu, J. Hu, P. Chen, *Ca-Na-N-H system for reversible hydrogen storage*, J. Alloys Comp. 441 (2007) 152-156

[145] Z. Xiong, P. Chen, G. Wu, J. Lin, K.L. Tan, *J. Mater. Chem.* 13 (2003) 1676-1680

[146] Dr. Zhitao Xiong, personal communication

[147] S. Hino, T. Ichikawa, K. Tokoyoda, Y. Kojima, H. Fujii, *Quantity of NH_3 desorption from the Li-N-H hydrogen storage system examined by Fourier transform infrared spectroscopy*, J. Alloys Comp. 446-447 (2007) 342-344

[148] H.Y. Leng, T. Ichikawa, S. Hino, H. Fujii, *Investigation of reaction between $LiNH_2$ and H_2*, J. Alloys Comp. 463 (2008) 462-465

[149] W.S. Tang, G.Wu, A.T.S. Wee, C.K. Yong, Z. Xiong, A.T.S. Hor, P. Chen, *Dalton Trans.* (2008) 2395-2399

[150] C.H. Christensen, R.Z. Sørensen, T. Johannessen, U.J. Quaade, K. Honkala, T.D. Elmøe, R. Køhler, J.K. Nørskov, *J. Mater. Chem.* 15 (2005) 4106-4108

[151] R.Z. Sørensen, L.J.E. Nielsen, S. Jensen, O. Hansen, T. Johannessen, U. Quaade, C.H. Christensen, *Catal. Commun.* 6 (2005) 229-232

[152] C.H. Christensen, T. Johannessen, R.Z. Sørensen, J.K. Nørskov, *Catal. Today* 111 (2006) 140-144

[153] T.D. Elmøe, R.Z. Sørensen, U. Quaade, C.H. Christensen, J.K. Nørskov, T. Johannessen, *Chem. Eng. Sci.* 61 (2006) 2618-2625

[154] J.S. Hummelshøj, R.Z. Sørensen, M.Y. Kustova, T. Johannessen, J.K. Nørskov, C.H. Christensen, *J. Am. Chem. Soc.* 128 (2006) 16-17

[155] A. Klerke, C.H. Christensen, J.K. Nørskov, T. Vegge, *J. Mater. Chem.* 18 (2008) 2304-2310

[156] E. Wiberg, E. Amberger, *Hydrides of the elements of main groups I-IV,* Elsevier (1971)

[157] *Comprehensive Inorganic Chemistry, Vol. 1-4*, Pergamon (1973)

[158] A.F. Holleman, E. Wiberg, *Inorganic Chemistry,* Academic Press (1995)

[159] J.O. Jensen, *Anodematerialer til metalhydridbatterier*, Ph.d. thesis*,* Den Kongelige Veterinær- og Landbohøjskole (1997)

[160] <http://www.hydrogen.energy.gov/pdfs/progress04/iiie1_page.pdf>, visited Nov 2008

[161] Y.-W. Lee, B.M. Clemens, K.J. Gross, *Novel Sieverts' type volumetric measurements of hydrogen storage properties for very small sample quantities*, J. Alloys Comp. 452 (2008) 410-413

[162] D.A. Skoog, D.M. West, F.J. Holler, *Fundamentals of Analytical Chemistry,* 7th edition, Saunders College Publishing (1996)

[163] *Instruction Manual for the Cahn RG Automatic Electrobalance*, Cahn Instrument Company, CA USA

[164] Dr. J.O. Jensen, personal communication

[165] M Seals catalogue September 2001

[166] L.A. Hansen, *Enhedsoperationer i den kemiske industri*, Polyteknisk Forlag, Lyngby (1999)

[167] L. Cahn, H. Schultz, *Anal. Chem.* 35 (1963) 1729-1731

[168] F.A. Carey, *Organic Chemistry,* 3rd edition, McGraw-Hill (1996)

[169] W.D. Callister, Jr., Materials Science and Engineering – An introduction, 7th edition, John Wiley and Sons, Inc. (2007)

[170] H.-M. Shih, H. H. Johnson, *Acta Metall.* 30 (1982) 537

[171] G.D. Sandrock, *Proc. 12th Intersociety Energy Conversion Engineering Conf. (Am. Nuclear Soc.)* 1 (1977) 951

[172] F.E. Pinkerton, *Decomposition kinetics of lithium amide for hydrogen storage materials*, J. Alloys Comp. 400 (2005) 76-82

[173] S.V. Alapati, J.K. Johnson, D.S. Sholl, *J. Phys. Chem. B*, 2006*,* **110**, 8769-8776

[174] S.V. Alapati, J.K. Johnson, D.S. Sholl, *Phys. Chem. Chem. Phys.*, 2007, **9**, 1438-1452

[175] S.V. Alapati, J.K. Johnson, D.S. Sholl, *First principles screening of destabilized metal hydrides for high capacity H_2 storage using scandium*, J. Alloys Compd. 446-447 (2007) 23-27

[176] S.V. Alapati, J.K. Johnson, D.S. Sholl, *J. Phys. Chem. C*, 2007, **111**, 1584-1591

[177] S.V. Alapati, J.K. Johnson, D.S. Sholl, *J. Phys. Chem. C,* 2008, **112**, 5258-5262

[178] A.T. Dadd, P. Hubberstey, *J. Chem. Soc. Dalton Trans.*, 1982, 2175

[179] R.J. Pulham, P. Hubberstey, *J. Nuclear Mater.*, 1983, **115**, 239-250

[180] H. Yamane, S. Kikkawa, M. Koizumi, *Solid State Ionics, 1986,* **25**, 183-191

[181] T.S. Bartnitskaya, O.N. Grigor'ev, L.A. Krushinskaya, A.A. Rogozinskaya, L.A. Klochkov, T.V. Dubovik, *Powder Metallurgy and Metal Ceramics,* 2002, **41**, 413-416

[182] Z. Wen, K. Wang, L. Chen, J. Xie, *Electrochem. Communications,* 2006, **8**, 1349-1352

[183] A. Anderson, R. Blair, S.M. Hick, R.B. Kaner, *J. Mater. Chem.,* 2006, **16**, 1318-1322

[184] R.Z. Sørensen, *Ph.D. Thesis* (2008)

[185] L. Guangming, M. Peihua, W. Zhiming, L. Mingzhen, C. Minxong, *Thermochim. Acta* 412 (2004) 149-153

[186] E. Lepinasse, B. Spinner, *Rev. Int. Froid* 17 (1994) 309

11 APPENDICES

11.1 Electronic circuits for microbalance controller

Top level cirquit of the microbalance controller

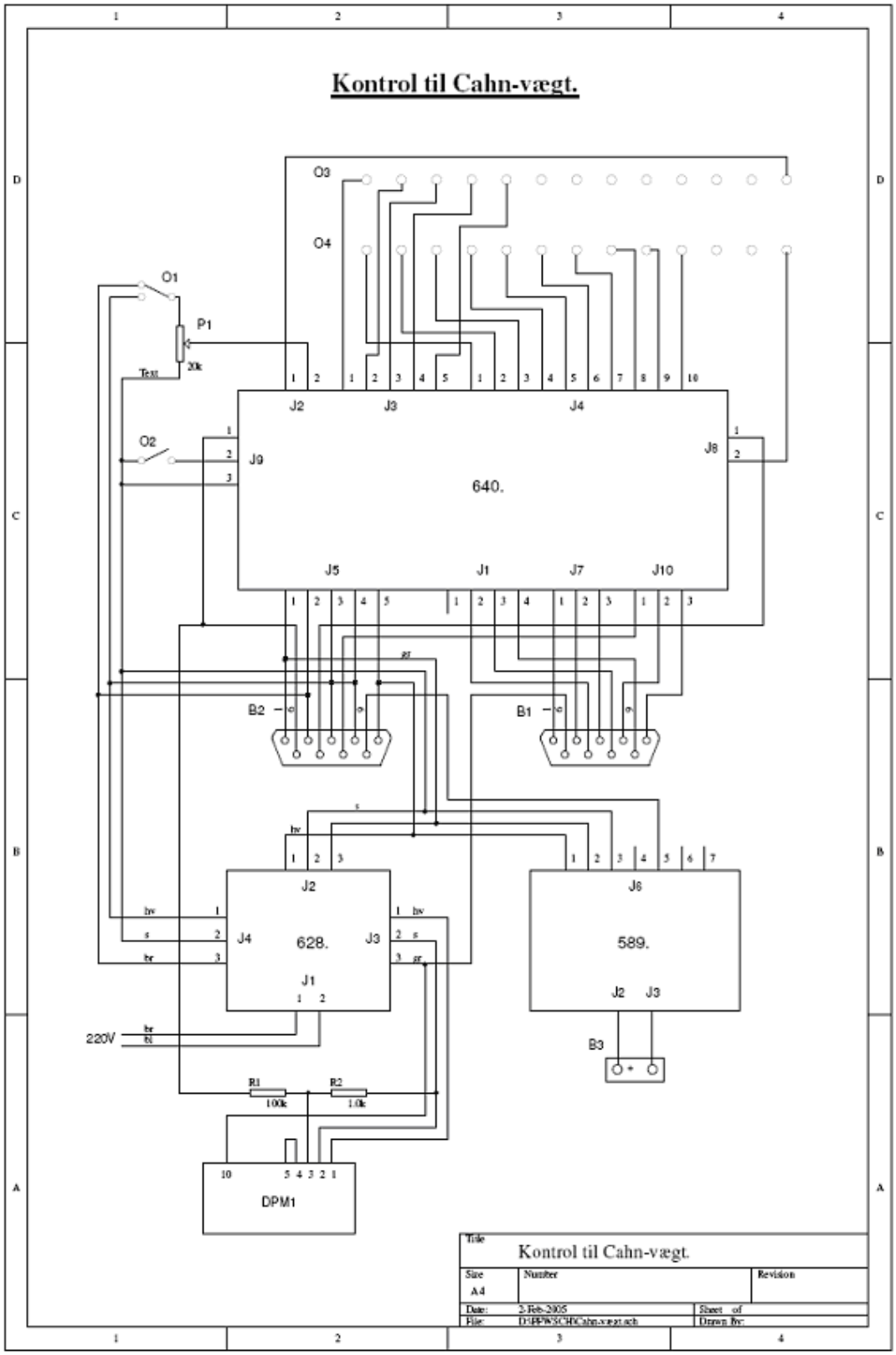

Electronic circuit "640". This part is the heart of the controller.

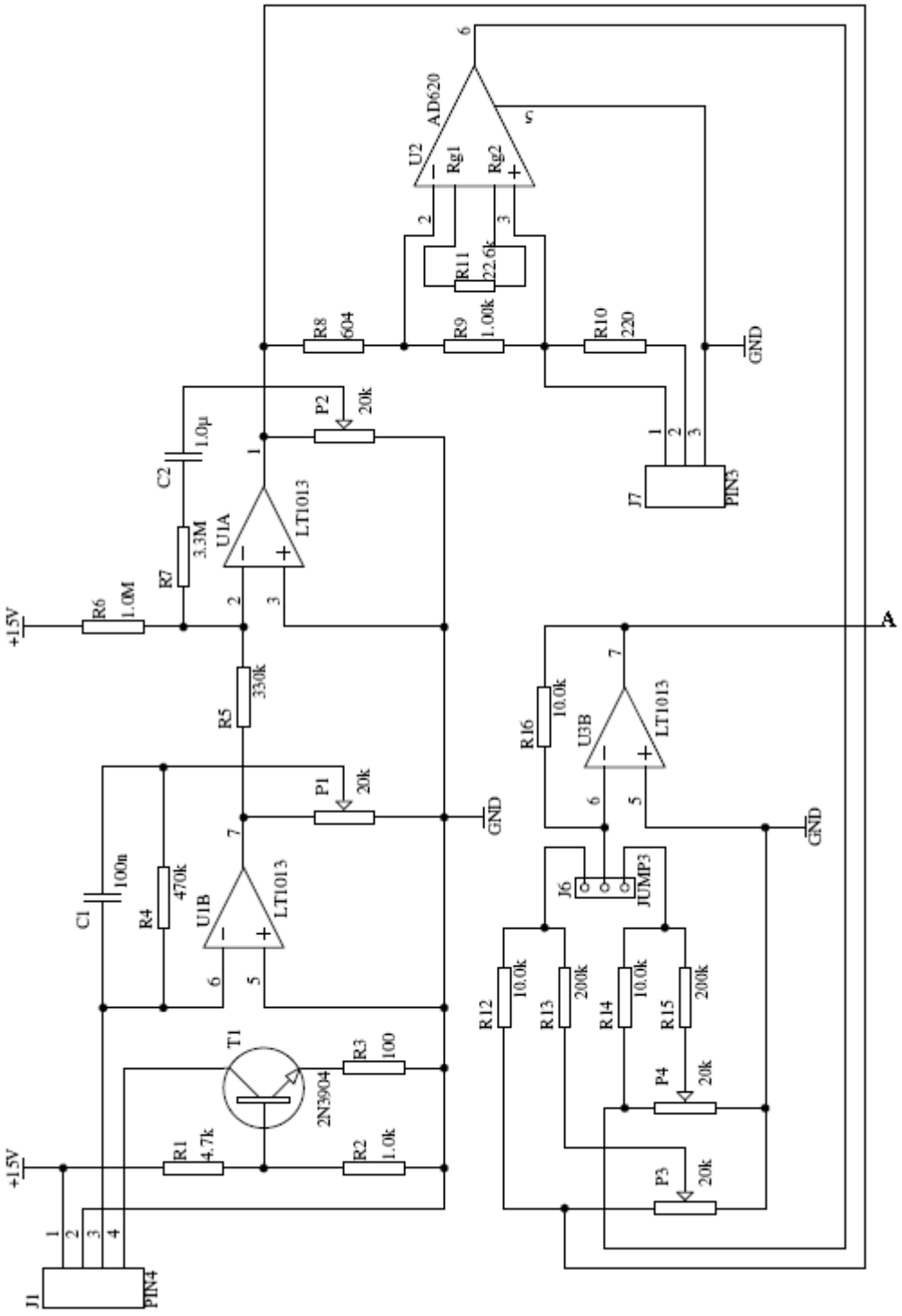

Continuation of the diagram on the previous page. This diagram is mainly related to the display of the controller.

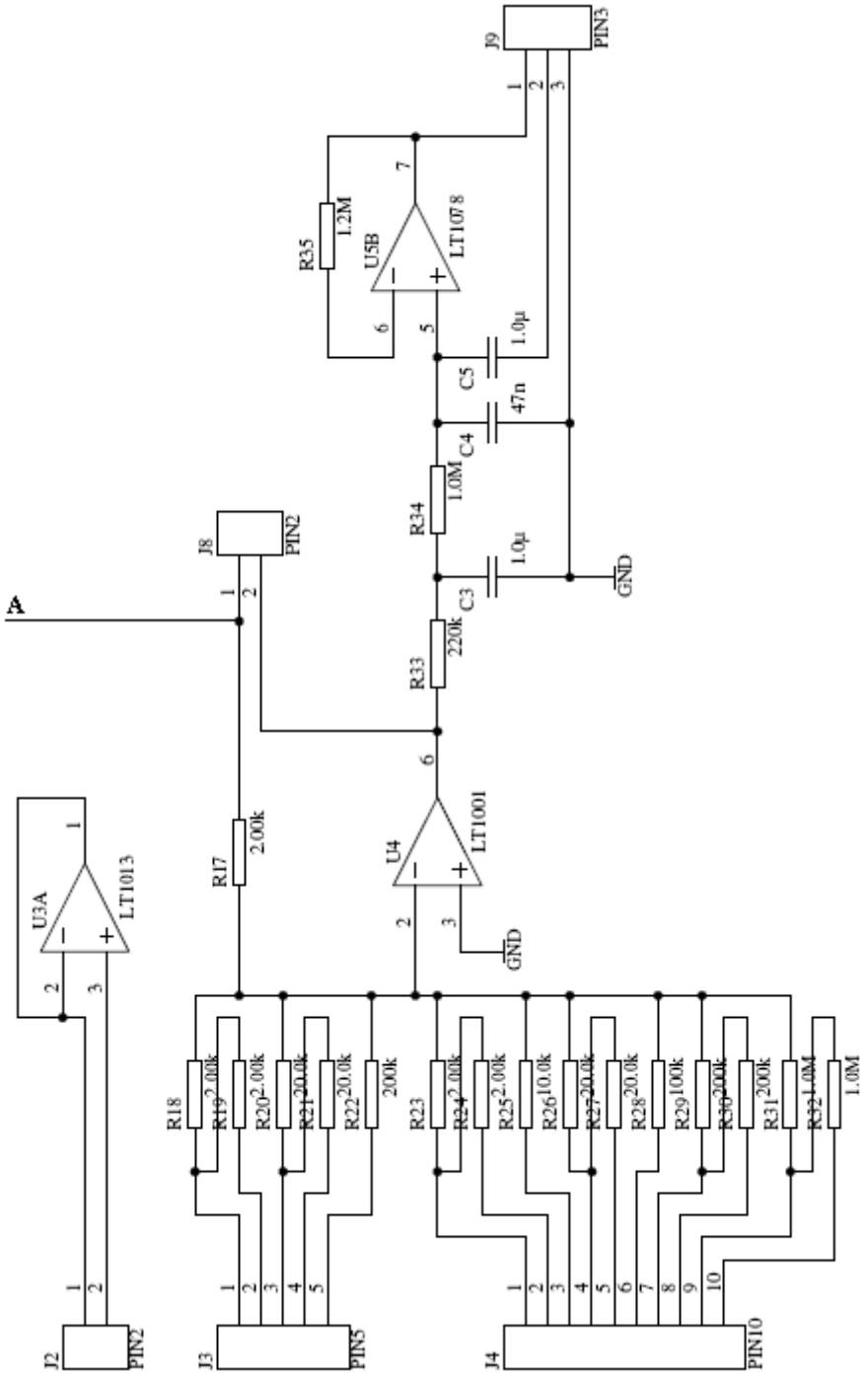

These diagrams are related to controlling an optional thermistor in the pressure chamber.

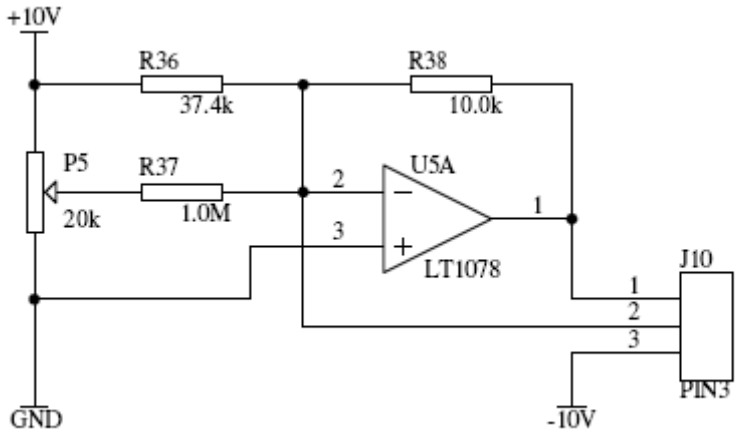

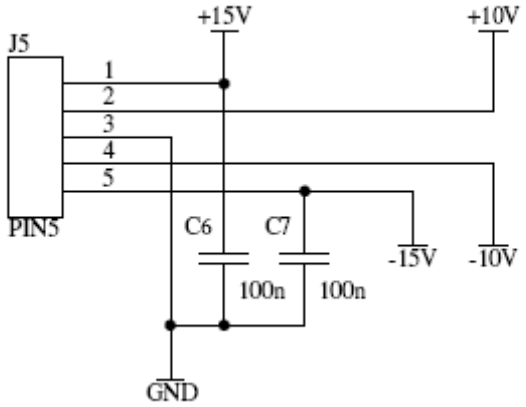

Component layout for the "640" part of the controller.

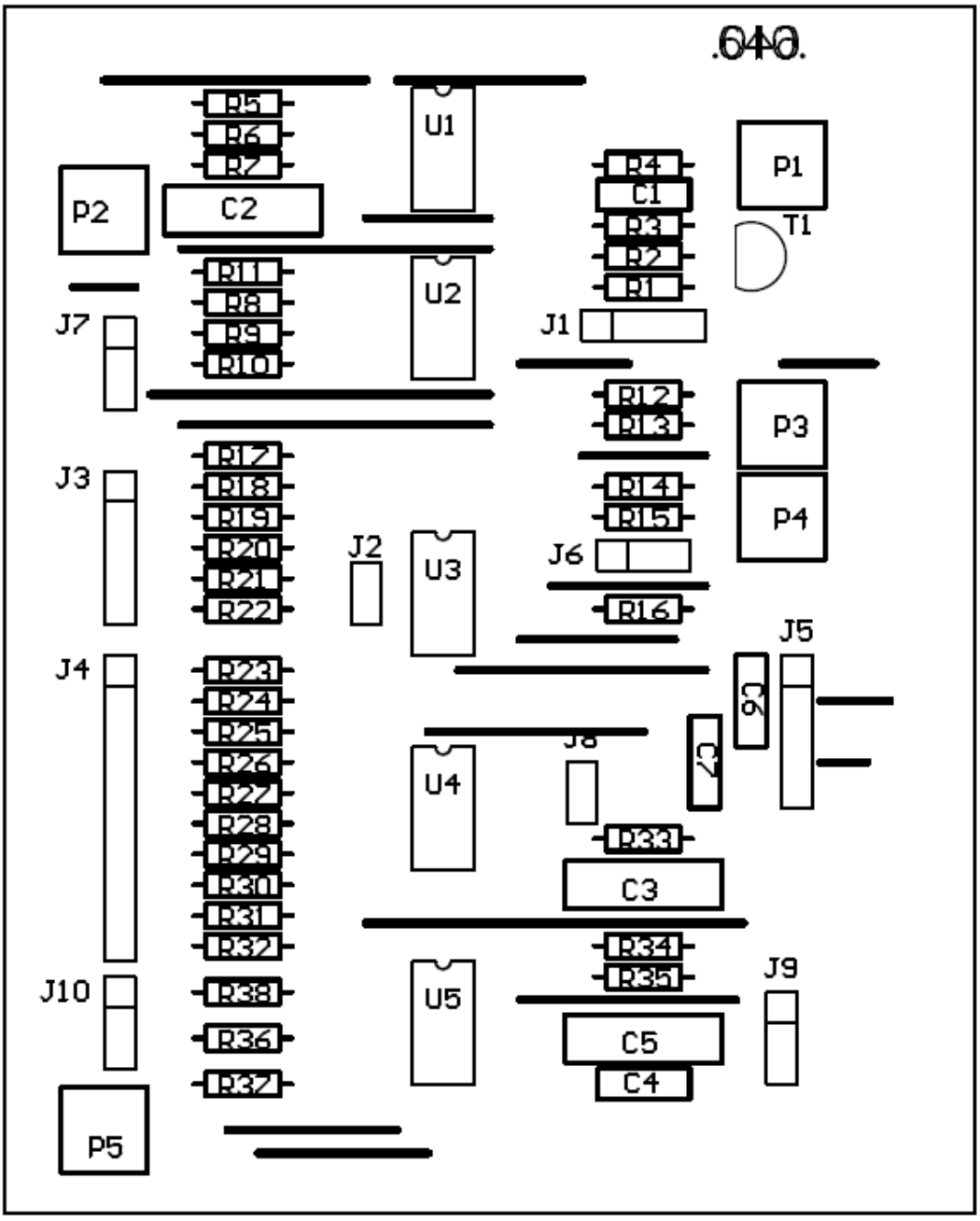

11.2 Documentation for block diagrams in LabVIEW application

11.2.1 Overview over and structure for block diagrams

The LabVIEW application goes through A, B, and C, step for step. C is repeated until the application is stopped by the user.

C.I, C.II, C.III.a and IV are repeated in a loop in the main frame, C. When the 'PCI start' button is pressed (see Fig. 129) C.III.b-h are run in place of C.III.a.

A. *OPEN COMMUNICATION PORT*
B. *INITIALIZATION*
    I. *Modules*
    II. *File and various variables*
C. *MAIN FRAME*
    I. *Serial communication*
        a. *7017: Microbalance, pressure transmitters, mass flow*
        b. *7018: Temperatures*
        c. *7024: Set values in mass flow controller and pressure controller*
        d. *7066: Relays (magnet valves)*
    II. *Update charts*
    III. *PCI acquiring*
        a. *Initialize*
        b. *New pressure (determine next pressure step)*
            i. *Automatic PCI 'ON': Algorithm calculates and saves next step in 'Run list'*
            ii. *Pick next pressure from 'Run list'*
        c. *Control reservoir (attain same pressure in reservoir and microbalance)*
        d. *Set pressure (build pressure up or down in gradual flows)*
        e. *Check reservoir (security against mass flow controller leak)*
        f. *Measure*
            i. *Automatic PCI 'ON': Continue measure until the change in hydrogen uptake for the current step is smaller than a pre-selected threshold value*
            ii. *Automatic PCI 'OFF': Continue measure for the time set by the "Step time" control variable*
        g. *End of point (save data to PCI list)*
        h. *End of series (save PCI list to file)*
    IV. *Write to file*
D. *CLOSE PORT*

A OPEN COMMUNICATION PORT

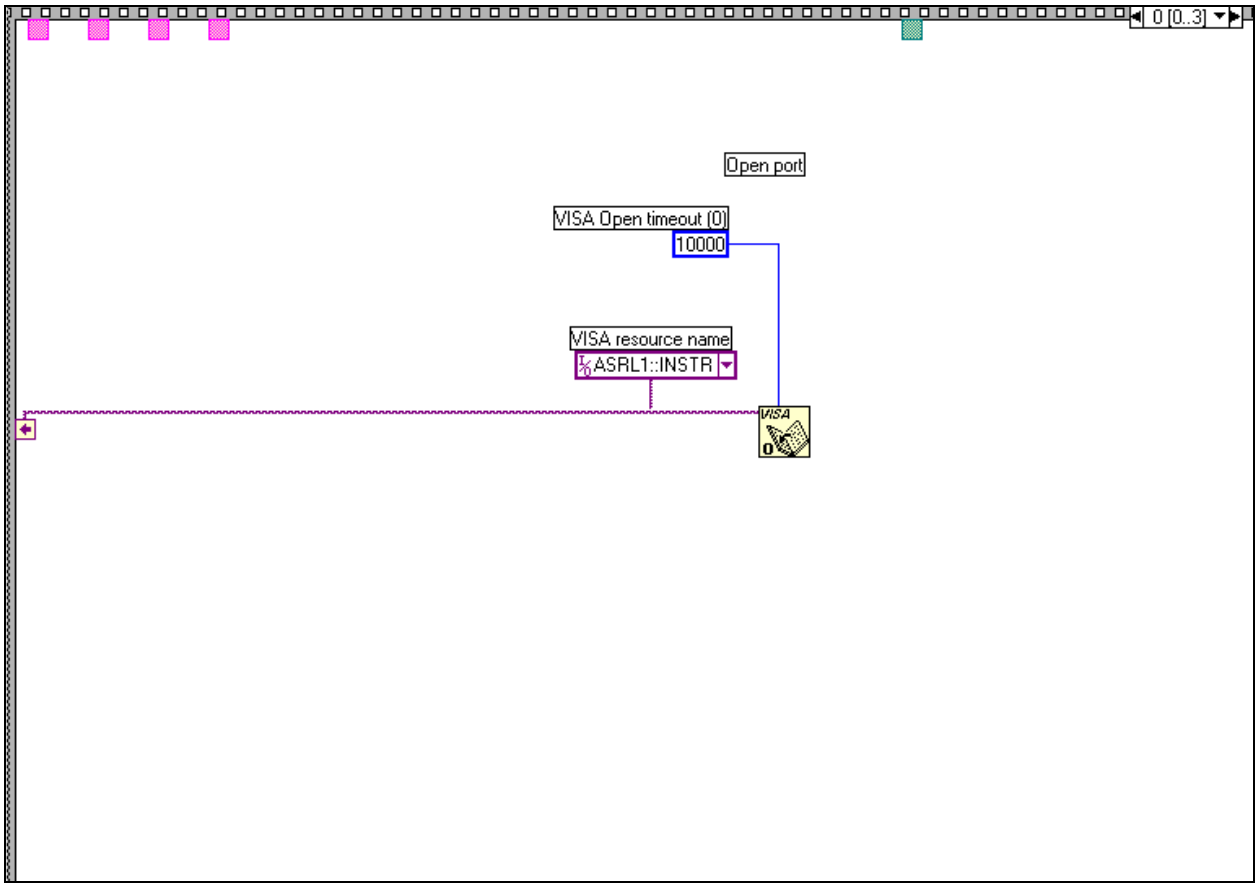

B INITIALIZATION

B.I Modules

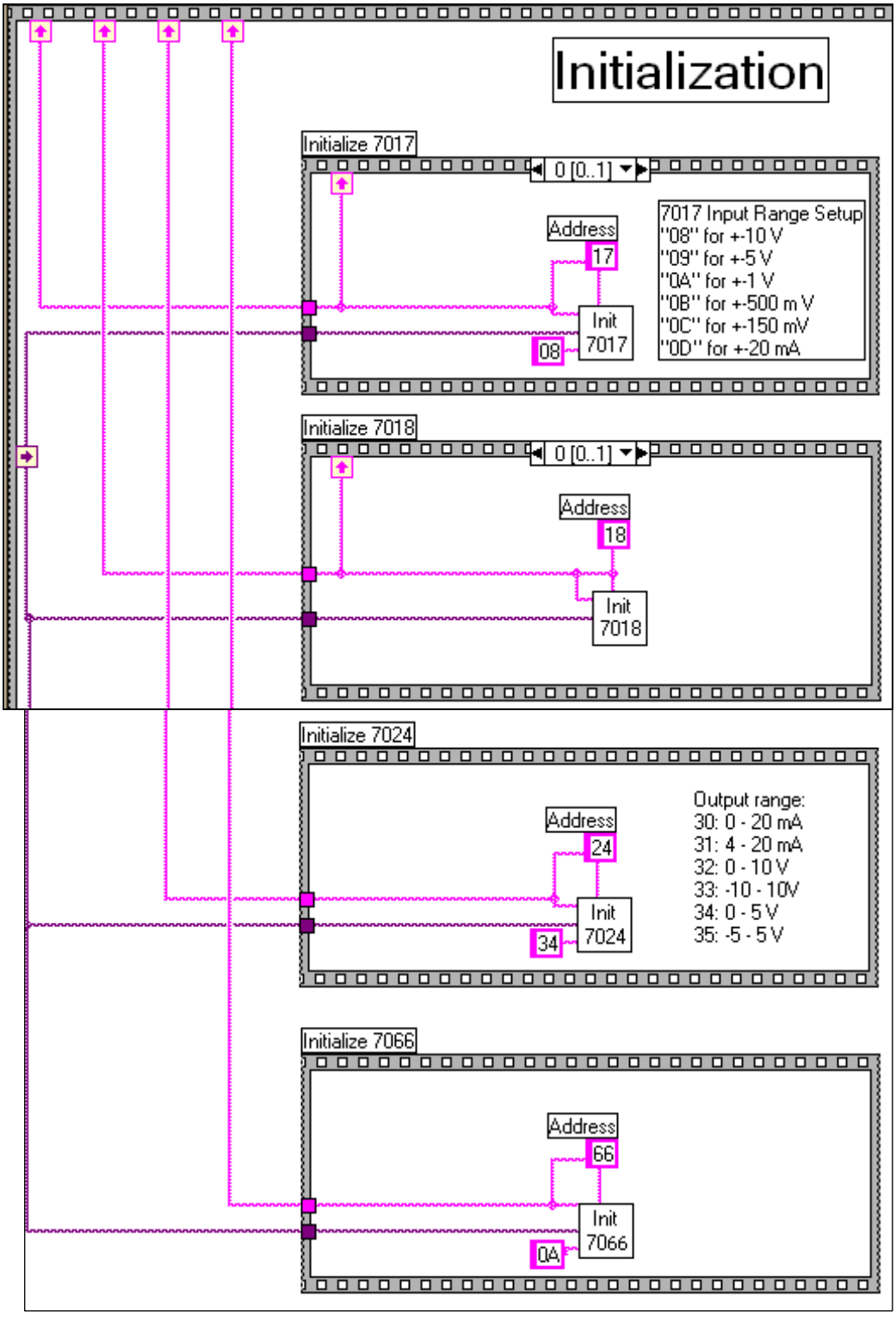

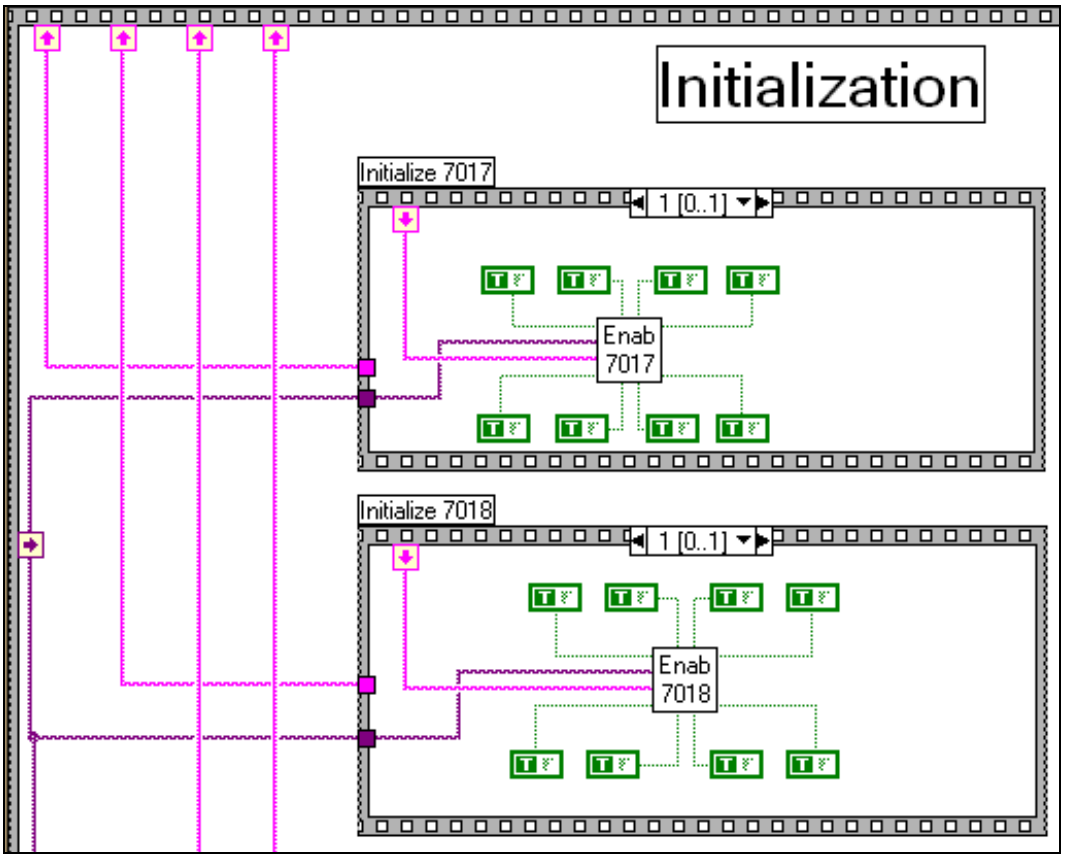
Initialization
Initialize 7017
1 [0..1]
Enab
7017
Initialize 7018
1 [0..1]
Enab
7018

B.II File and various variables

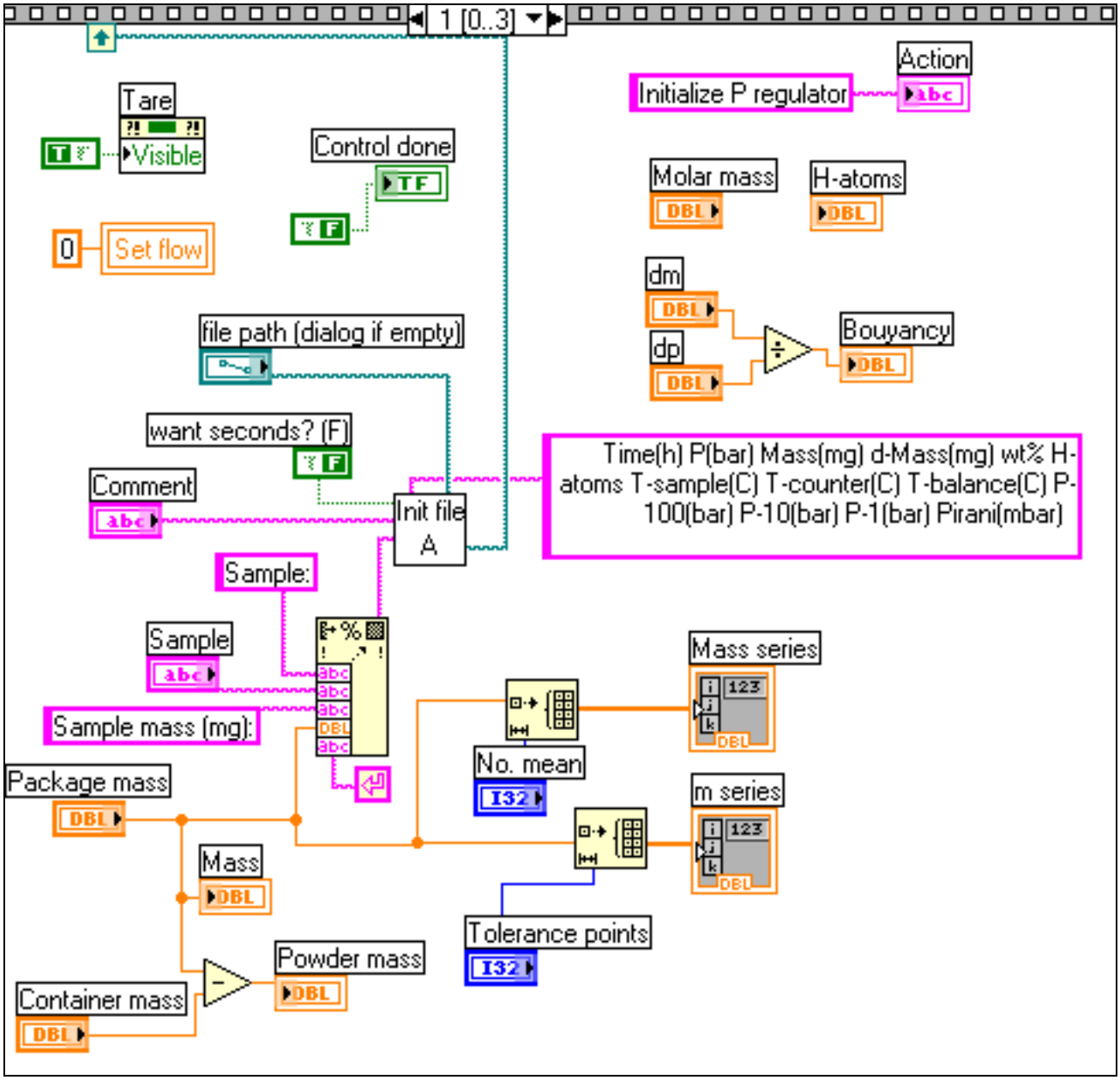

C MAIN FRAME

C.I Serial communication

C.I.a 7017: Microbalance, pressure transmitters, mass flow

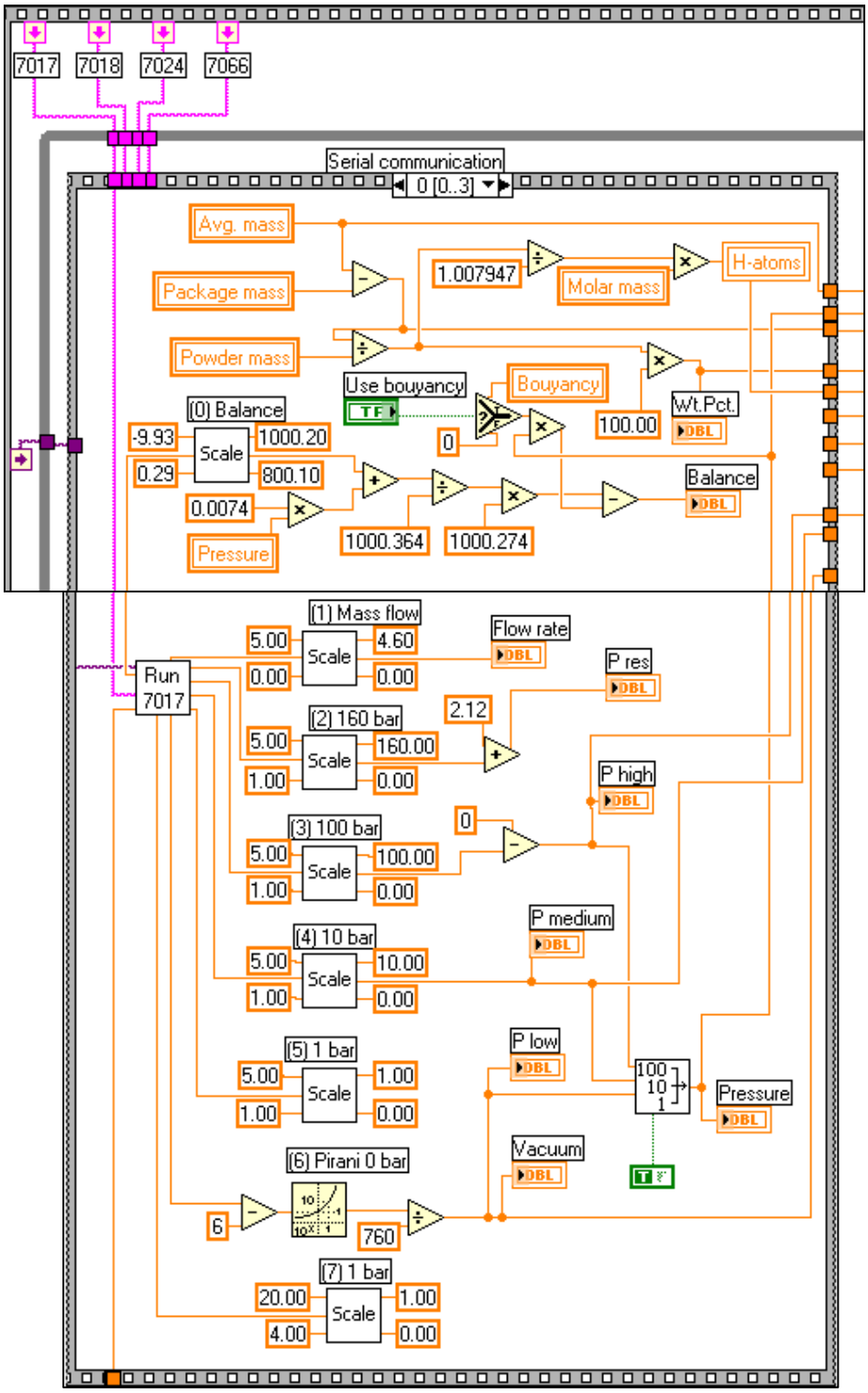

C.I.b 7018: Temperatures

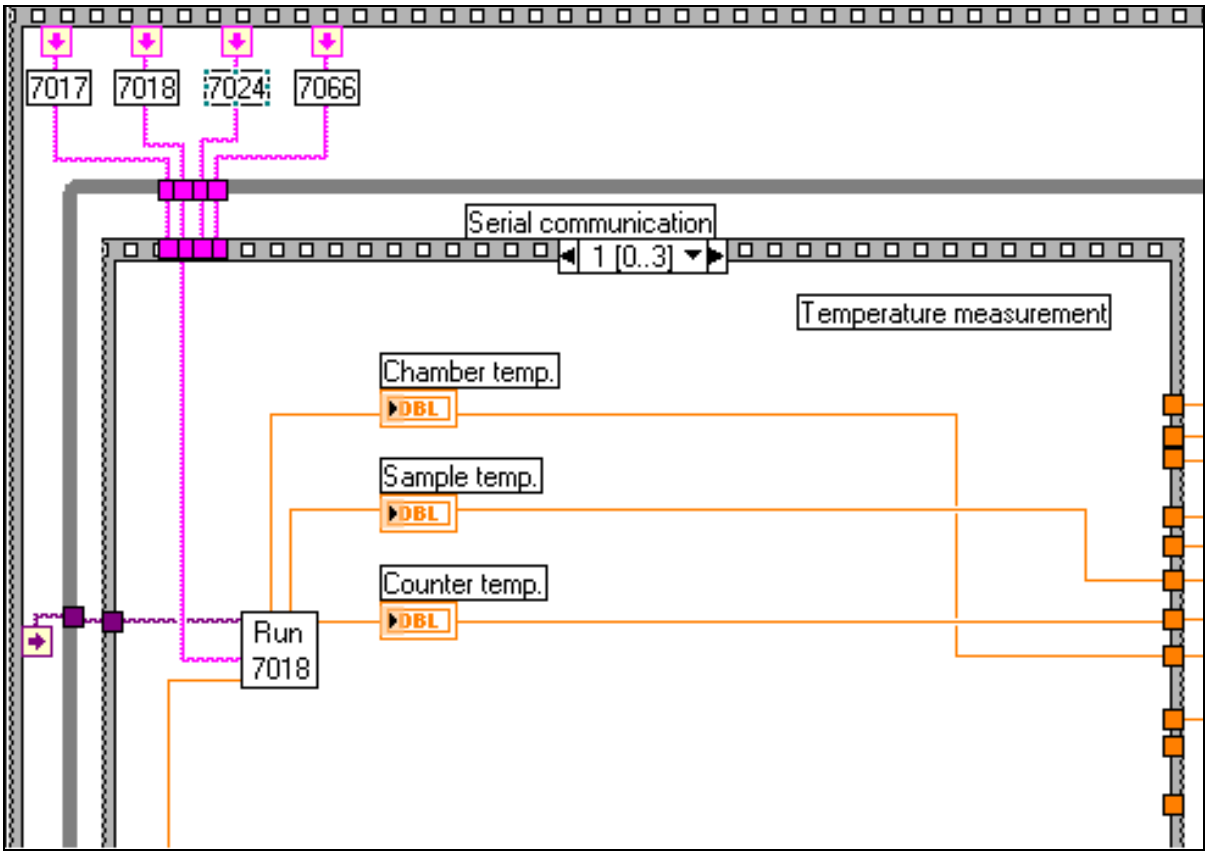

C.I.c 7024: Set values in mass flow controller and pressure controller

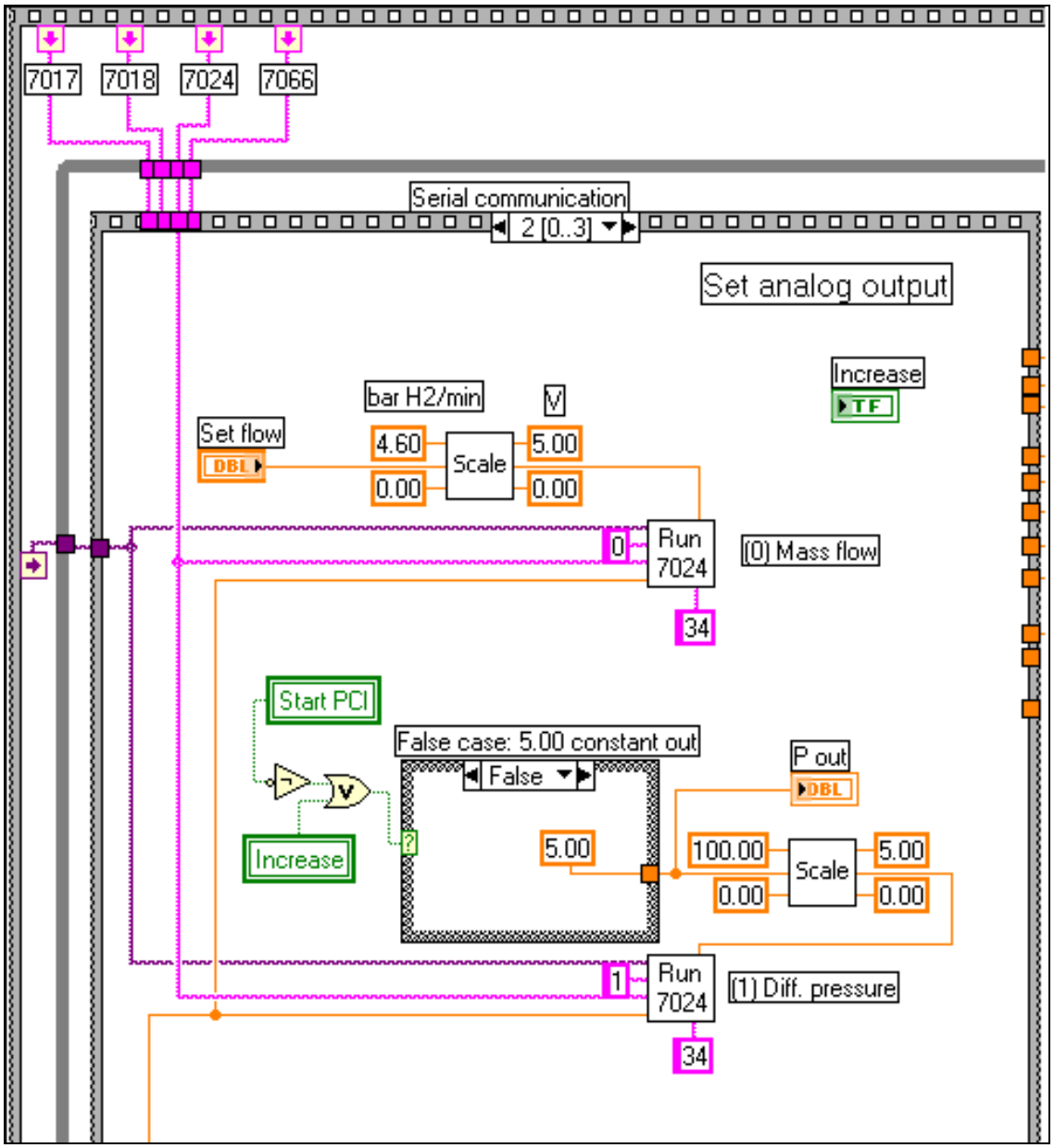

C.I.d 7066: Relays (magnet valves)

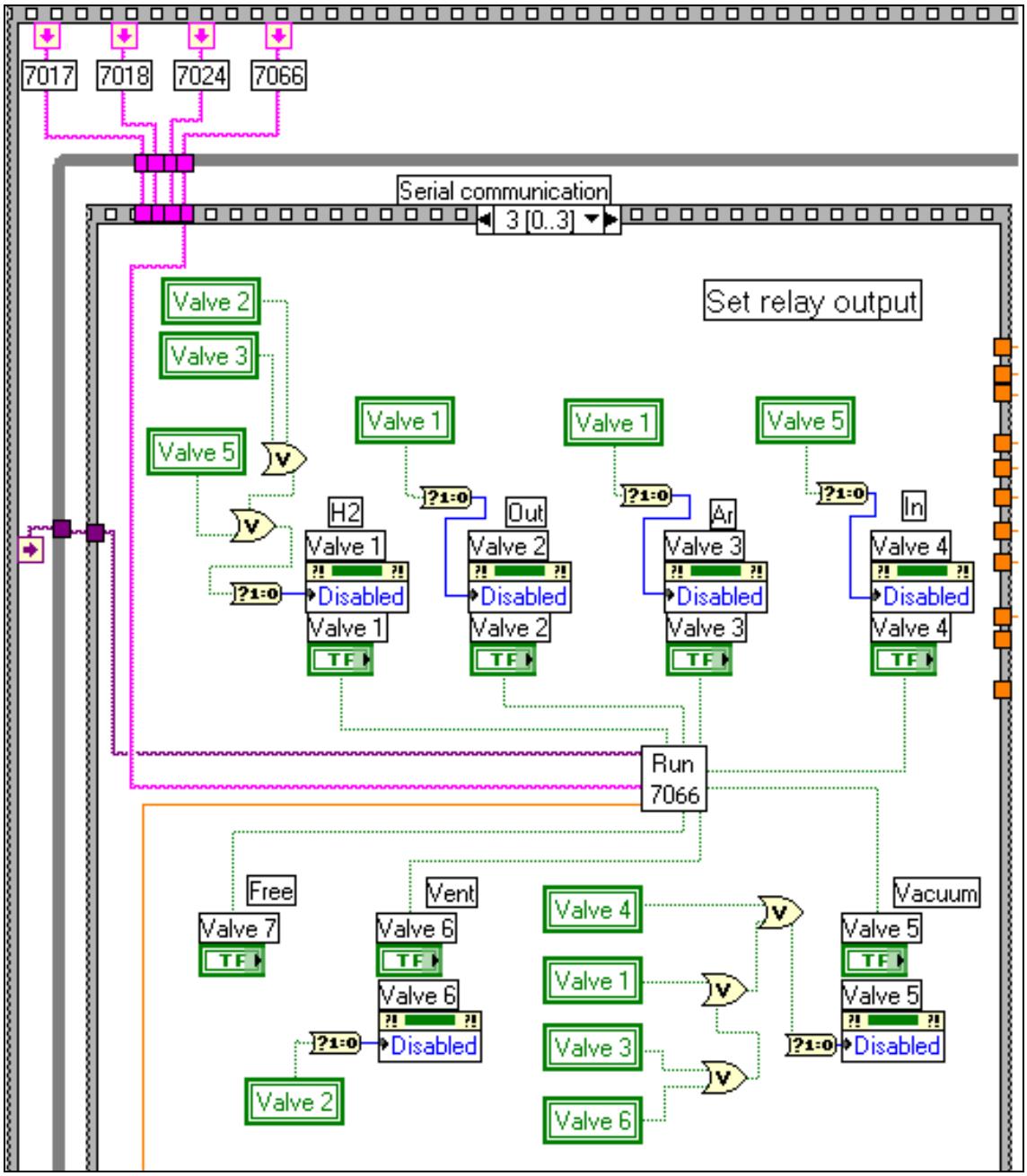

C.II Update charts

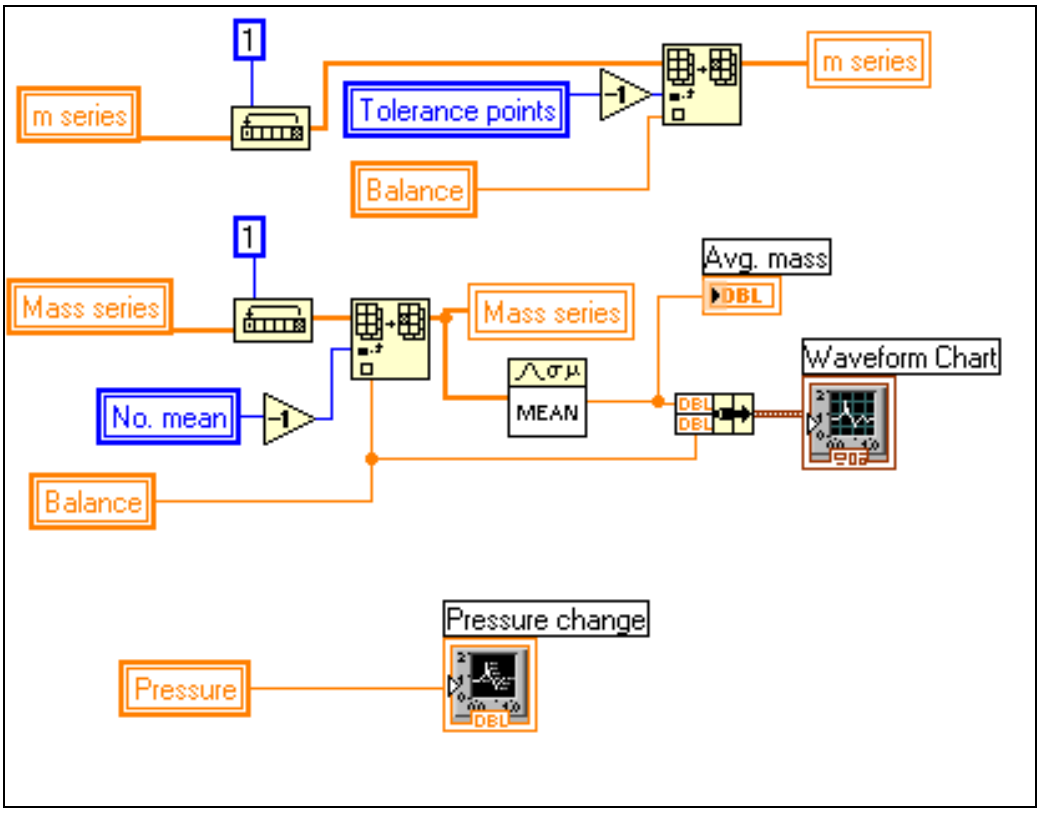

C.III PCI Acquiring

C.III.a Initialize

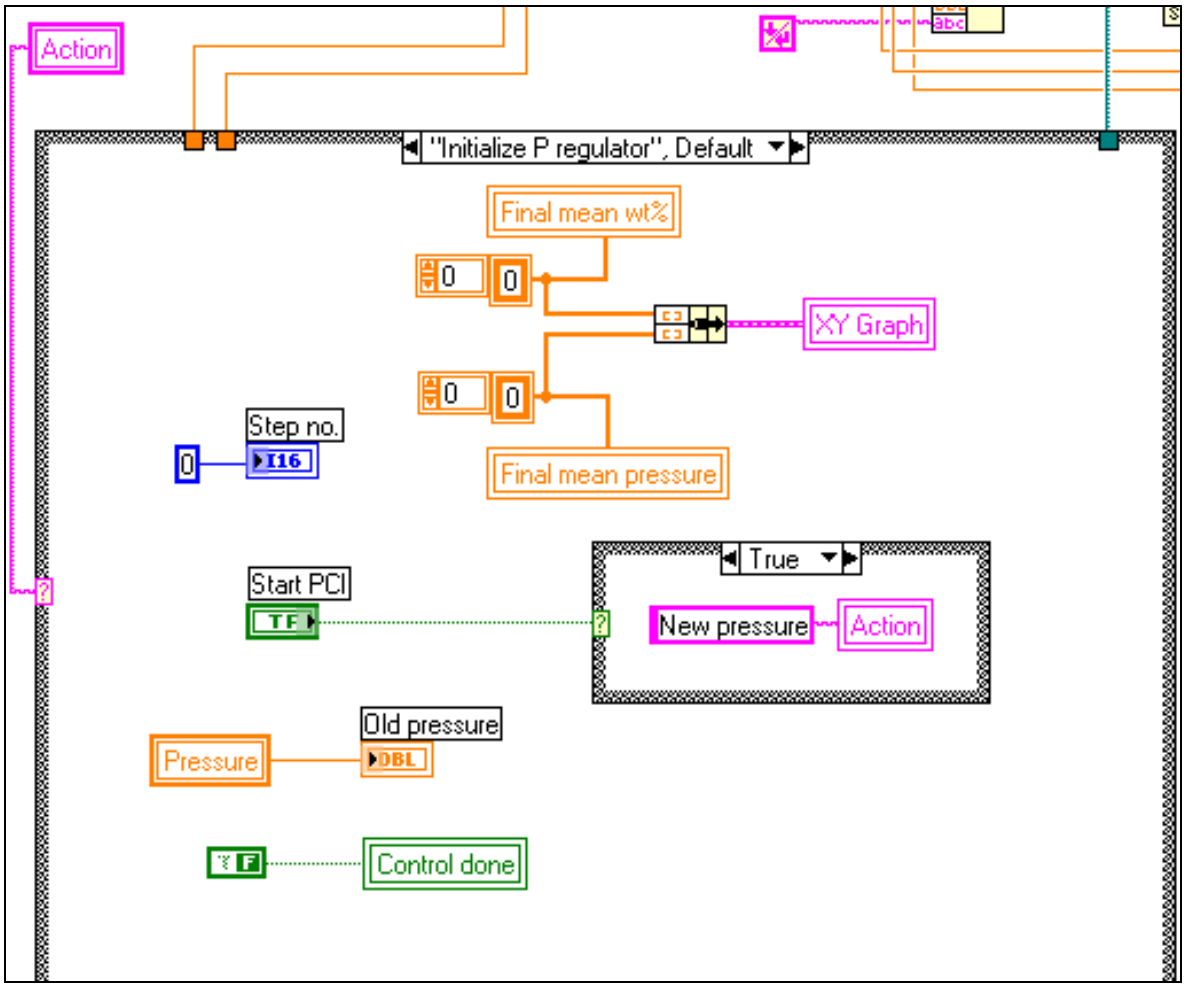

C.III.b New pressure (determine next pressure step)

C.III.b.i Automatic PCI 'ON': Algorithm calculates and saves next step in 'Run list'

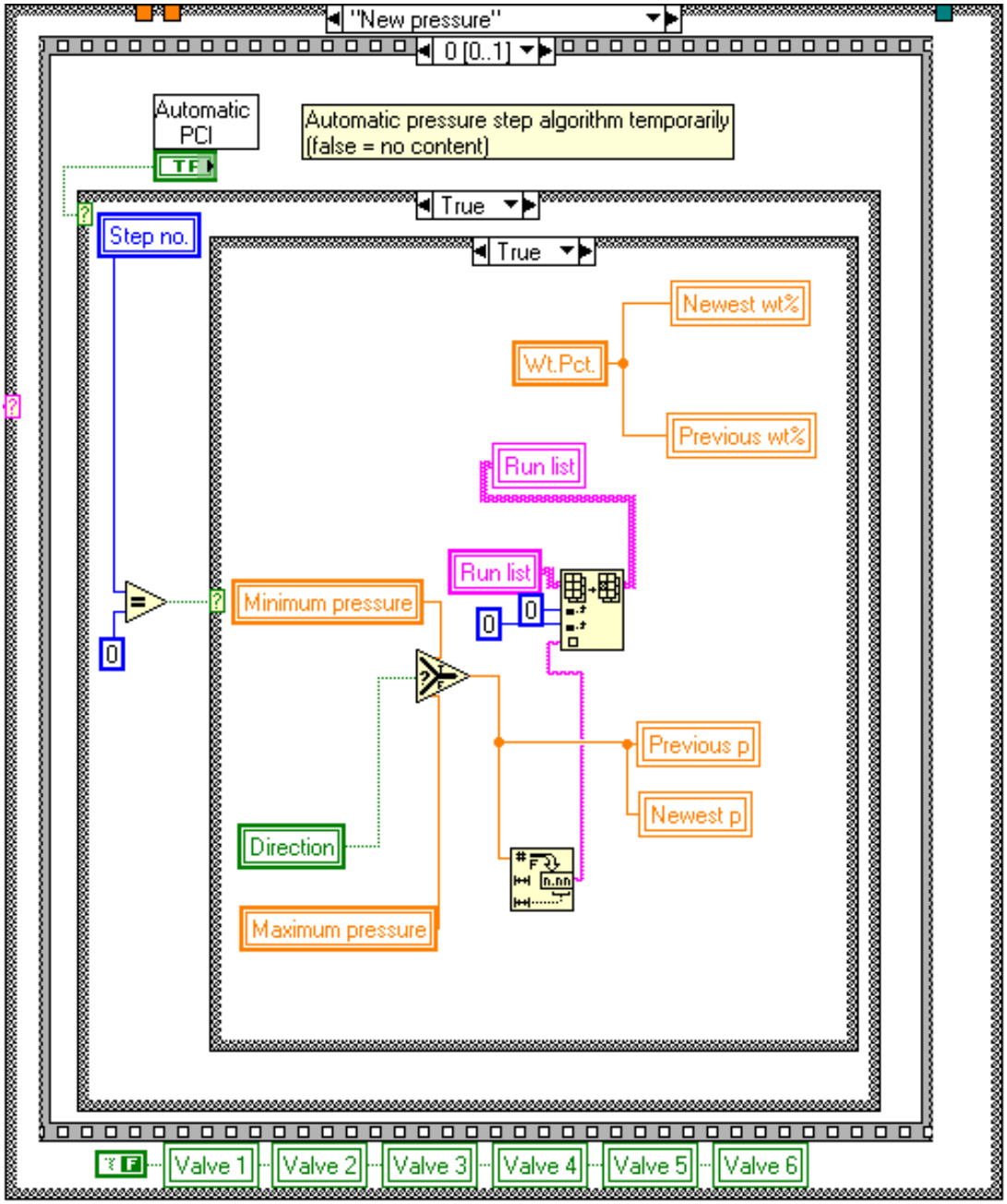

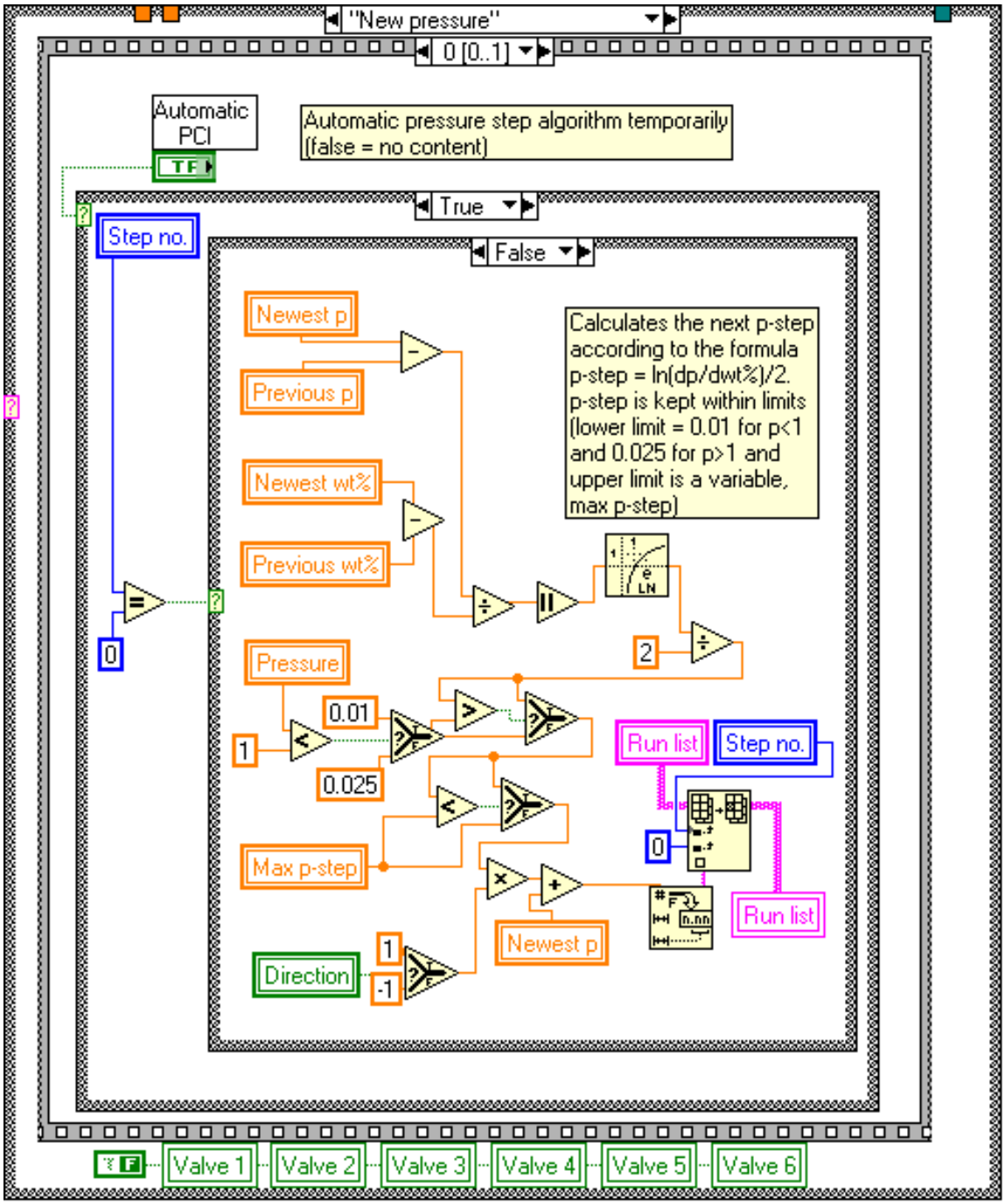
"New pressure"
0 [0..1]
Automatic PCI
TF
Automatic pressure step algorithm temporarily (false = no content)
True
False
Step no.
Newest p
Previous p
Newest wt%
Previous wt%
Calculates the next p-step according to the formula p-step = ln(dp/dwt%)/2. p-step is kept within limits (lower limit = 0.01 for p<1 and 0.025 for p>1 and upper limit is a variable, max p-step)
Pressure
0.01
0.025
Max p-step
Direction
Newest p
Run list
Step no.
Run list
Valve 1
Valve 2
Valve 3
Valve 4
Valve 5
Valve 6

C.III.b.ii Pick next pressure from ‘Run list’

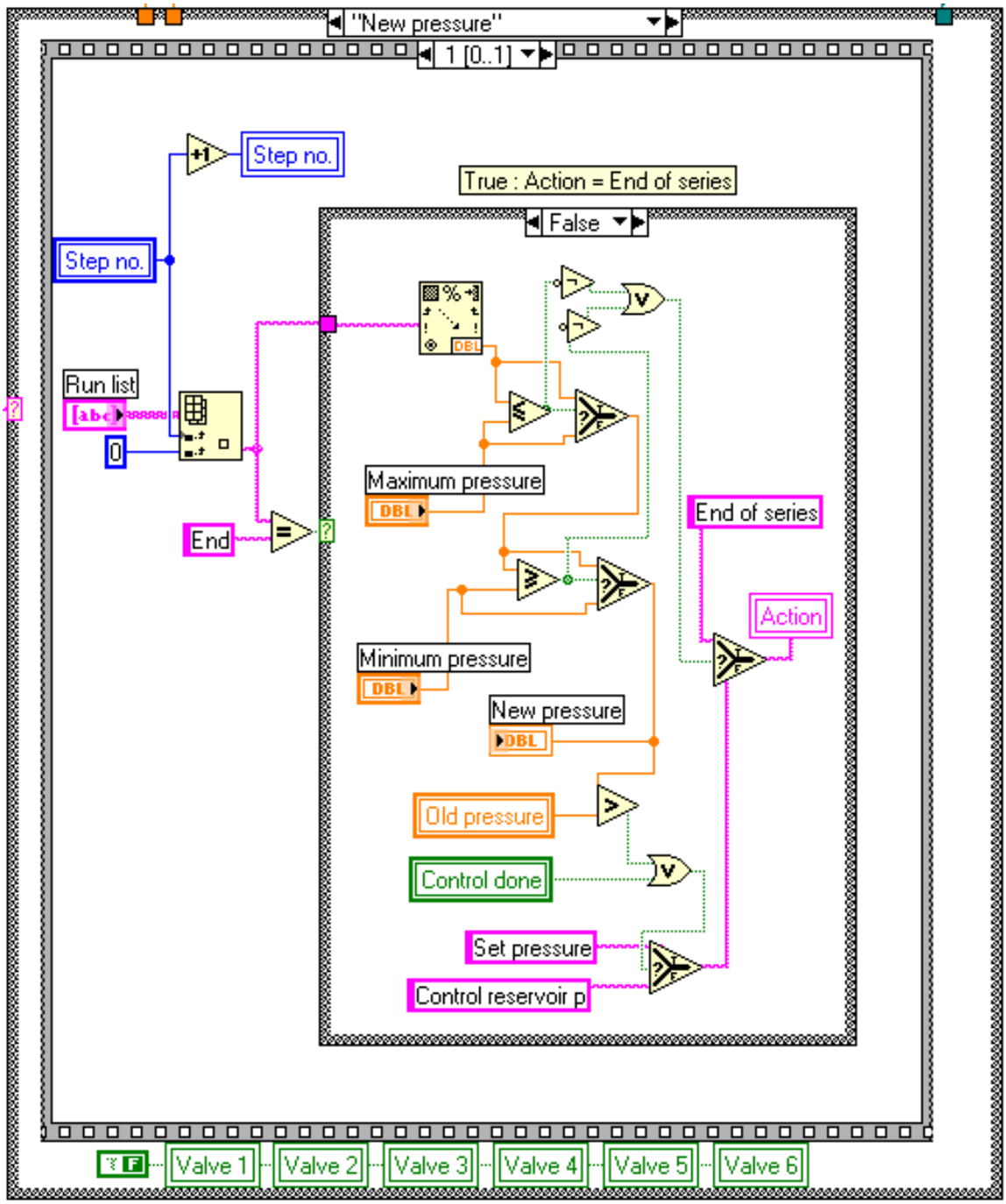

C.III.c Control reservoir (attain same pressure in reservoir and microbalance)

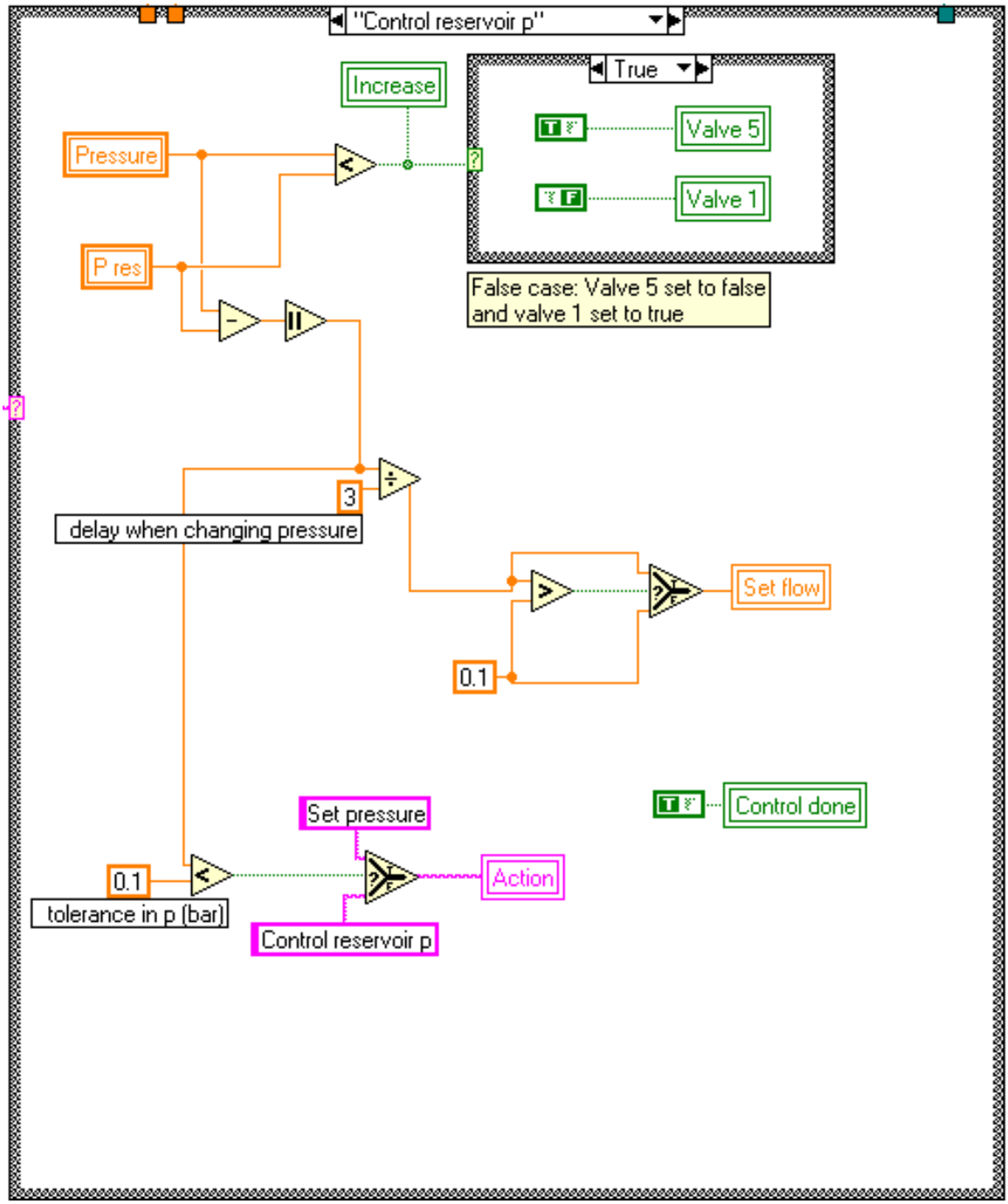

C.III.d Set pressure (build pressure up or down in gradual flows)

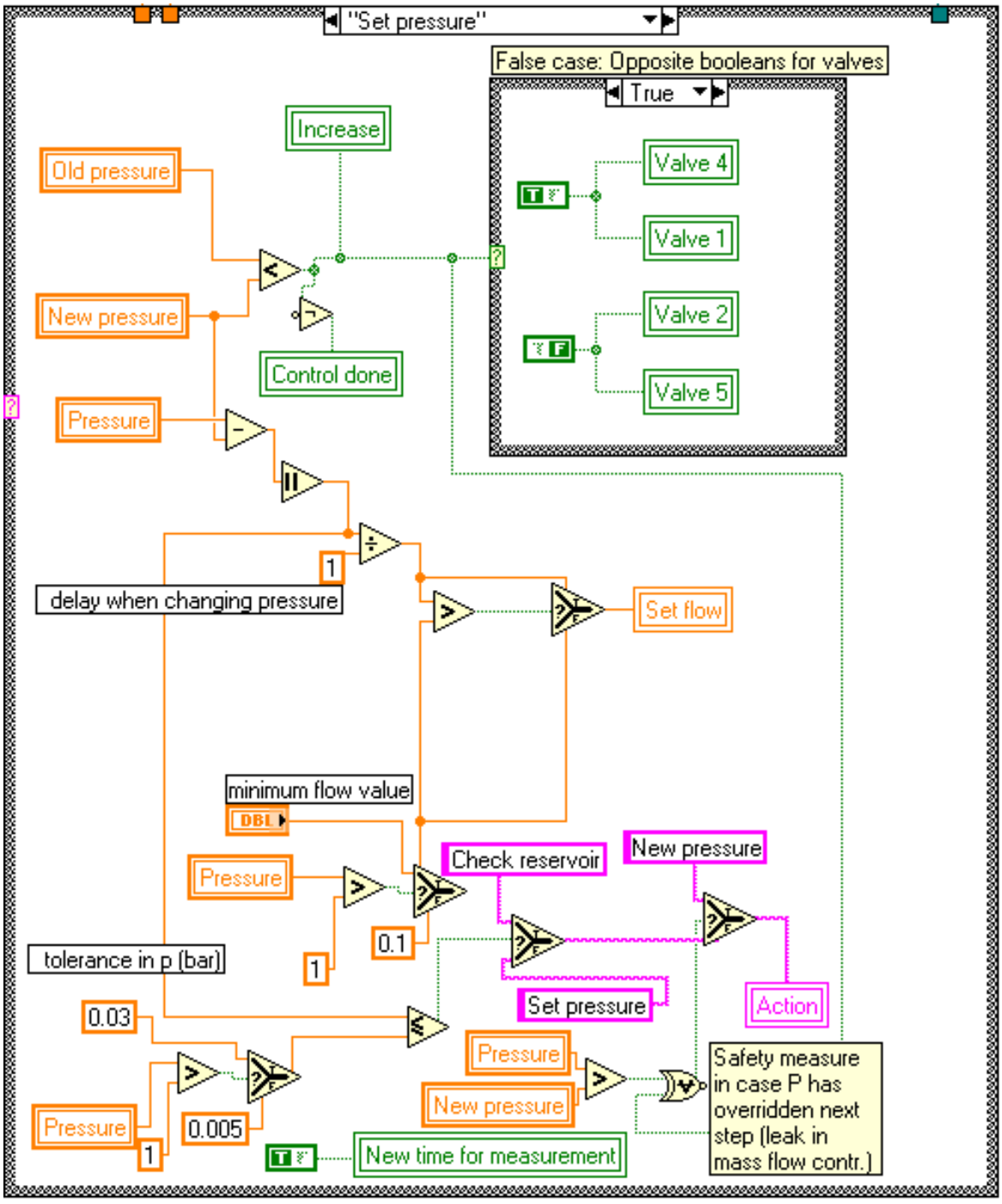

C.III.e Check reservoir (security against mass flow controller leak)

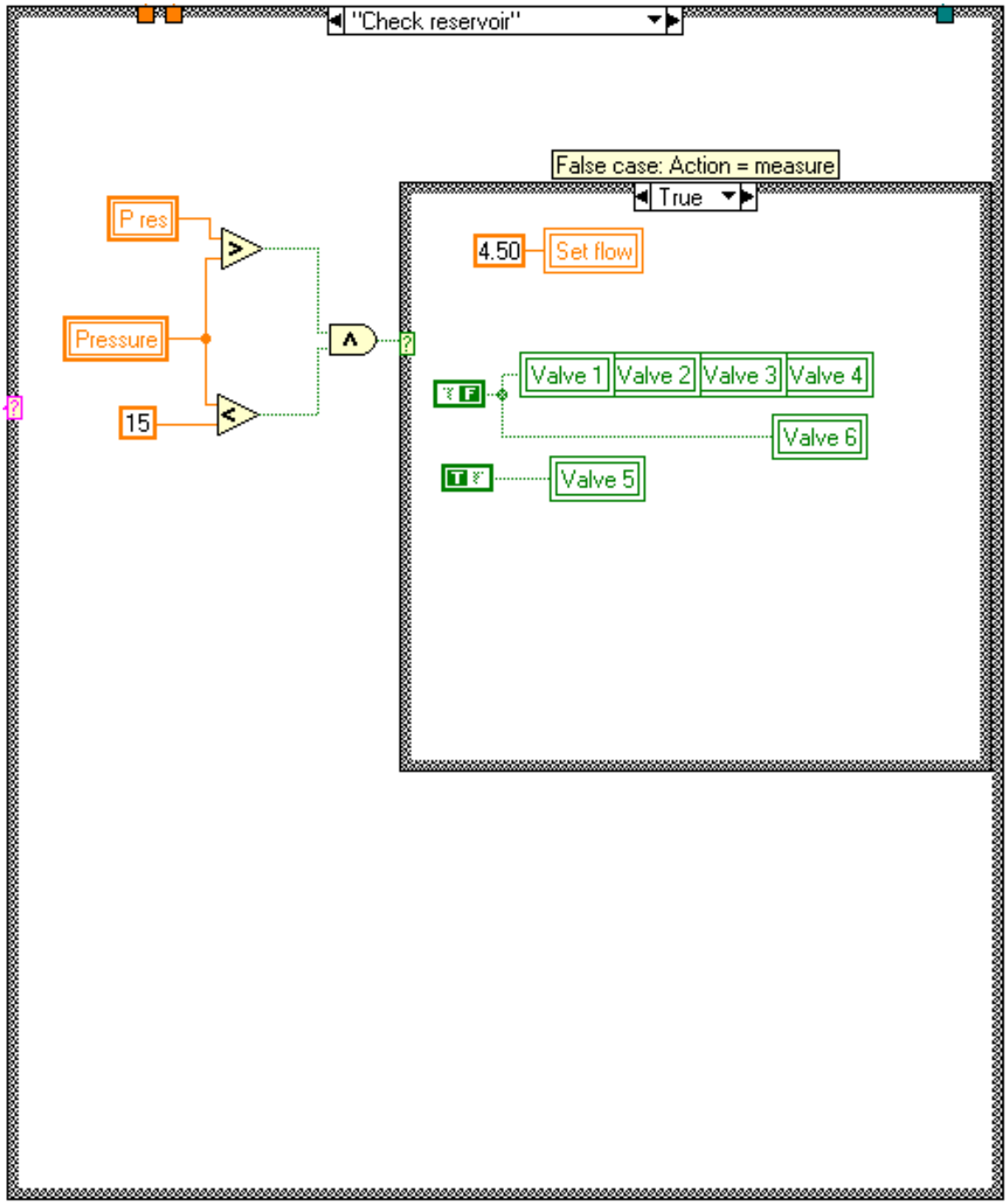

C.III.f Measure

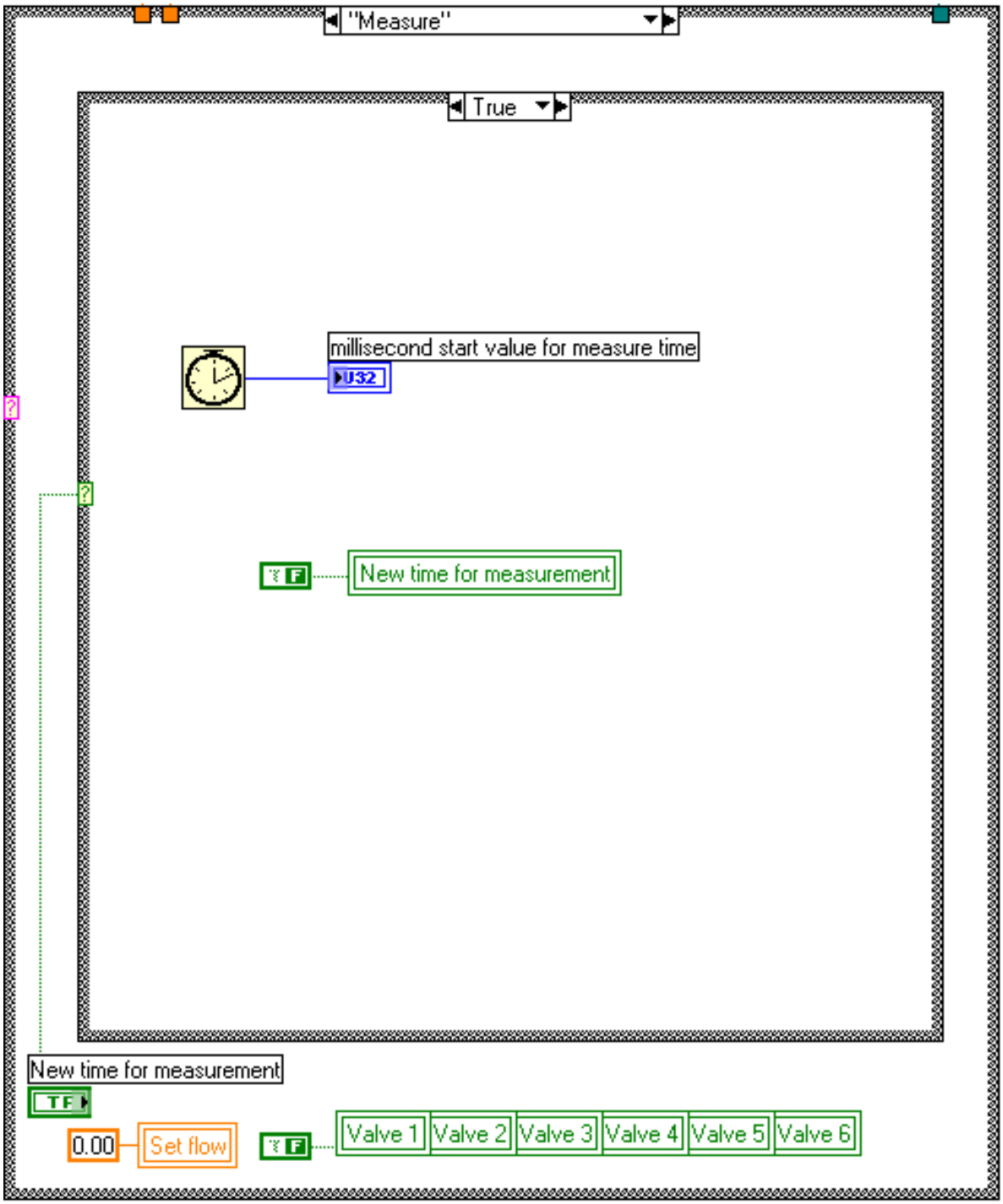

C.III.f.i Automatic PCI 'ON': Continue measure until the change in hydrogen uptake for the current step is smaller than a pre-selected threshold value

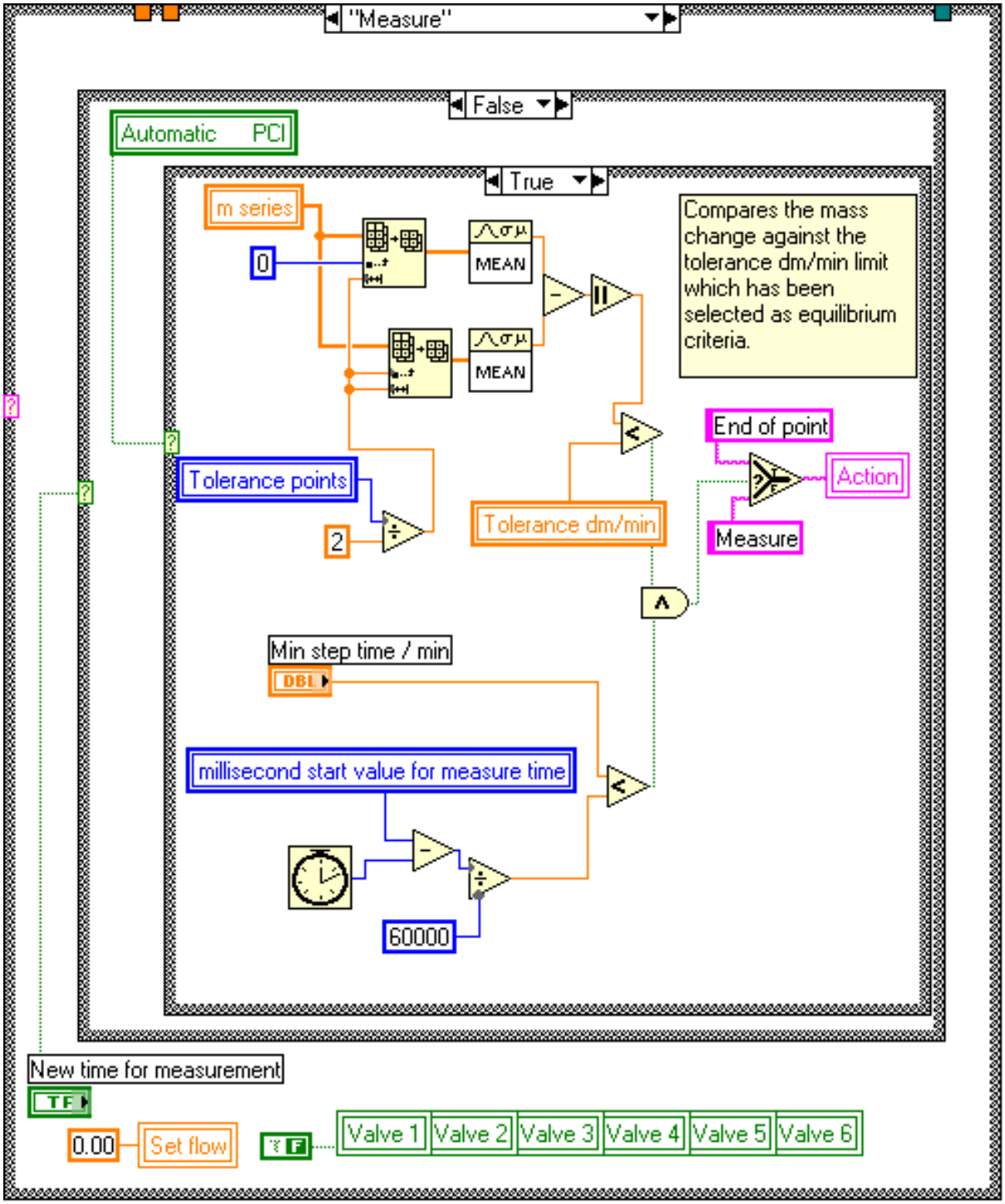

C.III.f.ii Automatic PCI ‘OFF’: Continue measure for the time set by the ‘Step time (min)’ control variable

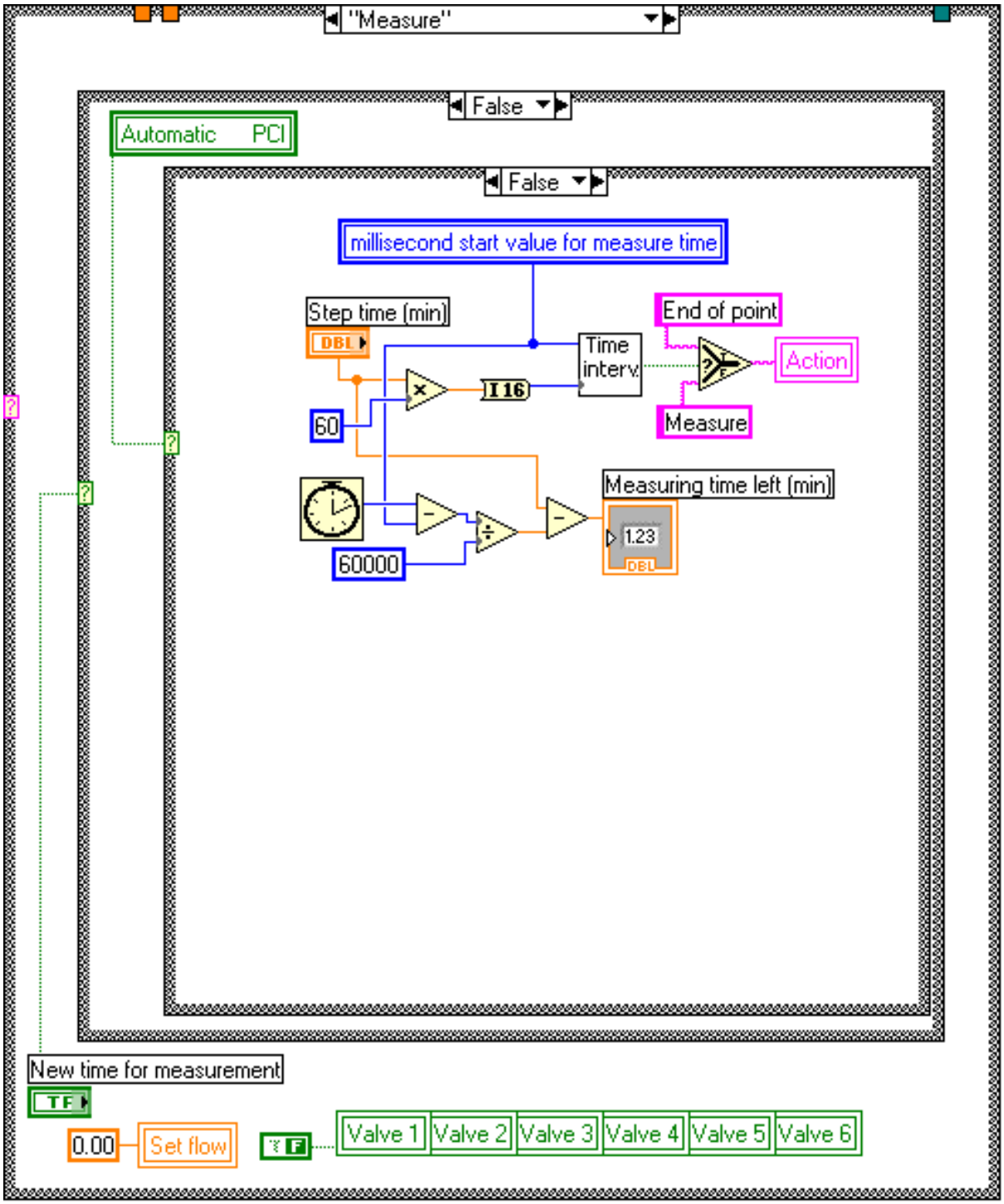

C.III.g End of point (save data to PCI list)

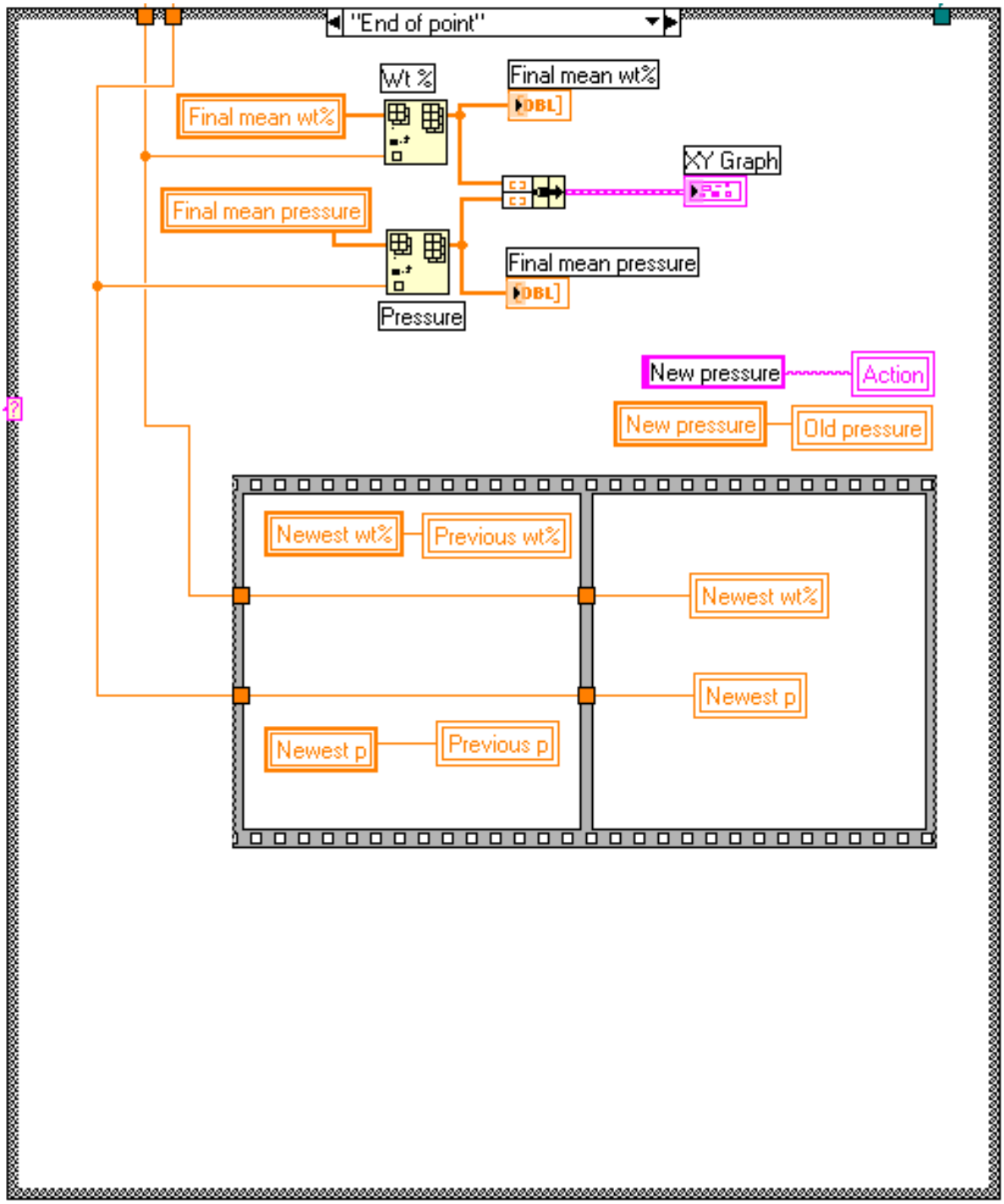

C.III.g End of series (save PCI list to file)

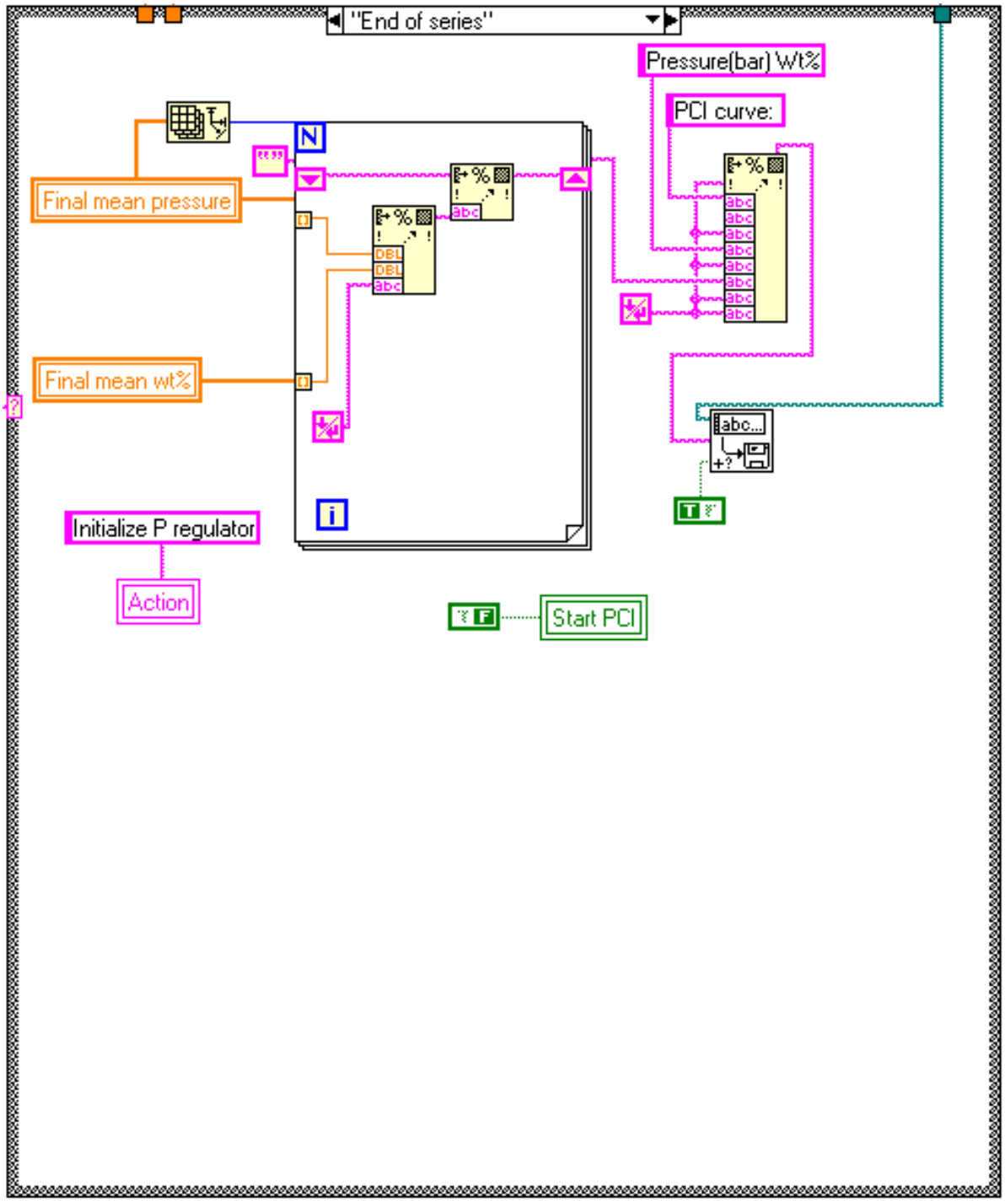

C.IV Write to file

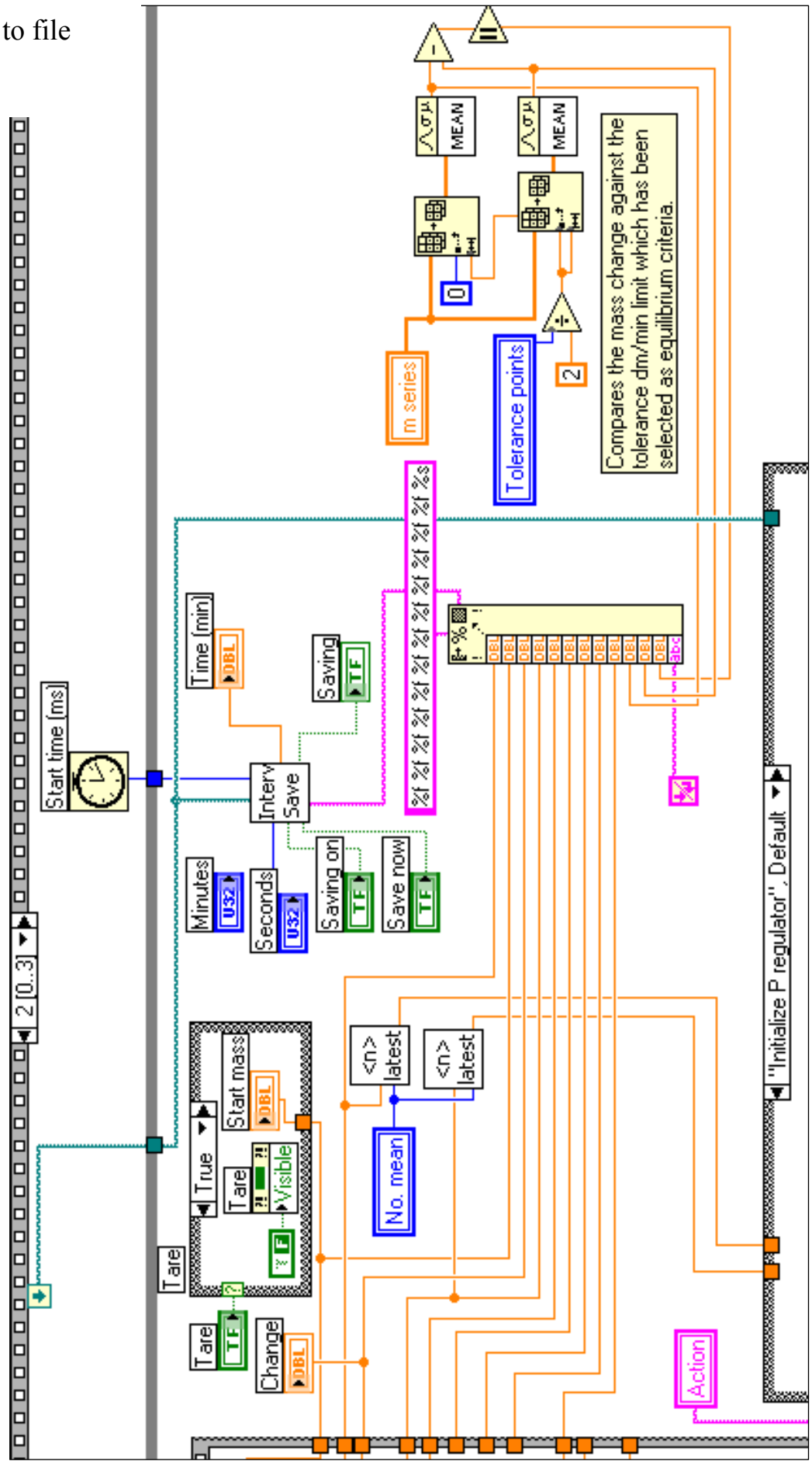

D CLOSE PORT

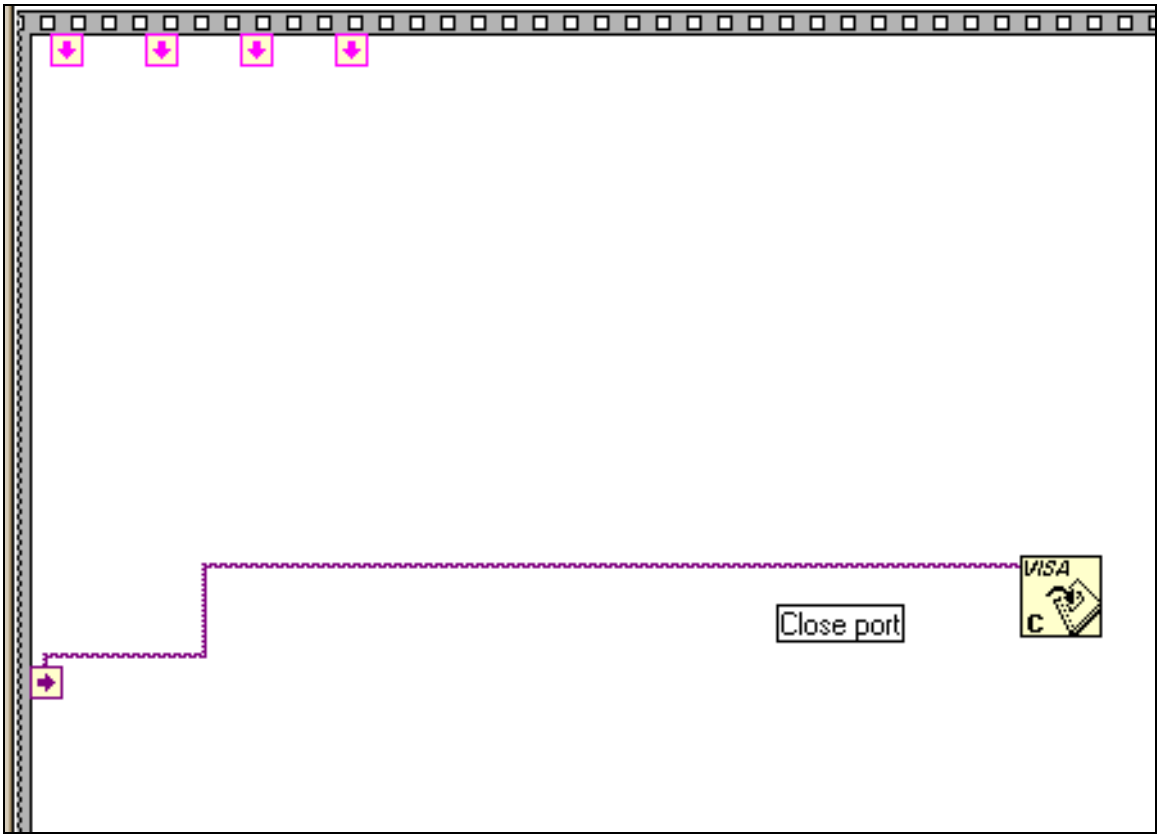

12 PAPERS

Available online at www.sciencedirect.com
ScienceDirect
International Journal of Hydrogen Energy 32 (2007) 1567–1571
International Journal of HYDROGEN ENERGY
www.elsevier.com/locate/ijhydene

High temperature PEMFC and the possible utilization of the excess heat for fuel processing

Jens Oluf Jensen[a,*], Qingfeng Li[a], Chao Pan[a], Andreas P. Vestbø[a], Kasper Mortensen[a], Henrik Nybo Petersen[a], Christian Lau Sørensen[a], Thomas Nedergaard Clausen[a], Jesper Schramm[b], Niels J. Bjerrum[a]

[a]*Department of Chemistry, Building 207, Technical University of Denmark, DK-2800 Lyngby, Denmark*
[b]*Department of Mechanical Engineering, Building 404, Technical University of Denmark, DK-2800 Lyngby, Denmark*

Available online 11 December 2006

Abstract

In this paper simple heat balances are calculated for systems with methanol and methane reformers in combination with a high temperature PEM fuel cell. In the methanol system at least 11.1% of the fuel energy can be saved by using the excess heat from the fuel cell for vaporization of water and methanol if the cell is operated at temperatures between 150 and 200 °C. Similarly, in the methane system, 9.6% can be saved under equivalent conditions. Integration of a high temperature PEM fuel cell with a metal hydride system based on $NaAlH_4$ is considered briefly with respect to desorption heat. Dead-end operation is studied, and stable performance is seen for 100 min at 150 °C without purging. Finally, experiments are reported indicating that preheating of the air has no influence on the fuel cell performance at 150 or 200 °C under moderate load.

Keywords: PEMFC; PBI; Reforming; Methanol; Methane

1. Introduction

PEM fuel cells operated at elevated temperatures of up to 200 °C have been addressed for a number of years in the Materials Science Group at Department of Chemistry [1,2]. The most successful membrane system so far has been phosphoric acid doped polybenzimidazole (PBI). See Fig. 1. The idea of using PBI in fuel cells was first reported by Wainright et al. in 1995 [3]. The benefits of operation at elevated temperature are plentiful. The tolerance to carbon monoxide is increased by many orders of magnitude as the temperature is raised from the normal 80 to 150–200 °C [4]. This is especially of interest when the hydrogen fuel is obtained in line via reforming of organic fuels. With a 200 °C PEM fuel cell no CO clean up is needed apart from a low temperature water gas shift. The PBI/H_3PO_4 membranes are conductive at very low relative humidity and consequently no water management is needed. Moreover, the high working temperature eliminates the possibility of water condensation in pores or channels of the fuel cell. Due to the higher temperature difference to the surroundings thermal management can be satisfactorily performed by a smaller cooling system. All together a simpler and less costly system is possible compared to conventional PEMFC systems.

In this paper, the possible utilization of the excess heat of the fuel cell is addressed. Due to the higher temperature the heat quality is higher and it seems obvious to try to make use of it for fuel processing. Fuel processing in the form of reforming is endothermic and requires a heat input at the reforming temperature. The cases for methanol and methane are treated in the following as steam reforming. Methane reforming takes place at 600–900 °C as follows:

$$CH_4 + H_2O = 3H_2 + CO. \quad (1)$$

It is followed by the water gas shift reaction

$$CO + H_2O = H_2 + CO_2 \quad (2)$$

at about 200 °C at which temperature the equilibrium is in favor of hydrogen and carbon dioxide.

* Corresponding author.
E-mail address: joj@kemi.dtu.dk (J.O. Jensen).

0360-3199/$ - see front matter © 2006 International Association for Hydrogen Energy. Published by Elsevier Ltd. All rights reserved.
doi:10.1016/j.ijhydene.2006.10.034

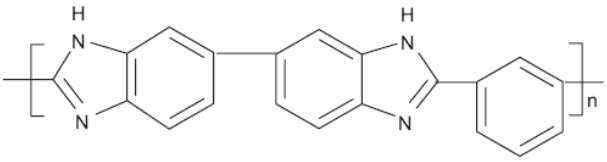

Fig. 1. The repeat unit of the PBI, poly 2, 2′-*m*-(phenylene)-5, 5′-bibenzimidazole.

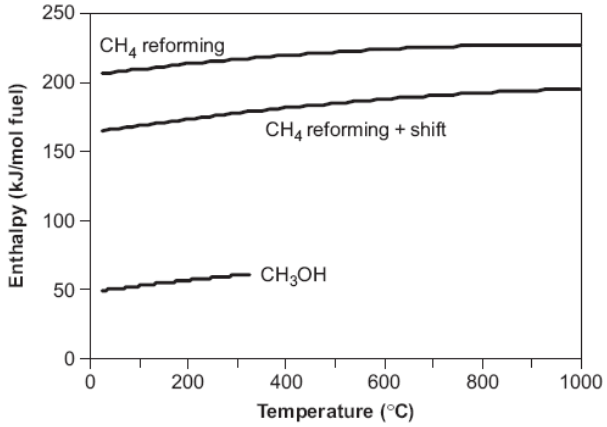

Fig. 2. Enthalpy of the reforming processes for methanol and methane as a function of temperature. For methanol the plotted value covers both reforming and shift as both processes take place in the same reactor. For methane the overall enthalpy of reforming and shift is plotted separately [8].

Methanol reforming takes place at 200–250 °C and no separate shift reactor is needed because the temperature is right for low temperature shift simultaneously and with a final carbon monoxide content below 1 mol%.

$$CH_3OH + H_2O = 3H_2 + CO_2 \quad (3)$$

The heat required for the two processes differs from each other and is a moderate function of temperature. See Fig. 2.

As methanol reforming can be carried out at temperatures in the same order as the working temperature of the high temperature PEMFC, the idea of heat integration is obvious. Experiments with a methanol reformer and a PBI cell at the same temperatures have been reported recently [5,6]. With both units operated at 210 °C the polarization was hardly distinguished from that of pure hydrogen and no CO clean up was applied [6]. In the same study, 92.0–99.9% conversion was calculated in the temperature range from 185 to 260 °C assuming equilibrium with a varied water stoichiometry. Methanol reforming at temperatures below 200 °C is thus possible from a thermodynamic point of view, and a fuel cell was successfully powered by a methanol reformer operated at temperatures as low as 185 °C. However, the conversion rate was slow compared to equivalent experiments at temperatures of 220 °C or higher [6].

In a broad sense, desorption of hydrogen from a metal hydride can also be understood as fuel processing. In the search for higher gravimetric hydrogen storage capacities the compound $NaAlH_4$ is regarded a breakthrough with 4–5 wt% hydrogen available reversibly at temperatures between 120 and 150 °C. Desorption takes place in two steps and the desorption enthalpy was measured by Bogdanovic [7] to be 37 kJ/(mol H_2) for the first step and 47 kJ/(mol H_2) for the second. The weighted average with respect to the liberated hydrogen is 40 kJ/(mol H_2).

2. Experimental

Thermodynamical quantities used for heat calculations were obtained from JANAF [8]. The PBI used in the experimental work was poly 2, 2′-*m*-(phenylene)-5, 5′-bibenzimidazole (Fig. 1) obtained from Celanese or later synthesized [9]. After casting to a thickness of about 50 μm the membranes were doped with phosphoric acid to a level of 5–6 H_3PO_4 molecules pr. repeat unit of PBI. The catalyst applied was platinum on carbon, about 0.5–0.6 mg/cm^2 for all electrodes. Single cells with an electrode area of 256 cm^2 were operated on hydrogen and air at near ambient pressure. In all cases, no humidification was applied. The experimental details for similar electrode and cell preparation are given elsewhere [1,9].

3. Results and discussion

3.1. Heat calculations

In Table 1 the fuel energy contents (heat of combustion) for hydrogen, methanol and methane are listed together with the heat of reforming and evaporation. Based on these figures Sankey diagrams are built for simple reformer/fuel cell systems on methanol and methane (Figs. 3 and 4, respectively). The working point of the fuel cell is arbitrarily chosen as 0.63 V because it reflects 50% electrochemical efficiency with reference to the lower heating value (LHV). All heat calculations are based on the LHV. They are simplified by leaving out the heat balances for heating and cooling the gasses between the different steps, because such a detailed calculation is highly system design dependent as heat to a large extend can be reclaimed by proper choice of heat exchangers. Moreover, the contributions from heating and cooling of the gasses are anyway small compared to the heat for evaporation and reforming. In both cases a minimum fuel overstoichiometry of 20% (fuel stoichiometry, $\lambda_{fuel} = 1.2$) is assumed in accordance with normal practice from CO_2 diluted hydrogen. The unconsumed fuel is meant for combustion in a burner producing high temperature heat.

3.2. Methanol reforming

In the methanol case (Fig. 3) one can see that the energy demand for vaporization and reforming amounts to 19.7% of the initial fuel energy and almost the same as is produced in the burner. Theoretically, the burner should just be able to supply all heat required, but even with moderate heat losses more heat will be necessary through combustion of either primary fuel or hydrogen (higher λ_{fuel}). In case of an 80 °C fuel cell the excess heat cannot be used. Theoretically, the temperature is high

Table 1
Heat calculation of reforming of methanol and methane

(Heat in kJ/mol fuel)	Hydrogen	Methanol	Methane
Heat of combustion			
HHV	−285.8	−726.1	−890.8
LHV	−241.8	−685.5	−850.2
Reforming and shift			
Heat of reforming		58.7 at 250 °C incl. shift	227.2 at 900 °C excl. shift
Heat of shift at 200 °C (1 mol CO)			−40.1
Heat of combustion of nH_2		($n = 3$)	($n = 4$)
HHV		−857.4	−1143.2
LHV		−725.4	−967.2
Heat of combustion of nH_2		($n = 3$)	($n = 4$)
% of primary fuel HHV		118.1%	128.3%
% of primary fuel LHV		105.8%	113.8%
Heat for reforming, as above			
% of primary fuel HHV		8.1%	25.5%
% of primary fuel LHV		8.6%	26.7%
Evaporation of fuel and water			
Heat of evaporation of fuel at b.p.		35.2	
Evaporation of n water at b.p. for reforming and shift		($n = 1$)	($n = 2$)
		40.6	81.2
Total evaporation		75.8	81.2
Heat of total evaporation			
% of primary fuel HHV		10.4%	9.1%
% of primary fuel LHV		11.1%	9.6%

Values are STP unless other temperature stated. "b.p." is boiling point.
Thermodynamical quantities from [8].

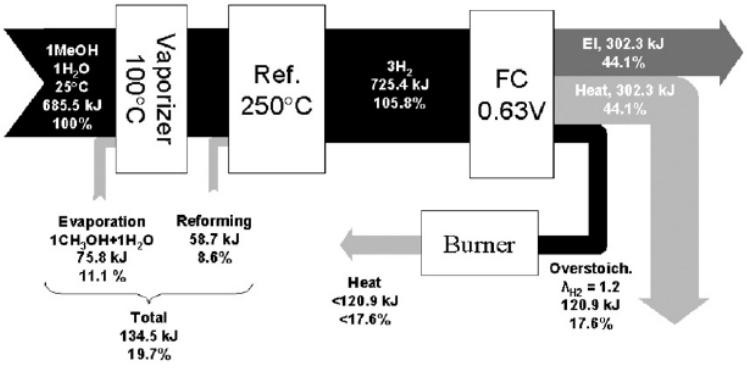

Fig. 3. An idealised energy flow for a methanol/PEMFC system. Heat for gas heating and cooling of gasses is not considered. All values are based on lower heating values and percentages refer to the initial fuel.

enough for methanol evaporation (b.p. 64 °C), but when temperature differences are considered as the driving force for the heat transfer, this becomes somewhat speculative. With a fuel cell operated at 150–200 °C the temperature is high enough for vaporization of both water and methanol, and 11.1% of fuel can be saved. With 44.1% heat energy available even significant heat losses can be accepted. Excess heat for methanol reforming is theoretically possible assuming a lower reforming temperature, but most likely impractical for kinetic reasons. An exception could be methanol reforming within the anode chamber. Anyway, the minimum λ_{fuel} can be maintained in the high temperature case because the burner needs only to provide heat for the reformer, not for evaporation.

3.3. Methane reforming

In the methane case (Fig. 4) water is the only component that has to be vaporized, and the excess heat of a high temperature PEM fuel cell can do this. Here 9.6% (+ losses) can be saved compared to the 80 °C fuel cell system. The heat for methane reforming is significantly larger than methanol, and the temperature is far too high for a utilization of the excess

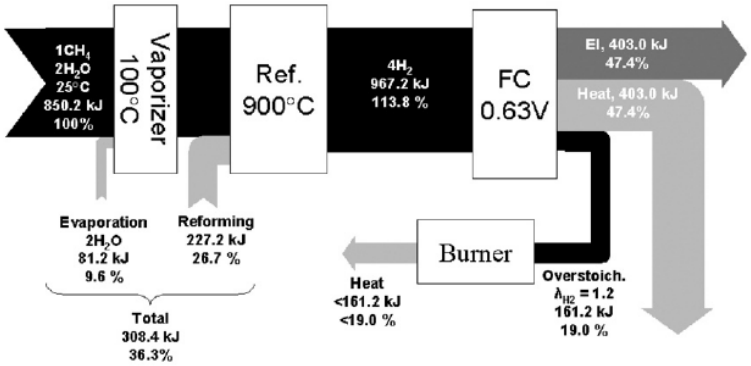

Fig. 4. An idealised energy flow for a methane/PEMFC system. Heat for gas heating and cooling of gasses is not considered. All values are based on lower heating values and percentages refer to the initial fuel.

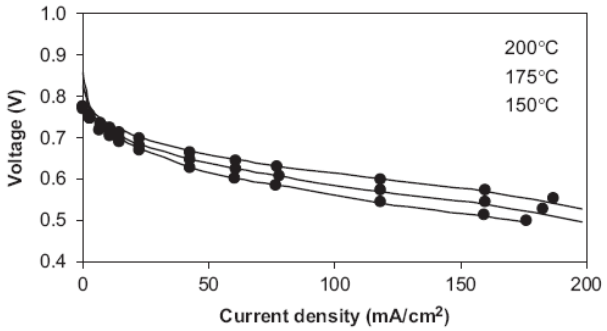

Fig. 5. Polarization curves at three temperatures for dead end operation (markers only) and overstoichimetric operation (lines only).

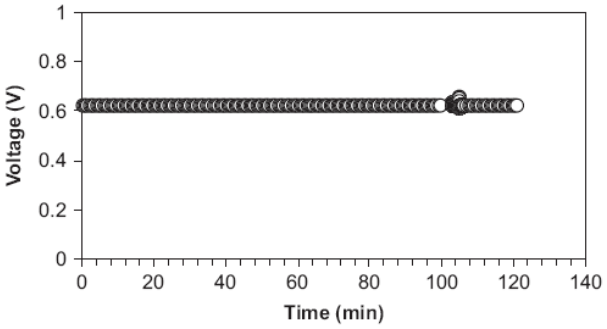

Fig. 6. A single cell operated in dead end mode at 150 °C. After 100 min a short purge was performed.

heat even with a high temperature PEM fuel cell. However, the savings on vaporization limit the theoretical λ_{fuel} to 1.31 in the high temperature PEM fuel cell case while for the low temperature system minimum λ_{fuel} is 1.47. However, in both cases the values must be larger to compensate for heat losses.

3.4. $NaAlH_4$

As mentioned, the heat needed to liberate hydrogen from $NaAlH_4$ is 40 kJ/(mol H_2). This figure corresponds to 16.5% of the LHV of the desorbed hydrogen. When powered by $NaAlH_4$

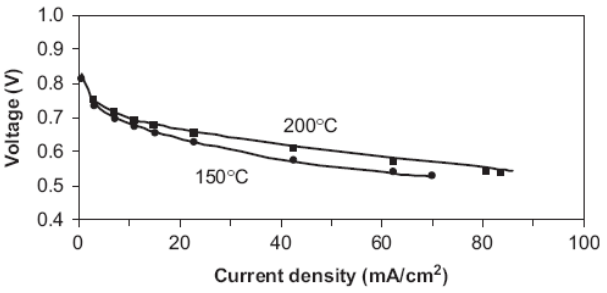

Fig. 7. Polarisation curves measured on a 256 cm^2 cell with (markers only) and without (lines only) preheating the air.

a fuel cell working at 80 °C will then have to use over 16.5% of the fuel to provide the desorption heat. This corresponds to a minimum λ_{fuel} of 1.2. If the electrical conversion efficiency in the fuel cell is, say 50% the system efficiency is brought down to below 41.8% (in reality lower due to losses). When the fuel cell working temperature is significantly higher than the desorption temperature the excess heat can be used instead, and assuming again 50% electrical efficiency, heat of 121 kJ/mol H_2 is theoretically available for the purpose. This issue is discussed in more detail elsewhere [10].

When no hydrogen is needed for the burner to provide heat for hydrogen release in a $NaAlH_4$/high temperature PEM fuel cell system, the question arises whether the cell can be operated in dead-end mode, i.e. with closed exit on the anode side and thus without overstoichiometry ($\lambda_{fuel} = 1.0$). The highest fuel utilisation is obtained this way because fuel is not passed through the cell like the air is. In this mode impurities, if any, are accumulated over time and must be purged regularly. Especially at temperatures below 100 °C water can condense in the anode chamber and measures must be taken to remove it. At higher temperatures this is not the case, and high temperature PEM fuel cells should therefore be ideal for dead-end operation when powered by pure hydrogen. The performance of a single cell in dead-end mode and in overstiochiometric mode is plotted in Fig. 5. It is evident that the dead-end measurements (the markers) correspond to a polarization almost identical to the reference curves (the lines) obtained with a high stoichiometry.

Table 2
Conclusions on fuel stoichiometries and savings in systems with methanol, methane and $NaAlH_4$

Fuel cell temperature	60–80 °C	120–200 °C	200–250 °C
Methanol system			
Evap. of methanol	Not practical	Save 11.1%	Save 11.1%
Evap. of water	Impossible		
λ_{fuel}	>> 1.23	1.2 Burner only heats reformer. FC heats vaporizer	1.2 Plenty of heat for both vaporizer and reformer
Methanol reforming	Impossible	Not practical	Possible
Methane system			
Evap. of water	Impossible	Save 9.6%	Save 9.6%
λ_{fuel}	>> 1.47	>> 1.31	>> 1.31
Methane reforming	Impossible	Impossible	Impossible
$NaAlH_4$			
λ_{fuel}	>> 1.2	1.0	1.0
H_2 liberation	Impossible	Save 16.5%	Save 16.5%

>> Means that considerably higher stoichiometries are expected to compensate for heat losses.
Minimum λ_{fuel} (fuel stoichiometry in the fuel cell) is arbitrarily set to 1.2 because of the dilution effect except in the case of pure hydrogen from $NaAlH_4$.

No real difference is seen. In Fig. 6, a constant performance is shown for 100 min. A short purge after that results in no changes apart from some fluctuations due to pressure disturbance.

3.5. Pre-heating of gasses

Finally, after discussing the utilization of the excess heat, one may ask if a certain portion of the heat produced should be allocated to preheating the air for the cathode. Over time the MEAs (membrane electrode assemblies) have been scaled up from a few cm^2 to our present standard of 16 by 16 cm (256 cm^2). It is our experience that scaling up is accompanied by decreased performance. One reason for this could be the cooling effect of the cold reactant gasses normally applied. Traditional PEMFC often have the gasses heated automatically when the water management is carried out, but in this case without water management gasses are by default at ambient temperature. When the electrode size is increased each gas channel covers a larger electrode area and consequently a larger flow is needed. Especially on the air side this can be expected to cause more cooling in the beginning of each channel leading to lower temperatures and lower performance locally. The performance was measured with and without preheating the air. Fig. 7 shows double polarisation curves measured on the same cell at 150 and 200 °C. The lines are reference curves without preheating. The markers represent measurements with the air preheated to the working temperature of 150 or 200 °C. No significant difference is seen. Judging from this the predicted cooling effect is of minor importance at the moderate loads applied, and poorer performance in large cells cannot be explained this way. Instead the results indicate that a heat exchanger for the cathode air can be omitted.

4. Conclusions

- Simplified heat balances were established for reformer–fuel cell systems fueled by either methanol or methane. The conclusions are summarized in Table 2.
- The use of excess heat for hydrogen liberation from the hydride $NaAlH_4$ was discussed and in that relation it was shown that PBI fuel cells are well suited for operation in dead-end mode at 150 °C. Hundred minutes of totally stable performance without purging was demonstrated. This means that a $NaAlH_4$/high temperature PEM fuel cell system can be fuelled with unit stoichiometry and that a catalytic burner therefore may be omitted in such a system.
- Preheating of the air had no visible effect on the performance at moderate current densities as compared with operation on ambient temperature air.

Acknowledgments

The authors wish to thank the Nordic Energy Research Programme and the European Commission in the 6th Framework Programme for the financial support of the present work.

References

[1] Li Q, He R, Jensen JO, Bjerrum NJ. Fuel Cells 2004;4(3):147–59.
[2] Li Q, He R, Jensen JO, Bjerrum NJ. Chem Mater 2003;15:4896–915.
[3] Wainright JS, Wang J-T, Weng D, Savinell RF, Litt M. J Electrochem Soc 1995;142:L121.
[4] Li Q, He R, Gao J, Jensen JO, Bjerrum NJ. J Electrochem Soc 2003;150(12):A1599–605.
[5] Li Q, Hjuler HA, Hasiotis C, Kallitsis JK, Kontoyannis CG, Bjerrum NJ. Electrochem Solid State Lett 2002;5(6):A125–8.
[6] Pan C, He R, Li Q, Jensen JO, Bjerrum NJ, Hjulmand HA, Jensen AB. J Power Sources 2005;145:392–8.
[7] Bogdanovic B, Brand RA, Marjanovic A, Schwickardi M, Tolle J. J Alloys Comp 2000;302:36–58.
[8] Chase MW. JANAF thermochemical tables, 3rd ed., J Phys Chem Ref Data 14, (suppl 1) (1985).
[9] He R, Li Q, Xiao G, Bjerrum NJ. J Membr Sci 2003;226:169–84.
[10] Jensen JO, Li Q, He R, Pan C, Bjerrum NJ. J Alloys Comp 2005;404–406:653–6.

ELSEVIER

Journal of Alloys and Compounds 446–447 (2007) 723–728

Journal of ALLOYS AND COMPOUNDS

www.elsevier.com/locate/jallcom

The energy efficiency of onboard hydrogen storage

J.O. Jensen*, A.P. Vestbø, Q. Li, N.J. Bjerrum

Department of Chemistry, Kemitorvet, Building 207, Technical University of Denmark, DK-2800 Lyngby, Denmark

Received 31 October 2006; received in revised form 30 March 2007; accepted 2 April 2007
Available online 13 April 2007

Abstract

A number of the most common ways of storing hydrogen are reviewed in terms of energy efficiency. Distinction is made between energy losses during regeneration and during hydrogen liberation. In the latter case, the energy might have to be provided by part of the released hydrogen, and the true storage density is then equivalently smaller. Systems covered include compressed and liquid hydrogen, reversible and irreversible metal hydrides, and methanol and ammonia.

Keywords: Hydrogen storage; Metal hydride; Compressed hydrogen; Liquid hydrogen; Efficiency

1. Introduction

The vision of a hydrogen-based energy system faces several technical challenges that will act as show stoppers if not dealt with. One key issue is hydrogen storage, and in particular, onboard hydrogen storage in vehicles. Generally speaking, the production of hydrogen from renewable sources only makes sense, if hydrogen is stored for later use or for use elsewhere. Otherwise, one might as well use the extracted electricity directly (one exception could be the use of biofuels in a fuel cell through a stage where hydrogen is liberated by reforming for immediate use, but this is not really within the idea of hydrogen as an energy carrier).

The publications and discussions on possible storage techniques often focus solely on the storage density, and the question of round trip energy efficiency is then forgotten. The round trip is in this relation the full circle from primary hydrogen through storage, transfer, and re-extraction of hydrogen. The different steps in the chain are associated with different energy balances that must be taken into account when storage systems are evaluated. In small systems, such energy losses might, although significant, be of less importance, but for vehicular applications, they cannot be neglected. After all, improved efficiency is one of the arguments when future fuel cell vehicles are compared with conventional ones.

Numerous techniques for storing hydrogen have been suggested, and they can be roughly ordered in a line ranging from pure physical storage to a gradually more chemical technique. A tendency that goes with this is that the more chemical the technique, the less easily available is the hydrogen. This less easy availability of hydrogen is seen as higher energy demands for hydrogen release and/or higher release temperatures.

The following comprises the different ways being considered for hydrogen storage: (1) compressed hydrogen is kept in a dense state by external physical forces only. (2) Liquid hydrogen is kept together by weak chemical forces (van der Waals) at very low temperature but at ambient pressure. Heat must be supplied to release hydrogen through boiling, but due to the low boiling point of 20 K, the heat can be taken from the surroundings or any waste heat. (3) Adsorbed hydrogen is also bound weakly (van der Waals) to a substrate either through a high pressure or at low temperatures. Release is comparable to either compressed or liquid hydrogen or a combination. (4) Hydrogen stored in interstitial metal hydrides is bound into interstitial positions in a host metal alloy in a more or less metallic way. This bond is stronger than the van der Waals forces mentioned before and a significant amount of heat is required to release hydrogen. (5) In the true chemical systems, real chemical bonds ranging from ionic to covalent are formed between hydrogen and the carrier atoms. The hydrogen release reactions in these cases typically

* Corresponding author. Tel.: +45 45 25 23 14; fax: +45 45 88 31 36.
E-mail address: joj@kemi.dtu.dk (J.O. Jensen).

0925-8388/$ – see front matter © 2007 Elsevier B.V. All rights reserved.
doi:10.1016/j.jallcom.2007.04.051

require a significant energy input and also elevated temperatures. This group comprises numerous solids, liquids, and gases, such as hydrocarbons, alcohols, ammonia, and chemical hydrides. Most of these are not reversible hydrogen carriers, but are manufactured through chemical synthesis. All of these techniques have their own energy balances for both storage and release of hydrogen and this is the focal point of the present work.

2. The approach

The aim of this study is first of all to compare the fundamental limitations and advantages of the different hydrogen storage techniques in terms of energy efficiency and capacity really available. A true comparison would involve a detailed analysis of whole systems. Such analyses are truly relevant but also complicated with numerous assumptions on which the outcome will strongly depend. Instead, transparency is aimed at with the hope that the conclusions are less questionable, although they do not tell the whole story.

Throughout, the lower heating value (LHV) of the fuel is used instead of the higher heating value (HHV). This is because in several of the systems, heat for hydrogen liberation must be supplied at temperatures above 100 °C likely by combustion of hydrogen. It is also assumed that hydrogen or a hydrogen mixture is released at no less than ambient pressure.

3. Compressed hydrogen

3.1. Energy for storage

The theoretical minimum work needed for gas compression can be calculated based on integration of the infinitesimal pressure–volume work, dw

$$dw = V\,dp \tag{1}$$

where V is the tank volume and p is the pressure. Assuming ideal gas behaviour, integration of Eq. (1) results in the expression of the work, W, of ideal isothermal compression

$$W = p_0 V \ln\left(\frac{p_1}{p_0}\right) \tag{2}$$

where p_0 and p_1 are initial and final pressures. At hydrogen pressures over 100 bar, deviations from non-ideality become significant in this connection, and the compression factor, Z, shall compensate for the non-ideality. The real gas equation is then

$$PV = ZnRT \tag{3}$$

Z depends on both pressure and temperature and is tabulated elsewhere [1]. At 300 K and pressures up to 1000 bar, the compression factor is modelled well as

$$Z = 1 + k_{z,300}\left(\frac{p}{p^\circ}\right) \tag{4}$$

where $k_{z,300} = 0.000631$, and p° is the standard pressure. Integration including Eqs. (3) and (4) gives

$$W = p_0 V\left[k_{z,300}\frac{(p_1 - p_0)}{p^\circ} + \ln\left(\frac{p_1}{p_0}\right)\right] \tag{5}$$

However, the compression is never isothermal, as heat is formed during the process. If the compression is very slow, most heat will dissipate to the surroundings, but in practical high-pressure systems, a significant amount of heat is formed. The other extreme is adiabatic compression in which all heat produced is kept in the gas by ideal insulation. The work of adiabatic compression is

$$W = \frac{\gamma}{\gamma - 1} p_0 V\left[\left(\frac{p_1}{p_0}\right)^{(\gamma-1)/\gamma} - 1\right] \tag{6}$$

where γ is the ratio of specific heats (C_p/C_v). $\gamma = 1.41$ for hydrogen. The work of adiabatic compression to a fixed final density is much larger than the work of isothermal compression because the heat accumulated creates a higher pressure for the compressor to work against.

Both isothermal and adiabatic compression are plotted in Fig. 1 as a function of the final pressure. Isothermal compression is the absolute minimum theoretically possible, and in reality, due to the discussed heat effect and losses in the compressor, the work of compression lies somewhere between the two curves.

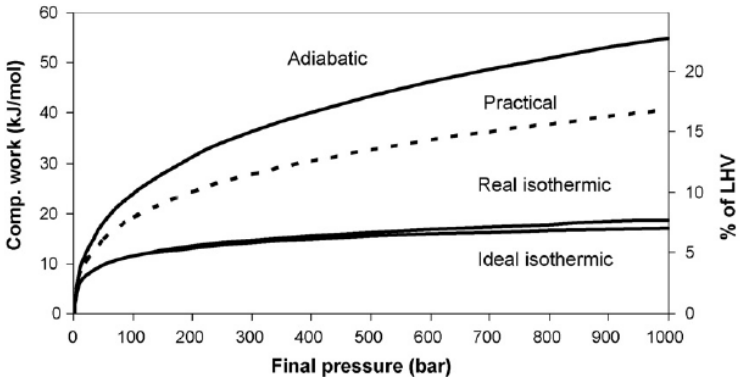

Fig. 1. The energy required to compress hydrogen from 1 bar to the final pressure specified on the primary axis.

3.2. Energy for release

One strong advantage of compressed hydrogen it that it is easily available at a pressure high enough for fast transport through tubes. Even though the pressure vessel will cool during release, the pressure will in most cases still be way above ambient pressure. Therefore, no energy is needed for the release. In principle, part of the compression energy can even be reclaimed via an expander, but as it adds to complexity and cost, it can be argued whether or not it is feasible.

3.3. Discussion

The work of compression in real systems is estimated by Bossel et al. [2] and Weindorf et al. [3]. According to these studies, compression to 800 bar is possible using 18% (Bossel) or 13% (Weindorf) of LHV. The estimated curve for a real system added to Fig. 1 is between these values. Compression to a final pressure of 800 bar then costs 15.5% of LHV.

One way to minimize the work of compression is to produce hydrogen by high-pressure electrolysis. The extra voltage (corresponding to energy) for reducing hydrogen at high pressure is close to the theoretical value because the reaction kinetics are very fast.

It is evident from Eq. (2) that the minimum ideal work of compression of 1 mol hydrogen from 100 to 1000 bar is the same as from 1 to 10 bar. This means that there is a significant benefit even if the electrolyser is operated at just 10–50 bar. Industrial electrolyzers working at 32 bar are commercially available today [4].

4. Liquefied hydrogen

4.1. Energy for storage

A simple theoretical pathway for liquid hydrogen is to cool it from room temperature to the boiling point at 20 K and then condense it. The average heat capacity in the interval is 28.48 J/mol K, and the heat of vaporization at 20 K is 892 J/mol [5]. Based on this, the minimum energy required is 8.81 kJ/mol H_2 or 3.7% of LHV. However, liquefaction is carried out via a series of different techniques and according to an energy analysis for that, the theoretical energy demand is 28.4 kJ/mol H_2 [2] or 11.8% of LHV.

4.2. Energy for release

Because the temperature is very low compared to the surroundings, all heat for hydrogen evaporation should be available. Nevertheless, in practical systems, a built-in electrical heater is often used because heat transfer fluids freeze if passed through heat exchange tubes in the tank. In this study, it is assumed that heat from the surroundings is used.

4.3. Discussion

The practical energy demand for liquefaction is significantly larger and depends on the size of the plant. Today, the energy demand in a modern plant is on the order of 40–45% of LHV, but according to Bossel et al. [2], 35% and to Weindorf et al. [3], 21% of LHV should be possible in very large liquefaction plants.

5. Adsorbed hydrogen

It is the general experience that sorption capacities of over 1% are only possible in cryogenic systems at, say 77 K (liquid N_2). This, as well as the fact that the sorption properties of different materials differ a lot, makes calculation of the energy balance quite complex. When, on top of that, hydrogen storage by adsorption has not yet shown advantages over the other techniques discussed here, the calculation was not attempted.

6. Reversible metal hydrides

The term “reversible hydride” refers to both interstitial and complex or chemical hydrides as long as they can be charged as well as discharged by direct solid/gas reactions (or liquid/gas).

6.1. Interstitial hydrides

Interstitial hydrides are the most studied metal hydride systems for hydrogen storage. Examples are plentiful, such as $LaNi_5H_6$, $TiFeH_{\sim 2}$, and $LaNi_5$-based alloys for nickel metal hydride batteries. They are considered very safe and easy to operate, and their main drawback apart from the price in some cases is the fact that the hydrogen storage capacity (with few exceptions) is below 2 wt.%. One convenient characteristic is that the alloys can be tailored to a moderate equilibrium pressure of a few bars at ambient temperature. The heat of absorption is then around −30 kJ/mol H_2 or 12% of LHV. During charge, this heat is liberated. In small canisters, the heat can be exchanged with the surroundings, but in larger systems like in a vehicle, active cooling by water is necessary. The energy balance of such a cooling system depends highly on the charging rate aimed at.

When hydrogen is liberated, the hydride cools and the plateau pressure must still be above ambient pressure to avoid subsequent compression. This implies that the plateau pressure will be correspondingly higher when the hydride is heating up during charge and the charging pressure must match that. A 20–50 bar charging pressure can be suggested. Based on the discussion above, compression to 20 bar is set to 4–5% of LHV (or 3% with isothermal compression).

The amount of heat for desorption is the same as for absorption. It can be taken from the excess heat of the fuel cell or combustion engine provided that the temperature is high enough. The interstitial hydride can be designed for that.

6.2. Other reversible hydrides

Other reversible hydrides obey the same thermodynamic laws but possibly with other pressure–temperature characteristics. They are not as easily tailored, and the reaction enthalpy is generally more or less fixed.

Table 1
Desorption properties of selected reversible metal hydrides

Hydride	Rev. capacity (wt.%)	Heat of desorption (kJ/mol H_2)	Temperature for 1 bar (°C)
Interstitial MH	1–2	~30 (~12.4% of LHV)	Near room temperature
MgH_2	7.6	74.5 (30.8% of LHV)	300
Mg_2NiH_4	3.6	64.5 (26.7% of LHV)	255
$NaAlH_4$ (one step)	3.7	37 (15.3% of LHV)	35
Na_3AlH_6	1.9	47 (19.4% of LHV)	110
$NaAlH_4$ (two steps)	5.6	40 (16.5% of LHV)	–

Examples of other reversible metal hydrides are MgH_2, Mg_2NiH_4, and $NaAlH_4$. The two magnesium-based hosts are both characterized by one flat plateau, while $NaAlH_4$ desorbs hydrogen in two steps with different stabilities. The first step is $NaAlH_4 \leftrightarrow (1/3)Na_3AlH_6 + (2/3)Al + H_2$, and the second step is $(1/3)Na_3AlH_6 + (2/3)Al + H_2 \leftrightarrow NaH + Al + (3/2)H_2$ [6].

The key desorption properties of the mentioned hydrides are listed in Table 1. The column "Temperature for 1 bar" is based on thermodynamics. For kinetic reasons, $NaAlH_4$ needs temperatures of around 150 °C even when Ti-doped. This means that the charging hydrogen pressure must be on the order of 100 bar, which assuming isothermal compression, takes 4.8% of LHV or practically 7–8% of LHV in reality. The other systems can be charged at low pressures like the interstitial hydrides.

7. Irreversible hydrides

7.1. $NaBH_4$

$NaBH_4$ does not easily liberate hydrogen like the hydrides discussed so far, but it reacts with water over a catalyst. $NaBH_4$ is stored in an alkaline aqueous solution in which it is stable. When passed over a catalyst the following reaction takes place

$$NaBH_4 + 2H_2O \rightarrow NaBO_2 + 4H_2 + \text{Heat} \quad (7)$$

The reaction is exothermic with the enthalpy −212 kJ/mol $NaBH_4$ or −53 kJ/mol H_2 (22% of LHV). The hydrogen storage capacity is 21.2 wt.% disregarding the water, but the practical capacity is much lower due to the water. Besides the role as a reactive solvent, the water also acts as a heat sink for the heat liberated during the process. The system is commercialized by Millennium Cell®, and several demo cars have been fitted with such a system. The concept can also be used directly in alkaline fuel cells with the catalyst being the anode catalyst [7].

Being irreversible, $NaBH_4$ must be regenerated through other chemical pathways. As a minimum, the 212 kJ/mol must be supplied during that process, but the real number is significantly larger and depends on how regeneration is done.

8. Methanol and ammonia

In this group, the hydrogen evolution reactions are characterized by equilibria with both reactants and products in the gas phase. There is no such thing as a desorption temperature at which the hydrogen pressure is 1 bar. The minimum hydrogen release temperature is therefore chosen as the temperature at which kinetics are reasonably fast and the equilibrium is strongly in favour of hydrogen formation.

The liberated hydrogen is in these cases mixed with either carbon dioxide or nitrogen. This fact affects the way a fuel cell is fuelled. As the fuel part of the mixture is consumed, the inert gas content increases, and this dilution effect can lead to local starvation of the electrode and poor performance. To overcome this problem, fuel is fed in excess of at least 20% (this problem can to some extent apply to any fuel cell operating below the boiling point of water because of water vapour accumulation followed by condensation. However, it can be solved by eventual purging without large losses). The overstoichiometry is labelled λ. λ = 1 means strictly stoichiometric and λ = 1.2 means 20% excess. The 20% excess fuel is normally combusted in a burner, and the resulting heat can then be used for fuel processing.

8.1. Methanol (CH_3OH)

Methanol can be steam reformed according to

$$CH_3OH + H_2O \rightarrow CO_2 + 3H_2 \quad (8)$$

The hydrogen storage capacity is 18.8 wt.% disregarding the water. The process is fast at 230–250 °C with a suitable catalyst, and the equilibrium is strongly in favour of hydrogen. The enthalpy of reaction at 250 °C is +58.7 kJ/mol CH_3OH, +19.6 kJ/mol H_2 or 8.1% of LHV of the hydrogen. Prior to reforming, methanol and water must be evaporated and this takes another +75.8 kJ/mol methanol or 10.5% of LHV of the hydrogen. The total minimum requirement is then 18.6% of LHV of the hydrogen. Moreover, the energy for evaporation can be taken from the waste heat of a fuel cell provided it is operated above 100 °C. In that case, only 8.1% of LHV is needed for fuel processing. This should be easily obtained from the excess stoichiometry assuming λ = 1.2.

8.2. Ammonia (NH_3)

Ammonia is sometimes considered as an attractive onboard hydrogen carrier because of its high hydrogen content of 16.6 wt.%, the absence of carbon, and the easy storage. At room temperature, its vapour pressure is less that 10 bar and consequently it can be stored as a liquid at moderate pressure. The major drawbacks are its chemical properties and its stability. It

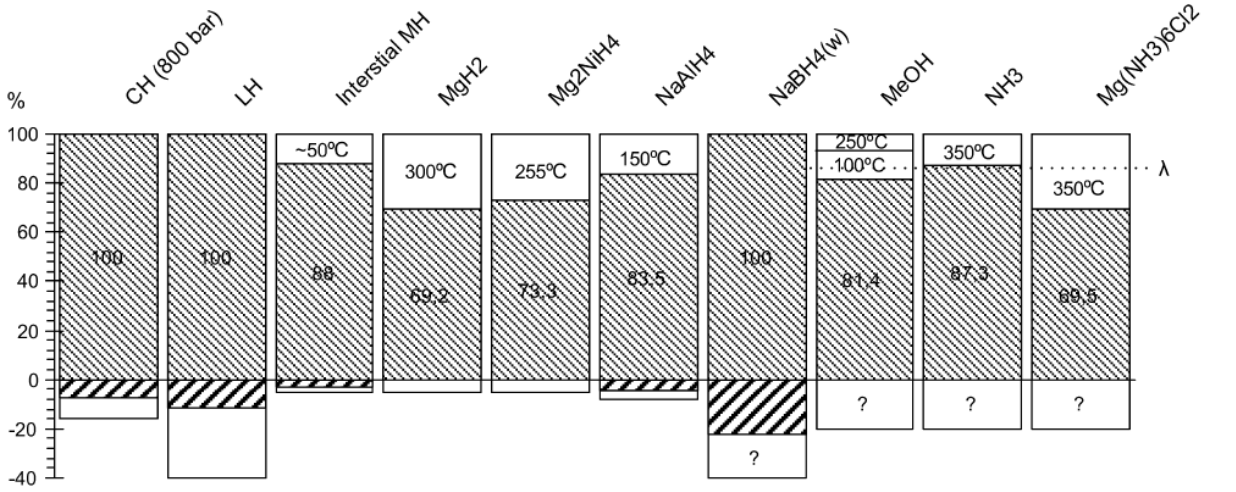

Fig. 2. Maximum hydrogen storage efficiencies of the storage systems. Onboard hydrogen is set to 100%. Negative columns represent energy to charge the system. White fractions in the positive columns are the heats for hydrogen liberation. White parts in the negative columns are the practical energy demands exceeding the theoretical minimum for charging the system.

is corrosive and poisonous. As a base, it reacts with acids and it is therefore considered a poison to PEM fuel cells because it reacts with the perfluorosulfonic acid membrane even at levels of 10 ppm [8]. Solid oxide fuel cells are claimed to be able to run on ammonia.

The process of ammonia splitting is endothermic:

$$NH_3 \rightarrow 0.5N_2 + 1.5H_2 + 30.6\,\text{kJ/mol}\,H_2 \text{ or } 12.7\% \text{ of LHV} \quad (9)$$

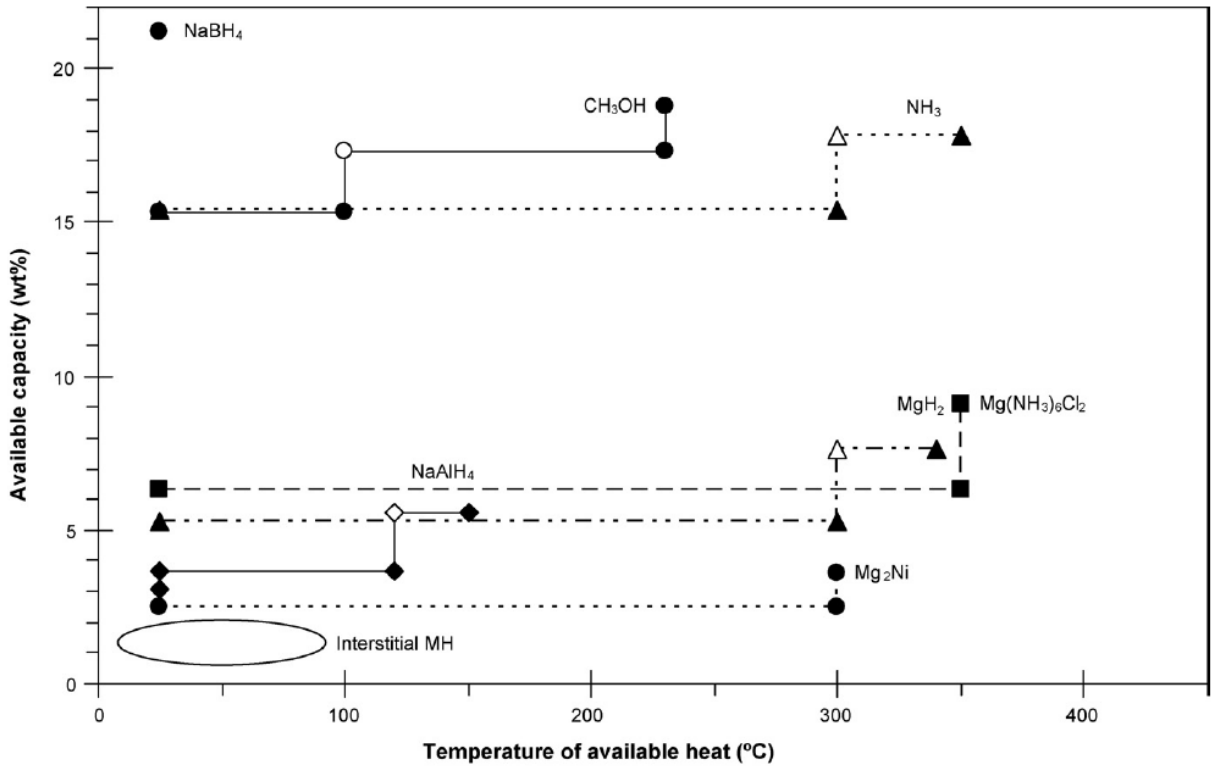

Fig. 3. The maximum available hydrogen from different storage techniques as a function of temperature of available heat. Only the host material is considered, not the tank. Open markers represent thermodynamic values and filled markers represent values assumed kinetically realistic.

and thus, high temperature and low pressure favours hydrogen formation.

If the pressure is set to 1 bar and only a few percent of ammonia are accepted for a subsequent clean-up process, then the temperature must be at least 300–400 °C, and the reaction heat must be supplied at that temperature (practically the temperature cannot be lower for kinetic reasons either).

Ammonia synthesis is exothermic, and in principle, the heat produced can be utilized. Today however, ammonia is manufactured from natural gas and nitrogen from the air, and the plants are consuming energy. A minimum energy required for synthesis is not estimated.

One approach addressing the safety issue is to store ammonia as a complex with a salt, e.g., $MgCl_2$. This idea was recently presented as hydrogen storage in tablet form [9]. Dry $MgCl_2$ can reversibly take up six molecules of ammonia, and the vapour pressure of ammonia becomes many orders of magnitude smaller. Moreover, in contrast to the hydrides, the complex can be stored in air with only a slow liberation of ammonia. The complex contains 9.1 wt.% hydrogen. Liberation of ammonia is endothermic and the enthalpy for the process is +43 kJ/mol H_2 [9] or 17.8% of LHV. When the enthalpy for ammonia splitting is added, the overall minimum energy is +75 kJ/mol H_2 or 30.5% of LHV. Liberation of all NH_3 requires a temperature of 350 °C, although 2/3 of the ammonia is liberated at 200 °C. The system is reversible with respect to ammonia storage, but not with respect to hydrogen storage. Ammonia can be charged onboard, but hydrogen cannot, and ammonia must be synthesized in a plant.

9. Heat available from fuel cells

Fuel cell systems operate with different efficiencies, but in most cases, at least 50% of the fuel energy is liberated as heat due to different losses, mainly in the fuel cell. This corresponds to 120.9 kJ/mol H_2 (LHV) and is plentiful for any of the storage systems discussed here, even with large transfer losses. The determining factor is the working temperature of the fuel cell (or the exhaust temperature of the combustion engine) because the heat must be delivered at the working temperature of the storage device. Today the PEM fuel cell is almost exclusively considered for vehicles, due to, among other things, the low working temperature of around 80 °C. This advantage becomes a disadvantage when heat is needed at higher temperatures, but today there are PEM fuel cells with working temperatures up to 200 °C [10].

10. Conclusion/comparison

In Fig. 2, the maximum hydrogen storage efficiencies of the different storage systems are compared. For each system, the onboard hydrogen content is arbitrarily set to 100%. A top fraction is kept white, representing the energy that must be supplied as heat for hydrogen liberation. This part can be reclaimed if waste heat is available at the temperature indicated. If heat is not available, fuel must be burned to provide it, thus limiting the practical storage capacity. The negative columns represent the energy consumption offboard, i.e., for charging the hydrogen. The striped parts are the theoretical minima and the white parts are the excess necessary in reality. These values are relevant to the overall energy efficiency, but they do not reduce the practical storage capacity onboard.

In Fig. 3, the available storage capacities are plotted as a function of temperature of the waste heat available (e.g., from a fuel cell).

Acknowledgements

The authors wish to thank Nordic Energy Research Programme and Danish Energy Authority for the financial support of the present work.

References

[1] R.H. Perry, D.W. Green, Perry's Chemical Engineers' Handbook, sixth ed., Mc Graw-Hill, 1984.
[2] U. Bossel, B. Eliasson, G. Taylor, The Future of the Hydrogen Economy: Bright or Bleak? Version of 15 April 2003 updated for distribution at the 2003 Fuel Cell Seminar 3–7 November 2003, http://www.efcf.com/reports.
[3] W. Weindorf, U. Bünger and J. Schindler, Comments on the paper by baldur Eliasson and Ulf Bossel "The future of the hydrogen Economy: bright or bleak". L-B-Systemtechnik GmbH, LBST (available from http://www.hyweb.de, archive 15-07-2003).
[4] IHT Industire Haute Technologie, http://www.iht.ch.
[5] Values by Air Liquide.
[6] B. Bogdanovic, R.A. Brand, A. Marjanovic, M. Schwickardi, J. Tolle, J. Alloys Compd. 302 (2000) 36–58.
[7] Z.P. Li, B.H. Liu, K. Arai, N. Morigazaki, S. Suda, J. Alloys Compd. 356–357 (2003) 469–474.
[8] R. Halseid, P.J.S. Vie, R. Tunold, J. Power Sources 154 (2006) 343–350.
[9] C.H. Christensen, et al., J. Mater. Chem. 15 (2005) 4106–4108.
[10] Q. Li, R. He, J.O. Jensen, N.J. Bjerrum, Fuel Cells 4 (3) (2004) 147–159.

ELSEVIER

Journal of Alloys and Compounds 446–447 (2007) 703–706

Journal of ALLOYS AND COMPOUNDS

www.elsevier.com/locate/jallcom

Development of a high-pressure microbalance for hydrogen storage materials

Andreas Peter Vestbø *, Jens Oluf Jensen, Niels J. Bjerrum

Materials Science Group, Department of Chemistry, Technical University of Denmark, Building 207, DK-2800 Lyngby, Denmark

Received 30 October 2006; received in revised form 29 March 2007; accepted 2 April 2007
Available online 12 April 2007

Abstract

Pressure–composition isotherms (PCI's) help to determine thermodynamic properties related to hydrogen uptake of materials. PCI's are normally obtained volumetrically with a Sieverts type apparatus or gravimetrically with a microbalance. A potential problem with the gravimetric technique is that the sample is momentarily exposed to air when transferring it to the system often causing unwanted changes such as oxidation and reaction with moisture in the air. In this study, a high-pressure microbalance was built from scratch inside a glove box with inert atmosphere. The system consists of an electromagnetic microbalance, pressure resistant casing for up to 100 bar hydrogen, a flow system for hydrogen and inert gas, heating elements for temperature control, and software for controlling the system. Thermal convection effects are observed and dampened by heating on both the sample and a counterweight. The precision of the mass measurements for a 1 g sample was ±5 μg, and this range proved to be the same independent of pressure and temperature.

Keywords: Metal hydrides; Hydrogen absorbing materials; Gas–solid reactions; Thermodynamic properties; High-pressure

1. Introduction

Much effort has been put into characterizing and experimenting on materials in the search of a practical hydrogen storage system. Following studies of a broad range of conventional hydrides, the discovery of Ti-doped sodium alanate by Bogdanovic and Schwickardi [1] as a material for a reversible, relatively fast, high capacity system (around 5.6 wt.%) operating under 200 °C led to an interest for the so-called complex hydrides. A further breakthrough appeared in 2002 when Chen et al. published results [2] that showed that systems based on lithium nitride would yield high capacity reversible systems. Since then many results have broadened the field leading to groundbreaking results [3–9].

In the continuing efforts to discover new and more practical hydrogen storage systems it is worth looking at the equipment for characterization of the materials used. In particular, the enthalpy of hydriding, and the gravimetric and volumetric capacities as a function of operating temperature and pressure are of much use in order to test the practicality of the system. In order to determine these properties, it is useful to record pressure–composition isotherms (PCI's), which normally yields pressure plateaus during which either a phase change or chemical reaction occurs. The thermodynamic relationship between the hydrogen pressure and the temperature is contained in the equation:

$$\ln p = \frac{\Delta H}{RT} - \frac{\Delta S}{R} \quad (1)$$

where p is the plateau pressure, ΔH the enthalpy change, R the gas constant, T the absolute temperature, and ΔS is the entropy change. Assuming that ΔH and ΔS are constant, a plot of $\ln p$ versus $1/T$ for plateau pressures from several isotherms, a straight line with slope $\Delta H/R$ and intersection $-\Delta S/R$ will result.

Equipment used to record PCI's are generally divided between volumetric equipment based upon measuring hydrogen uptake indirectly by observing pressure changes in the system and gravimetric equipment which is based upon measuring the hydrogen uptake directly as observed as mass change in the sample.

* Corresponding author. Tel.: +45 45 25 23 09; fax: +45 45 88 31 36.
E-mail address: av@kemi.dtu.dk (A.P. Vestbø).

0925-8388/$ – see front matter © 2007 Elsevier B.V. All rights reserved.
doi:10.1016/j.jallcom.2007.04.044

While gravimetric equipment has the advantage to add an online mass spectrometer during the analysis, there is a serious issue, which is that samples are contaminated during transfer to the equipment.

In this study we present a compact high-pressure microbalance made for obtaining PCI's of hydrogen storage materials gravimetrically and designed so it can fit inside a glovebox, allowing safe sample transfer. The details of the design is given below.

2. Description of the system

The high-pressure microbalance system consists mainly of three parts: (1) A microbalance in a pressure resistant casing, (2) controlled gas supply, and (3) temperature control.

2.1. Microbalance

An electromagnetic microbalance (we used an older Cahn model) was fastened inside a hollow stainless steel block, see Fig. 1. The block was sealed with a large O-ring and a plate, which was fastened with many bolts following the contour of the cavity. The block was pressure tested using oil under pressure and proved to resist pressure up to at least 250 bar.

An external controller for the microbalance utilizes the null balance principle [10], having a light source and null detector around one end of the double-beam, which has a foil flag that cuts off the ray from the light source (a LED) before it reaches the null detector (a photodiode). A correction voltage is supplied to the servo drive of the microbalance that moves the beam, so that a constant amount of radiation is received by the null detector. This voltage is proportional to the mass of the sample, and hence the mass of the sample can be recorded.

The sample and counterweight are placed upon stiff hooks at the end of thin flexible wires. The block with microbalance was fastened on a horizontal strong beam that could be fastened on the insides of the glovebox.

Fittings in the block with the microbalance was sealed with O-rings. However, in order to seal the sample and counterweight chambers where the temperature would approach 300 °C, copper gaskets were used. For each experiment these gaskets were replaced with fresh ones.

2.2. Controlled gas supply

Fig. 2shows the gas flow system that was built for the microbalance. The system operates by using software that receives input from the pressure transducers and sets current to the magnetic solenoid valves, pressure controller and mass flow controller. In our case, we programmed the software interface so we were able to execute measurements for a series of pressures, resulting in a PCI curve, for example by first raising the pressure sequentially for absorption and then decreasing the pressure sequentially for desorption. When decreasing the pressure, the gas flow runs from the microbalance and into the pressure and mass flow controller in the same direction as when increasing the pressure. Importantly, each time the sequence is changed from absorption (pressure increase) to desorption

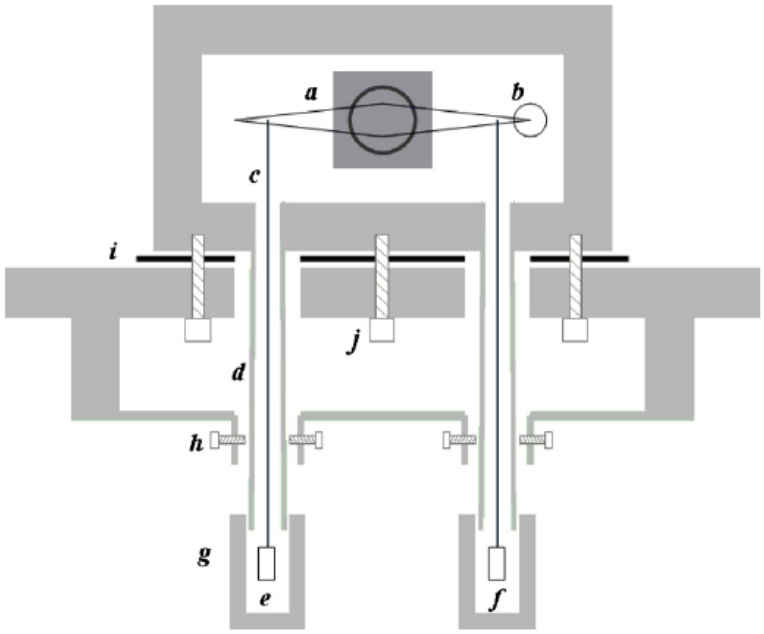

Fig. 1. Schematic diagram of the high-pressure microbalance. The material used is 316 stainless steel. (a) Electromagnetic microbalance with symmetrical double-beam; (b) LED and photodiode; (c) hang-down wire (0.1 mm Pt); (d) 10 mm tube; (e) sample hanging in Ni–Cr hook; (f) counterweight of inert material (Al or Al_2O_3); (g) round sample chamber to screw on the tube (via a fitting, not seen here); (h) screws to position the tube so the wire does not touch (four screws in a circle around each tube); (i) rubber (Viton®); (j) bolts.

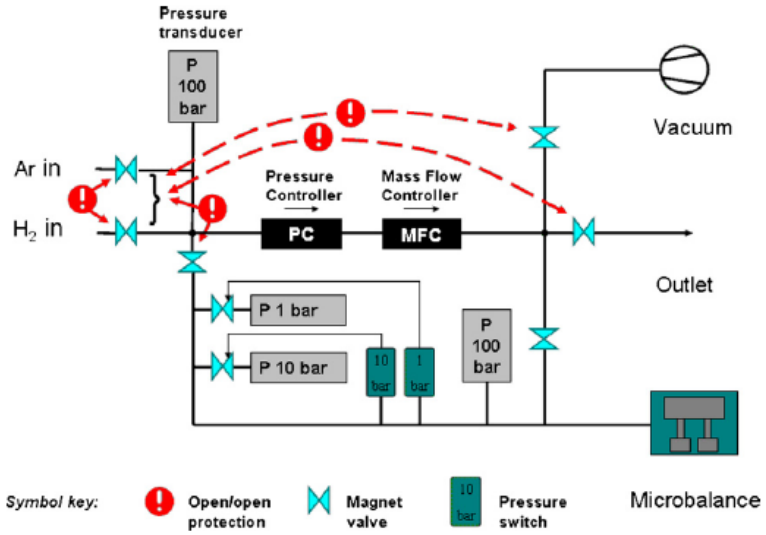

Fig. 2. Gas supply for the high-pressure microbalance. The pressure controller sets the pressure so that the differential pressure over the mass flow controller is no more than 5 bar. The open/open protections (controlled via software) ensure against damaging the low pressure transducers and various unwanted flow lines. The pressure switches protect the pressure transducers from higher pressure than they are meant for.

(pressure decrease), the gas reservoir between the pressure controller and valve to the hydrogen tank must be reduced in pressure to closely match the pressure in the microbalance cavity, so that there will not be a violent change in pressure when the valve between the microbalance and the pressure controller is opened, potentially knocking the sample off the hook.

In order to achieve a maximum range of resolution in the pressure reading, transducers for various ranges were used. Mechanical pressure switches were added to protect the lower range transducers against too high-pressure. Also, at the 1 bar transducer (Pirani in combination with piezo resistive) and at the vacuum outlet, overpressure valves were placed as an extra precaution to protect the equipment against accidental high-pressure.

The gas inlet to the microbalance was set in fittings that combine the tubes for the hangdown wires and sample/counterweight chambers (not seen in Fig. 1). In this way the hot gas in the chambers will not pass around the microbalance, which may not be able to sustain high temperatures.

2.3. Temperature control

Heating elements were placed around the sample and counterweight chambers. Sheets of flexible graphite (Papyex®) were used to provide a close connection between the heating elements and the chambers. Thermocouples were pressed down into the flexible graphite sheets. Furthermore, a thermocouple was placed inside the block with the microbalance, and thermocouples were welded through drilled holes in the fittings for the sample and counterweight chambers, so that the temperature could be read as close to the sample and counterweight as possible.

3. Testing of the system

The system was tested for stability with regard to variations in the readings of the mass as a function of time, pressure and temperature.

Fig. 3 shows the result for a stability test of the microbalance over several hours. As it is seen, there is some noise covering ca. 10 μg. However, this degree of noise did not increase significantly at neither temperatures up to 300 °C or pressures up to 40 bar.

The precision of ±5 μg for successive readings means that the precision in wt.% hydrogen uptake for a 1 g sample will be ±0.0005 wt.%.

The system was also tested for thermal convection effects. It is natural that there will be an effect of thermal convection as gas close to the sides of the sample and counterweight chambers heats up and moves upwards, then cools and moves down

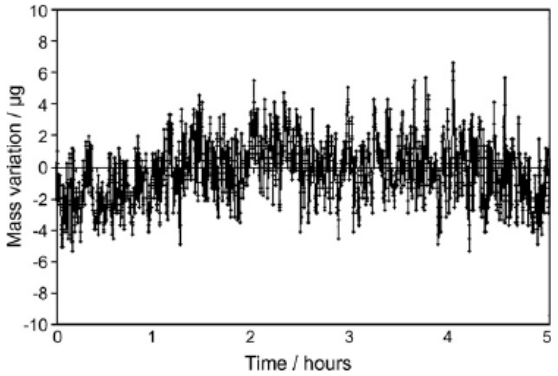

Fig. 3. Stability test of the microbalance. A 1 g aluminum sample and 800 mg aluminum counterweight in 10 bar hydrogen and 25 °C was used.

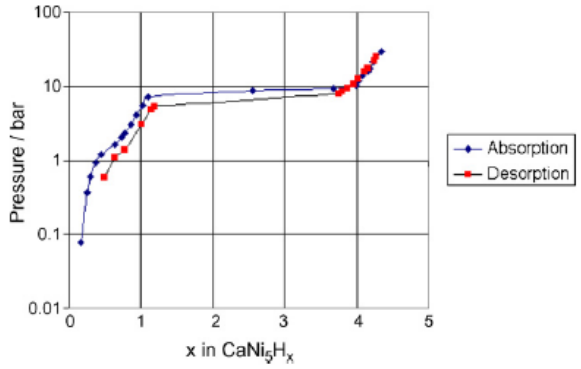

Fig. 4. PCI of $CaNi_5$ at 100 °C.

through the center of the tubes. The convection flow will exert force on the sample and counterweight effectively increasing the mass reading when the sample is larger than the counterweight (which will normally be the case). For this system, it was shown that while the mass reading increased 500 μg when heating the sample chamber to 200 °C and keeping the counterweight chamber at room temperature, the mass reading increased only 100 μg when heating both the sample and counterweight chambers to 200 °C. This shows that the thermal convection effect can be eliminated to some degree by heating on both chambers.

The temperature in the block with the microbalance was measured as a function of the temperature of the sample and counterweight chambers as they were heated up. The temperature only increased 3 °C close to the microbalance as a result of increasing the temperature in the chambers from room temperature to 300 °C. Hence, there will not be any risk of damaging the microbalance material while heating the sample to high temperatures.

No evidence of hydrogen embrittlement was observed even after lengthy exposure to hydrogen at high-pressures and temperatures. This is in agreement with a model by Shih and Johnson and experimental Nelson curves [11], which have shown that for plain carbon steel a safe area of operation at 300 °C for 100 h was up to at least 350 bar hydrogen pressure. At 100 bar for 100 h it was safe up to 350 °C. Embrittlement primarily stems from the formation of methane in the material, so plain carbon steel provides a worse scenario than austenitic stainless steel with a maximum carbon content of 0.15% compared to a maximum carbon content of 2.1% for plain carbon steel.

4. Using the system to obtain a PCI

In order to test the high-pressure microbalance for real use, a PCI for a $CaNi_5$ alloy, purchased from Ergenics, was obtained. A 750 mg sample was activated at 30 bar and 100 °C. Fig. 4 shows the result of an absorption and desorption cycle.

5. Conclusion

The design of a high-pressure microbalance for operation in a glovebox was presented. The precision of the system was ±5 μg corresponding to ±0.0005 wt.% for a 1 g sample. The system was able operate at temperatures up to 300 °C and pressures up to 100 bar hydrogen.

Acknowledgement

The present work is financially supported by the Danish Energy Authority and the Nordic Energy Research Programme.

References

[1] B. Bogdanovic, M. Schwickardi, J. Alloys Comp. 253/254 (1997) 1.
[2] P. Chen, Z. Xiong, J. Luo, J. Lin, K.L. Tan, Nature 420 (2002) 302.
[3] T. Ichikawa, S. Isobe, N. Hanada, H. Fujii, J. Alloys Comp. 365 (2004) 271.
[4] W. Luo, J. Alloys Comp. 381 (2004) 284.
[5] Y. Nakamori, G. Kitahara, S. Orimo, J. Power Sources 138 (2004) 309.
[6] Y.H. Hu, E. Ruckenstein, Ind. Eng. Chem. Res. 43 (2004) 2464.
[7] Z. Xiong, J. Hu, G. Wu, P. Chen, J. Alloys Comp. 395 (2005) 209.
[8] F.E. Pinkerton, G.P. Meisner, M.S. Meyer, M.P. Balogh, M.D. Kundrat, J. Phys. Chem. B 109 (2005) 6.
[9] T. Ichikawa, K. Tokoyoda, H. Leng, H. Fujii, J. Alloys Comp. 400 (2005) 245.
[10] D.A. Skoog, D.M. West, F.J. Holler, Fundamentals of Analytical Chemistry, Fundamentals of Analytical Chemistry, 7th ed., Saunders College Publishing, United States of America, 1996, pp. 780–787.
[11] H.-M. Shih, H.H. Johnson, Acta Metall. 30 (1982) 537.

Hydrogen storage in Li-Si-N ternary nitride (submitted)

Andreas Peter Vestbø[a, *], Qing Shi[b], Jens Oluf Jensen[a], Tejs Vegge[b], Allan Schrøder Pedersen[b], and Niels J. Bjerrum[a]

[a] *Department of Chemistry, Technical University of Denmark, Building 207, DK-2800 Lyngby, Denmark*
[b] *Materials Research Department, Risø National Laboratory for Sustainable Energy, Technical University of Denmark, DK-4000 Roskilde, Denmark*

* Corresponding author. Tel.: +45 45 25 23 09; fax: +45 45 88 31 36. E-mail address: av@kemi.dtu.dk

Abstract

The reaction of $Li_5SiN_3+2H_2 \rightarrow 3LiNH_2+2LiH+Si$ has a theoretical hydrogen capacity of 7.2 wt% and an enthalpy of reaction of ΔH = -34 kJ/mol H_2, and is therefore a potentially viable hydrogen storage system. In this study, the ternary nitride Li_5SiN_3 was synthesized by ball milling lithium nitride and elemental silicon under nitrogen atmosphere. The sample was heated up to 270 °C at 67 bar hydrogen and was able to absorb up to 3.8 wt% hydrogen. X-ray diffraction pattern (XRD) showed that lithium amide and lithium hydride were formed when absorbing hydrogen. Heating to 335 °C under about 0.1 bar released 2.5 wt%, which temperature programmed desorption (TPD) with mass spectrometry showed to be hydrogen. No ammonia was observed during the desorption process. X-ray diffraction showed the disappearance of lithium amide and lithium hydride, which indicates a reversible reaction of Li_5SiN_3 with hydrogen. Thermal gravimetric analysis (TGA) of the complimentary system of $3LiNH_2+2LiH+Si$ showed a mass change of 3.5 wt% beginning at about 100 °C and peaking at 220 °C. Attempted improvements in the system by using pre-ball milled silicon and including $TiCl_3$ as dopant showed a lower decomposition temperature of up to 10 K.

Keywords:
Hydrogen-absorbing materials; Gas-solid reactions; Hydrogen storage; Nitride; Hydride

1. Introduction

Materials that can reversibly react with hydrogen have been the object of much research during the last couple of decades. The interest in discovering materials with hydrogen storage properties, which infers practical use in cars, e.g., has accelerated greatly. While conventional metal hydrides have been studied extensively [1], new lines of research include carbon nanotubes [2] and metal-organic frameworks [3]. Since the discovery by Bogdanovic et al. in 1996 [4] that titanium-doped sodium aluminum hydride interacts reversibly with hydrogen at moderate conditions and reasonable speeds, research has turned much towards the so-called complex hydrides. In 2002, Chen et al. published results [5] that showed that lithium nitride can be thought of as a potential hydrogen storage material. These results led to studies of different systems involving metal amides and hydrides including $LiNH_2$/LiH [6-7], $LiNH_2/MgH_2$ [8], $Mg(NH_2)_2$/LiH [9], $Mg(NH_2)_2/MgH_2$ [10], $Mg(NH_2)_2$/NaH [11], and $Ca(NH_2)_2/CaH_2$ [12].

Good indicators for practical hydrogen storage materials are the enthalpy of reaction and the weight percentage of hydrogen. In 2004, Alapati et al. published calculations of the enthalpy of reaction for many reactions involving complex hydrides [13]. One promising results was that of

$$Li_5SiN_3 + 4H_2 \rightarrow 3LiNH_2+2LiH+Si \quad (1)$$

which had a theoretical hydrogen capacity of 7.2 wt% and an enthalpy of reaction of ΔH = -34 kJ/mol H_2 at ambient conditions.

In this study, this hydrogen storage system was examined from an experimental point of view, in order to determine the viability of Li_5SiN_3 as a good hydrogen storage material.

2. Experimental

Li_5SiN_3 was synthesized in two ways. In the first, lithium (Aldrich, 99%) was reacted with nitrogen at 1.3 MPa using no external heating in a steel reactor, according to the reaction

$$3Li + 1/2N_2 \rightarrow Li_3N \quad (2)$$

XRD showed that phases of both α-Li_3N and β-Li_3N were present, and the mass of the product showed a

yield of 99% Li_3N. The produced Li_3N was then ball-milled with Si (Alfa Aesar, 99.999%, 1-5 µm) under 3.5 MPa N_2 for 17 h according to the reaction:

$$5Li_3N + 3Si + 2N_2 \rightarrow 3Li_5SiN_3 \quad (3)$$

The product was characterized by XRD, which confirmed the synthesized Li_5SiN_3 phase.

In the other batch, Li_3N (Aldrich, ~80 mesh) and Si_3N_4 (Aldrich, 98.5%, <50 nm) were stoichiometrically ball-milled under argon according to the reaction:

$$5Li_3N + Si_3N_4 \rightarrow 3Li_5SiN_3 \quad (4)$$

XRD confirmed the product to be Li_5SiN_3.

A sample was taken from the first batch of Li_5SiN_3, and the hydrogen uptake was measured by a volumetrical method. The pressure was initially 6.7 MPa hydrogen, and the temperature was raised to 270 °C at 0.5 K/min. To test for reversibility, the hydrogenated sample was heated again at about 0.01 MPa from room temperature to 335 °C at 2 K/min, and the mass change was recorded. A part of the hydrogenated sample was taken out under argon and used for temperature programmed desorption (TPD). The sample was heated under argon flow, and levels of hydrogen and ammonia in the gas stream was recorded using a mass spectrometer.

A sample from the second batch was used to determine the phase changes in the system during the hydrogenation/dehydrogenation reactions. The sample was heated to 300 °C under 7 MPa hydrogen. Thereafter, it was heated to 400 °C and 600 °C under vacuum. The sample was characterized by XRD after each step.

Samples were also made from $LiNH_2$ (Aldrich, 95%), LiH (Aldrich, 95%), and Si (Alfa Aesar, 99.999%, 1-5 µm) in ratios 3:2:1, the reverse process of reaction (1). Two secondary samples were made with variations: one where the silicon powder had been pre-ball-milled for 17 h (hereafter denoted Si*) , in order to decrease the particle size, and one where the sample was doped with 1 mol% $TiCl_3$ (Aldrich, 99.999%). All samples were ball-milled under 0.1 MPa argon for 17 h.

The samples were characterized by thermal gravimetric analysis in order to measure the mass change by TPD and the phase change by XRD.

The volumetric method was used with a commercial gas reaction controller from Advanced Materials Corporation. TPD was made in a home-made reactor and an attached mass spectrometer. Thermal analysis was performed using a home made high pressure microbalance in an argon glovebox, which has been described elsewhere [14]. The applied ball mill was a Retsch PM 400 at 200 rpm with 200 ml steel vials with two 15 mm steel balls and seven 10 mm steel balls for the first batch and a Fritsch Pulverisette 7 at 450 rpm with 45 ml steel vials with five 14.5 mm steel balls for the second batch. XRD was made with a Bruker D8-advance diffractometer for the first batch and a Bragg-Brantano STOE diffractometer for the second (both with 40 kV, 30 mA, CuKα, λ = 1.5418 Å).

3. Results and discussion

The result of the hydrogenation of Li_5SiN_3 from the first batch is shown in Fig. 1. It can be seen, that the sample starts taking up hydrogen already from room temperature, although slowly. A total of 3.8 wt% hydrogen has been taken up after about 14 hours.

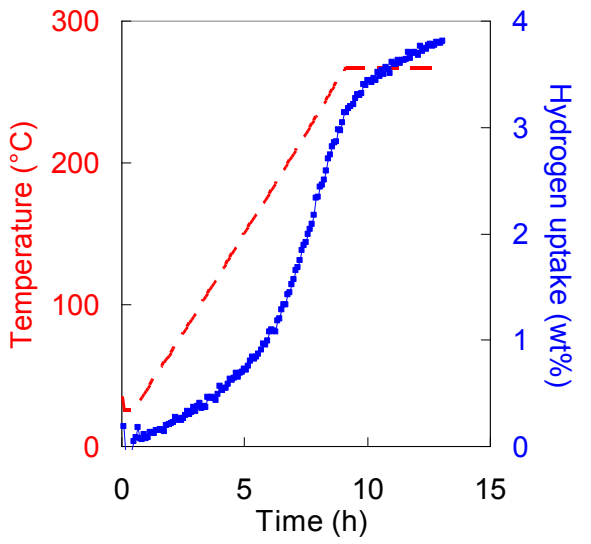

Fig. 1. Hydrogenation of Li_5SiN_3 at 6.7 MPa hydrogen. The temperature was raised at 0.5 K/min and kept steady at 270 °C. The broken line shows the temperature, and the thick line shows the hydrogen uptake as measured by the volumetric method.

As Fig. 2 shows, the hydrogenated sample starts releasing gas already at room temperature, and the release accelerates at around 180 °C. A total of 2.5 wt% is released.

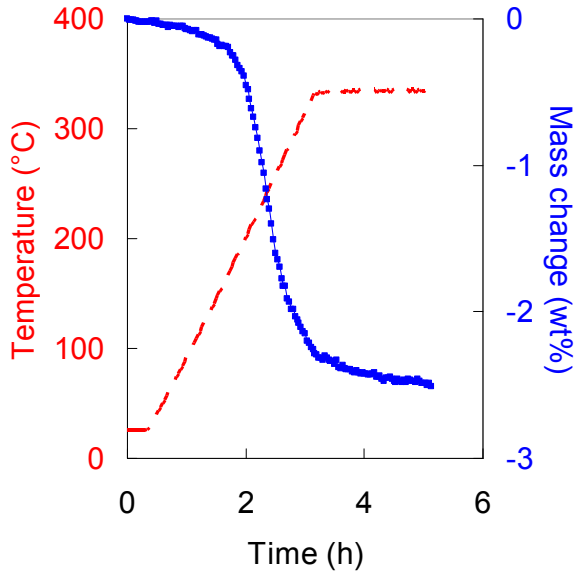

Fig. 2. Gas release of the hydrogenated Li_5SiN_3 sample at ~0.01 MPa hydrogen. The temperature was raised at 2 K/min. and was kept constant at 334 °C. The broken line shows the temperature, and the thick line shows the hydrogen release as measured by the volumetric method.

In order to verify that the released gas is hydrogen and not ammonia, which is a possible by-product for samples containing N/H species, Fig. 3 shows the result of the TPD of the hydrogenated sample. Hydrogen desorption data was recorded with a peak at ~260 °C. No ammonia was measured within the limits for the sensitivity of the mass spectrometer.

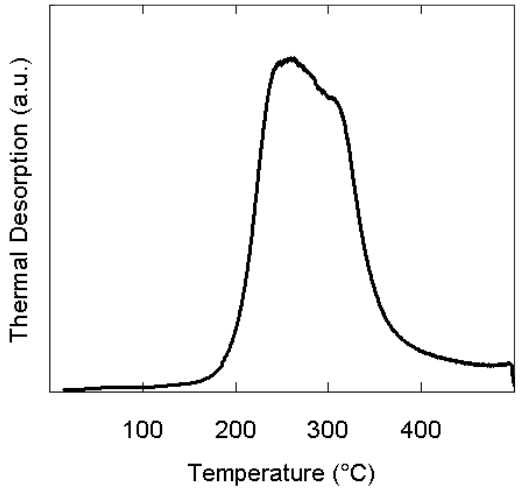

Fig. 3. Temperature programmed desorption of the hydrogenated Li_5SiN_3 sample. The temperature was increased from room temperature to 500°C at 2 K/min, and a flow of Ar carried the gaseous products to a mass spectrometer. The line shows the detected level of hydrogen. No ammonia desorption was detected within the limit of measurement.

The XRD spectra of Li_5SiN_3 are shown in Fig. 4, which were recorded at room temperature. After hydrogenation, phases of $LiNH_2$ and LiH appear which carry the hydrogen that has been taken up. This corresponds to reaction (1). However, the reaction is not complete, as Li_5SiN_3 is still present. As is seen in Fig. 1, the reaction slows down and ends with a weight percent that is about half of the theoretical amount.

After dehydrogenation at 400 °C, the $LiNH_2$ phase disappears, whereas a small amount of LiH appears to be present still. At 600 °C, the system produces a new phase, Li_2SiN_2.

These results show that reaction (1) is reversible to a certain degree.

Fig. 5 shows the TGA results of the $3LiNH_2+2LiH+Si$ system. It is seen that approx. 3.5 wt% is released at temperatures up to 300 °C. This end result is regardless of the variations of the systems made, with $TiCl_3$ or smaller Si-particles. However, a small decrease of about 10 °C in desorption temperature is observed for the $TiCl_3$-doped sample and a smaller decrease for the Si* sample. The $TiCl_3$-doped sample desorbs a little less than the other two. 3.5 wt% is approximately the weight loss which would result from present components of the well-known [15] competing reversible reaction

$$LiNH_2 + LiH \rightarrow Li_2NH + H_2 \qquad (5)$$

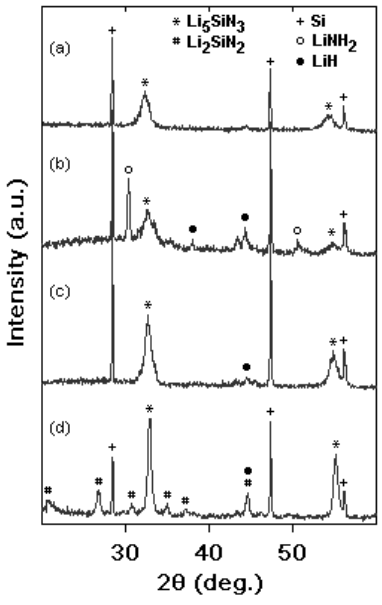

Fig. 4. XRD recordings for hydrogenation and dehydrogenation of Li_5SiN_3. (a) The ball-milled sample, (b) after hydrogenation at 300 °C and 70 bar hydrogen, (c) after dehydrogenation at 400 °C and vacuum, (d) after dehydrogenation at 600 °C and vacuum. The recurrent Si phase stems from an inherent Si calibration piece in the XRD apparatus.

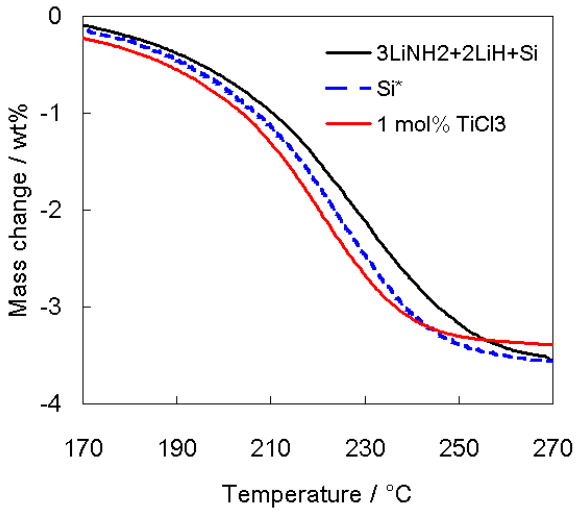

Fig. 5. Thermal gravimetric analysis for $3LiNH_2+2LiH+Si$, with variations of pre-milling Si for 17 hours to decrease particle size, denoted Si*, and doping with 1 mol% $TiCl_3$. The temperature was increased at a rate of 2 K/min.

However, as seen in Fig. 6, which shows the XRD results of heating $3LiNH_2+2LiH+Si$ in vacuum, a small amount of Li_5SiN_3 is created at 300 °C. This means, that the 3.5 wt% cannot stem completely from reaction (5). It is not easy to clearly distinguish $LiNH_2$ from Li_2NH based on XRD alone, so from these results, it cannot be concluded, whether Li_2NH has been produced, although this is probable, since there is not a full conversion to Li_5SiN_3, corresponding to 7.2 wt% hydrogen.

It is seen in the system at elevated temperatures, that the peaks for Li_5SiN_3 get clearer, and that the $LiNH_2$/LiN_2H peaks disappear at 600 °C. The peak for LiH is still present though, and this means, that the conversion to Li_5SiN_3 is not complete even at this high temperature.

TPD for $3LiNH_2+2LiH+Si$, see Fig. 7, shows that hydrogen is released from the system during desorption. As mentioned, the level of ammonia desorption, if any, was below the limit of detection. Furthermore, the use of Si* shows that the reaction proceeds with a slightly lower onset temperature and a significantly more pronounced peak at approx. 220 °C together with a much faster completion of the reaction. The reaction resulting in the bump around 450 °C for both samples cannot be detected from the XRD in Fig. 6, so it is at this point unclear what the reaction is.

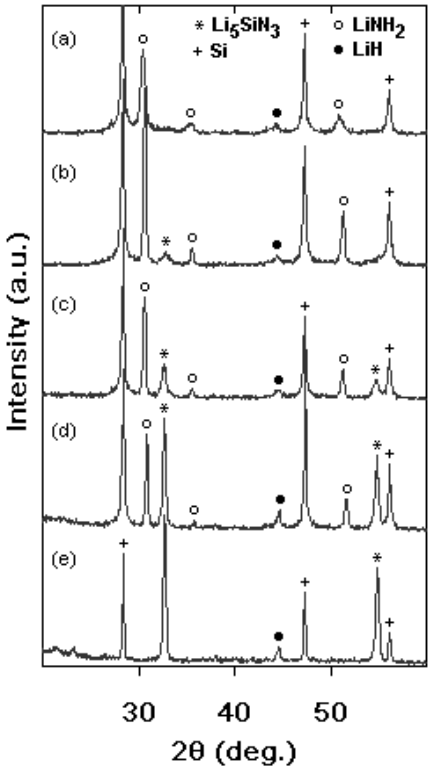

Fig. 6. XRD results for $3LiNH_2+2LiH+Si$ heated to various temperatures: a) Room temperature after ball-milling, b) 300 °C, c) 450 °C, d) 500 °C, e) 600 °C.

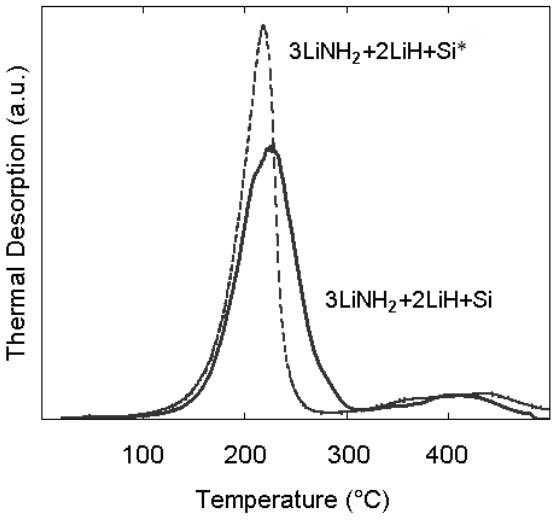

Fig. 7. Temperature programmed desorption of $3LiNH_2+2LiH+Si$ and $3LiNH_2+2LiH+Si$*. The temperature was increased from room temperature to 500°C at 2 K/min, and a flow of Ar carried the gaseous products to a mass spectrometer. The line shows the detection levels of hydrogen. No ammonia was detected within the limit of measurement.

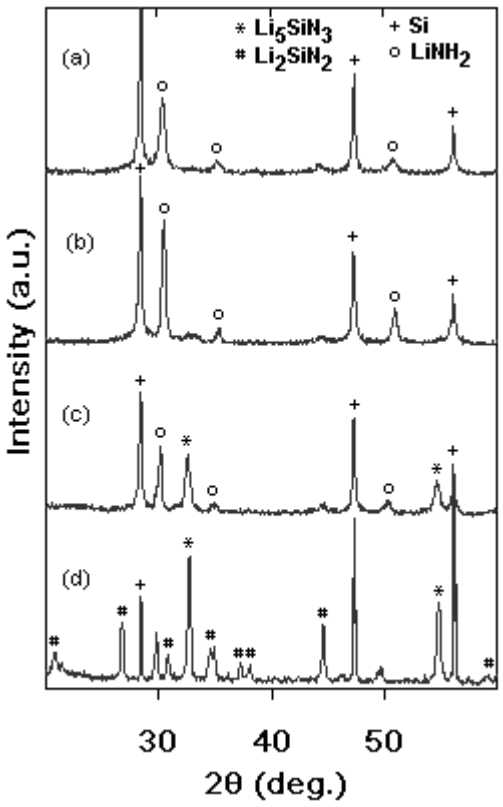

Fig. 8. XRD results for $3LiNH_2$+2LiH+Si doped with 1 mol% $TiCl_3$ heated to various temperatures: a) Room temperature after ball-milling, b) 300 °C, c) 450 °C, d) 600 °C.

XRD results for $3LiNH_2$+2LiH+Si doped with 1 mol% $TiCl_3$ shows an apparent delay in the production of the Li_5SiN_3 phase with regard to temperature. It is not visible until 450 °C, whereas it was visible in the undoped sample already at 300 °C. This means, that the reaction at 300 °C resulting in the mass loss observed in Fig. 5 could stem from reaction (5).

It thus appears that $TiCl_3$ in this system inhibits the formation of Li_5SiN_3 according to the reverse of (1). On the other hand it is seen that Li_2SiN_2 is created at 600 °C, which is comparable to the hydrogenated Li_5SiN_3 phase, which also yielded a Li_2SiN_2 phase at 600 °C. It would seem that $TiCl_3$ catalyzes the formation of Li_2SiN_2.

4. Conclusion

The results in this study show that Li_5SiN_3 react reversibly with hydrogen. It this work it was able to take up 3.8 wt% at 6.7 MPa and 270 °C. 2.5 wt% could be desorbed at temperatures up to 334 °C. It is shown that Li_5SiN_3 reacts with hydrogen to produce $LiNH_2$ and LiH, which act as hydrogen carriers. The system starting with $3LiNH_2$+2LiH+Si could desorb 3.5 wt% hydrogen below 300 °C.

5. References

[1] G. Sandrock, J. Alloys Comp. 293-295 (1999) 877-888.
[2] A. Züttel, P. Sudan, P. Mauron, T. Kiyobayashi, C. Emmenegger, L. Schlapbach, Int. J. Hydrogen Energy, 27 (2002) 203-212.
[3] M. Hirscher, B. Panella, Scripta Materialia, 56 (2007) 809-812.
[4] B. Bogdanovic, M. Schwickardi, J. Alloys Comp. 253-254 (1997) 1.
[5] P. Chen, Z. Xiong, J. Luo, J. Lin, K.L. Tan, Nature 420 (2002) 302.
[6] P.Chen, Z. Xiong, J. Luo, J. Lin, K.L. Tan, J. Phys. Chem. B 107 (2003) 10967.
[7] T. Ichikawa, S. Isobe, N. Hanada, H. Fujii, J. Alloys Comp. 365 (2004) 271.
[8] W. Luo, J. Alloys Comp. 381 (2004) 284.
[9] H.Y. Leng, T. Ichikawa, S. Hino, N. Hanada, S. Isobe, H. Fujii, J. Phys. Chem. B 108 (2004) 8763.
[10] Y. Nakamori, G. Kitahara, S. Orimo, J. Power Sources 138 (2004) 309.
[11] Z. Xiong, J. Hu, G. Wu, P. Chen, J. Alloys Comp. 395 (2005) 209.
[12] S. Hino, T. Ichikawa, H. Leng, H. Fujii, J. Alloys Comp. 398 (2005) 62-66.
[13] S.V. Alapati, J.K. Johnson, D.S. Sholl, J. Phys. Chem. B 110 (2006) 8769.
[14] A.P. Vestbø, J.O. Jensen, N.J. Bjerrum, J. Alloys Comp., 446-447 (2008) 703
[15] F.E. Pinkerton, J. Alloys Comp. 400 (2005) 76.